Friedrich-Alexander-Universität
Naturwissenschaftliche Fakultät

Bachelor Thesis
in Physics

Design and evaluation of a baffle system for the LOMlogger to be deployed in the IceCube Upgrade

Sky Blumberg

Supervisor: Dr. Martin Rongen

Erlangen Centre for Astroparticle Physics

Submission date: 15-04-25

Abstract

The IceCube Neutrino Observatory instruments ice to detect Cherenkov radiation emitted by secondary particles that are produced in interactions of cosmic neutrinos. In order to reconstruct the corresponding energy and direction in a precise way, knowledge about the optical properties of the instrumented ice is key. To quantify the amount of particulates interrupting light per slab of ice, a laser-based dust logger called LOMlogger will be deployed in the IceCube Upgrade. In order to block unwanted noise of light going through the water-filled borehole, a baffle system is designed. This thesis contributes to design decisions and successfully quantifies the drag of the baffles for two possible radii and positions in the device. Experimental data was recorded and evaluated for a test setup, as well as previously recorded data was reanalyzed. The drag results verify that a deployment in the IceCube Upgrade is possible.

Contents

1 Introduction

This chapter provides background information to the topic of this thesis. An introduction to neutrinos and their role in multimessenger Astronomy is given. Further, the IceCube Neutrino Observatory is described. In the last section of this chapter, the dust logger and the LOMlogger, devices to measure optical properties in IceCube, are explained.

1.1 Neutrino Astronomy

In 1912, Victor Hess discovered cosmic rays [24], charged particles like protons originating from astrophysical sources hitting the earths atmosphere. His discovery opened the possibility for multi-messenger astronomy - observing the universe not only with visible light, but also with the full spectrum of electromagnetic waves, gravitational waves, cosmic rays and neutrinos.

Neutrinos exist everywhere in an abundance, more than 60 billion pass through every square centimeter on earth in one second [27]. These neutrinos originate from different sources. They are produced in fusion reactions in stars like our sun or in manmade nuclear reactors, which were the first neutrinos to be detected [18]. Supernovas [25], blazars [4] and interactions of cosmic rays with the earths atmosphere also produce neutrinos.

Neutrinos are very suitable messengers for astronomy since they are almost massless and free of charge. Therefore, they do not get deflected by intergalactic or galactic magnetic fields. Due to their low interaction probability, their flux is almost unattenuated and allows conclusions about the processes that happen at the point of origin, for example in galactic cores [9]. These often are inaccessible for optical astronomy, since photons undergo scattering processes.
These factors make them excellent pointers to interesting sources, especially sources of cosmic rays, since the travel direction of neutrinos points straight back to the source, whereas the charged particles from cosmic rays are deflected in intergalactic and galactic magnetic fields [27].

For the past decades, several neutrino experiments have been and still are carried out to detect such astrophysical neutrinos, like KM3net [28], Super-Kamiokande [21] and IceCube. Neutrinos only interact via the weak force, which has a very low interaction probability. Therefore, detectors need to instrument a large volume of material to achieve useful statistics of neutrino interactions. To filter out muons produced in the atmosphere and other radiation causing noise, the detectors are often placed underground [27].

1.2 The IceCube Neutrino Observatory

The IceCube Neutrino Observatory, located at the geographic South Pole, detects neutrinos originating from astrophysical sources and the atmosphere of the earth. An overview of the components of the IceCube detector is seen in Figure 1.
The main IceCube detector instruments the Antarctic ice at depths of 1450 m to 2450 m below the ice surface.

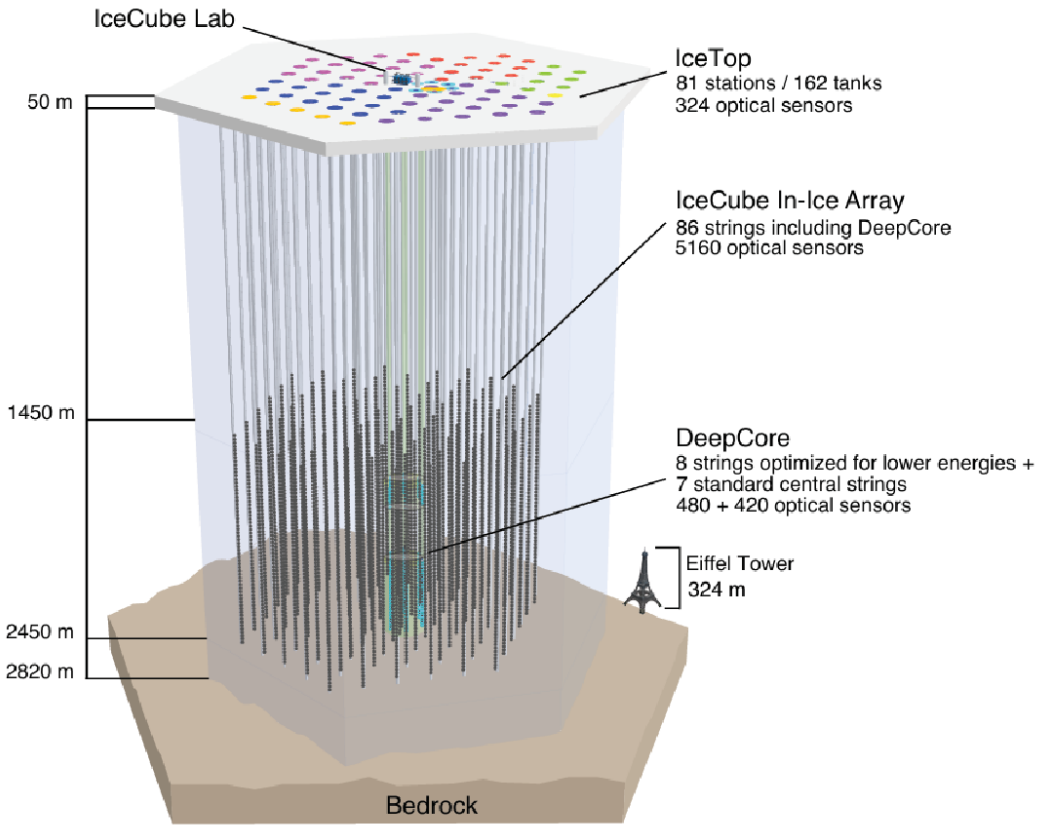

Figure 1: The IceCube detector and its components. Taken from Aartsen et al. [5]

Neutrinos interact with electrons or nucleons in the ice via Neutral Current (NC) or Charged Current (CC) interactions and produce an electromagnetic or hadronic shower. In NC interactions, only energy is transferred and the flavor of the neutrino can not be reconstructed. In CC interactions, the main secondary particle is the lepton corresponding to the flavor of the incoming neutrino, typically an electron or muon. The lepton flavor influences the event signature seen in the detector.

The secondary particle propagates through the ice with a speed faster than the local speed of light, and therefore emits photons via Cherenkov Radiation. To detect this light, Photomultiplier Tubes (PMTs) are placed inside the ice. 78 cables called strings are frozen in ice columns 125 m apart. Each string holds 60 Digital Optical Modules (DOMs) per string, which covers a total of one cubic kilometer of ice. The DOM is a pressurized glass sphere, housing one down-looking PMT with a diameter of 25 cm, calibration and electronics for readout and digitization [5].

The digital signal, produced when photons are detected by the optical modules, is then transferred to the IceCube Laboratory on the surface, where the data between the different DOMs is correlated, filtered and processed further [5]. Based on the position information, timing information and the amount of light that each PMT detected, the energy, flavor and direction of origin of the neutrino can be deduced.

A primary challenge is to distinguish neutrino events from muons originating from other sources like interactions of cosmic rays with the earths atmosphere. For this, several veto principles are used, including the IceTop detector array and using the earth as a shield by filtering for arrival direction.

In the center of the detector volume, 8 additional strings in narrower spacing form the DeepCore sub detector. With specialized DOMs with a higher quantum efficiency, the DeepCore is sensitive to lower neutrino energies [5] and measures neutrino oscillations [6].

The current setup was deployed between 2005 and 2011 and has made interesting discoveries since. This includes the discovery and characterization of the high-energy neutrino flux, originating from astrophysical sources [17, 10, 11]. An elevated flux of neutrinos was related to the direction of a blazar [4] and a galaxy [9], suggesting active galactic nuclei as sources for neutrinos. A neutrino flux from the Galactic plane was also identified [12]. With the DeepCore, the mixing parameters for neutrino oscillations were measured [6].

In an effort to observe neutrinos with higher energies of TeV to EeV, to get a higher event rate and improve the angular resolution of reconstructed events, a next generation of the detector called IceCube-Gen2 is planned. A total detector volume of $8\,\mathrm{km}^3$ surrounding the existing array will be instrumented with new, enhanced optical modules with increased photon sensitivity. With the new generation of the detector, sources of ultrahigh energy cosmic radiation will be resolved, deepening our understanding of the highest energy processes happening in our universe [3].

1.3 The IceCube Upgrade and the LOMlogger

The first step towards IceCube Gen2 is marked by the IceCube Upgrade, which will be deployed in the 2025/26 Antarctic summer. This upgrade adds 7 more strings inside the original detector array to enhance sensitivity and low energy detection possibility. The optical modules on these new strings are prototypes for Gen2. The multi-PMT Digital Optical Module (mDOM) houses 24 small PMTs for photon detection with directional information [16]. The D-Egg (Dual optical sensors in an ellipsoid glass for Gen2) sensor contains two large PMTs for limited directional information but lower power consumption [7]. The LOM is optimized for small borehole diameters, a large effective area and low poer consumption [14]. Additional calibration devices are deployed on the strings to measure ice properties and recalibrate the DOMs of the existing array. Among others, this includes the POCAM, a self-monitored high-intensity calibration light source [23] and acoustic sensors [26]. The results from these calibration modules are also used to recalibrate the data recorded by IceCube since its commissioning.

The deployment of the new strings is realized in a similar way as the strings of the original detector. A borehole is drilled with the Enhanced Hot Water Drill (EHWD) [15], which was developed for the unique requirements of IceCube. High pressurized hot water is pumped through a continuous hose to a nozzle in the drill head tip, melting the ice below and allowing the drill to advance further into the ice. The downgoing drill operations create the initial water filled hole. In a second phase, the borehole is reamed to the desired diameter while the drill is retrieved. Simultaneously, the diameter of the hole is logged with calipers on the drill [15].
After drilling operations, the hole refreezes. This sets a time window during which the deployment of the string is possible. The deployment includes suspending the bottom of the string into the borehole, while optical and other modules are attached one by one. After attachment and electrical connection of the uppermost module, the string is lowered in the "drop" phase with increased speed [5].

Ice properties
For precise reconstruction of energy and direction of the neutrinos arriving in IceCube, a detailed understanding about the glacial ice inside the detector volume and the way light propagates in that medium is necessary.

The glacial ice in IceCube has formed over millennia by the compression of snow [8]. Alongside the snow, particulates are deposited. These particulates mainly consist of mineral dust and volcanic ash. A layer of ice formed at the same time is called an isochron and has a similar amount of particulates.
The amount of particulates determines the effective scattering length of photons propagating through the ice. Other factors determining the scattering and absorption length are seasalts, liquid acid droplets and soot [22]. Additionally, the attenuation of light in the glacial ice is also influenced by the direction of glacial flow. This introduces an anisotropy to the direction of light propagation [8]. In ice layers above the detector volume (depths of up to $\approx 1350\,\mathrm{m}$ [2]), air bubbles decrease the effective scattering length significantly [13].

In Figure 2, the layers of the Antarctic ice can be seen from a stratigraphy measurement.

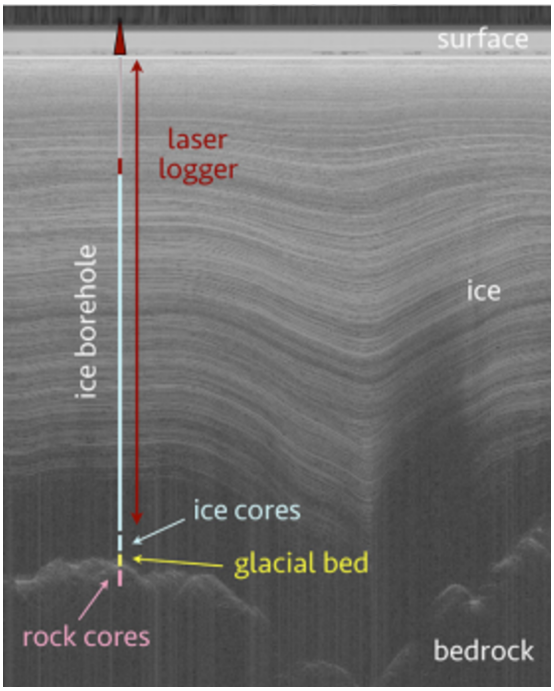

Figure 2: Radargram showing the stratigraphy of bulk ice in IceCube [29]

The bedrock underneath the ice is not even but instead has valleys and hills. The ice layers follow that shape and vary in thickness depending on position. This means, isochrons are not located at the same depth for every borehole location in the detector. Measuring the dust amounts per depth in one borehole does not provide accurate information about the whole detector volume. Measurements at several different positions throughout the detector is necessary for an accurate 3D-mapping of the ice layers [30].

Knowledge about the depth-dependency of the scattering length is helpful for accurate reconstruction of photon propagation in the IceCube detector. For this purpose, the "dust logger" was developed and deployed in 8 different boreholes of IceCube. The respective locations are shown in Figure 3. To probe the ice, laser light is emitted horizontally and scattered in the ice surrounding the borehole. Some light is scattered back and is detected with an optical sensor located about 1 m downward on the string. The intensity of the incoming light corresponds to the effective scattering length of the ice at the current position of the laser [2]. In Figure 3 on the left, the measured optical signal over depth is shown. Prominent features like the large peak at around 2050 m depth are visible in every borehole but the position is shifted slightly in depth. This shift is due to the tilt of ice layers described above.
The dust logger provided valuable insights into the particulate content in Antarctic ice, which is not only useful for calibration of the IceCube detector, but also interesting for reconstruction of paleoclimate records [2].

The LOMlogger
For the IceCube Upgrade, a new version of the dust logger called LOMlogger is developed. It is designed to attach to the bottom of a string. The scan is performed

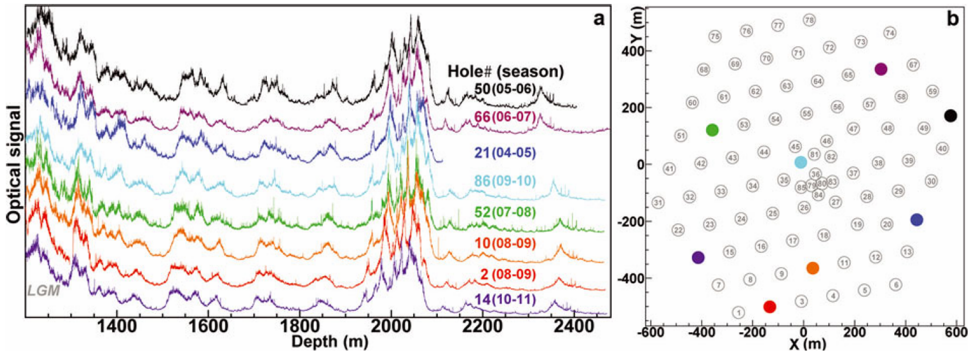

Figure 3: On the left (a): The optical signal per depth of south pole bulk ice, measured by the dust logger. Different colors indicate different boreholes where the measurement was taken. The signal in hole 21 stops at around 2100 m due to an instrument failure. The borehole locations on the detector grid are marked on the right (b). Y-axis points to Greenwich, UK, coordinate (0,0) is the center of the detector. (Taken from Aartsen et al. [2])

during the deployment of the string and the device will remain in the ice after finishing measurements. This saves fuel and time in comparison to retrieving the LOMlogger. For Gen2, it would be ideal to deploy a LOMlogger on every string.

The working principle of the LOMlogger is seen in Figure 4, it is similar to that of the dust logger. The LOMlogger is attached at the bottom of the string. During deployment of the string, the LOMlogger scans the ice layers while being lowered into the water filled borehole. The Precision Optical Calibration Module (POCAM) at the bottom, a laser system modified for this usage, sends out a fan of 405 nm pulsed laser light horizontally into the ice. This wavelength is used specifically because it is close to the absorption minimum for glacial ice [13]. The light gets scattered at the particulates trapped inside the ice. A fraction of it is scattered back in such a way that it reaches the LOM seen at the top of Figure 4, which detects these photons. From the amount of light arriving at the LOM, a relative value for the scattering length of the ice layer can be calculated for the current position of the LOMlogger. Due to the very well defined geometry of the laser fan-out, this measurement is very precise in terms of depth resolution. The predecessor device achieved a depth resolution of a few millimeters [2]. To get an absolute value for the scattering length, additional scans with flashed LEDs between different strings will be done. After deployment, and therefore end of LOMlogger operation, the LOM can be used for regular neutrino detection purposes.

Not all light emitted from the POCAM laser enters the ice. Some of it gets scattered and reflected inside the water-filled borehole and can reach the LOM without ever going through the ice. To block this noise that contains no information about the dust layers, a baffle system is developed.
A "baffle" is a circular brush consisting of black Polypropylen bristles with a diameter of 0.8 mm. The bristles are clamped in an aluminum rail with ≈1 cm width and depth. The two types of prototypes used for this thesis are seen in Figure 6.
The baffle system includes baffles at two different positions as seen in Figure 7 on the

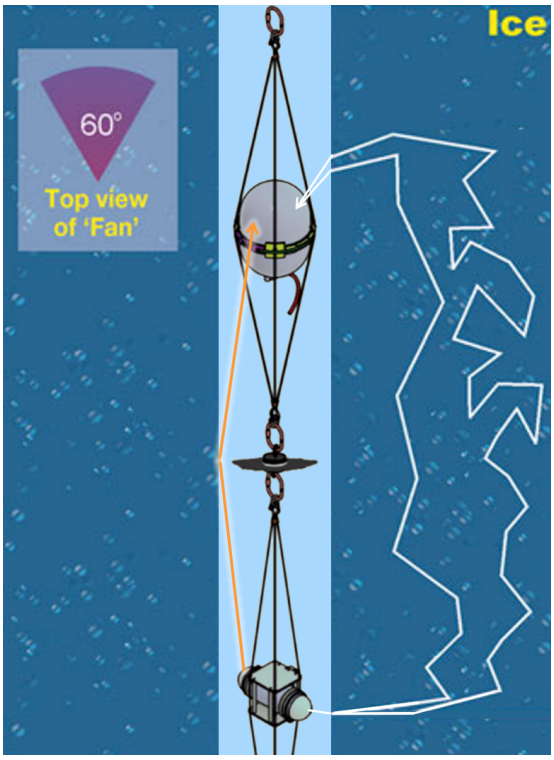

Figure 4: Measurement process of the LOMlogger measuring ice stratigraphy while being lowered into the borehole ([]adapted from Aartsen et al. [2]). The white lines are exemplary light rays emitted by the POCAM laser at the bottom and scattered in the ice in a way that the LOM at the top is reached. The orange light path is an example for light passing through the borehole, which is noise in the detector.

left. The two mechanically possible positions are a "top baffle" in the middle between POCAM and LOM, and a "bottom baffle" located directly on top of the steel harness containing the POCAM.
The bottom baffle is not supposed to be circular. Instead, two bristle segments are supposed to cover the area right above the laser emitting parts of the POCAM. The other two segments are cut out in order to leave space for cables and water flow. This segmentation was not done for this thesis due to time restrictions.

The light attenuation properties and therefore reasoning behind these baffles, their outer diameter and their positions was analyzed in a previous Bachelor Thesis by Fleischmann [20]. It is currently planned to deploy a stack of two top baffles with a diameter of 50 cm which will not brush against the sides of the borehole, and one segmented bottom baffle with a diameter of 54 cm which is supposed to drag along the walls of the borehole [30] to block light at the edges of the hole. The exact diameter of the borehole during deployment is not known since there is a time window for deployment, during which the hole refreezes and changes diameter.

Maintaining a constant speed during deployment is important, and for that reason the drag of all components on the string have to be considered. The goal of this work is to determine the drag of the baffle system at the targeted deployment speeds of 0.15 m/s to 0.3 m/s [30]. A previous Bachelor Thesis by Tekbiyik [32] developed the lab setup and experimental methods and recorded first measurements for the top baffle type. This work performs a reanalysis of those results and adds newly measured data. Additionally, the drag of the bottom baffle was measured.

An overview over the forces acting on the system and the calculations needed to determine the drag are given in section 2. A description of the experimental setup is given in section 3. The method of analyzing the data is described in section 4, as well as the process of finding the best way to do so. In section 5, the determined drag values depending on deployment speed are presented.

2 Drag theory and calculations

To obtain drag values, a detailed understanding about the forces acting on the experimental system are key. This chapter describes the acting forces and presents the calculations needed to obtain the drag force of the baffles.

The drag force is a force acting on objects moving through gases or fluids. It is characterized by the movement of the fluid around the object and acts against the direction of movement of the object. The flow around an object can either be laminar or turbulent. In both regimes, the drag force F_{D} depends on the velocity v of the object. For laminar flow, this dependence is linear $F_{\mathrm{D,laminar}} \propto v$, while for turbulent flow, the dependence is quadratic $F_{\mathrm{D,turbulent}} \propto v^2$ [19]. Even without knowing which regime is the case for our experiment, it is therefore important to measure the drag force at the targeted speeds.
Other factors that determine the drag force as well as friction in the pulley system do not need to be known or quantified here: Drag measurements were done with the baffle attached (baffle measurements) and without the baffle attached (reference measurements), without changing anything else in the setup. The drag force on the baffle is given by the difference between the measured drag force of baffle measurements and reference measurements. The calculations necessary for this are described in this section.

An overview of all acting forces on the system and baffle is seen in Figure 5. In section 3, a detailed explanation of the setup is provided.
During a measurement, the baffle is accelerated upwards. Forces contributing to that acceleration are defined to be positive. Forces acting against this direction of movement have a negative algebraic sign.

All acting forces on the system without attached baffle (blue and black in Figure 5), which are reference measurements, are in equilibrium described by

$$F_{\mathrm{measured,ref}}(v) = F_{\mathrm{G,counterweight}} + F_{\mathrm{buoyancy,sys}} - F_{\mathrm{G,sys}} - F_{\mathrm{drag,sys}}(v) - F_{\mathrm{friction}}(v). \quad (1)$$

$F_{\mathrm{measured,ref}}(v)$ is the speed-dependent net force that is measured with reference measurements. $F_{\mathrm{G,counterweight}}$ is the weight force acting on the counterweight outside the tank. The subindex $_{\mathrm{sys}}$ marks forces acting on everything on the tank side of the pulley system apart from the baffle, like the buoyancy $F_{\mathrm{buoyancy,sys}}$, the weight force $F_{\mathrm{G,sys}}$ and the speed-dependent drag force $F_{\mathrm{drag,sys}}(v)$ of all parts suspended in water. F_{friction} describes all friction that is introduced by the wheels of the pulley system or any friction in air.
With the baffle attached, additional forces acting on the baffle (red in Figure 5) have to be considered:

$$\begin{aligned} F_{\mathrm{measured,baf}}(v) =& F_{\mathrm{G,counterweight}} + (F_{\mathrm{buoyancy,sys}} + F_{\mathrm{buoyancy,baf}}) - (F_{\mathrm{G,sys}} + F_{\mathrm{G,baf}}) \\ & - (F_{\mathrm{drag,sys}}(v) + F_{\mathrm{drag,baf}}(v)) - F_{\mathrm{friction}}(v) \\ =& F_{\mathrm{measured,ref}}(v) + F_{\mathrm{buoyancy,baf}} - F_{\mathrm{G,baf}} - F_{\mathrm{drag,baf}}(v) \end{aligned} \quad (2)$$

The index $_{\mathrm{baf}}$ marks all forces acting on the baffle and its mount, namely the speed-dependent net force $F_{\mathrm{measured,baf}}(v)$, the buoyancy $F_{\mathrm{buoyancy,baf}}$, the weight force $F_{\mathrm{G,baf}}$

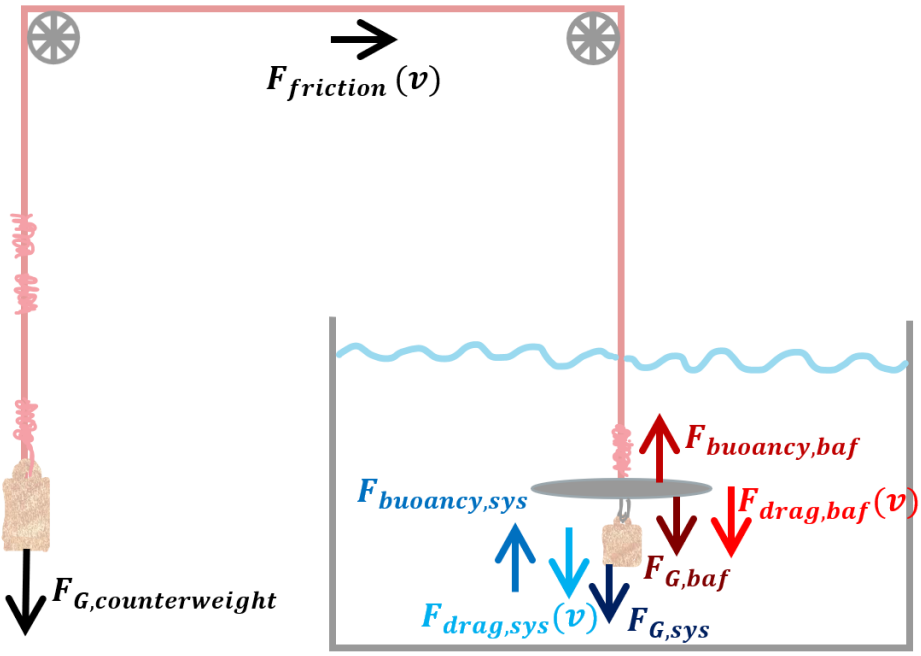

Figure 5: Forces acting on the pulley system (blue and black) and baffle (red), if attached, during measurements.

and the speed-dependent drag force $F_{\text{drag,baf}}(v)$ that we want to determine. The last step was obtained using Equation 1.
The general weight dependence of the friction is not considered here, so we approximate $F_{\text{friction,ref}}(v) = F_{\text{friction,baf}}(v) = F_{\text{friction}}(v)$.

If we solve Equation 2 for $F_{\text{drag,baf}}(v)$, we obtain

$$F_{\text{drag,baf}}(v) = F_{\text{measured,ref}}(v) - F_{\text{measured,baf}}(v) + F_{\text{buoyancy,baf}} - F_{\text{G,baf}}. \tag{3}$$

The drag force of the baffle is therefore obtained by subtracting the net force of the baffle measurement from the net force of the reference measurement, plus the additional, constant term $+F_{\text{buoyancy,baf}} - F_{\text{G,baf}}$. This term describes the net force acting on the baffle submerged in water at rest.

This constant term was determined using spring scales. The results of these measurements done for the setup of this thesis are seen in Table 1. A measurement for the bottom baffle and u-screws with the spring scale was not done, since they float on water. Since reference measurements for the top baffle were done without attached eye bolt, the constant term for the top baffle measurements of this thesis is $-2.4\,\text{N}$. It is smaller than zero since the weight force of the baffle with the bolt is greater than the buoyancy force.
For measurements from Tekbiyik [32], the value for the constant term of the net force acting on one top baffle in water is $3.05\,\text{N}$ as given in the thesis. Ergo the setup with one baffle layer attached experiences an additional force upward in comparison to the setup for reference measurements.

Table 1: Spring scale (in air and water) and scale (last column) measurements of different components of the setup for measurements for this thesis.

	in air	in water	scale
top baffle and eye bolt	$(14.8 \pm 0.2)\,\mathrm{N}$	$(2.4 \pm 0.2)\,\mathrm{N}$	$(1.503 \pm 0.001)\,\mathrm{kg}$
weight below top baffle	$(6.1 \pm 0.1)\,\mathrm{N}$	$(5.4 \pm 0.1)\,\mathrm{N}$	$(0.496 \pm 0.001)\,\mathrm{kg}$
eye bolt	$(7.3 \pm 0.1)\,\mathrm{N}$	$(6.3 \pm 0.2)\,\mathrm{N}$	$(0.709 \pm 0.001)\,\mathrm{kg}$
POCAM harness	$(26.5 \pm 0.1)\,\mathrm{N}$	$(19 \pm 1)\,\mathrm{N}$	$(2.838 \pm 0.001)\,\mathrm{kg}$
POCAM harness and bottom baffle	$(29 \pm 1)\,\mathrm{N}$	$(19.0 \pm 0.5)\,\mathrm{N}$	$(3.113 \pm 0.001)\,\mathrm{kg}$
bottom baffle and u-screws			$(0.340 \pm 0.001)\,\mathrm{kg}$

For two baffle layers, this value was doubled, since the two layers were identical and therefore have the same buoyancy and weight force. This leads to a value of 6.1 N for the net force on two layers of the top baffle.
For the bottom baffle, the net force in water is determined to be 0 N. The spring scales were not able to detect the small difference of the baffle compared to the weight of the harness.

From the reference and baffle measurements, one gets timestamps t in relation to distances x that the system traveled. Deriving the distance twice with respect to time gives the velocity $v = \frac{\mathrm{d}x}{\mathrm{d}t}$ as well as the acceleration of the system: $a = \frac{\mathrm{d}^2x}{\mathrm{d}t^2}$. For the setup with baffle as well as for the setup for reference measurements, the net force per measurement F_{measured} was calculated by using the inertial mass of the system m_{inertial} :

$$F_{\mathrm{measured,baf/ref}}(v) = m_{\mathrm{inertial,baf/ref}} \cdot a_{\mathrm{baf/ref}}(v) \tag{4}$$

This is then inserted into Equation 3 to obtain the drag force.

In principle, the gravity of the rope should be considered, since the rope length on each side of the pulley changes by almost 2 m during measurement and is likely at a different length for reference and baffle measurements where the acceleration values are compared. For example, the velocity of 0.2 m/s might be reached after 10 cm in reference measurements but only after 50 cm in baffle measurements, which changes the influence of the rope gravity, it does not cancel out. The theoretical maximum of this change in net force is $\pm\Delta F_{\mathrm{G}} = g\Delta m_{\mathrm{rope,2m}} = 2.252\,\mathrm{N}$ and it was not considered in calculations.

(a) Top baffle with 50 cm outer diameter (b) Bottom baffle with 60 cm outer diameter

Figure 6: Baffle prototypes used for the experiments of this thesis

3 Experimental methods

In this section, an explanation of the baffles and their fixtures is given. Furthermore, the experimental setup that was used to determine the drag force of the baffles is described in detail.

3.1 The baffle system

The baffle prototypes used in this thesis are shown in Figure 6. The baffles in their respective fixtures are shown in Figure 7 on the right side.
The top baffle (see top right in Figure 7) is clamped between two Polyactide (PLA) 3D-printed disks. A cylinder sitting in the center of the baffle prevents it from slipping out. Additionally, a lip at the edge of the disks sits on the bristles and prevents the aluminum rail from bending open. The clamping is realized with an eye bolt going through the center of the disks, secured with an eye nut. For measurements from Tekbiyik [32], this bolt and nut was a 3D-printed prototype. For this thesis, the bolt and nut used was made of steel.
This fixture was developed by Tekbiyik [32]. The dimensions were modified slightly for the measurements of this thesis. It allows for 1 or 2 layers of the baffle to be stacked. In the final LOMlogger design, the eyes of the nut and bolt will attach to steel ropes holding the POCAM and LOM.

The bottom baffle sits on top of the harness which will contain the POCAM (see bottom right in Figure 7). The lid of the harness with additional holes was 3D printed with PLA. The aluminum ring of the baffle is held in place by u-screws that go through the holes in the lid and are secured with nuts on the bottom side. At the vertical edges of the metal box, four steel ropes are attached that end in a carabiner $\approx$1 m above the baffle.

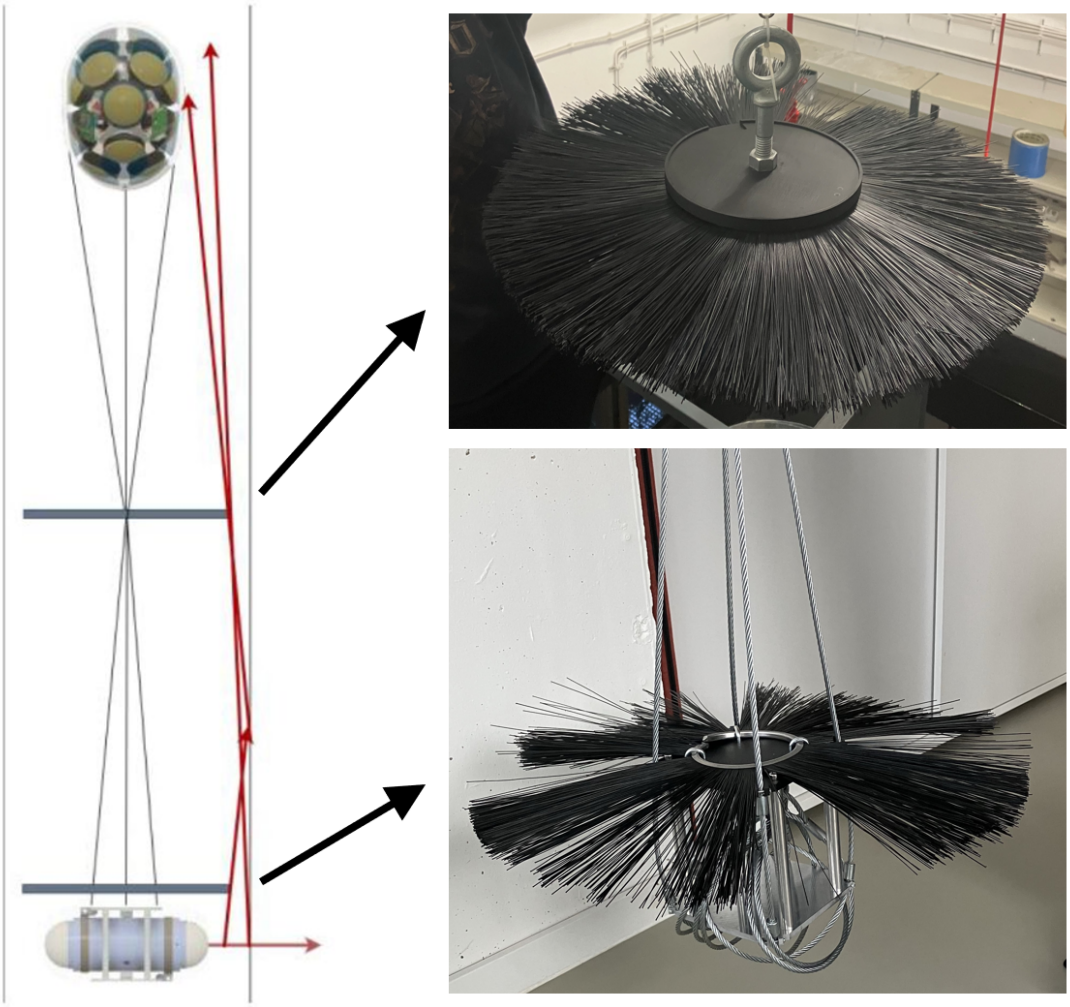

Figure 7: On the left, the positioning of baffles inside the LOMlogger is shown. The LOM is shown on top, the POCAM at the bottom, the blue lines represent the two chosen baffle positions. The red lines represent exemplary light rays emitted from the POCAM. On the right, the top baffle and the prototype for the bottom baffle in their respective fixtures are shown.

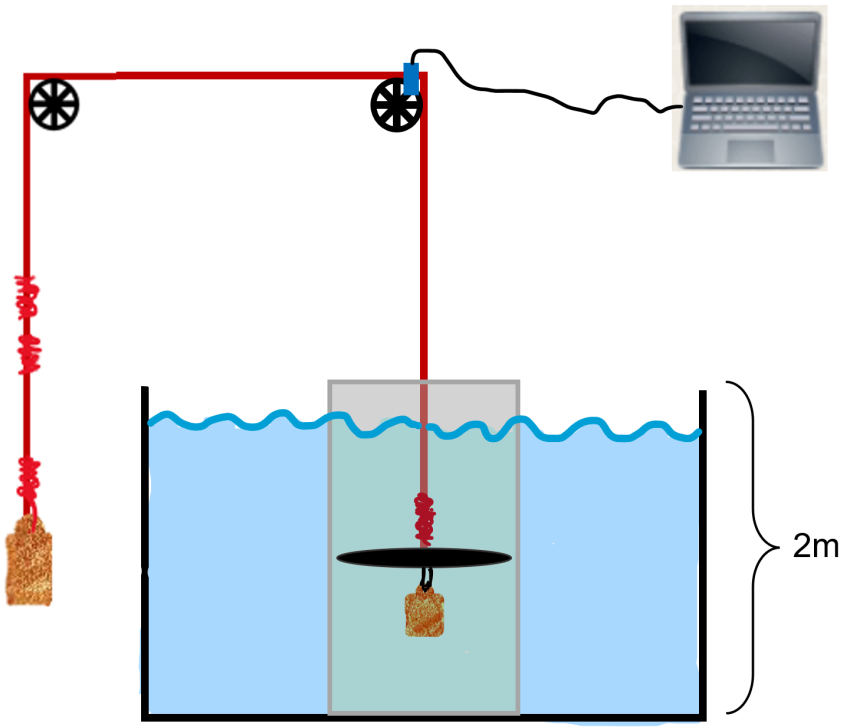

Figure 8: The experimental setup used to measure drag force of the baffle. The baffle with additional weight underneath is suspended in a 2 m deep water tank and attached to a rope with a total of 4 knots, which is lead over two ball bearing mounted wheels and connects to a variable counterweight outside the tank. At one of the wheels, an infrared sensor connected to a micro controller detects transitions of spokes and sends these timestamps to a computer.

3.2 Experimental setup

To determine the drag force of the baffles experimentally, the previously constructed setup by Tekbiyik [32] was used. The measurement setup is shown in Figure 8.

The top or bottom baffle on its respective fixture is suspended into a steel pipe with a diameter of 56 cm, serving as a borehole simulation. Since the borehole will be filled with water, the steel pipe is placed inside a water tank. The height of water inside the pipe was ≈180 cm.
The baffle fixture is tied to a rope with a total length of 10 m for this thesis and ≈ 7.9 m for data from Tekbiyik [32]. The rope has a diameter of 12 mm and a weight of 0.0574 kg/m. The rope is led via two 3D-printed wheels with a diameter of 85.12 mm, mounted in ball bearings to reduce friction. On the other side of the rope outside the tank, a variable counterweight of 2 kg to 5 kg is attached onto the rope with a carabiner to accelerate the system.
For measurements with the top baffle, an additional weight of 1 kg for measurements done by Tekbiyik [32] and 0.5 kg done by this work was attached underneath the baffle with a carabiner, since the baffle itself floats on water. For bottom baffle measurements, this additional weight was not necessary since the steel harness weighs enough to pull

the baffle underwater.

The top baffles used for the drag experiments (see Figure 6 (a)) have an outer diameter of 50 cm. This means the bristles did not touch the wall of the simulated borehole.
The bottom baffle prototype (see Figure 6 (b)) used for the experiments has a diameter of 60 cm. This diameter is larger than the one used for the final LOMlogger design. A larger diameter was necessary so that the bristles brush against the wall of the steel pipe in the test setup.
The amount of bristles was not specified for production, this resulted in the bottom baffle prototype to have a significantly lower bristle density than anticipated. This has a significant influence on the drag force. Knowledge about the drag of this prototype is still helpful to better understand the influence of bristles brushing against the walls. For the final LOMlogger design, a higher bristle density is wanted in order to block enough light.

The total inertial masses for the different setups were determined using weight scale measurements shown in Table 1, since the inertial and gravitational mass have the same value. The inertial mass includes the weight of the counterweight, the rope, the two carabiners and the baffle, its fixtures and, for the top baffle, the weight attached below.

The procedure of one measurement started with the top or bottom baffle held in place at the bottom of the pipe with zero velocity. At time $t = 0$, the pulley system was released to act freely. The counterweights accelerate the system and pull the baffle through the water inside the pipe, until the baffle reaches the water surface. This process was repeated several times and done with varying counterweights to achieve different velocities. To isolate the influence of the baffle on the drag force, for each measurement with the baffle, a second reference measurement was done where the baffle was not attached. The difference of measured drag forces is the drag force of the baffle. A detailed description of all acting forces is provided in section 2.
For all measurements with the top baffle from both this work and Tekbiyik [32], the reference measurements were done without the baffle and without the eye bolt. For measurements with the bottom baffle, only the baffle and the screws were removed for reference measurements.

The available data from Tekbiyik [32] include top baffle measurements of one baffle layer with counterweights of 2.5 kg and 4.5 kg with each three repetitions with and without baffle. Additionally, there are measurements of two top baffles stacked with counterweights of 2.5 kg, 4 kg and 4.5 kg with each three repetitions, and 5 kg with two repetitions.
This thesis recorded data for one top baffle layer with counterweights of 2 kg, 3 kg and 4 kg with each five repetitions. For the bottom baffle, six repetitions of measurements were done for a counterweight of 3 kg, 4 kg and 5 kg. The masses of the counterweights were chosen due to practical reasons and according to the velocity of the system during measurement, since this is aimed to be in the range of targeted deployment speeds of the LOMlogger.

In additional measurements with the bottom baffle, a camera was attached to the

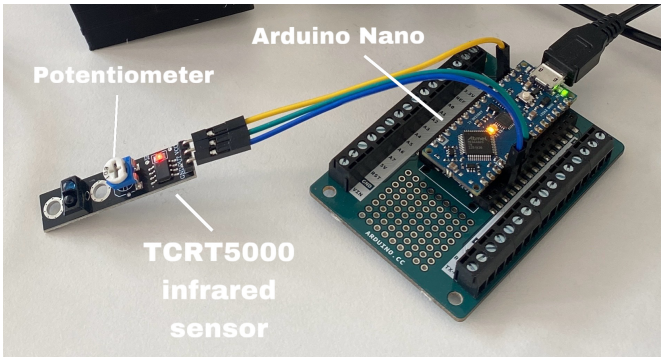

Figure 9: The TRCT5000 infrared sensor connected to an Arduino Nano micro controller. Taken from Tekbiyik [32] since the exact same equipment was used.

steel ropes above the baffle. Videos were recorded during a measurement process with different counterweights to visually analyze the behavior of the bristles at certain speeds.

3.3 Recording data

To record measurement data, the infrared sensor TRCT5000 [31] was used to detect the transitions of the spokes of the wheel. The sensor sends out infrared light which gets reflected at the next object in the way. The intensity of the reflected light is compared to a threshold value which can be adjusted with a potentiometer, and either sends out a digital 1 or 0 at the data pin. This digital signal therefore holds the information whether an object (in our case a spoke of the wheel) is in front of the sensor or not. The wheel used in the setup has 8 spokes of the same width as the gaps in between. This design leads to 16 equidistant transitions per full rotation of the wheel. The sensor data was sent to an Arduino Nano microcontroller [1] that calculated the timestamps of each change in signal with a program adopted from Tekbiyik [32]. The microcontroller was connected to a computer to save the data and perform further analysis. The sensor and Arduino setup is shown in Figure 9.

Systematic errors

In the original data from Tekbiyik [32], the infrared sensor periodically created additional timestamps that did not correspond to transitions between a spoke and a gap. Instead, these timestamps were caused by a non-even surface on one of the spokes due to imperfections in the 3D-printed surface of the wheel. To account for this systematic error, the data recorded previous to this work was corrected by summing up the time intervals measured during the transit of one spoke. The functionality of this correction is depicted in Figure 10. The affected timestamps were selected manually.
This systematic error was successfully eliminated by taping clear glossy adhesive tape over the problematic spoke surface. This eliminated the issue for all further measurements done for this thesis. The difference due to this tape is shown in Figure 11, where a deceleration of the wheel only by friction inside the bearings is shown before and after attaching the tape.

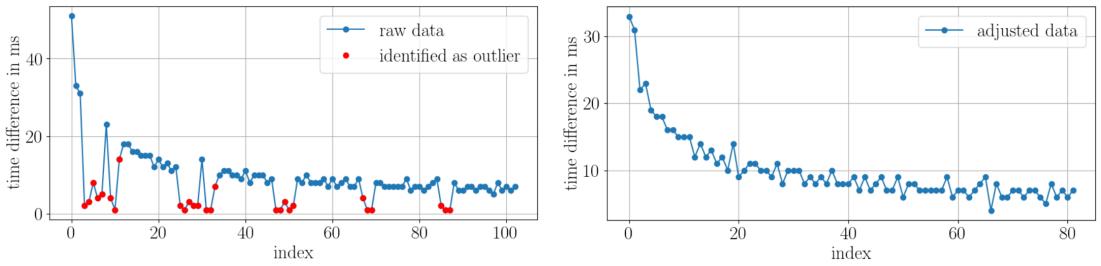

(a) Raw data (time difference as a function of timestamp index) with identified outliers (in red) caused by a rough spoke surface

(b) Corrected data (time difference as a function of timestamp index) with adjusted time differences

Figure 10: Comparison of raw and corrected data to show the correction of systematic errors. The example measurement is the reference measurement iteration 1 with two baffles and a counterweight of 4 kg

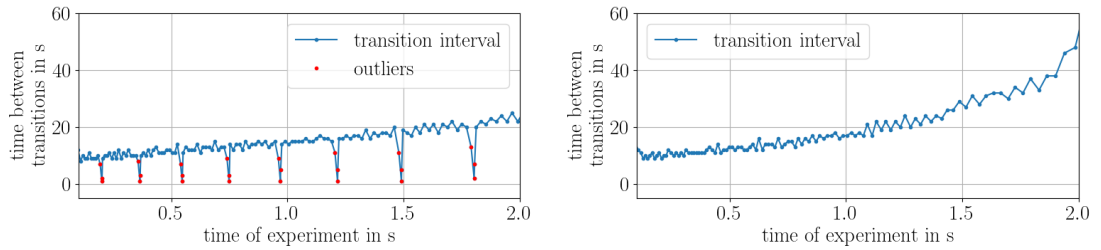

(a) Test measurement (time interval between transitions as a function of experiment time) showing periodic systematic error in data points due to one spoke causing additional data points (in red) to be recorded.

(b) Test measurement (time interval between transitions as a function of experiment time) with added adhesive tape on the problematic spoke, which eliminated the systematic error.

Figure 11: Two similar measurements showing that adding adhesive tape onto the problematic spoke fixed the periodic systematic errors.

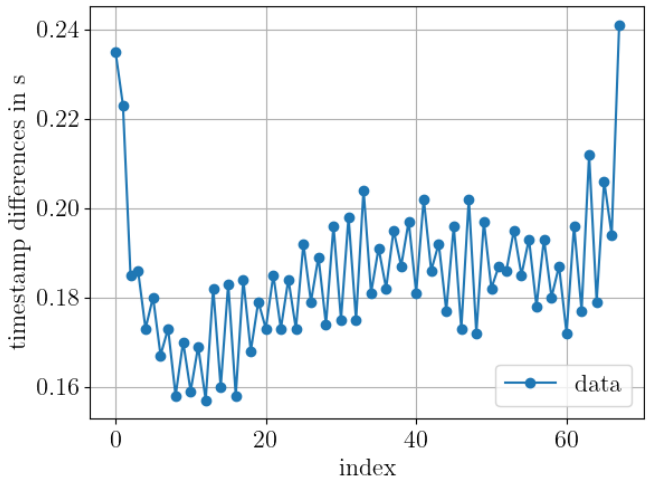

Figure 12: The systematic error appearing in new measurements for this work, where the time difference between two transitions are slightly higher for every second data point and slightly lower for every other second data. Time differences between transitions (y-axis) are shown as a function of timestamp index (x-axis).

Another systematic error is visible in the recorded data: Every other timestamp is higher than those in between, leading to a zigzag shape as shown in Figure 12. This can be explained by the shape of the infrared light ray sent out by the sensor: It is cone shaped and detects changes in the intensity of the light that gets reflected back to the sensor. So, for a transition from gap to spoke, the edge of the spoke turning into the light cone is detected slightly earlier than when it reaches the center of the sensor. Opposed to that, when the transition is from spoke to gap, the spoke edge is still seen by the sensor although it already passed behind the center, which leads to a slightly later timestamp than it should.
This systematic error is known, but due to its low amplitude and symmetric influence on the timestamps, it was not corrected for.

4 Data analysis

In the following section, the methods of data processing are presented. The optimal settings for fitting methods are analyzed per baffle type.

4.1 General process

The data analysis and plotting was done in python.
The wheel as described in the previous section has 8 spokes which leads to 16 transitions per full rotation. With this information and the diameter of the wheel, the timestamps from the infrared sensor are correlated with the distances that the baffle has traveled in that time interval ($\approx$17.9 mm), resulting in data points of distance over time as shown in Figure 13 top left.

A spline fit was then fitted to these data points with the `make_splrep` method from the `scipy.interpolate` package. An exemplary spline fit is shown in Figure 13 on the top left panel. The goal is to create a smooth curve function that represents the data and can be derived two times. The used method constructs a smoothing B-Spline around the data points. For that, a low-level polynomial of degree k is fitted on a subset of the data points in between knots. The location and number of knots is determined automatically. The method has two setting parameters: k and s. For the degree k of the fitted polynomials, the default is $k = 3$ which are cubic polynomials. s defines the smoothness of the spline by limiting the deviation of the spline fit $g(x)$ from the data points (x, y) with

$$\sum_{(x,y)} (g(x) - y)^2 \leq s \ . \tag{5}$$

Therefore, higher values for s result in a higher smoothness, while low s values ensure closeness to the data. Setting $s = 0$ yields a linear interpolation.

To find the spline settings to fit onto the data, a thorough analysis was conducted regarding the stability and consistency of the resulting drag forces between iterations. This is described later in this section.

To obtain acceleration values, the first and second derivative of the spline were calculated (see Figure 13 on the top right and bottom left panel). This leads to acceleration values as a function of velocity, as shown in Figure 13 on the bottom right panel.
The goal is to compare acceleration values between reference and baffle measurement at the same velocities, since the drag is velocity dependent (see section 2). An example for this is shown in Figure 14 (a). From that, the drag force can be calculated as described in section 2. The acceleration values are interpolated from the reference and baffle data for the range of "overlapping velocities". This means velocities, where there are acceleration values for both measurements with and without the baffle.

In all measurements with the top baffle, the recorded velocities of the reference and the baffle measurements did not overlap. The maximal velocity for the setup with the baffle is given by the terminal velocity $v_{\text{terminal,baf}}$. This means, the accelerating forces (e.g. the weight force of the counterweight) and the decelerating forces (e.g. the drag) are

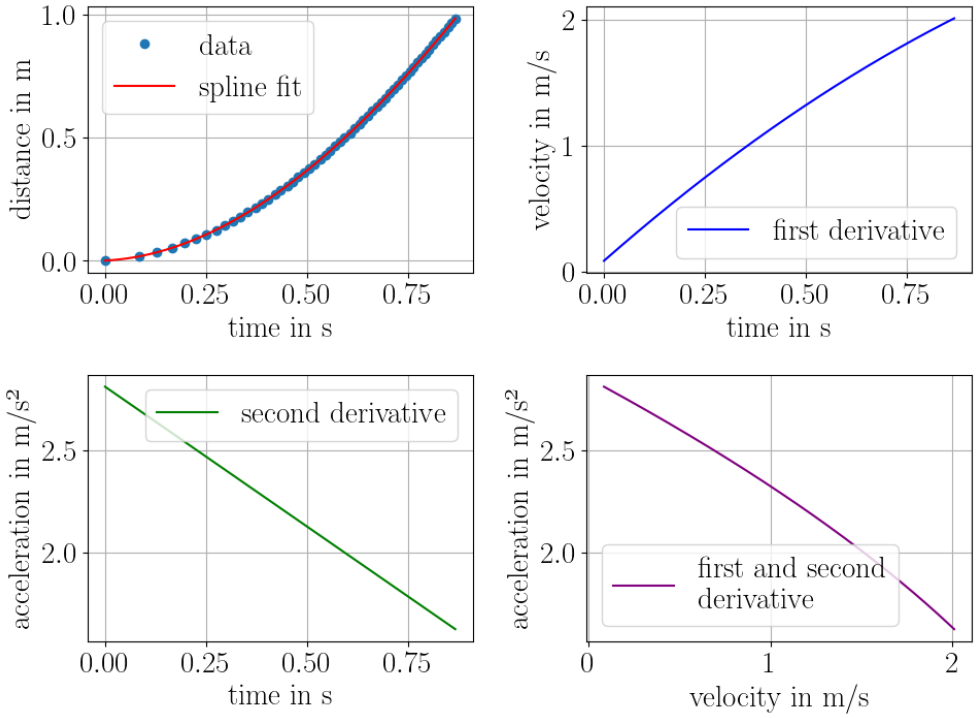

Figure 13: Spline fit (top left) on an example measurement, first (top right) and second (bottom left) derivative of the spline, and a combination of the first and second derivative (bottom right). The measurement is the reference measurement 1 with a counterweight of 2.5 kg.

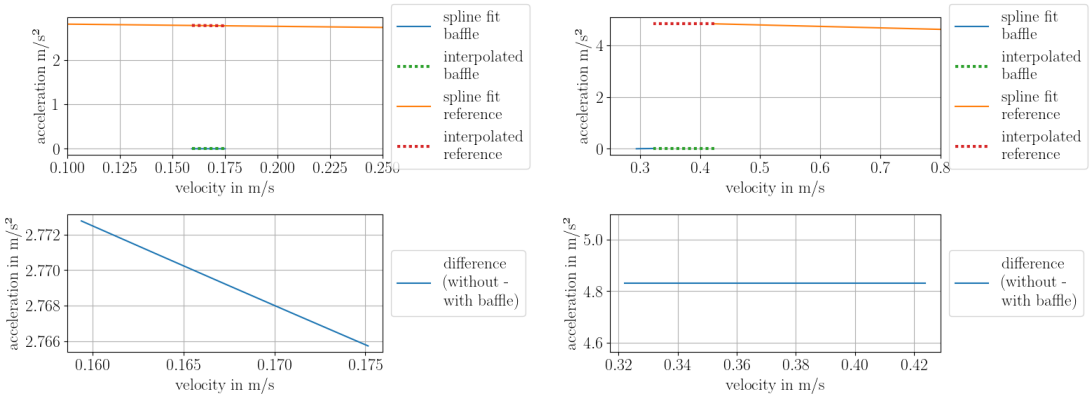

(a) iteration 0 with 2.5 kg counterweight, where velocities overlap.

(b) iteration 0 with 4.5 kg counterweight. The velocities do not overlap.

Figure 14: Top plots: Acceleration (y-axis) as a function of velocity (x-axis) for both reference and baffle measurements with different counterweights. Interpolated values are dotted. Bottom plots: Acceleration and corresponding velocity ranges used for drag force calculation.

equal in magnitude. Ergo, no net acceleration is acting on the system. The terminal velocity is therefore a constant value for a given system.
The reference measurement has a much higher net acceleration that leads to velocities exceeding $v_{\text{terminal,baf}}$ in the first few data points, where it is difficult to get accurate acceleration values due to the low amount of data. Since a timestamp was only recorded for every transition after 17.9 mm and it was not controlled when the first data point occurred, in many cases the system without the baffle already accelerated to higher velocities than $v_{\text{terminal,baf}}$ before valid data points could be recorded.
For this case of disjunct velocity values between baffle and reference measurements, the acceleration at velocities that are most close together was used for the calculation of the drag force. This means, for the reference measurements, the acceleration at the lowest recorded velocity was used ("interpolated"). For the baffle measurements, the acceleration at the highest recorded velocity was used. The velocity range for this drag force value is defined as the range in between the two velocity values, where the acceleration value was taken from. An example for this is shown in Figure 14 (b). The "interpolated" accelerations for the reference and baffle measurements in the velocity range are marked in dotted lines in the upper plot.

4.2 Determining fit settings

Additionally to making own measurements and evaluating those, this work reevaluated results presented by Tekbiyik [32]. This was necessary because some of the presented drag forces in that work were impossibly high if considering the forces acting on the system: The drag for a counterweight of 4.5 kg was determined to be (51.32 ± 13.73) N. The counterweight accelerates with a force of $4.5\,\text{kg} \cdot 9.81\,\text{m/s} = 44.145\,\text{N}$, which forms the upper limit of possible measured values for the drag force. While this limit is in the range of uncertainty of the measured drag and there is no direct contradic-

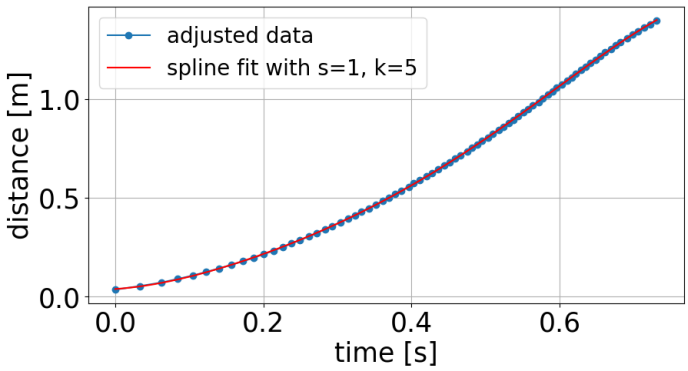

(a) Data and spline fit, distance (y-axis) over time (x-axis)

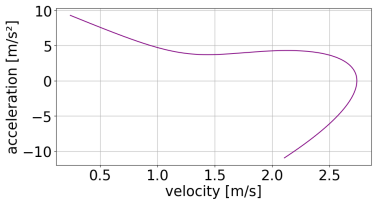

(b) Combination of second and first derivation of spline fit, acceleration (y-axis) over velocity (x-axis). Acceleration is proportional to drag.

Figure 15: Spline fit of a reference measurement with counterweight 4.5 kg. The spline settings chosen are the same as in Tekbiyik [32] which is $k = 5$, $s = 1$ and a cutoff distance of 1.45 m.

tion, it gives enough reason to reanalyze the results. Additionally, the uncertainties on the values are very high since there was a high fluctuation between different iterations.

In Tekbiyik [32], a spline fit with a degree of $k = 5$ and smoothness $s = 1$ was used to fit to the data. The data was cut off at a distance 1.45 m. This is the estimated distance that the system travels while recording valid data. The derivation of this spline fit with these chosen settings show nonphysical behavior as shown in the acceleration curve in Figure 15 (b), where the acceleration takes on negative values. The acceleration having negative values in this distance range is not reasonable when looking at the experimental setup. The counterweight is accelerating until an equilibrium of forces is reached, and until the setup reaches the water surface, so the net acceleration should always be positive.

In order to find a function that represents the data well, different spline settings as well as bootstrapping were tested mainly on the top baffle data from Tekbiyik [32].

A fit is considered to be good, when the resulting drag force is consistent for several iterations of the experiment and has a small variation. Additionally, the residual of the fit (defined by the distance of the fit to the data at a given x) should be spread randomly. This condition ensures that the fit does not have a bias of being consistently lower or higher than the data in certain areas.

In the following, the tests of spline fit settings are described for the different baffle types.

4.2.1 Top baffle measurements

In this section, the spline settings are optimized for the data from measurements with the top baffle. The analysis was done only on the data from Tekbiyik [32], which are measurements with one top baffle with counterweights of 2.5 kg and 4.5 kg. The measurements done for this thesis are not considered explicitly.

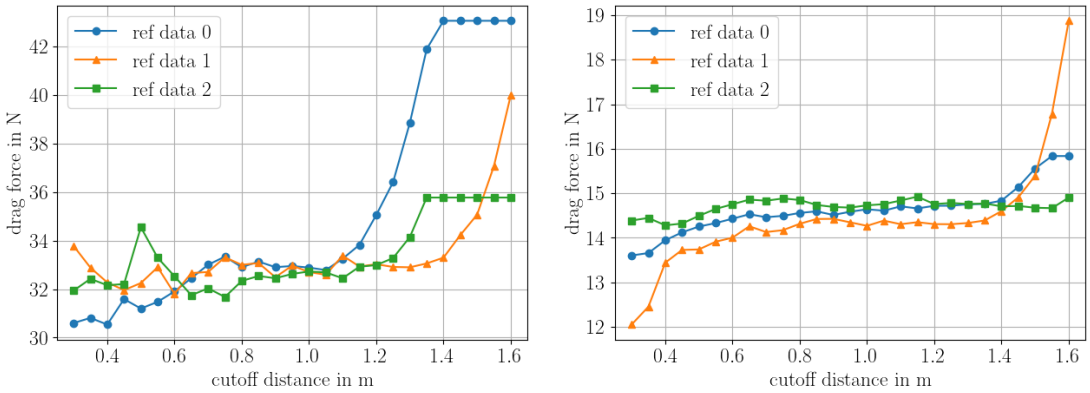

(a) 4.5 kg counterweight

(b) 2.5 kg counterweight

Figure 16: Drag force (y-axis) dependent on the cutoff distance (x-axis) for different counterweights. The different iterations of reference measurements, shown in different colors, were all combined with the same baffle measurement to obtain drag values.

Variation of spline settings

For fitting the baffle and reference data, the different setting parameters of the fit method were varied: Smoothness factor s, degree k and cutoff distance, after which the data points are not considered. A fit parameter is considered to have an good value, when the difference between the resulting drag forces for different repetitions of the same measurements are as small as possible. Since the problem of high variation occurred only for reference measurements, for each counterweight (2.5 kg and 4.5 kg), all analyses are done for all reference measurements, each compared with the same baffle measurement (iteration 1 for both) per counterweight.
This section presents the results of this analysis.

Variation of cutoff distance

At first, the cutoff distance was varied from 0.3 m to 1.6 m in steps of 0.05 m. The available data is already cut off at around 1.5 m, this is slightly different for each measurement.
As seen in Figure 16, the drag values change depending on the chosen cutoff distance. This change is especially high for low or high distances in the considered range. For low values, there are few measurement points to fit onto, which makes the influence of statistical fluctuations higher. This causes the high variation between different iterations. For high distances, the drag eventually reaches a constant value that is different between each iteration. The constant value above a certain distance means that there were no additional data points in the measurement. The reason why the drag at high distances is so different between iterations is unclear.
Since the values seem to be most consistent in the middle range of chosen distances, the cutoff distance was chosen to be 1.0 m.

Variation of smoothness factor s

The smoothness factor s was varied in the range of $4 \cdot 10^{-5}$ to $15 \cdot 10^{-5}$ in 20 steps. s sets a limit for how far the spline fit values can deviate from the measured value at a

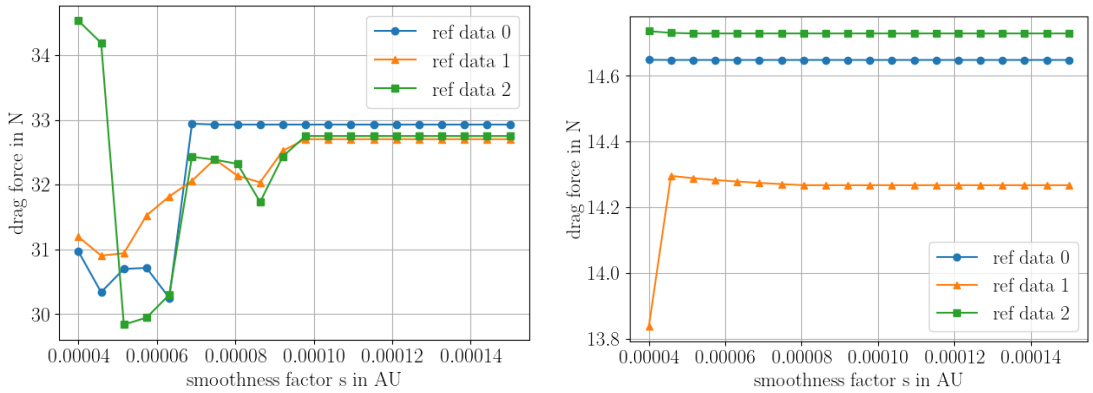

Figure 17: Resulting drag forces over smoothness s for all reference iterations with 4.5 kg (left) and 2.5 kg (right) counterweight, compared to the same baffle measurement per counterweight.

given x value, as described by Equation 5.
In Figure 17, the resulting drag forces depending on chosen s parameter are shown. Below a certain threshold which for this data file is $\approx 1 \cdot 10^{-5}$, drag forces are not consistent and indicate a spline fit that is heavily influenced by statistical fluctuations in the data. For higher values, the result does not change since the fit found its optimal values inside the bounds. Therefore for drag force calculation, $s = 1$ was chosen, to be sure to be far above the fluctuations. It was confirmed that this does not change the result of the fit.

Variation of degree *k*

Here we will look at variation of k which sets the degree of the polynomials in the spline fit. The values considered are $k = 3$ and $k = 5$, since $k = 5$ is the value that was used in Tekbiyik [32]. $k = 3$ is recommended by the `make_splrep` method, an even numbers are not recommended [33].
Again, the stability of the drag force regarding different k values is analyzed. In Figure 18b, the influence of k (different colors) on the drag force dependent on cutoff distance and s value is displayed. The drag force value is more stable between iterations when using $k = 3$ (orange curve), so that value was chosen for further analysis.

To conclude, the chosen fit settings are polynomials of the degree $k = 3$, a smoothness factor $s = 1$ and a cutoff distance of 1.0 m. Figure 19 shows an exemplary spline fit with these settings. These settings were used for all fits on both reference and baffle measurements for all measurements of the top baffle, including those with two baffles stacked and those done for this thesis.

Bootstrapping

To verify that the resulting drag force values do not depend on artifacts in the measurement data, "bootstrapping" was used to analyze the stability of the resulting drag forces. In bootstrapping, a certain number of data points is chosen randomly out of the full set of data. Already chosen points are not eliminated out of the drawing pool, therefore it is possible to draw data points more than once. The amount of draws is

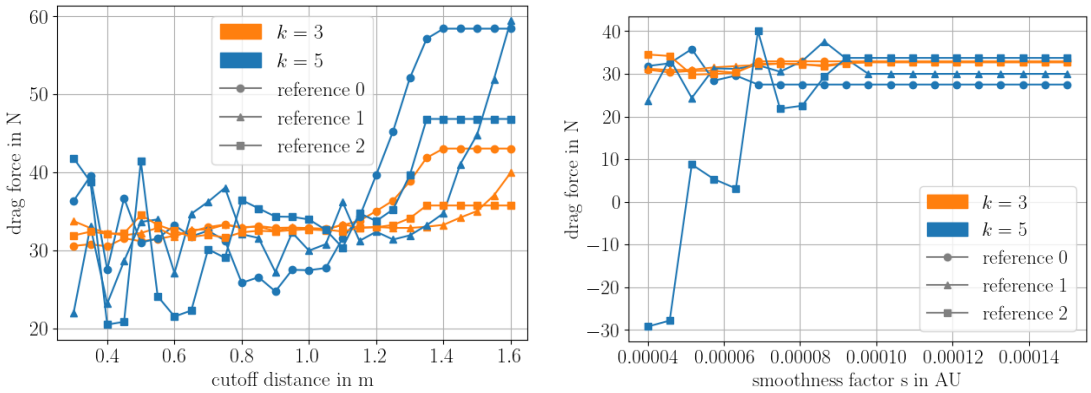

(a) Drag force (y-axis) over cutoff distance (x-axis) for different k values (color).

(b) Drag force (y-axis) over smoothness s (x-axis) for different k values (color).

Figure 18: The influence of fit parameter k on drag values for a counterweight of 4.5 kg.

defined relative to the total number of data points in the set, for example when there is a total of 60 data points in a measurement and the pull amount is 80 %, 48 random points will be drawn.
Following that, the analysis including spline fit and comparison of accelerations as described in section 4 are performed on this subset of drawn data points. This whole process is repeated 100 times for each measurement to be able to perform statistical analysis. Here, the bootstrapping was done only on the datasets of the reference measurements, since the baffle data is very similar between iterations and is not the reason for these high variations in results, as already described in section 4.

Variation of pull amount

Figure 20 shows the drag values as a function of the pulled amount exemplarily for one file pair of baffle and reference measurement with 4.5 kg counterweight. It is clear that the lower the pull amount, the higher the results vary between different iterations. For low pull amounts, the spline fit highly depends on the very small amount of data points and the random factor therefore has as high influence on the result. For pull amounts close to 1, almost all data points are taken into account for the fit and therefore the resulting values do not vary much. The reason for the result still varying slightly even for a pull amount of 100 % is the possibility of drawing data points more than once. Therefore a pull percentage of 100 % does not mean that the drawn subset is identical to the original data set.

As also seen in Figure 20, the resulting drag forces are lower than the result obtained without bootstrapping. The reason for this is found in the way the acceleration difference is calculated. For the drag force result, the acceleration of reference measurement at lowest velocities is decisive. With bootstrapping, the lower the pull amount, the higher the probability of these very first data points to not be selected. Therefore the lowest velocity found in the subset of data is higher than without bootstrapping. With that, the crucial acceleration is smaller, since the acceleration is smaller for higher velocities. This is the reason for this bias towards smaller drag forces.

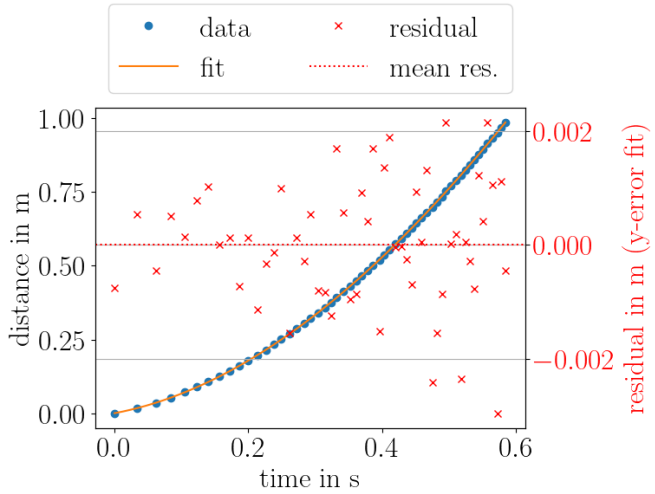

(a) Spline fit on the data with residuals

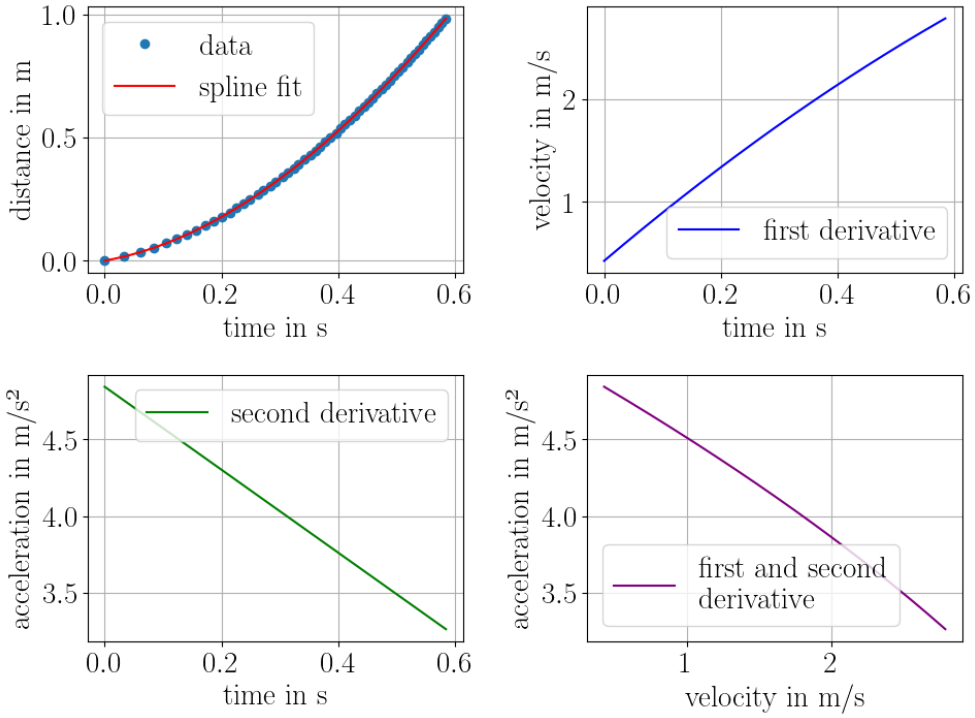

(b) Spline fit on the data (top left), first (top right) and second (bottom left) derivative of the spline, and a combination of the first and second derivative (bottom right)

Figure 19: Example reference data (iteration 0) with 4.5 kg counterweight and spline fit with spline settings as determined in this section.

For all analyzed reference files, the standard error on the mean is smaller than 1 N, which is small enough for our purpose and further confirms the validity of the drag force results.

4.2.2 Bottom baffle measurements

In this section, the spline settings regarding data for the bottom baffle mounted on the harness are considered. The data was measured by the author of this thesis.

For measurements with the bottom baffle, when naively adapting setting parameters as smoothness $s = 1$, degree $k = 3$ and cutoff distance 1.0 m, an additional problem of the fit was introduced in the drag force calculation. This is shown in Figure 21. The interpolated acceleration values for the baffle data are discontinuous, there is a leap. In the plot, this is shown as a vertical line since values are connected in a line. To find the explanation for this, we look at the process that leads there.

For baffle measurements, the setup reaches a constant terminal velocity after the first few data points, which results in a straight line in the data as shown in Figure 21 (c) in the top left panel. The spline fit, trying to fit a cubic polynomial which is curved, does not represent the data well, as shown in the residual in Figure 21 (b). For different time intervals, the fitted function is either higher or lower than all of the data points in the interval.
According to the fit derivation in Figure 21 (c) on the top right, the velocity of the baffle seems to decrease after a distance of about 0.6 m. From a physics standpoint, this does not make sense. After reaching the terminal velocity, no additional decelerating force is introduced to the setup. The velocity should only increase or stay at the terminal velocity. In the raw data points, this decrease in velocity is not visible, which points to the non-representative fit as the reason for this.
When deriving the spline fit two times, some velocity values correspond to two acceleration values, so the acceleration as a function of velocity in Figure 21 at the bottom right is not injective. An interpolation method is used to select overlapping velocity and acceleration values between reference and baffle measurement. This interpolation of a non-injective function leads to this edge in the acceleration curve that is used for drag calculation, which is not physical.
Ideally, a spline fit would only be used for the lower end of the baffle measurement curve. For the part where the terminal velocity is reached, a linear fit would be best. This more complicated fitting process could not be done due to the time constraint of this thesis.

In order to improve the spline fit and its closeness to the data without using a new fitting method, the smoothness s is instrumented. This spline setting limits the maximal distance of the fit to the data points (see Equation 5). The result for this is shown in Figure 22, where the drag force of one example measurement is calculated with different settings for s. For lower s, the resulting drag is higher. For higher s, the drag is lower, and the vertical gap increases. For s values above those plotted, the drag curve does not change, since the result of the spline already is inside the limits imposed by s. In our case, we already know from the residuals in Figure 21 (b), that the most stable

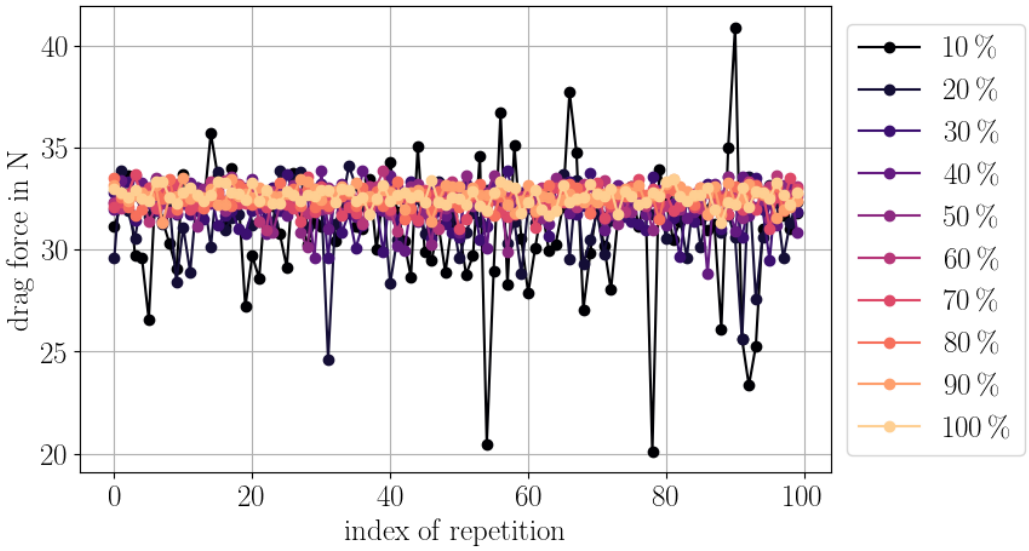

(a) The drag force (y-axis) for 100 repetitions (x-axis) of bootstrapping are shown for different pull amounts (color)

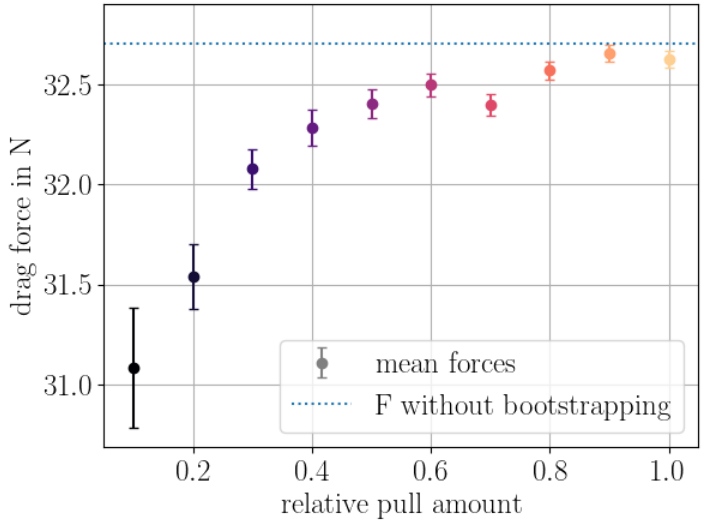

(b) Averaged drag force (y-axis) in dependence of the pull amount (x-axis and color). Error bars show standard error on the mean from averaging over 100 repetitions. The dotted line marks the drag force value determined without bootstrapping.

Figure 20: The drag forces determined via bootstrapping for different amounts of draws from data points.

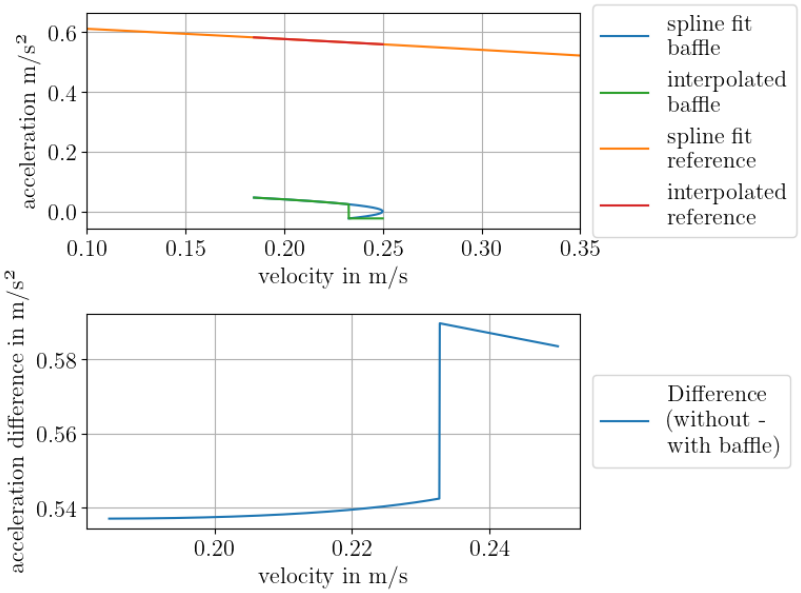

(a) Acceleration over velocity for baffle and reference measurement

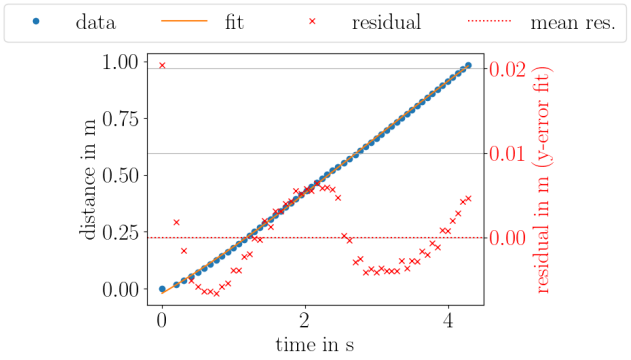

(b) Spline fit on baffle measurement data with residual

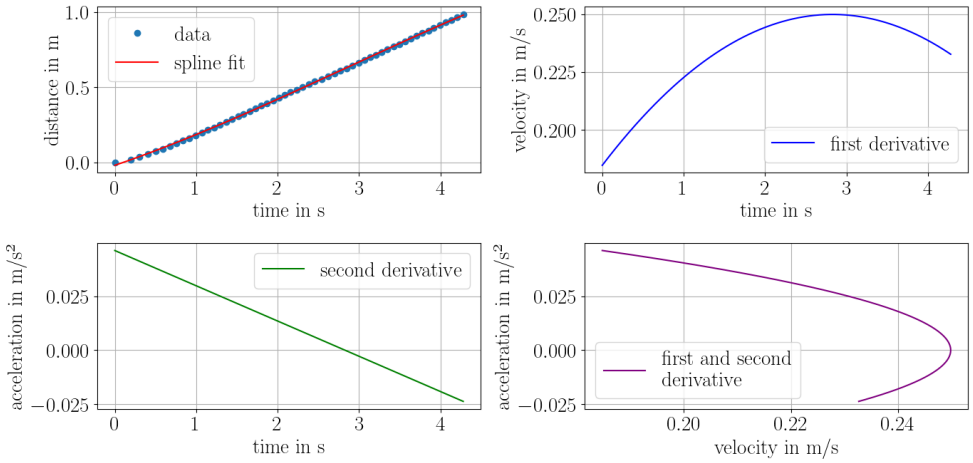

(c) Spline fit on the baffle data (top left), first (top right) and second (bottom left) derivative of the spline, and a combination of the first and second derivative (bottom right)

Figure 21: Example measurement with the bottom baffle (iteration 3) with a counterweight of 4 kg. The spline fit settings optimized for the top baffle measurements were used.

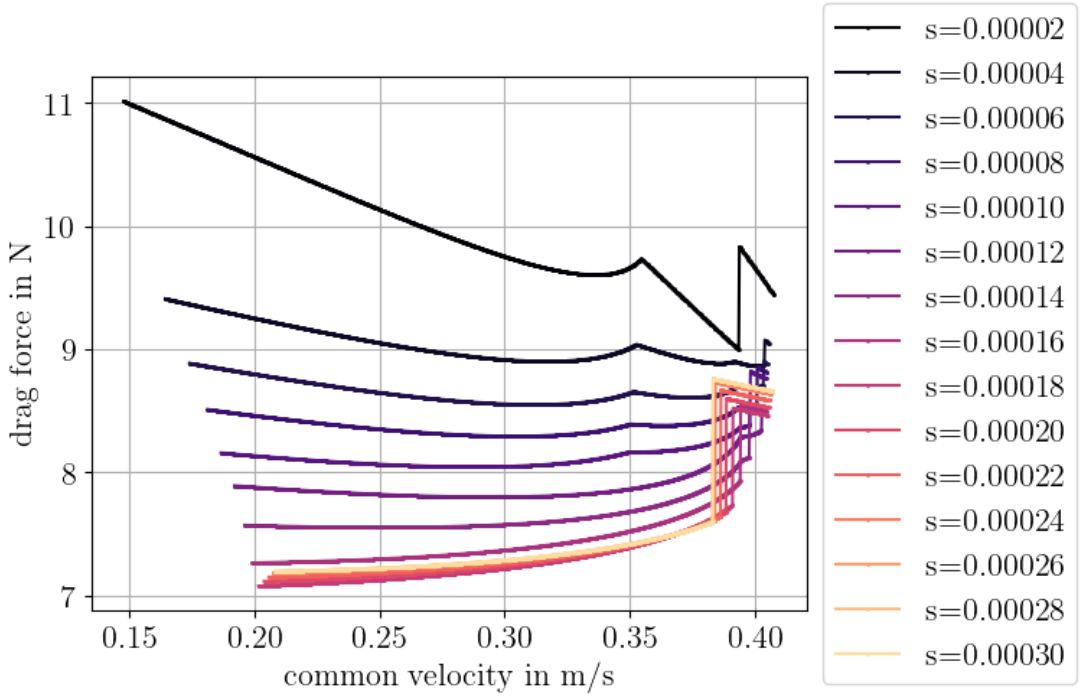

Figure 22: Drag force for different chosen values for the smoothness s for an example bottom baffle measurement (iteration 2) with counterweight 4 kg.

drag force value is not the one that is most representative of our data.
To choose a representative fit, the residuals were considered. The smoothness s was set to the highest value where residuals looked randomly spread, which is $s = 2 \cdot 10^{-5}$. The resulting spline fit with derivations and residuals for one example measurement is shown in Figure 23. Some velocity values still have two acceleration values (shown in (c)). The resulting vertical gaps in the spline are smaller in size compared to Figure 21. The additional edges in the spline derivations are there because the spline is constrained so much that it is not able to produce smooth curves.

The value $s = 2 \cdot 10^{-5}$ is chosen for all drag force calculations for the bottom baffle, since the fit is closer to the data and therefore represents them better. This was also used for the fit on reference measurements. An analysis of behavior of the fit when changing the cutoff distance and the degree k was not done rigorously. Therefore, the same values as for the measurements with the top baffle are chosen which are 1.0 m and $k = 3$.

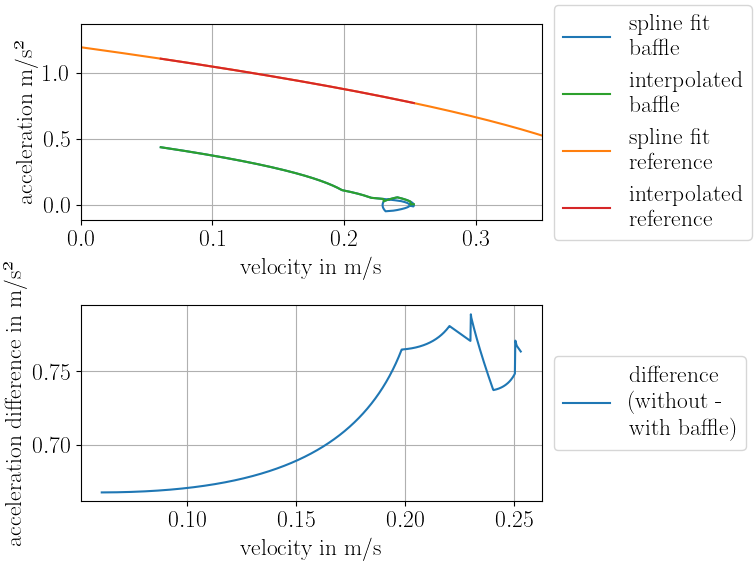

(a) Acceleration over velocity for baffle and reference measurement

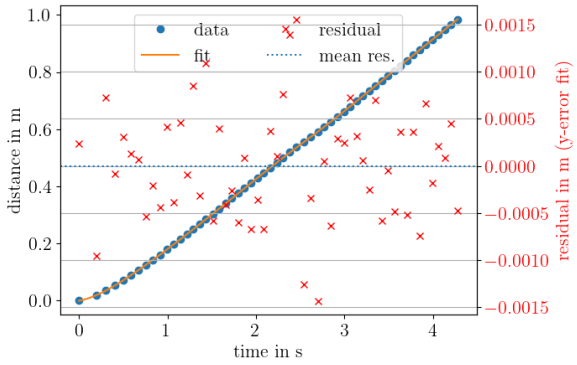

(b) Baffle data, spline fit and residuals

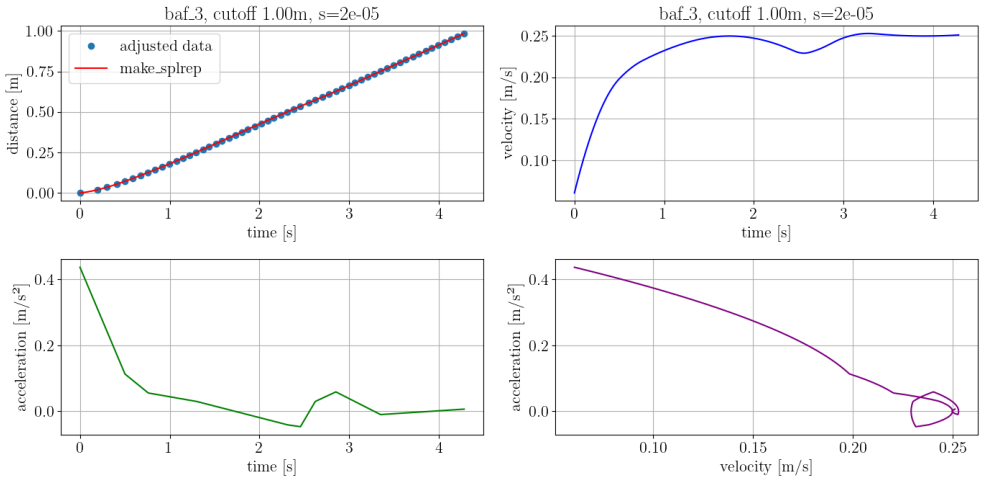

(c) Spline fit on the baffle data (top left), first (top right) and second (bottom left) derivative of the spline, and a combination of the first and second derivative (bottom right)

Figure 23: Spline fit on an example bottom baffle measurement (iteration 2) with counterweight 4 kg with fit setting $s = 2 \cdot 10^{-5}$.

5 Drag force results

The goal of this thesis is to determine the drag forces of the baffles. In this chapter, the drag forces are presented.

5.1 Top baffle

In Figure 24, all final drag values are displayed for all measurements and counterweights for one top baffle. It includes measurements with different counterweights done by Tekbiyik [32] (in red) and also done by the author of this work (in blue). The average drag force and average velocity for each counterweight were also calculated. These are shown in the Figure 24 and in Table 2.

These values are lower than the ones presented in [32], although the analysis is done partially on the same data. This is due to spline fit settings being chosen differently and the different inertial masses considered, which is described in detail in section 4.
The deployment velocity range of 0.15 m/s to 0.3 m/s is covered well by these measurements, the drag force in that range is $\approx$ 10 N to 20 N. A velocity dependence of the drag is visible, the drag is higher for higher velocities. Neither a quadratic nor a linear dependence as predicted in section 2 is clearly visible in the data.
The drag value is constant for the whole velocity range for all measurements. This is due the fact that no pair of measurement with and without baffle had acceleration values at the same velocities. The displayed velocity ranges mark the range in between the velocity values of the two measurements, that are closest together.

For the measurements marked in blue in Figure 24, which are done by this thesis, not every graph is actually an entirely new measurement. Some reference measurements were ineligible, so that other iterations had to be used for more than one baffle measurement. The 3 kg measurements all are calculated with the same reference measurement (but different baffle measurements). For the measurements with 4 kg counterweight, one reference measurement was used for iteration 3, 4 and 5. This is valid since in principle every iteration should be the same, and assigning certain reference to certain baffle measurements is arbitrary.

5.2 Two top baffles

The measurement data presented here was taken by Tekbiyik [32] with two top baffles stacked into the fixture (described in section 3). In Figure 25 the resulting drag forces for all counterweights with two baffles attached are shown. The averaged drag forces per counterweight are presented in Table 2. The drag at the deployment speed of 0.15 m/s to 0.3 m/s (marked in green) is roughly 15 N to 30 N. Neither a quadratic nor a linear dependence on velocity as predicted in section 2 can be verified reliably, since the ranges of velocity are large. As explained in section 4.2.1, this means, the drag for reference and baffle measurements were determined at different velocities with a large gap in between. To get more values in the range of the deployment velocities, more measurements with a counterweight in between 2.5 kg and 4 kg would be useful.
In comparison to only one baffle, the drag does not increase linearly but instead by a factor of $\approx$ 50 %. This is plausible, since the water arriving at the second baffle is already

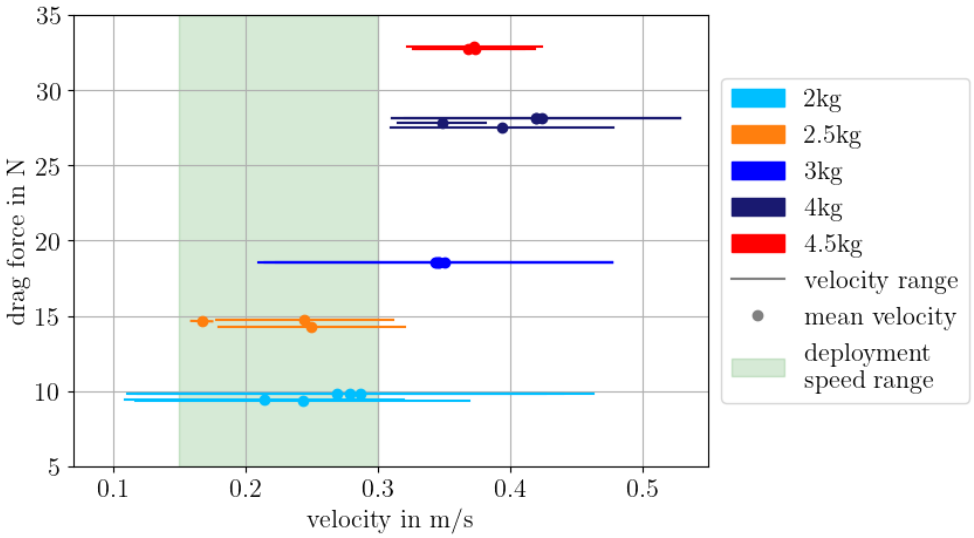

Figure 24: Drag forces with corresponding velocity range for different counterweights for measurements with the top baffle. Red and orange are measurements done by Tekbiyik [32], shades of blue are new measurements done for this thesis. Note that the bars are not error bars but rather the range of velocities, for which this drag value is calculated. The green area marks the targeted deployment speed.

disturbed by the first baffle. The drag of the two baffles are not independent of each other.

For the counterweight of 4 kg, there were only two reference measurement datasets available for evaluation, since something went wrong in the first iteration of the measurement. In order to still include all three iterations of baffle data, the second reference measurement iteration was used for the drag force combination for both baffle measurement iterations one and two. In the same way, for a counterweight of 5 kg, only one valid iteration of reference measurement is available and used for the drag calculation for both baffle measurements.
As seen in Figure 25, the obtained drag forces and velocities of these two iterations of baffle data with the same file of reference data are so close together, that they are not visually distinguishable. This is also the case for the 4 kg measurement, where one reference measurement was used with two baffle measurements. It suggests that the fluctuations in between different iterations are actually fluctuations in reference data, while the values from the baffle data are not that much different.

5.3 Bottom baffle

For the bottom baffle, several measurements for different counterweights were taken with an improved setup as described in section 3. The results can be seen in Figure 26. The average drag per counterweight is given in Table 2. The results with counterweights of 4 kg and 5 kg provide a good coverage of the targeted deployment speed range of 0.15 m/s to 0.3 m/s, marked with green in the plot. At deployment speeds, the drag force is $\approx$ 7 N to 10 N. These values are significantly lower than the drag for the top baffle. This can be explained by the lower bristle density. Furthermore, the bristles are

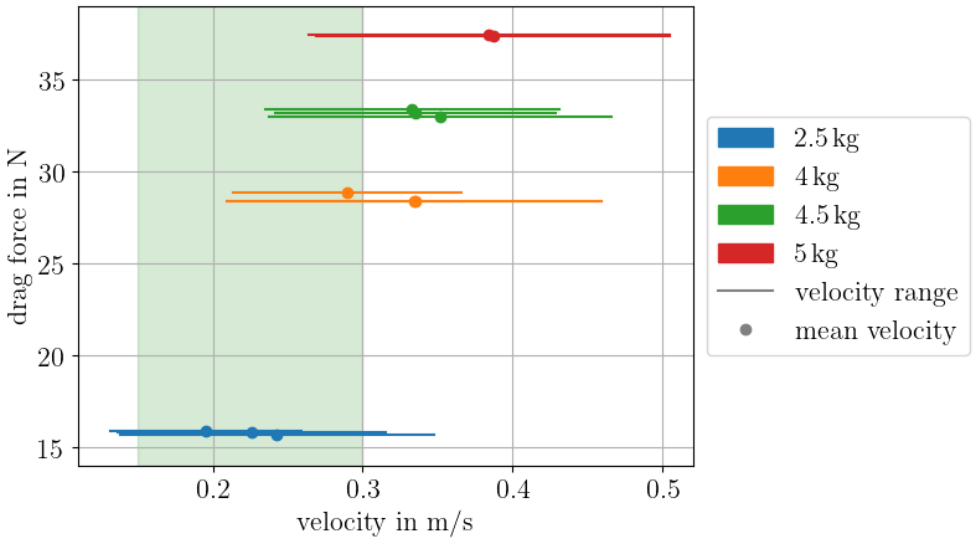

Figure 25: Drag forces of two top baffle layers for different counterweights, plotted over velocity. Each graph represents one iteration of measurement. The green area marks the targeted velocity for deployment.

bent by the drag, as explained later when evaluating the video recordings. This further reduces the drag.
In section 2, a velocity dependence of the drag force is predicted to be either linear ($F_\mathrm{D} \propto v$, laminar flow) or quadratic ($F_\mathrm{D} \propto v^2$, turbulent flow). The velocity dependence is visible in the data when comparing between the measurements with different counterweights. For higher counterweights, the average velocity is higher, and the values for the drag force are higher. Within one measurement, the drag force does not change much for different velocities. For the measurements with 5 kg where a large velocity range is covered, the drag is lower for higher velocities. This does not match either of the predicted velocity dependencies. The reason for this could be an inaccurate spline fit.
As explained in section 4, the edges and vertical lines in the graphs are the result of the spline fit, which was constrained to sit very close to the data. For the 4 kg counterweight, the graphs for measurements 2 and 4 are lower than the others and lie very close together. It is unclear why this is the case, since neither the spline fits nor the residuals are noticeably different from the other iterations.

The amount of bristles was not quantified for manufacturing; this resulted in the bottom baffle prototype to have a significantly lower bristle density than anticipated. This has an influence on the drag force, which is why the drag for the final version of the baffle likely is different than the one presented here. For a higher bristle density, a higher drag is expected since there is more volume of material to disrupt the water flow.
Furthermore, in the final version, the bottom baffle will be segmented. Approximately half of the bristles will be cut away in two sections, which leaves two fans of bristles and two areas where the water can pass through without disruption. This will significantly decrease the drag force. More tests are needed to determine this new drag.

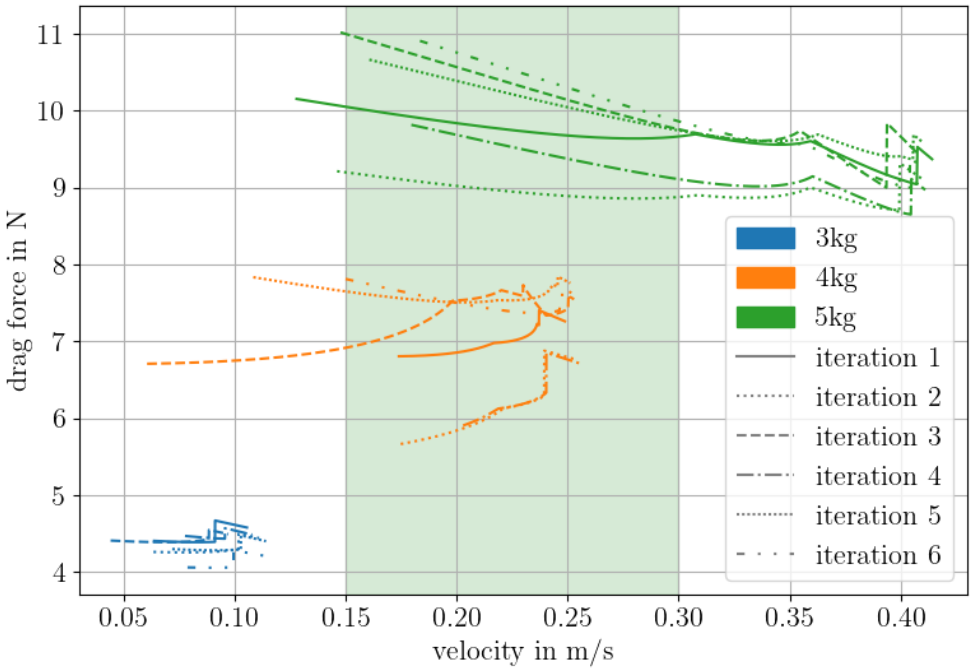

Figure 26: Drag forces for different counterweights for the bottom baffle. Each graph represents one iteration of measurement. The green range signifies the targeted deployment speed.

Video recordings

In Figure 27, screenshots from the video recordings can be seen. The baffle is moving through the water inside the steel pipe towards the camera. The edge of the harness and the aluminum rail of the baffle is visible at the bottom left of the images, the bristles are in the center. The vertical stripes on the wall of the steel pipe, seen on the top right, are sediments that are partly brushed away by the baffles.
In the measurement with a counterweight of 3 kg, the bristles brush against the borehole. They are slightly bent backwards by the steel pipe. In 4 kg and 5 kg measurements, the bending of the bristles away from the direction of motion is visibly stronger. These are the measurements where the deployment speed was reached, as shown in Figure 26. The higher the counterweight, the greater is the amount of bending. The bristles are bent in such a way that there is no contact with the walls of the simulated borehole. This fact was acoustically verified during the recordings. The bending of the bristles is caused by the drag of the water.
This bending influences the drag force, since brushing against the walls introduces additional friction. This effect can not be seen in the data due to the low amount of data and the high velocity ranges where the drag results do not change. Measurements with a higher precision are needed to observe this influence.
Additionally, the water does not hit the bristles at a 90° angle, so it is possible for the water to flow radially alongside the bristles. This further reduces the drag.

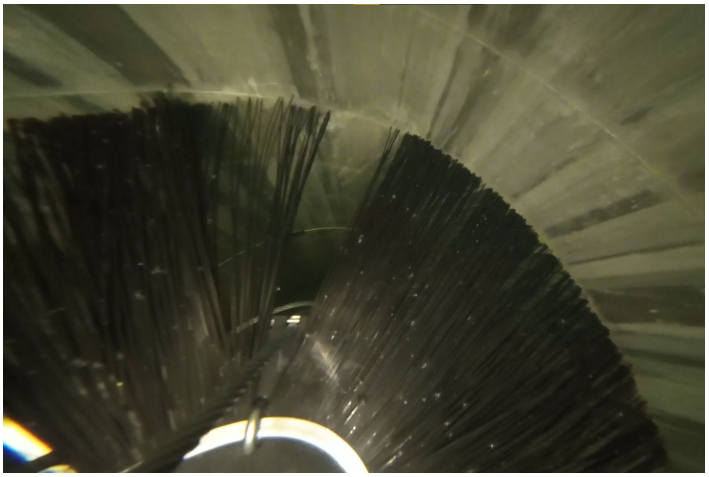

(a) 3 kg counterweight at $\approx 0.09\,\mathrm{m/s}$

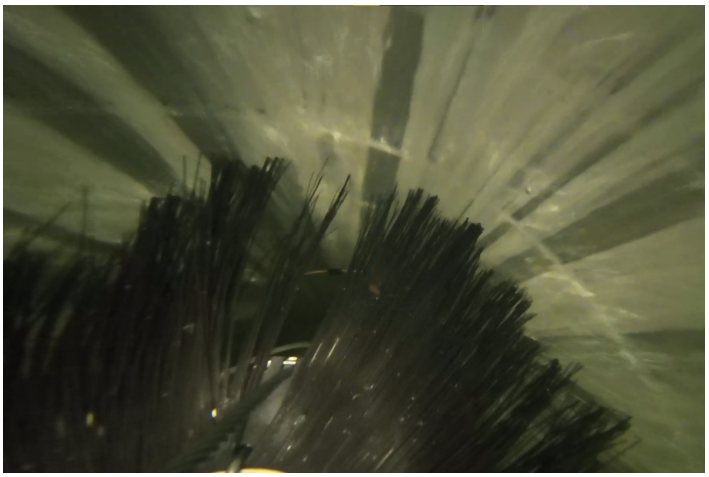

(b) 4 kg counterweight at $\approx 0.20\,\mathrm{m/s}$

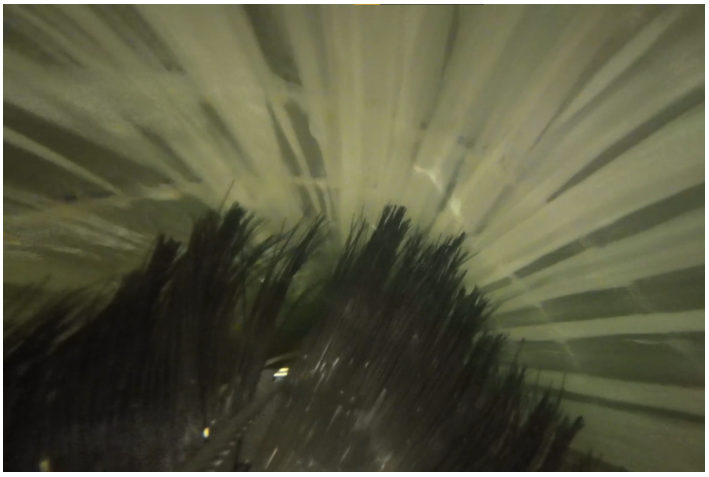

(c) 5 kg counterweight at $\approx 0.28\,\mathrm{m/s}$

Figure 27: Screenshots from video recordings of the bottom baffle inside the simulated borehole at different velocities.

6 Summary and Conclusion

The goal of this work was to determine the drag force for one and two layers of the top baffle and for the bottom baffle prototype. For this, the measurement setup from Tekbiyik [32] was improved and the systematic errors were successfully reduced. Additionally to own recorded measurements, data recorded by Tekbiyik [32] was reanalyzed. The settings for the spline fit were optimized for the given data, so that the resulting drag values have a low variation between repetitions.

The drag was successfully determined in a simulated borehole with a diameter of 56 cm. The drag in the targeted range of deployment speed of 0.15 m/s to 0.3 m/s was determined to be $\approx$ 10 N to 20 N for the top baffle, $\approx$ 15 N to 30 N for two layers of top baffles, and $\approx$ 7 N to 10 N for the prototype of the bottom baffle.
The main challenge was finding accurate fit settings to represent the data well. Additionally, evaluating the baffle and reference measurements at the same velocities proved to be a challenge.

The drag determined by this thesis was confirmed to be small enough, so that a deployment of the LOMlogger with the tested baffles is possible in the IceCube Upgrade. Further data with different counterweights might be useful in the range of deployment speeds, so that this drag can be determined more precisely. An improved method of fitting to the data, especially the bottom baffle, improves the precision of recorded data. To improve the significance of the data, a new method could be developed to obtain more data at the beginning of the measurement. With that, more data for smaller velocities for the reference measurement would be produced. This increases the overlap of velocities between reference and baffle measurements, so that the drag can be evaluated at the same velocities.

Video recordings show that at deployment speeds, the prototype of the bottom baffle used in this thesis does not brush against the walls of the borehole, since the bristles are bent away by the drag. That means, light rays at the walls of the borehole can still pass through undisturbed. Therefore, the bottom baffle prototype does not fulfill the requirements of light attenuation.
Changing geometrical properties that improve the optical properties, like increasing bristle density, changes the drag. Additionally, the final version is supposed to have cutouts at two sides. This decreases the drag. Therefore, further measurements are required for the new baffle type to get accurate values for the drag force.
Further, it would be interesting to test the whole assembled system with top and bottom baffles. This might change the drag, if the bottom baffle causes turbulence that change the drag for the top baffle.

A Appendix

Table 2 shows all determined drag forces at their corresponding velocity. The drag values were averaged for each measurement, and then averaged over all iterations of that counterweight and baffle type. The second averaging yields the standard error on the mean which is given as well. For the velocity, the average per counterweight over all iterations and the corresponding standard deviation was calculated and is given in the table.

Table 2: Drag force values averaged over all iterations with standard error on the mean, as well as corresponding averaged velocities with standard deviation for different baffles and different counterweights

Baffle Type	Counterweight (kg)	Average Velocity (m/s)	Average Drag Force (N)
Top baffle	2	0.26 ± 0.09	9.66 ± 0.09
	2.5	0.22 ± 0.05	14.55 ± 0.12
	3	0.35 ± 0.08	18.57 ± 0.01
	4	0.40 ± 0.06	27.95 ± 0.12
	4.5	0.37 ± 0.03	32.79 ± 0.06
Two top baffles	2.5	0.22 ± 0.05	15.90 ± 0.05
	4	0.32 ± 0.07	28.65 ± 0.13
	4.5	0.34 ± 0.06	33.29 ± 0.09
	5	0.39 ± 0.07	37.53 ± 0.03
Bottom baffle	3	0.09 ± 0.02	2.55 ± 0.05
	4	0.20 ± 0.04	5.13 ± 0.23
	5	0.28 ± 0.07	7.81 ± 0.16

In this section, all measurements from this and Tekbiyik [32] used in the analysis are shown. For each reference and baffle measurement, the spline fit, its residual and its derivations are presented. For each pair of reference and baffle measurement, the velocity ranges and acceleration values are shown in comparison, as well as the interpolated values that were used for the calculation of the drag force.

A.1 Measurements with the top baffle

Measurements for the top baffle are presented with different counterweights. For the 3 kg counterweight, all five baffle measurements are compared with the same reference measurement, which is included in the plots each time. For the measurements with 4 kg counterweight, one reference measurement was used for iteration 3, 4 and 5, the respective plots are also shown every time.
For bootstrapping, the plots of the averaged drag force dependent on pull percentage are shown for all iterations of top baffle measurements with a counterweight of 4.5 kg.

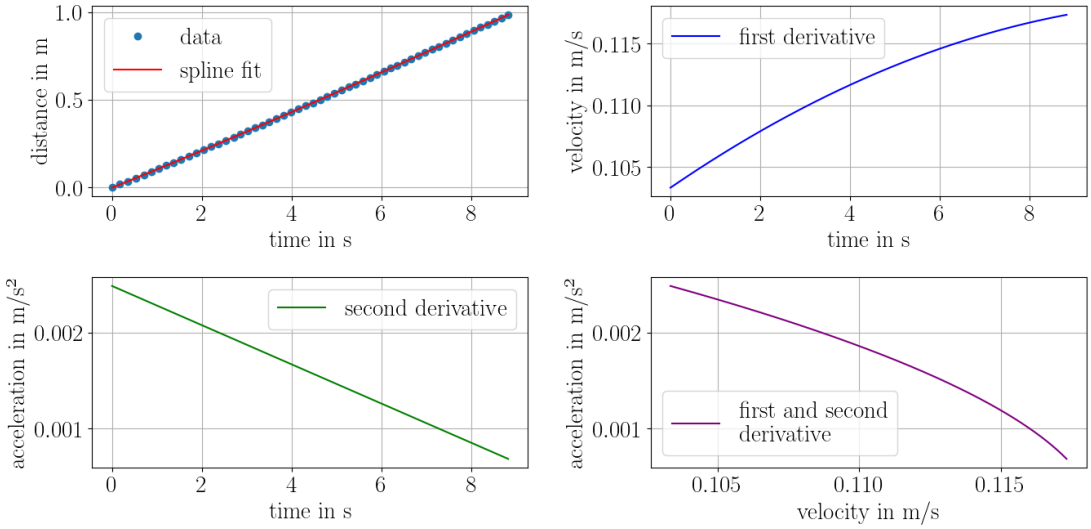

(a) Baffle data with spline fit and spline derivations

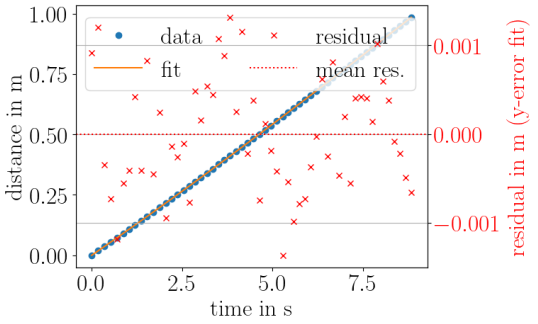

(b) Baffle data with spline fit and residuals

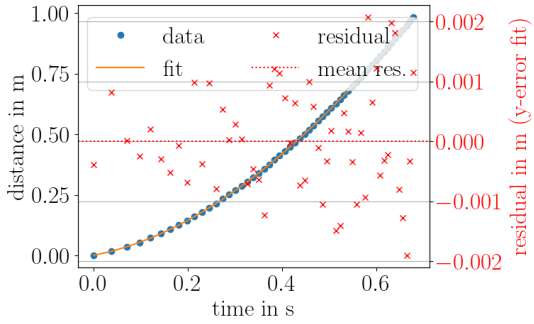

(c) Reference data with spline fit and residuals

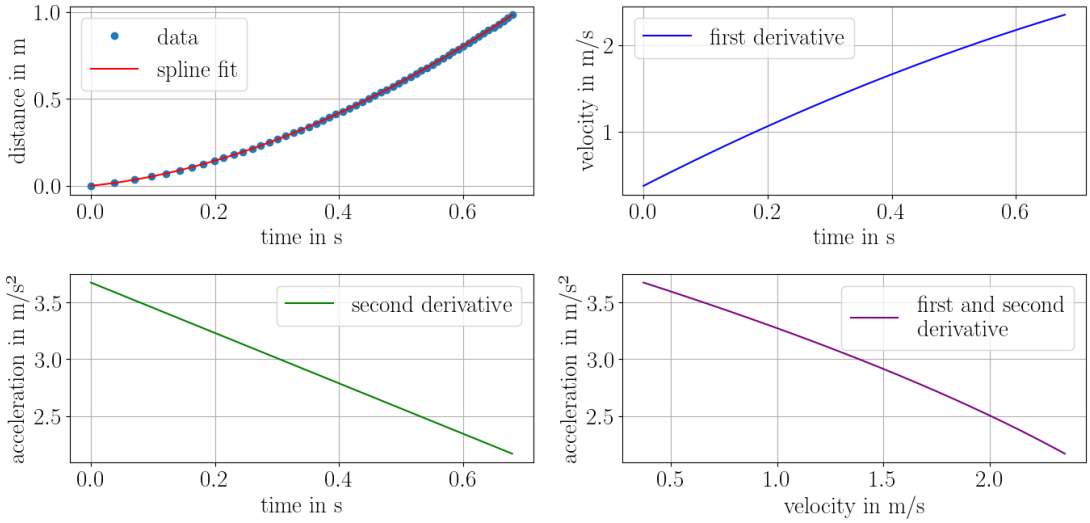

(d) Reference data with spline fit and spline derivations

Figure 28: Data, spline fits and residuals for top baffle measurement 1 with 2 kg counterweight

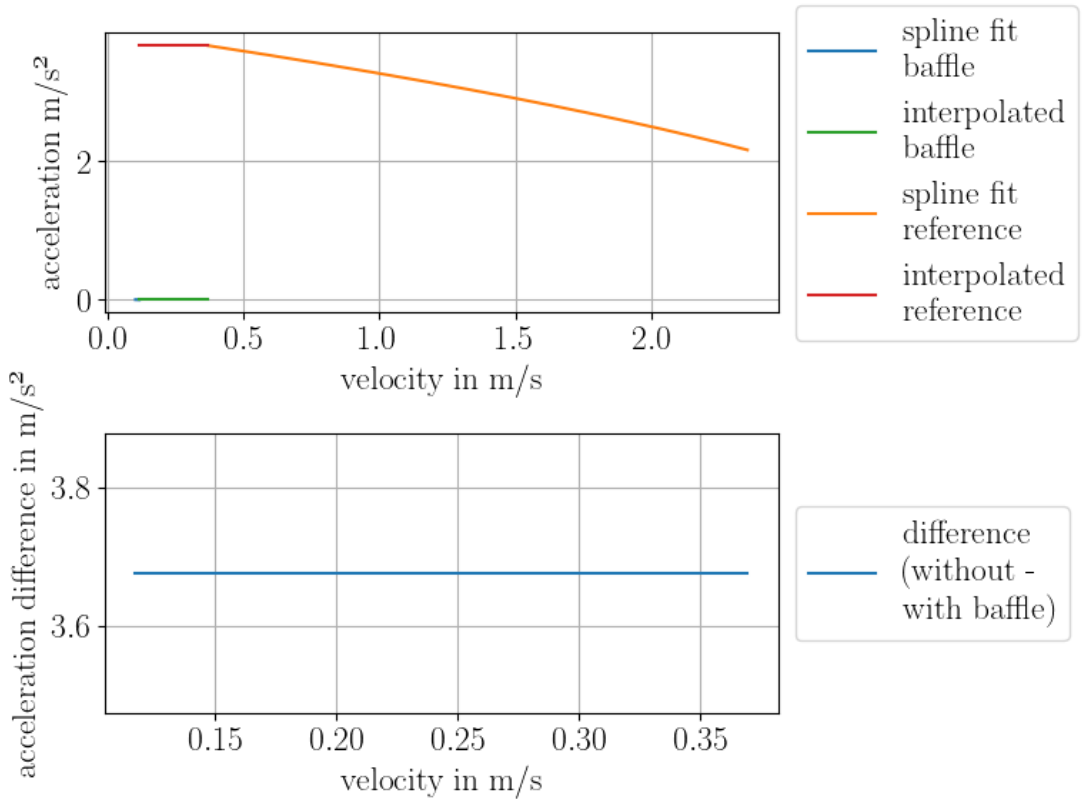

Figure 29: Acceleration over velocity of reference and baffle data with interpolated acceleration values for top baffle measurement 1 with 2 kg counterweight

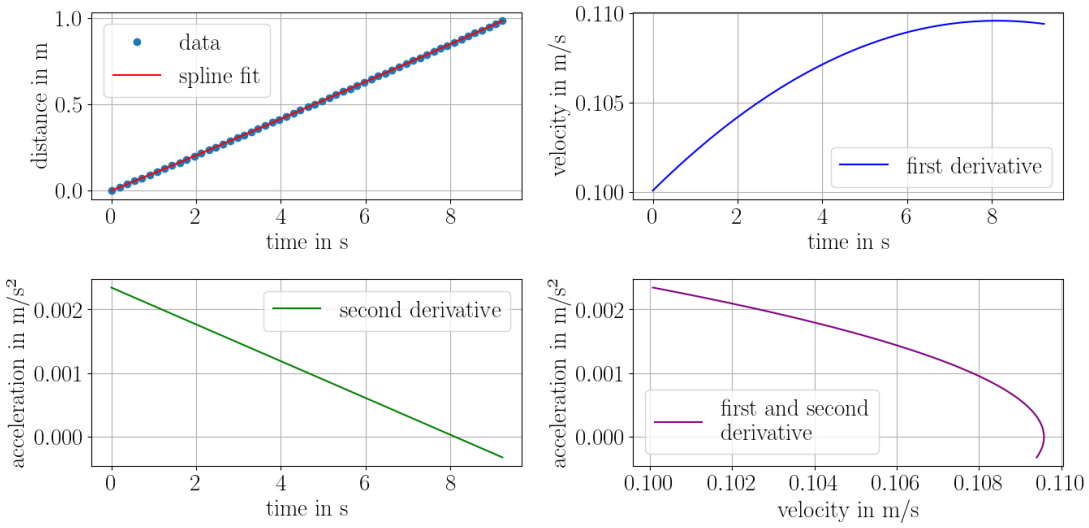

(a) Baffle data with spline fit and spline derivations

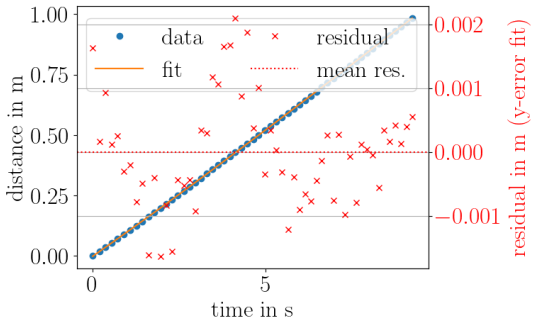

(b) Baffle data with spline fit and residuals

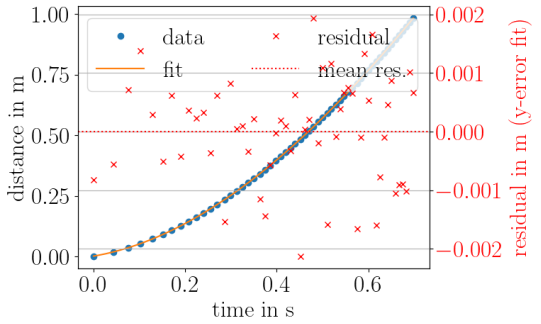

(c) Reference data with spline fit and residuals

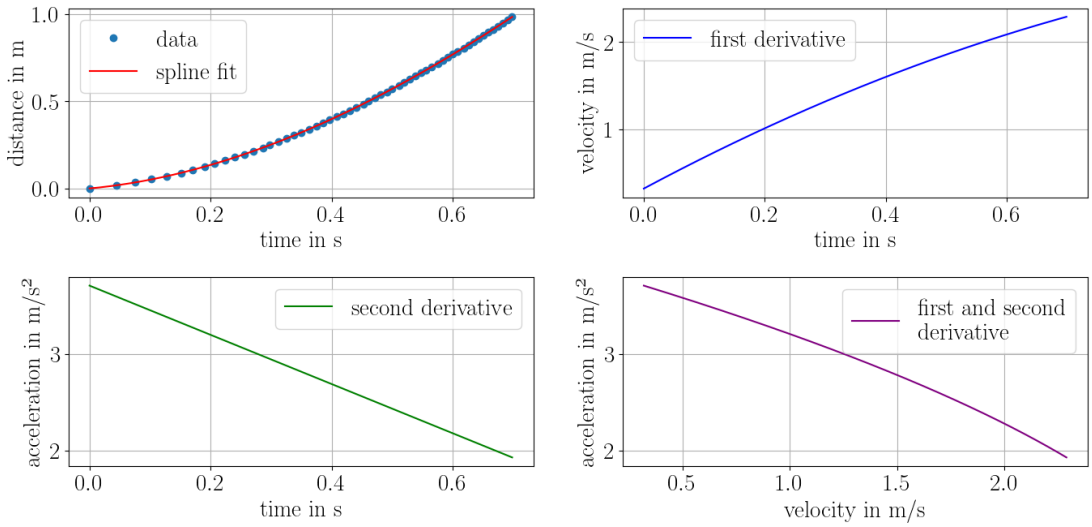

(d) Reference data with spline fit and spline derivations

Figure 30: Data, spline fits and residuals for top baffle measurement 2 with 2 kg counterweight

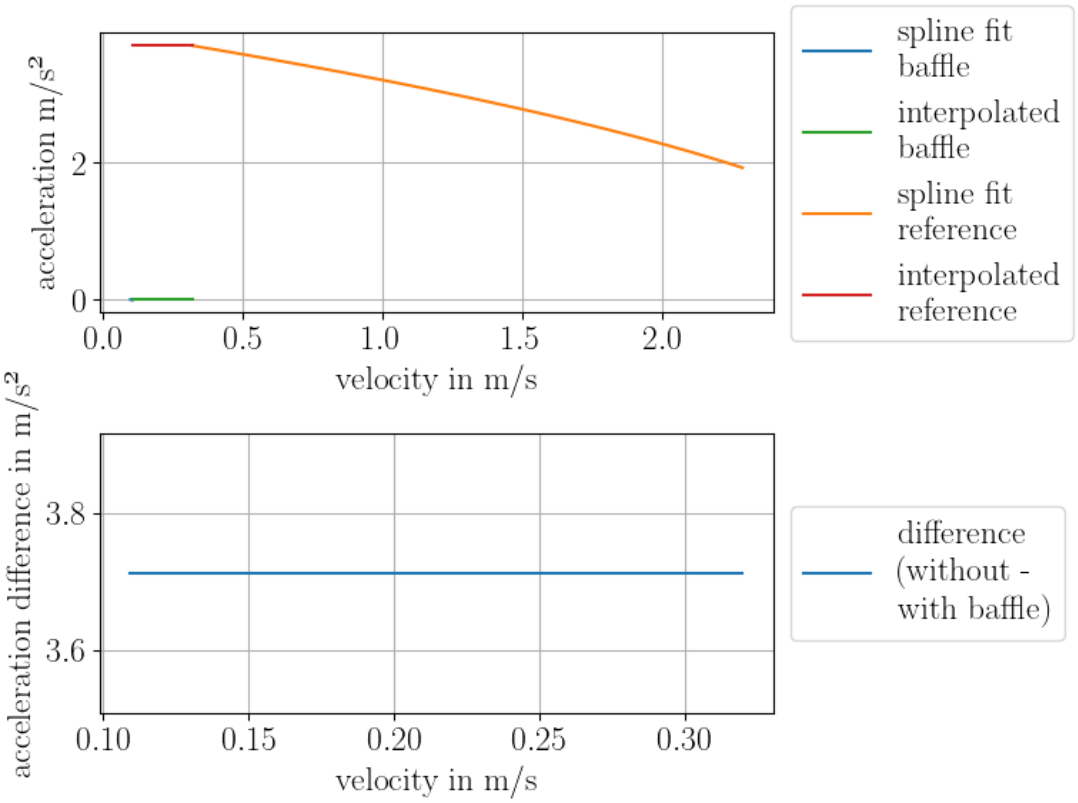

Figure 31: Acceleration over velocity of reference and baffle data with interpolated acceleration values for top baffle measurement 2 with 2 kg counterweight

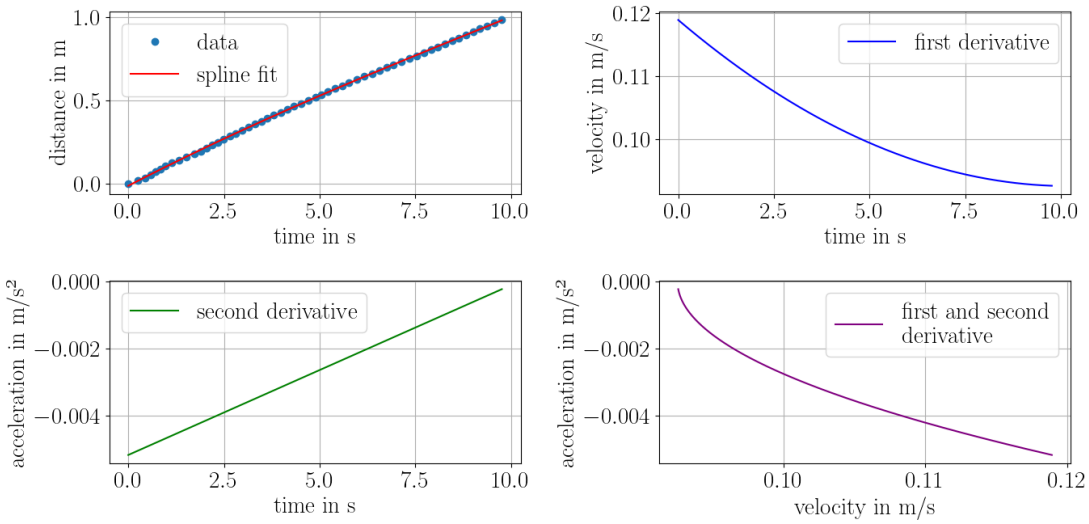

(a) Baffle data with spline fit and spline derivations

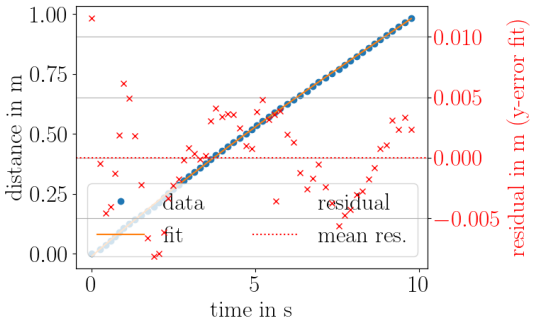

(b) Baffle data with spline fit and residuals

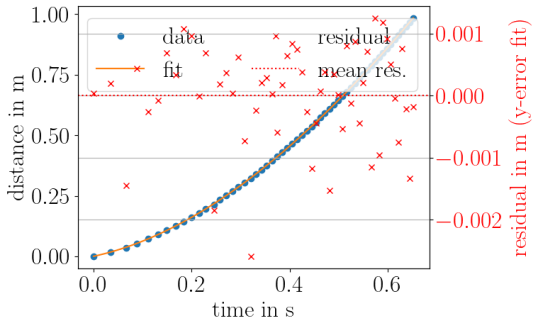

(c) Reference data with spline fit and residuals

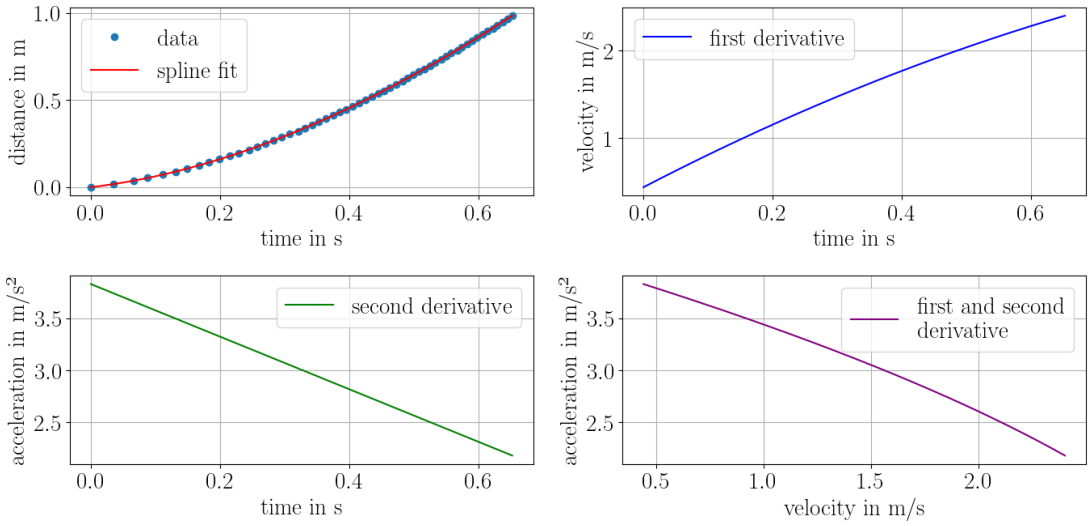

(d) Reference data with spline fit and spline derivations

Figure 32: Data, spline fits and residuals for top baffle measurement 3 with 2 kg counterweight

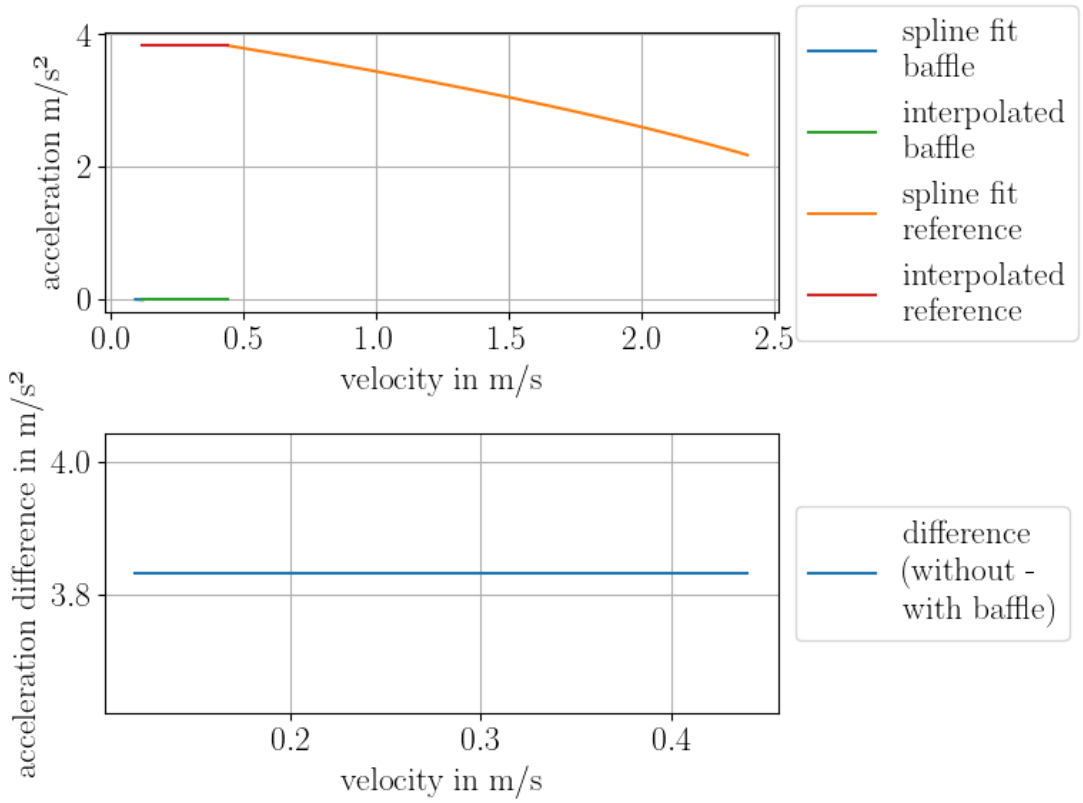

Figure 33: Acceleration over velocity of reference and baffle data with interpolated acceleration values for top baffle measurement 3 with 2 kg counterweight

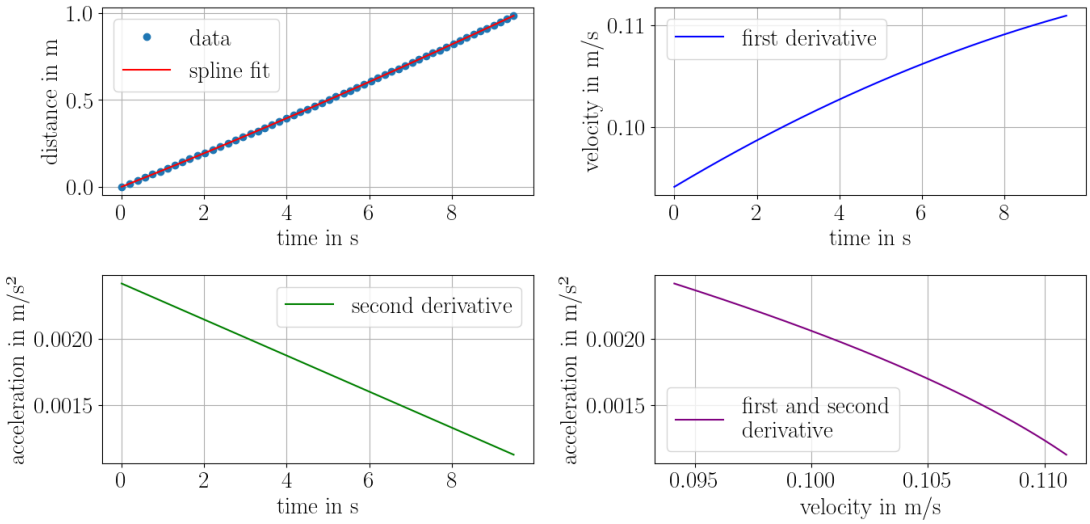

(a) Baffle data with spline fit and spline derivations

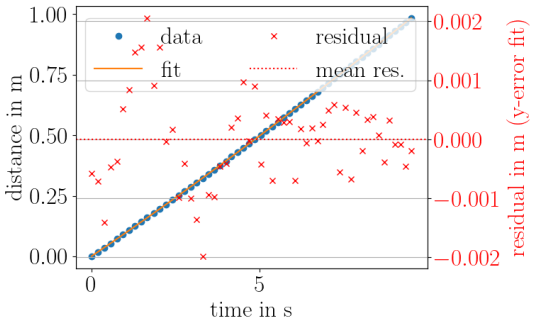

(b) Baffle data with spline fit and residuals

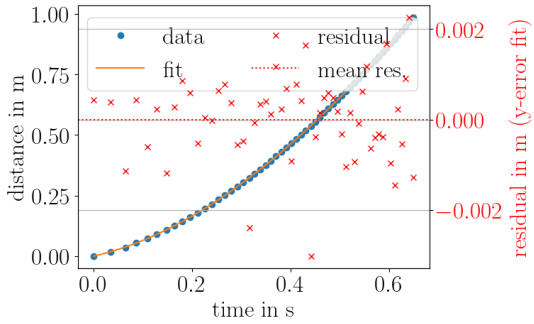

(c) Reference data with spline fit and residuals

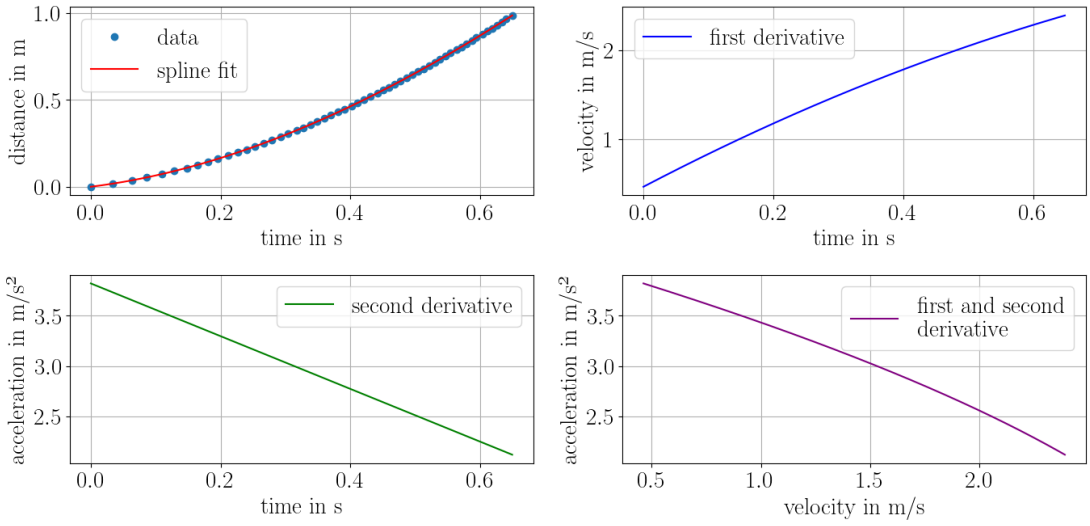

(d) Reference data with spline fit and spline derivations

Figure 34: Data, spline fits and residuals for top baffle measurement 4 with 2 kg counterweight

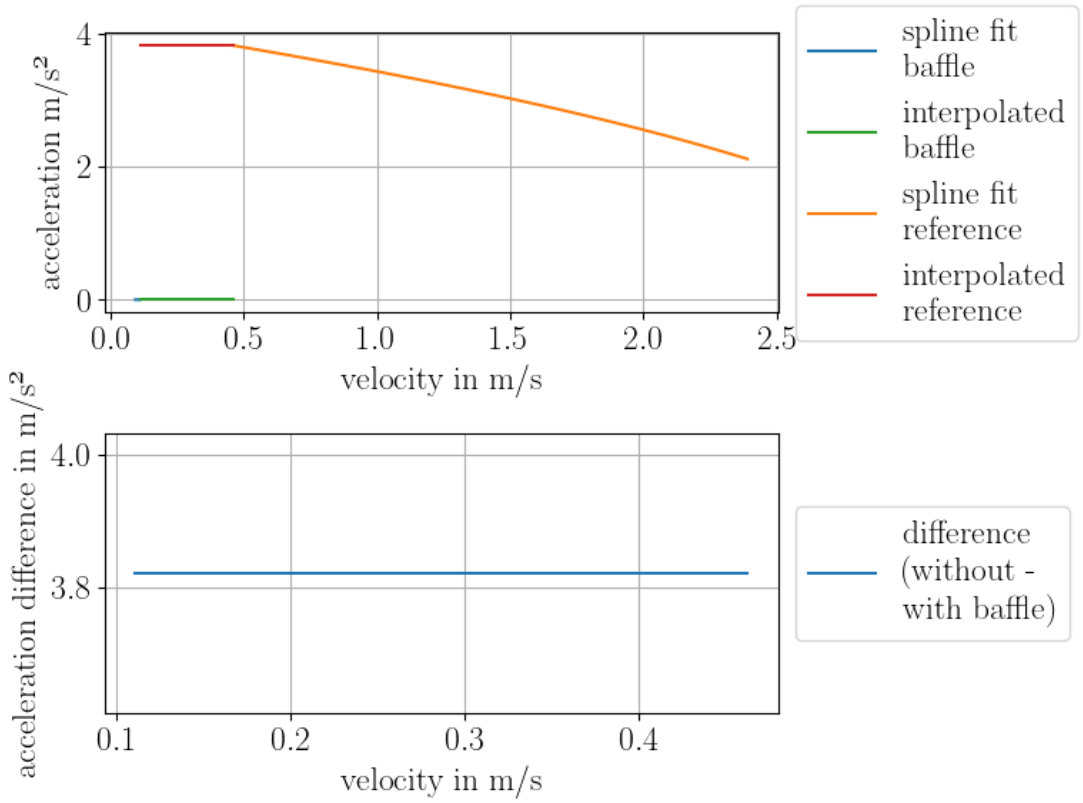

Figure 35: Acceleration over velocity of reference and baffle data with interpolated acceleration values for top baffle measurement 4 with 2 kg counterweight

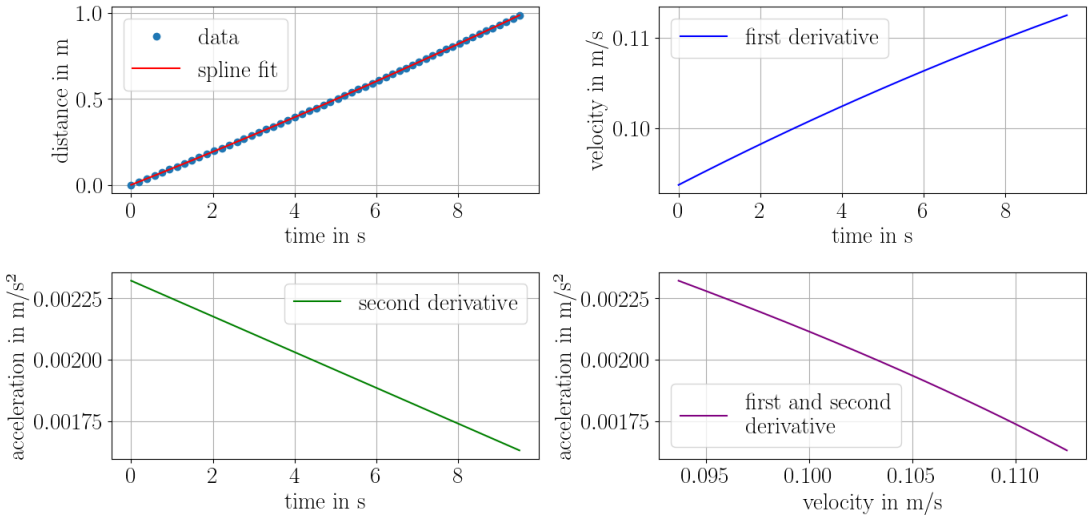

(a) Baffle data with spline fit and spline derivations

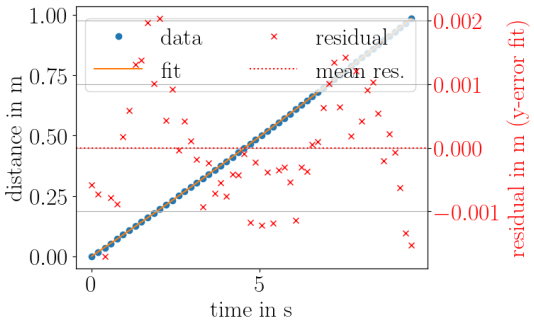

(b) Baffle data with spline fit and residuals

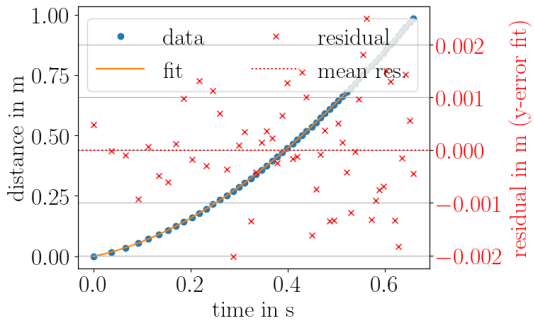

(c) Reference data with spline fit and residuals

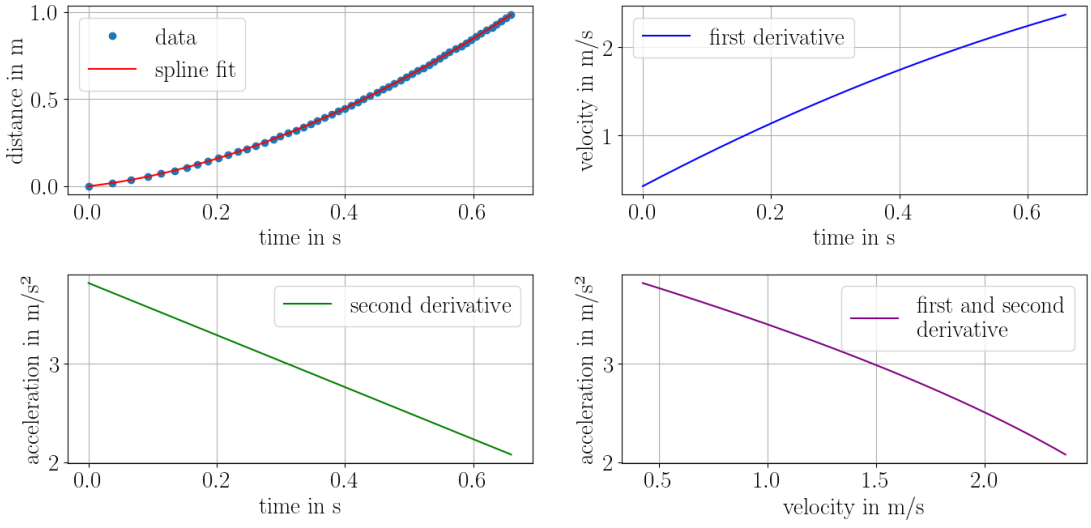

(d) Reference data with spline fit and spline derivations

Figure 36: Data, spline fits and residuals for top baffle measurement 5 with 2 kg counterweight

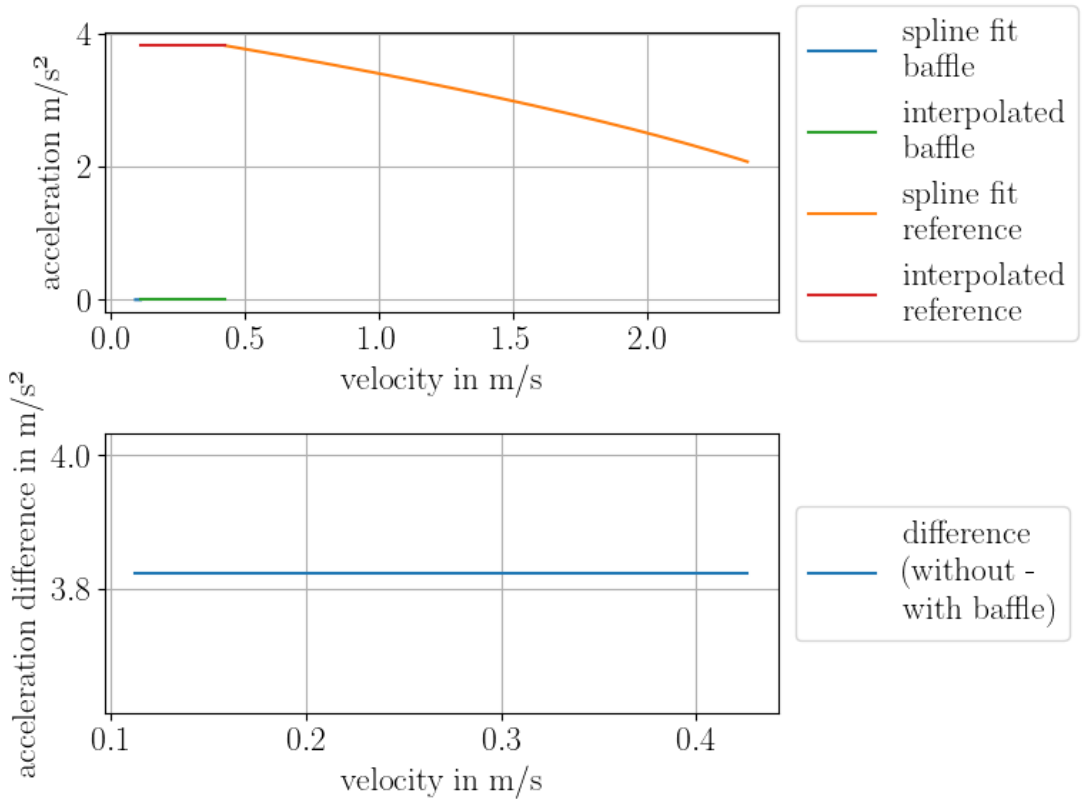

Figure 37: Acceleration over velocity of reference and baffle data with interpolated acceleration values for top baffle measurement 5 with 2 kg counterweight

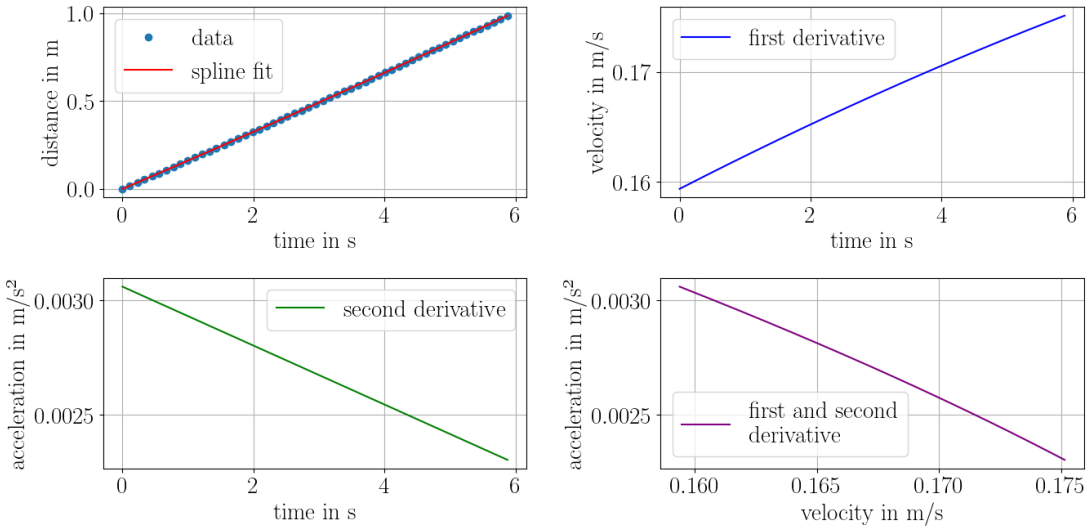

(a) Baffle data with spline fit and spline derivations

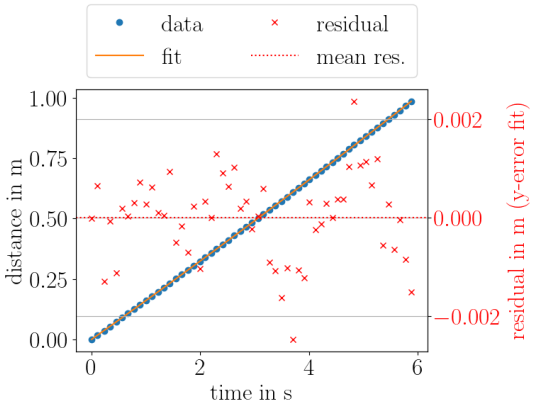

(b) Baffle data with spline fit and residuals

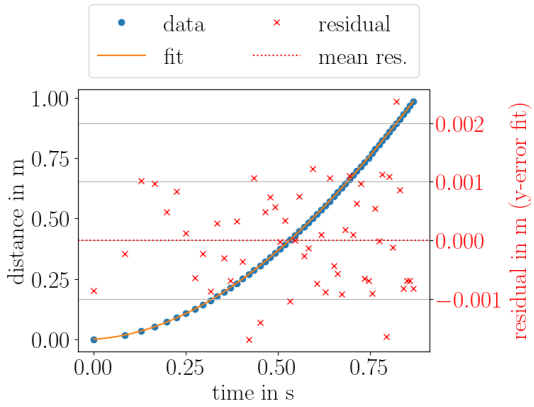

(c) Reference data with spline fit and residuals

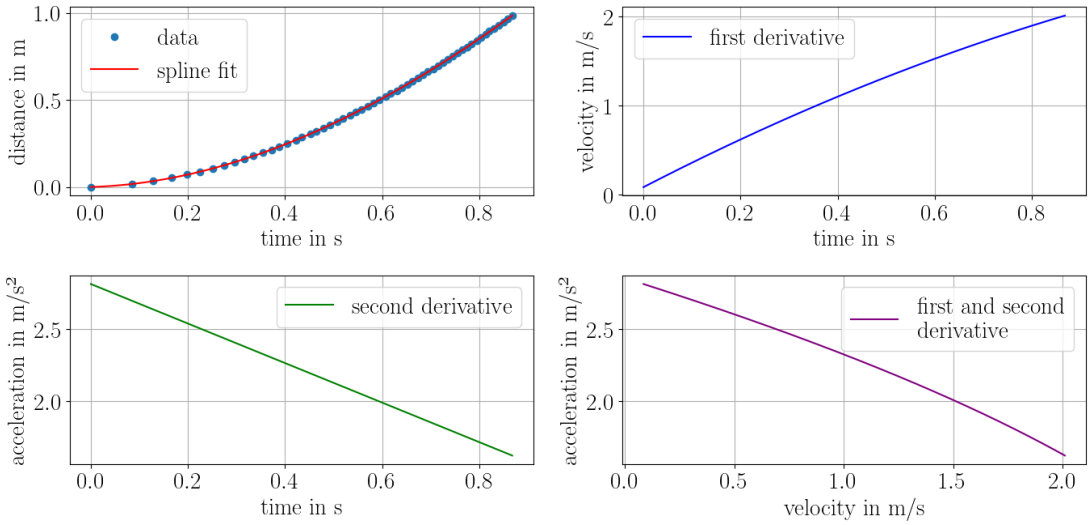

(d) Reference data with spline fit and spline derivations

Figure 38: Data, spline fits and residuals for top baffle measurement 0 with 2.5 kg counterweight

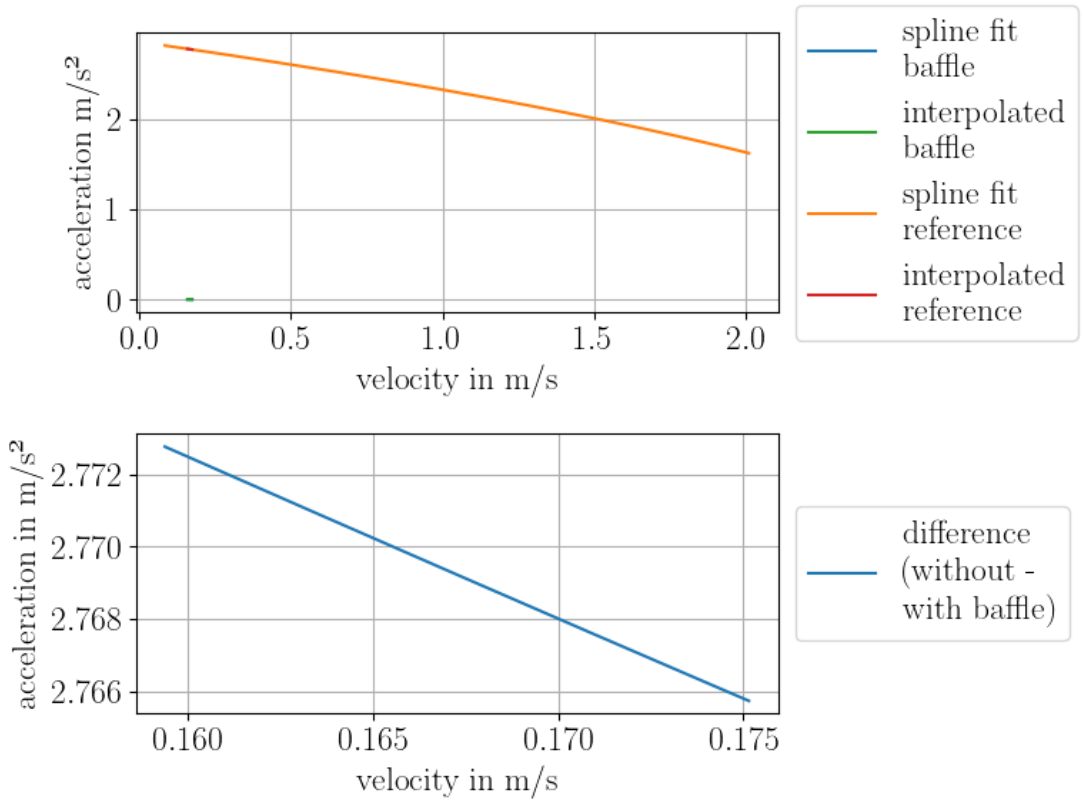

Figure 39: Acceleration over velocity of reference and baffle data with interpolated acceleration values for top baffle measurement 0 with 2.5 kg counterweight

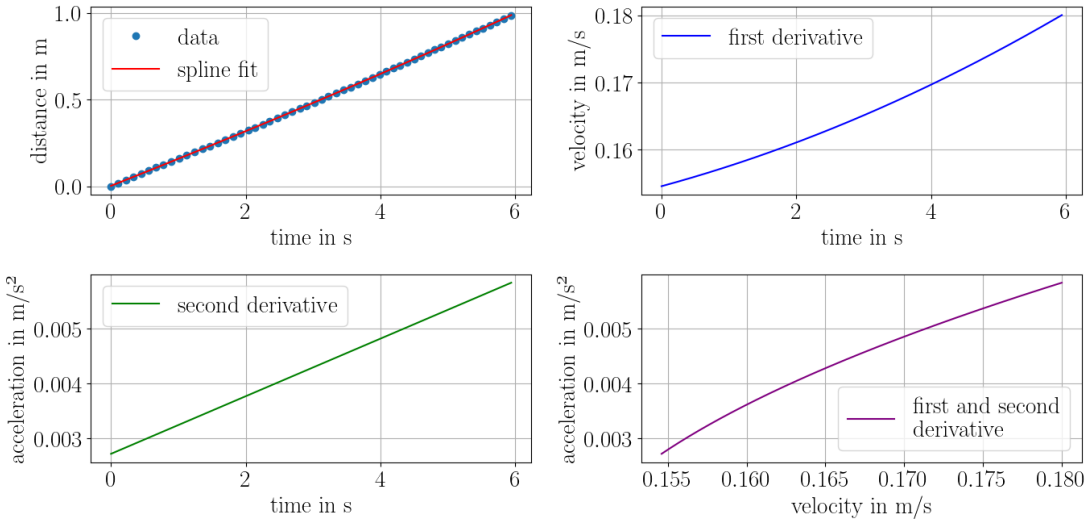

(a) Baffle data with spline fit and spline derivations

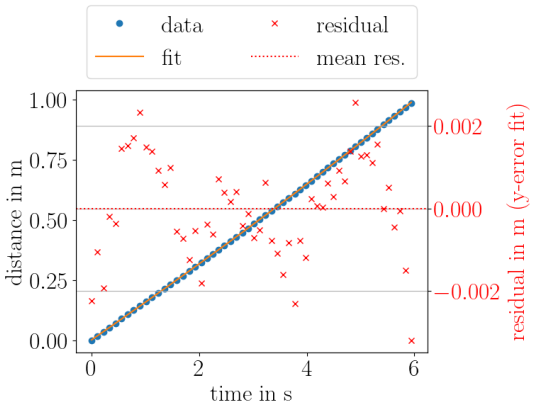

(b) Baffle data with spline fit and residuals

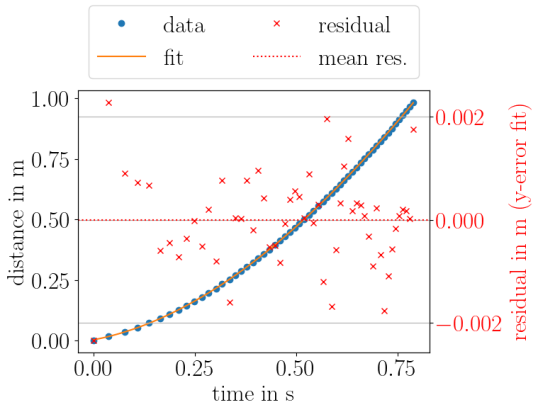

(c) Reference data with spline fit and residuals

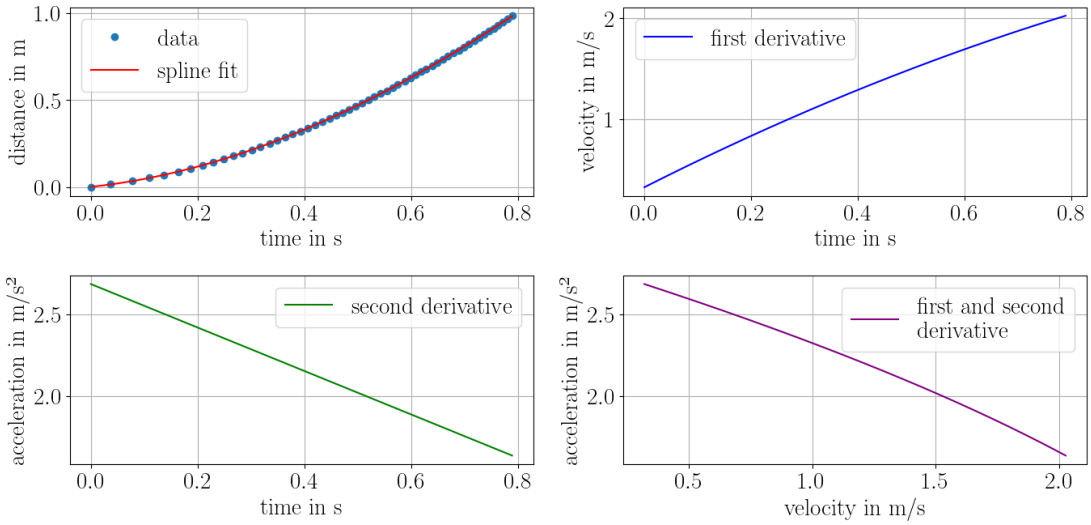

(d) Reference data with spline fit and spline derivations

Figure 40: Data, spline fits and residuals for top baffle measurement 1 with 2.5 kg counterweight

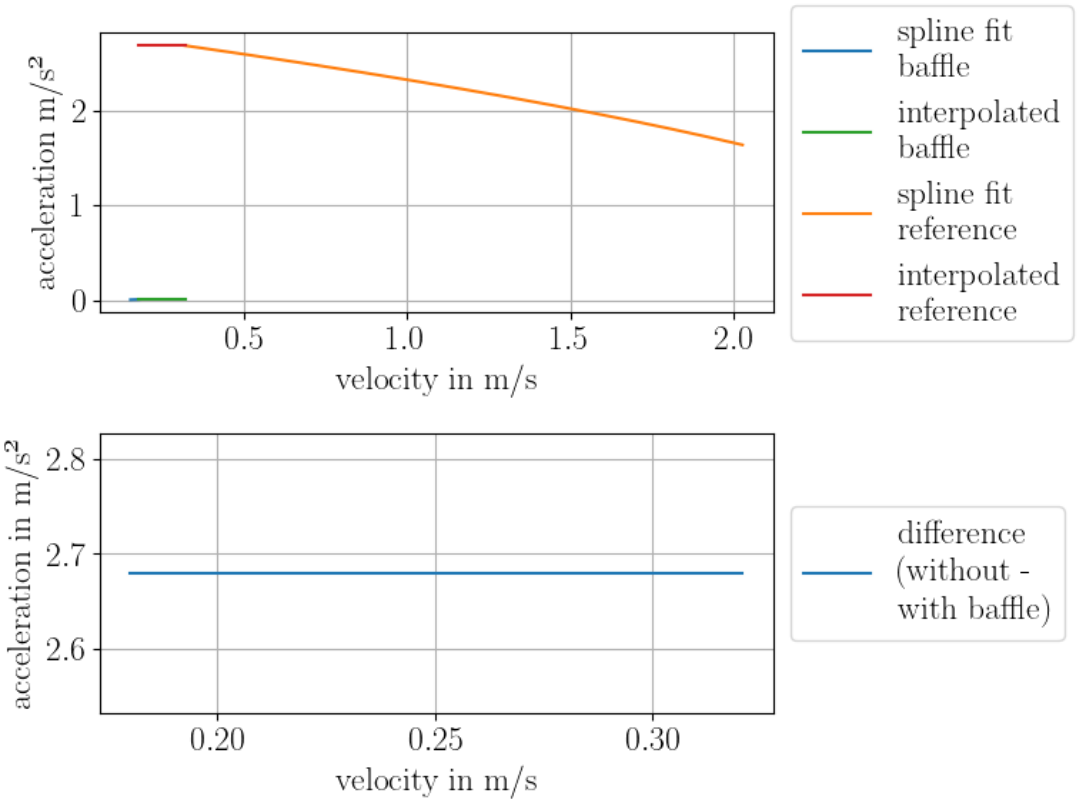

Figure 41: Acceleration over velocity of reference and baffle data with interpolated acceleration values for top baffle measurement 1 with 2.5 kg counterweight

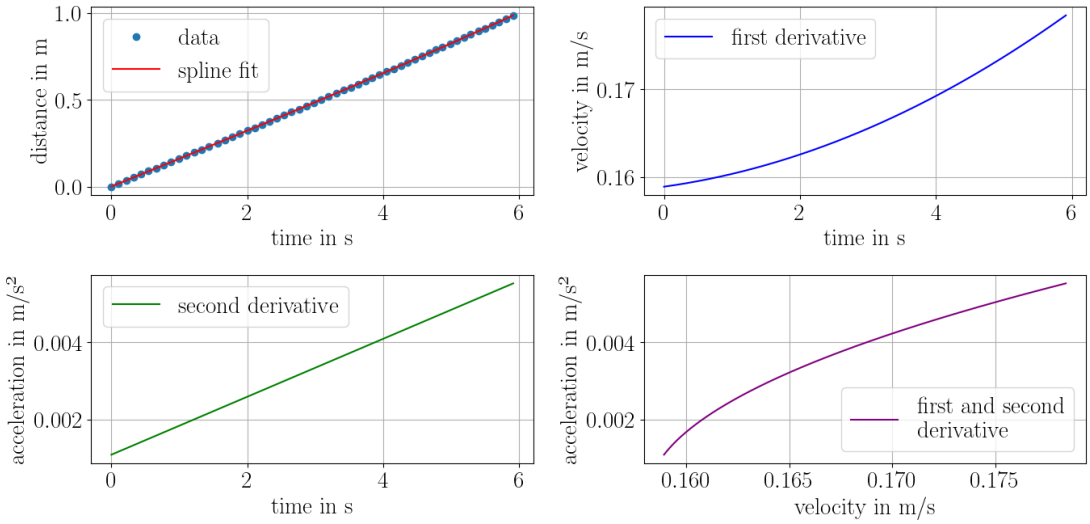

(a) Baffle data with spline fit and spline derivations

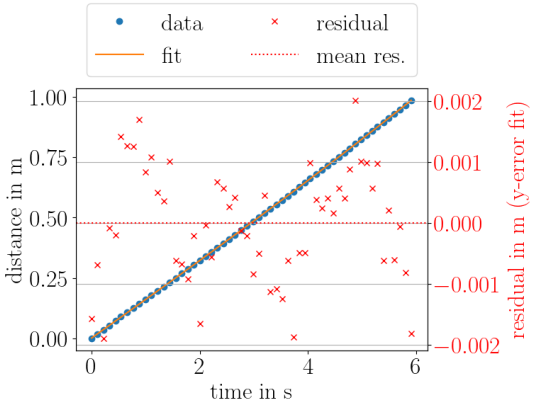

(b) Baffle data with spline fit and residuals

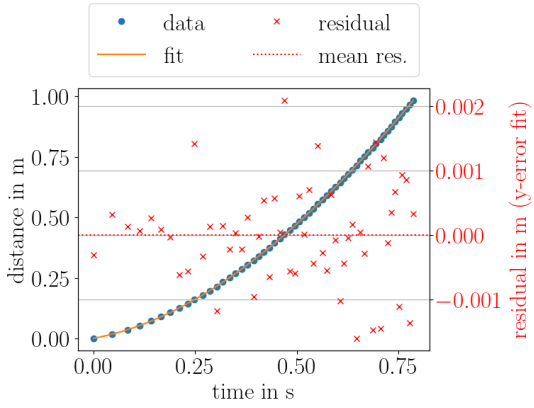

(c) Reference data with spline fit and residuals

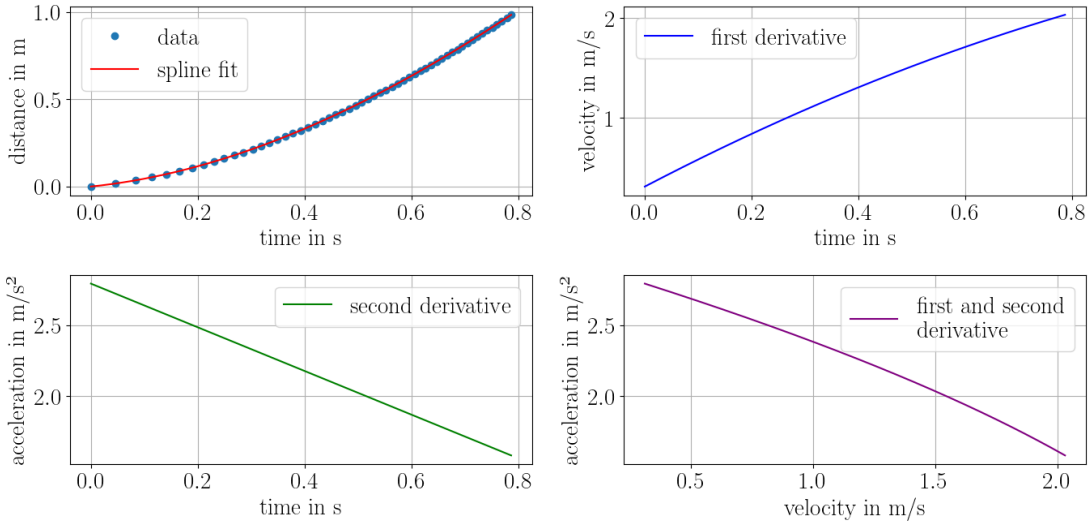

(d) Reference data with spline fit and spline derivations

Figure 42: Data, spline fits and residuals for top baffle measurement 2 with 2.5 kg counterweight

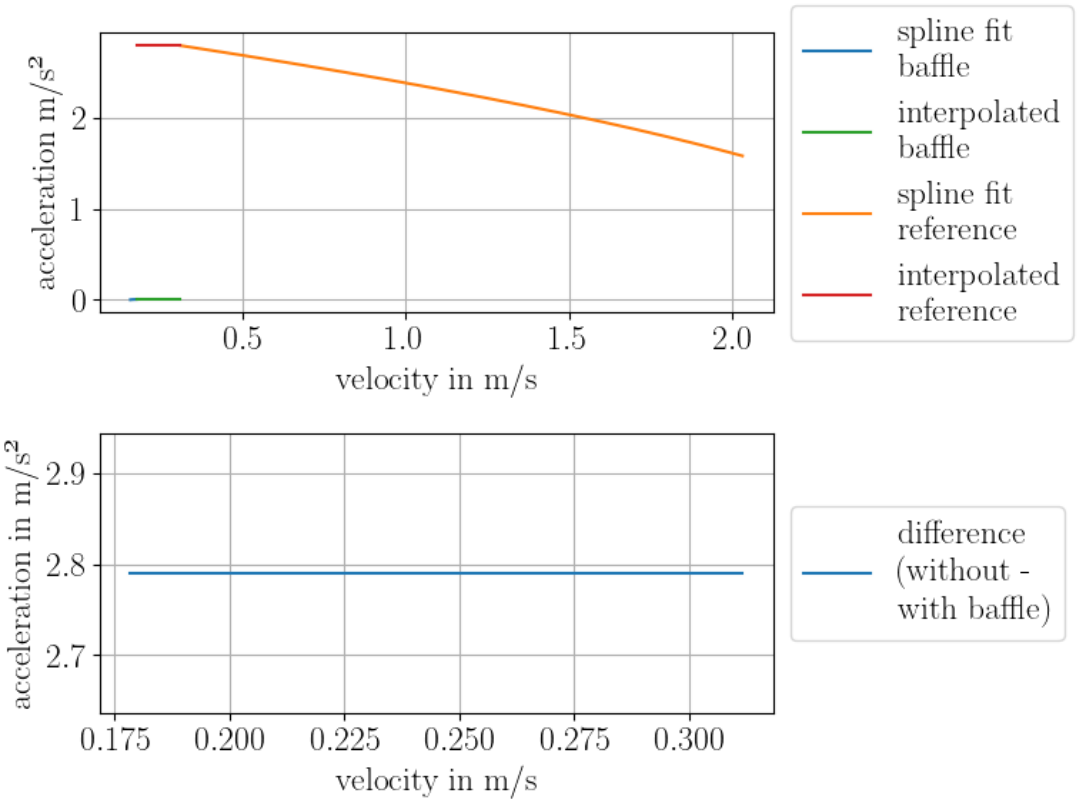

Figure 43: Acceleration over velocity of reference and baffle data with interpolated acceleration values for top baffle measurement 2 with 2.5 kg counterweight

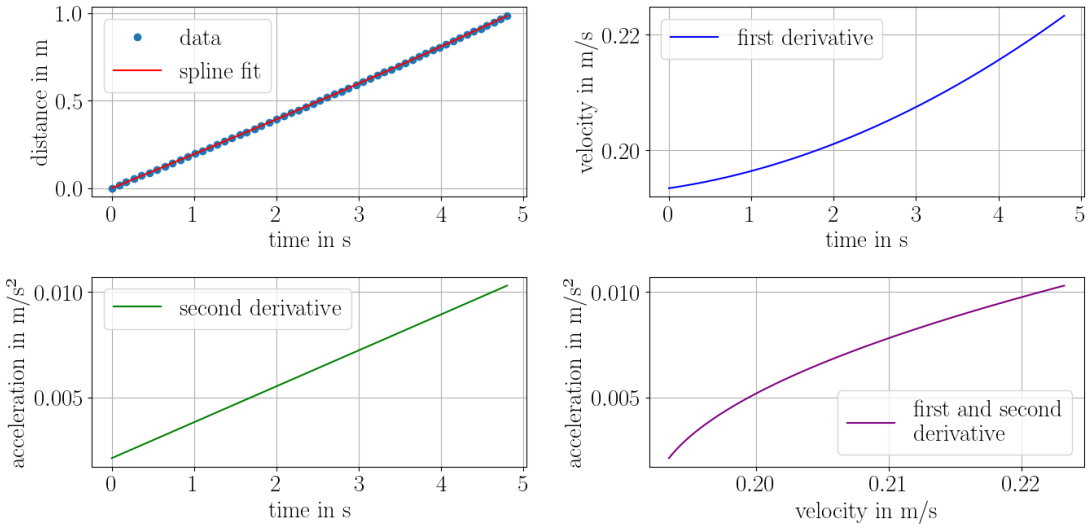

(a) Baffle data with spline fit and spline derivations

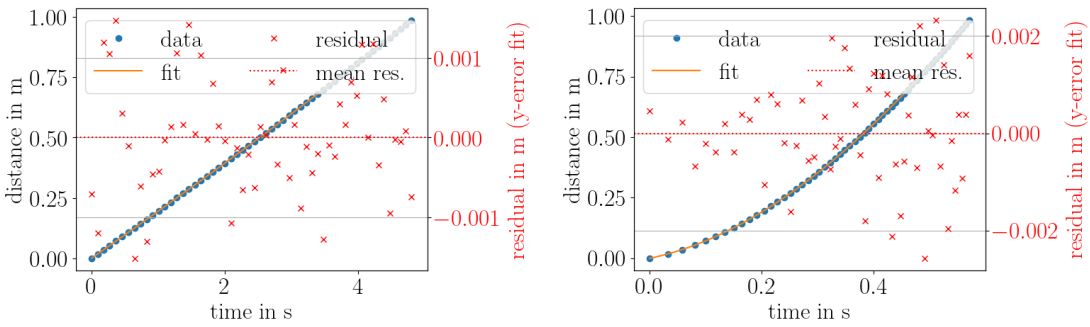

(b) Baffle data with spline fit and residuals

(c) Reference data with spline fit and residuals

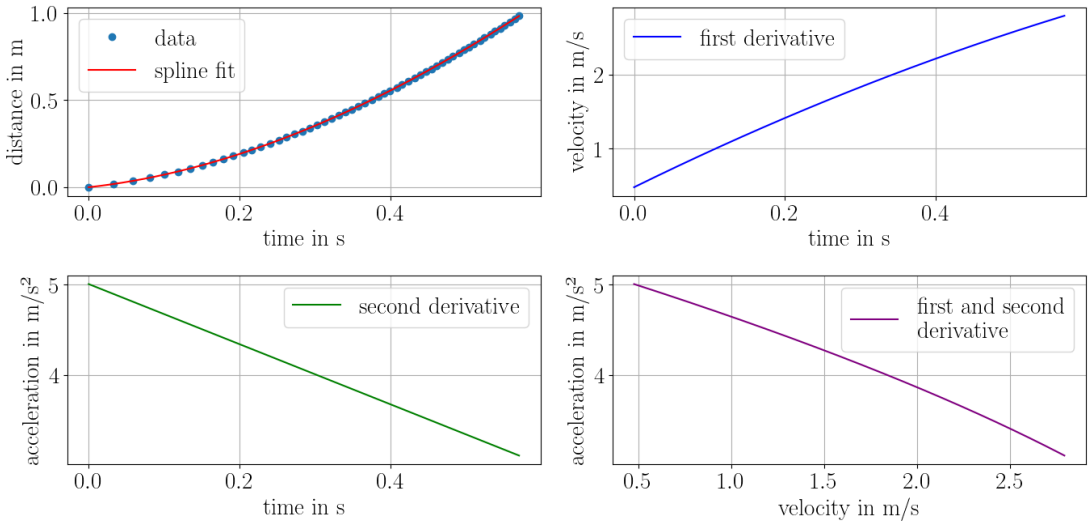

(d) Reference data with spline fit and spline derivations

Figure 44: Data, spline fits and residuals for top baffle measurement 1 with 3 kg counterweight

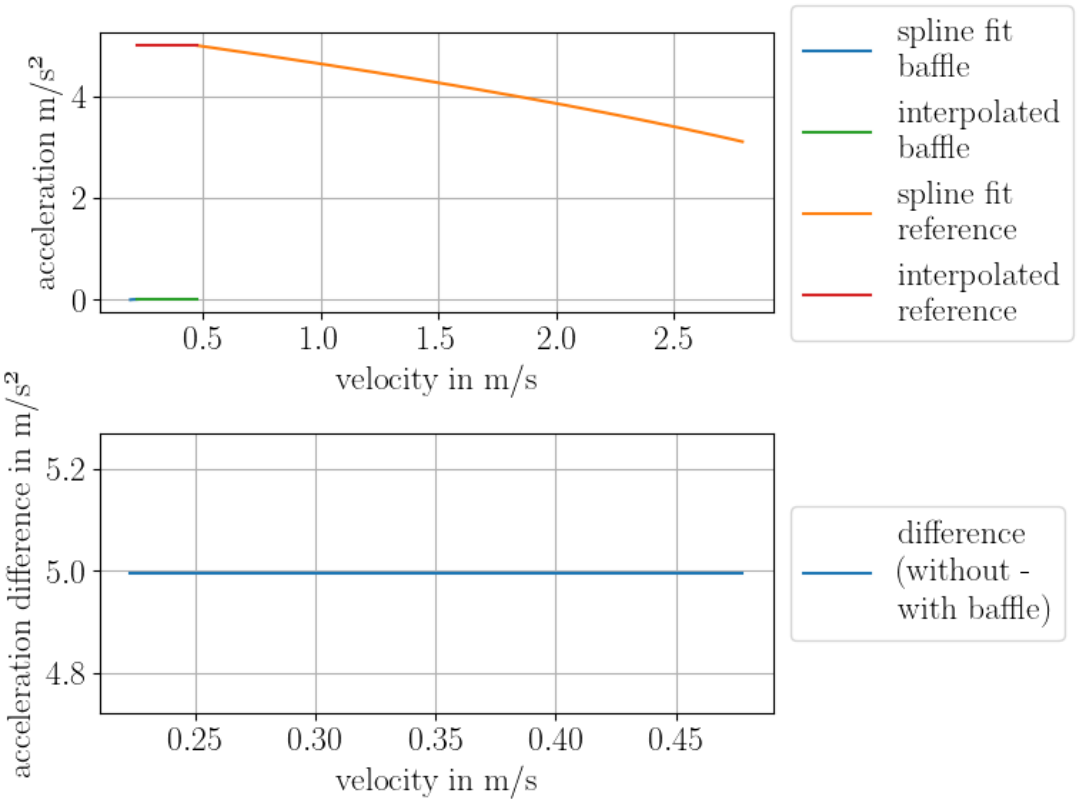

Figure 45: Acceleration over velocity of reference and baffle data with interpolated acceleration values for top baffle measurement 1 with 3 kg counterweight

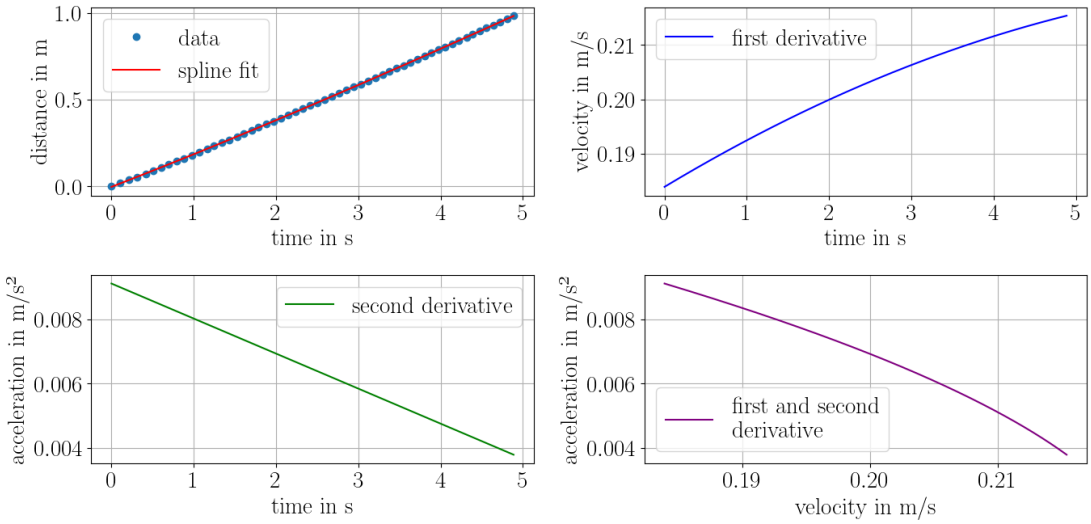

(a) Baffle data with spline fit and spline derivations

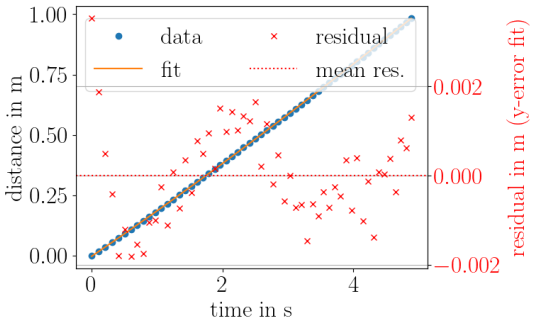

(b) Baffle data with spline fit and residuals

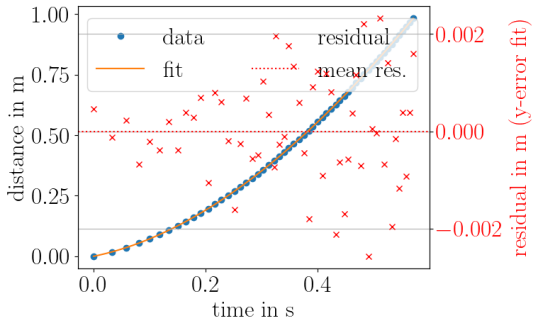

(c) Reference data with spline fit and residuals

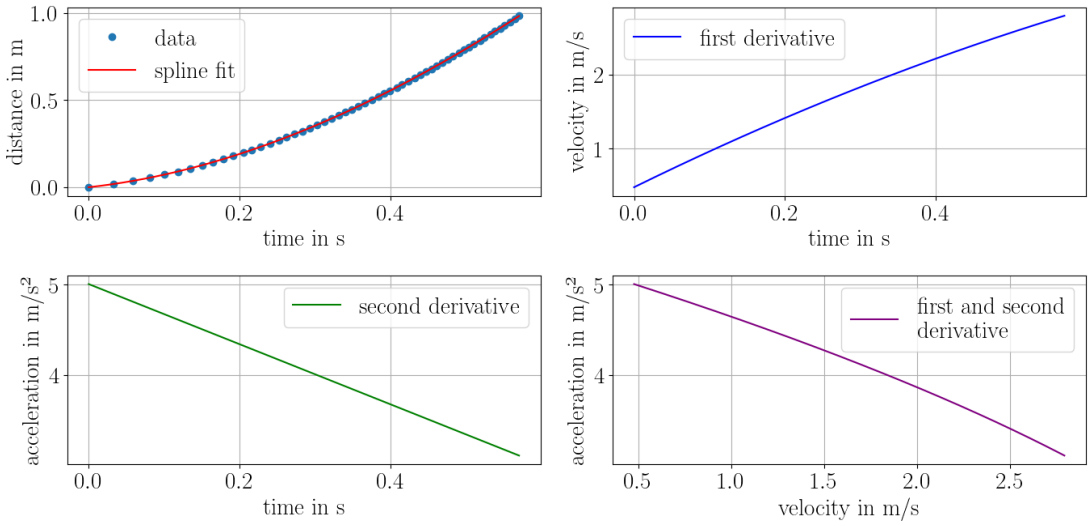

(d) Reference data with spline fit and spline derivations

Figure 46: Data, spline fits and residuals for top baffle measurement 2 with 3 kg counterweight

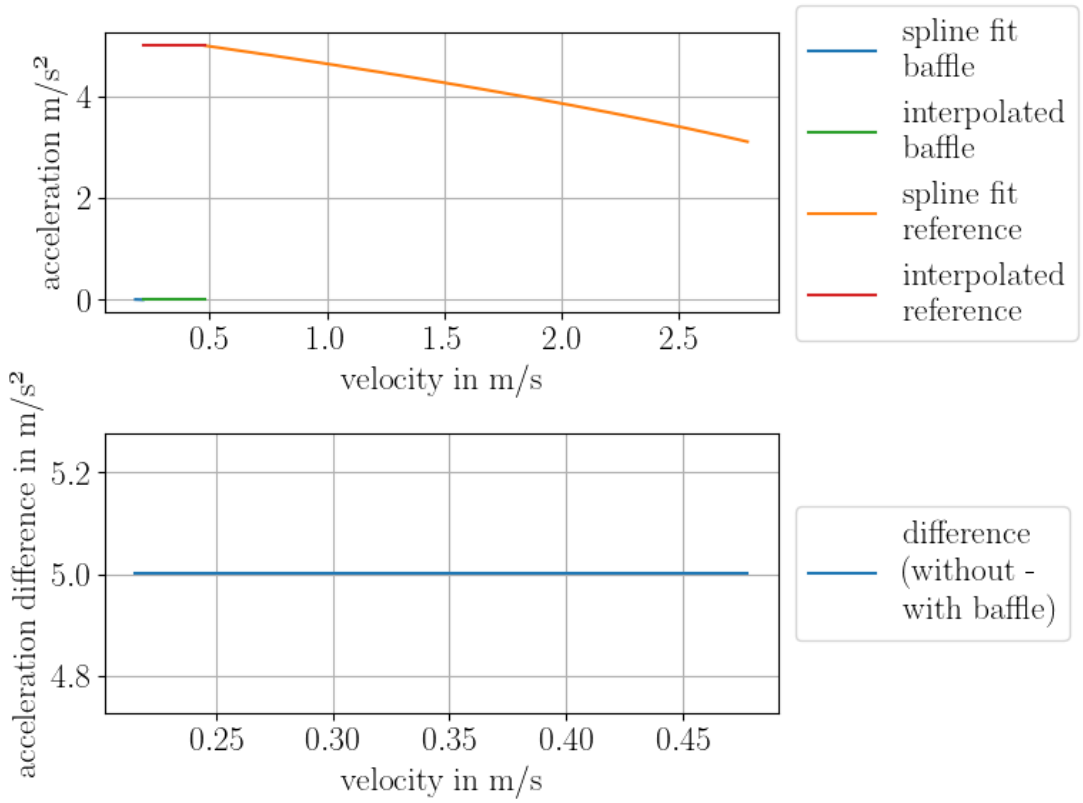

Figure 47: Acceleration over velocity of reference and baffle data with interpolated acceleration values for top baffle measurement 2 with 3 kg counterweight

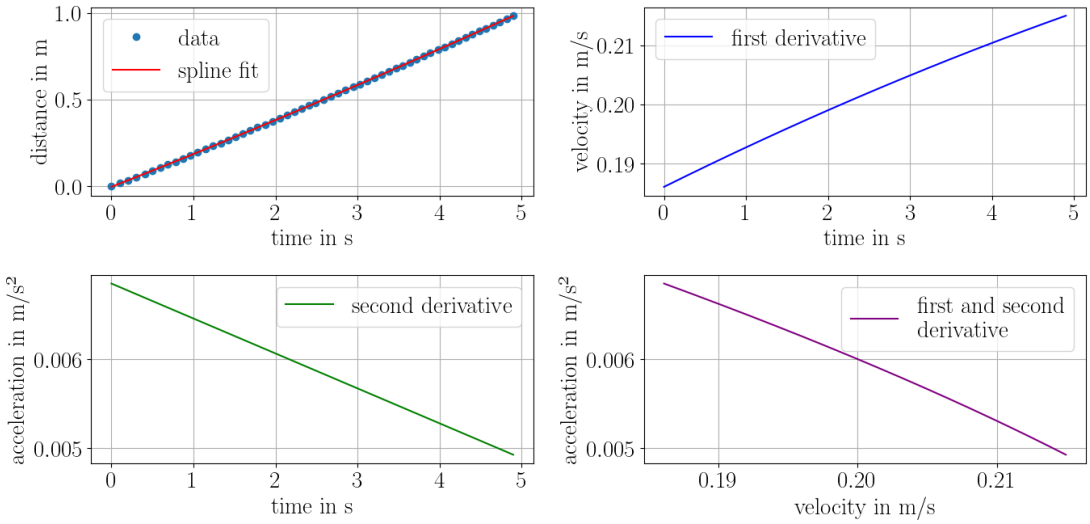

(a) Baffle data with spline fit and spline derivations

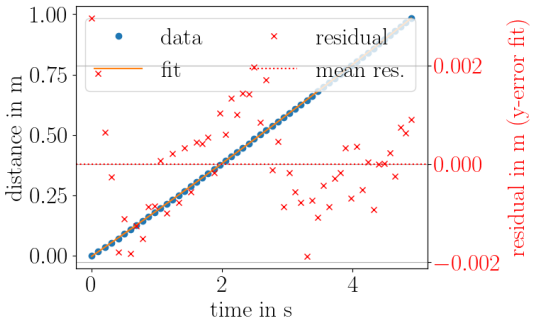

(b) Baffle data with spline fit and residuals

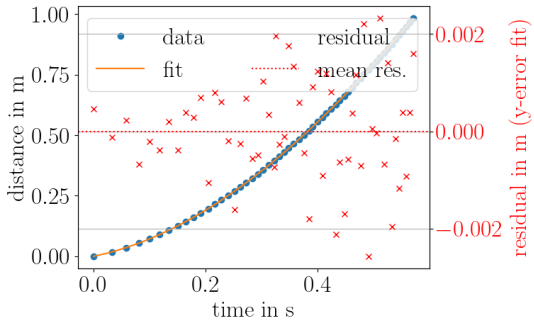

(c) Reference data with spline fit and residuals

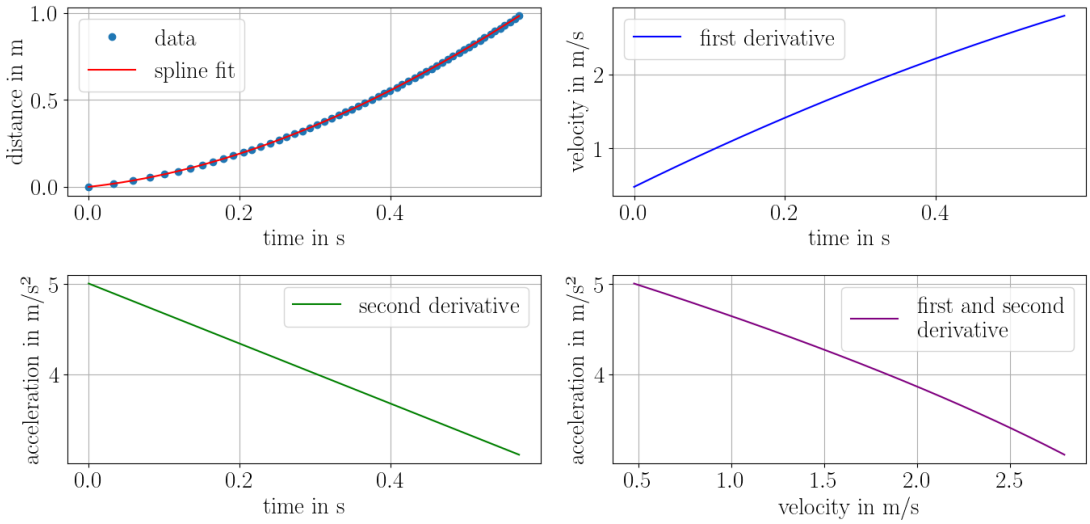

(d) Reference data with spline fit and spline derivations

Figure 48: Data, spline fits and residuals for top baffle measurement 3 with 3 kg counterweight

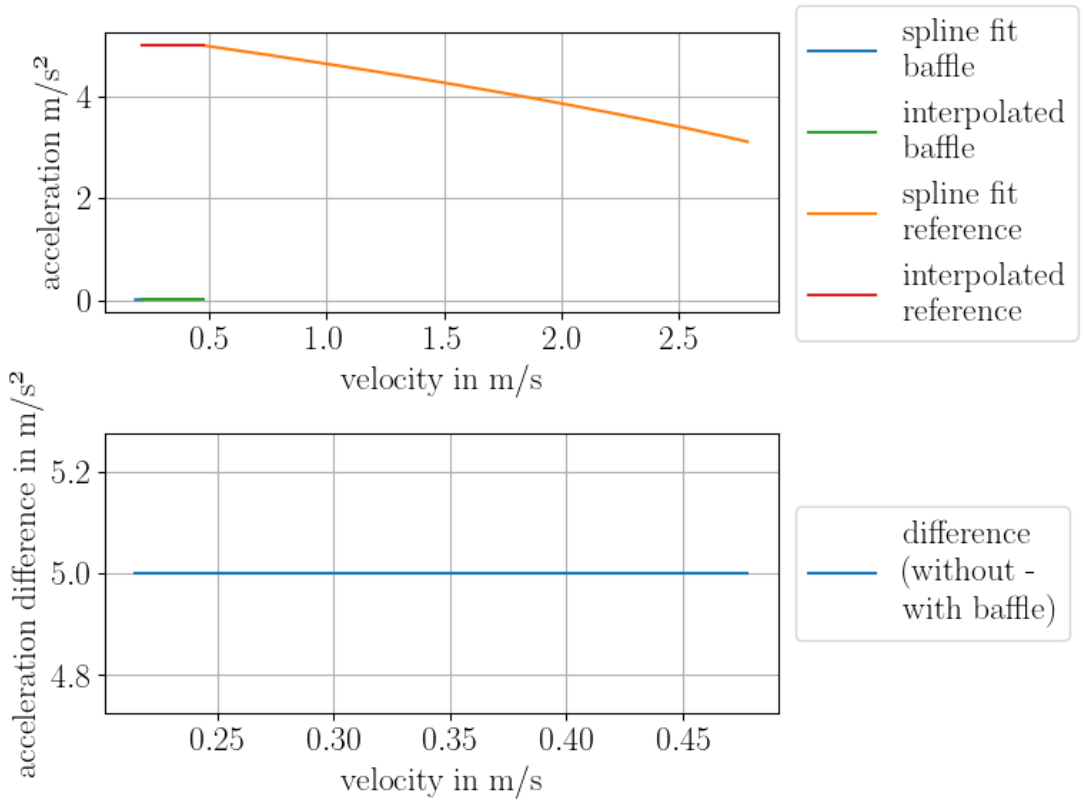

Figure 49: Acceleration over velocity of reference and baffle data with interpolated acceleration values for top baffle measurement 3 with 3 kg counterweight

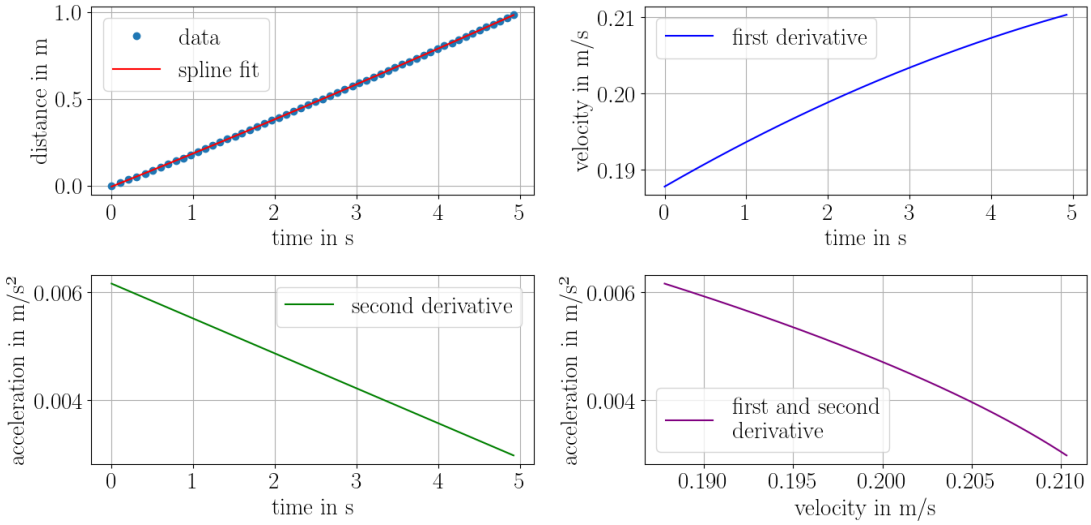

(a) Baffle data with spline fit and spline derivations

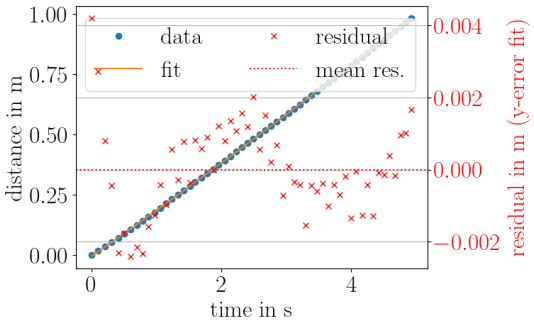

(b) Baffle data with spline fit and residuals

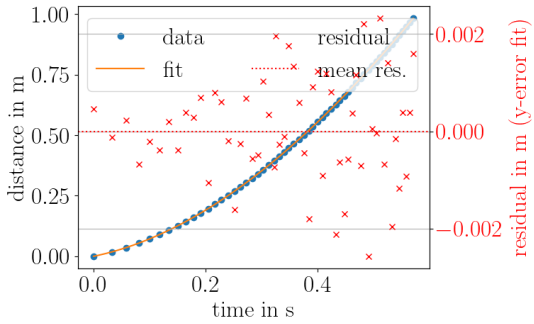

(c) Reference data with spline fit and residuals

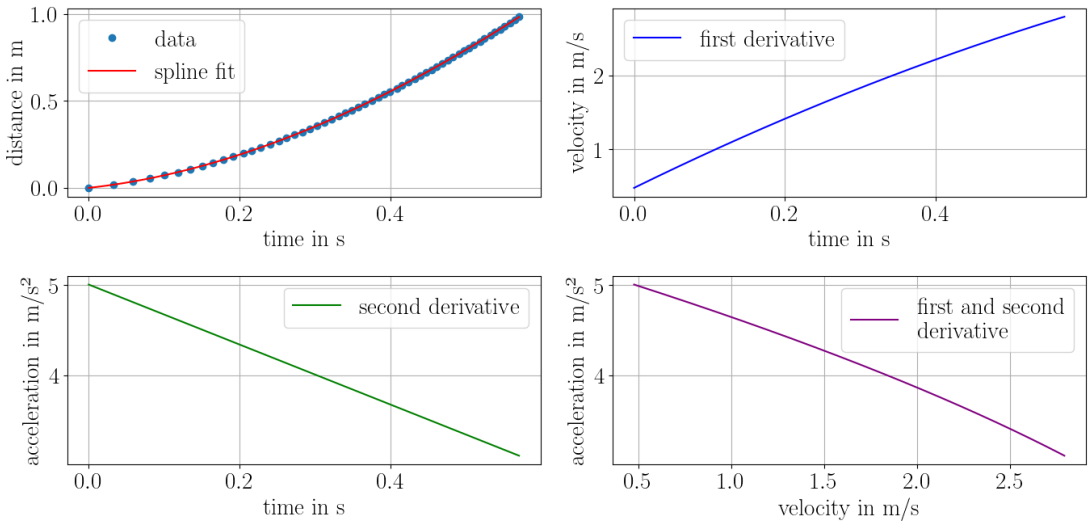

(d) Reference data with spline fit and spline derivations

Figure 50: Data, spline fits and residuals for top baffle measurement 4 with 3 kg counterweight

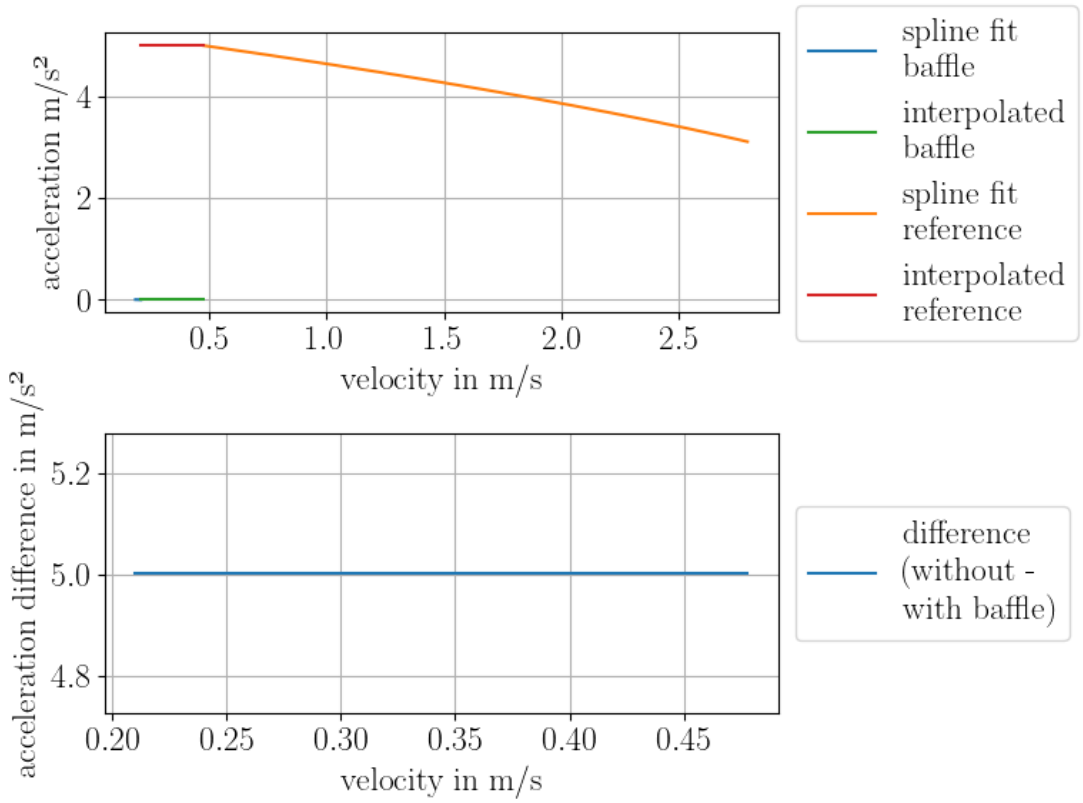

Figure 51: Acceleration over velocity of reference and baffle data with interpolated acceleration values for top baffle measurement 4 with 3 kg counterweight

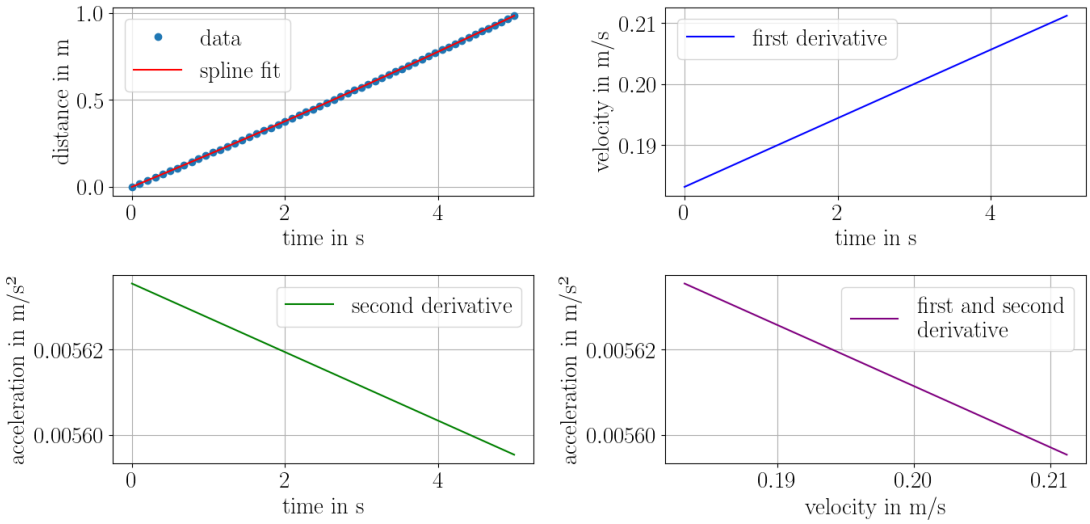

(a) Baffle data with spline fit and spline derivations

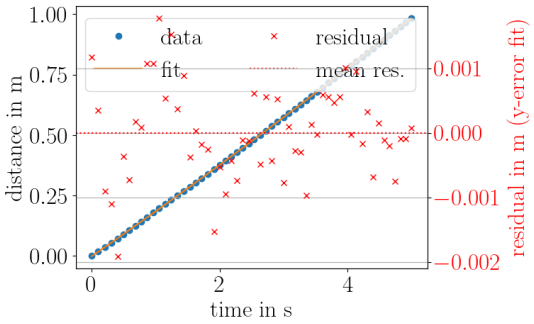

(b) Baffle data with spline fit and residuals

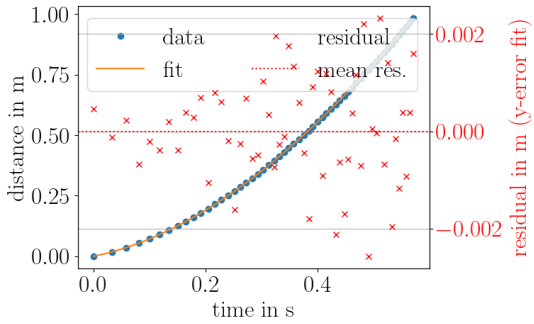

(c) Reference data with spline fit and residuals

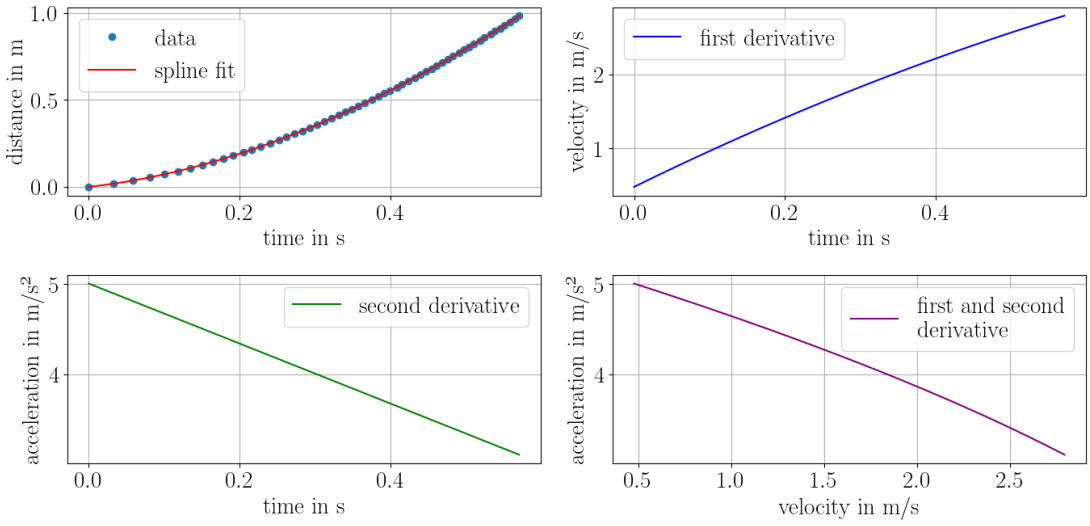

(d) Reference data with spline fit and spline derivations

Figure 52: Data, spline fits and residuals for top baffle measurement 5 with 3 kg counterweight

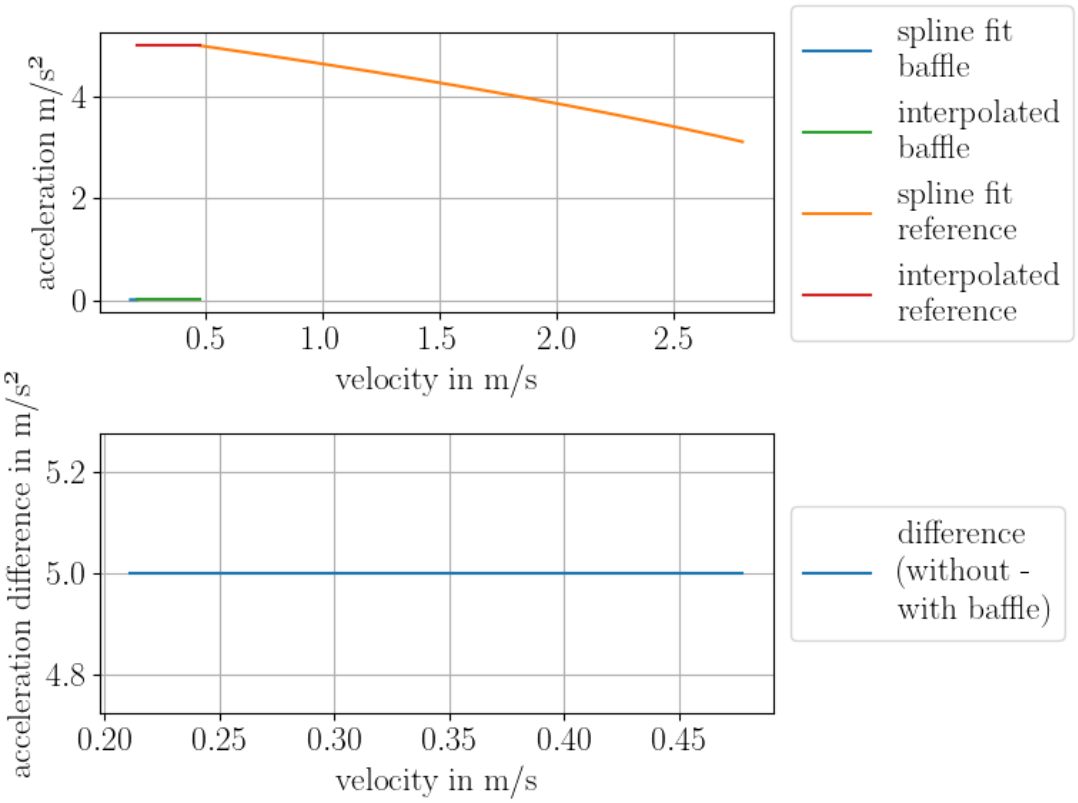

Figure 53: Acceleration over velocity of reference and baffle data with interpolated acceleration values for top baffle measurement 5 with 3 kg counterweight

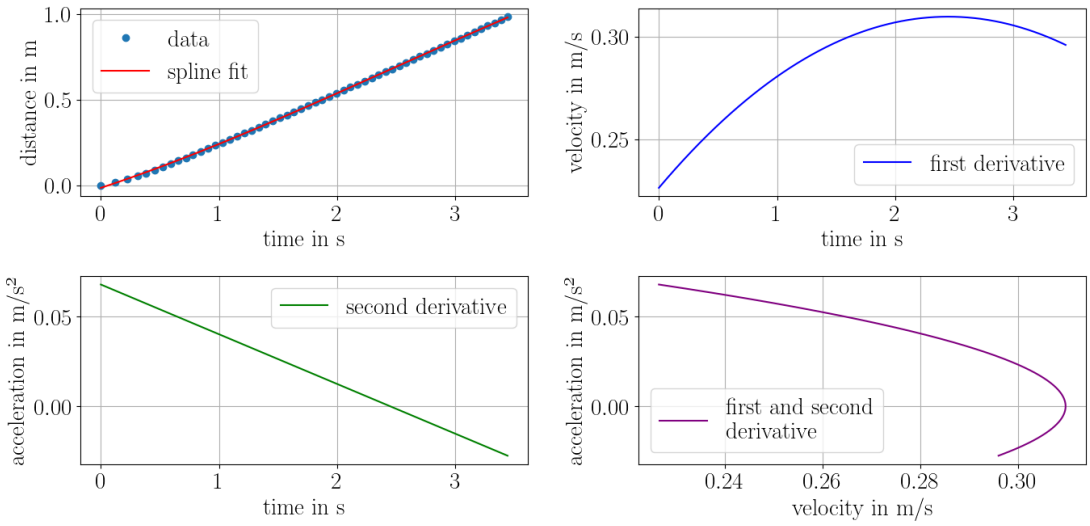

(a) Baffle data with spline fit and spline derivations

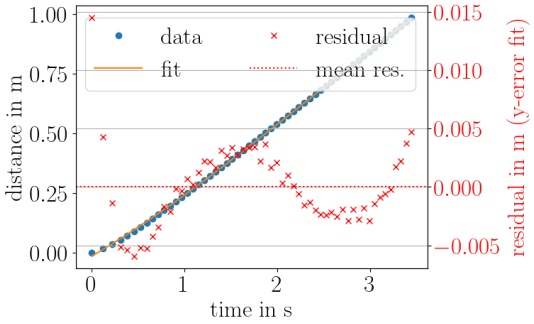

(b) Baffle data with spline fit and residuals

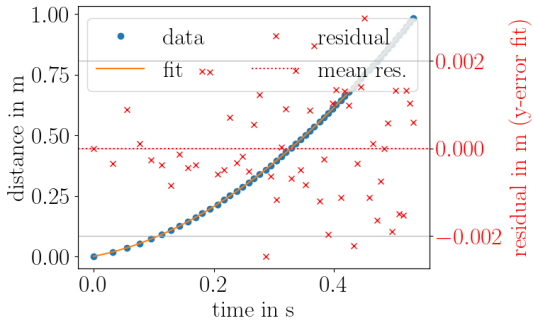

(c) Reference data with spline fit and residuals

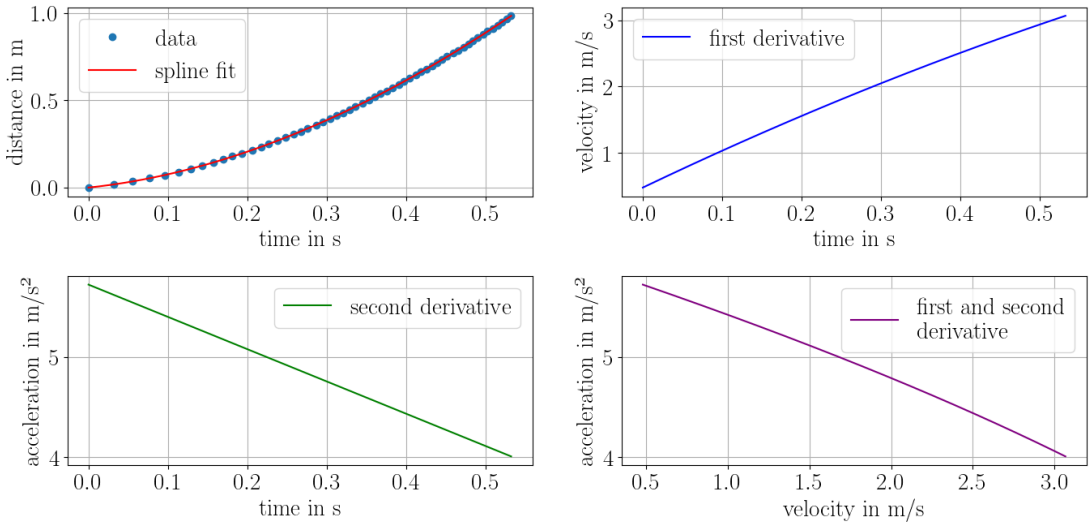

(d) Reference data with spline fit and spline derivations

Figure 54: Data, spline fits and residuals for top baffle measurement 1 with 4 kg counterweight

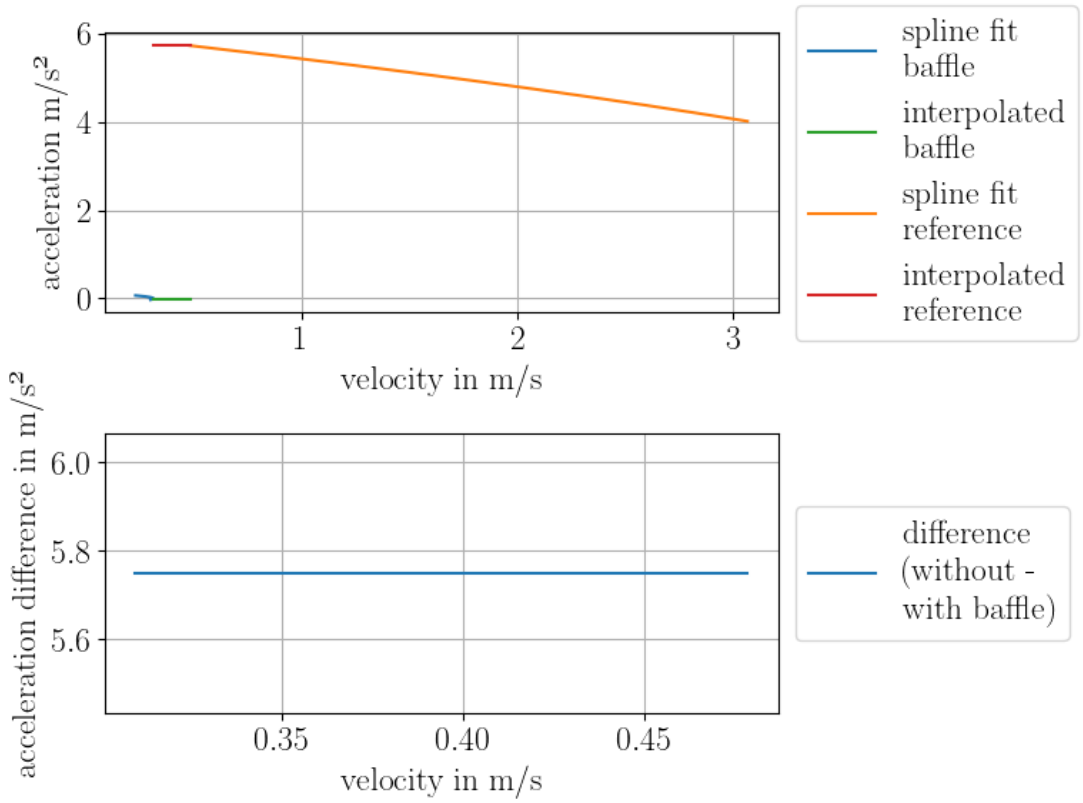

Figure 55: Acceleration over velocity of reference and baffle data with interpolated acceleration values for top baffle measurement 1 with 4 kg counterweight

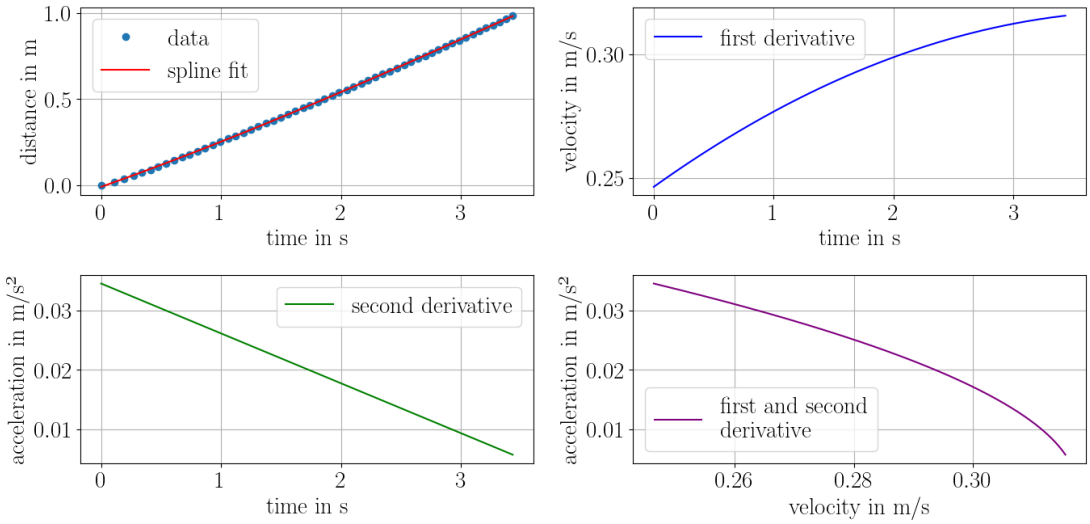

(a) Baffle data with spline fit and spline derivations

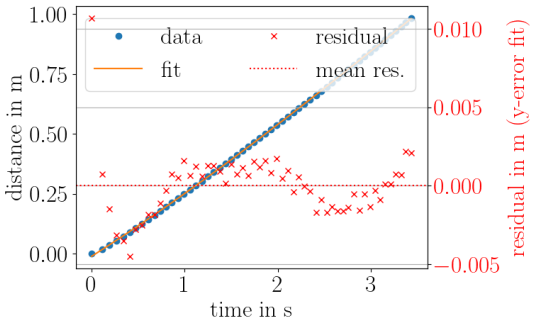

(b) Baffle data with spline fit and residuals

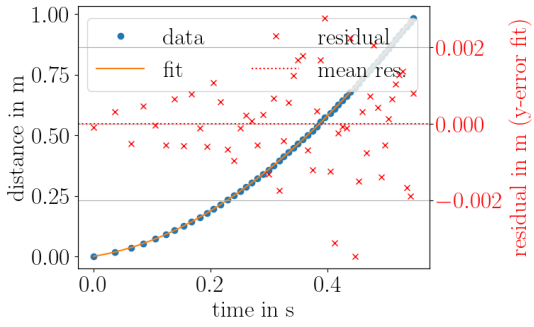

(c) Reference data with spline fit and residuals

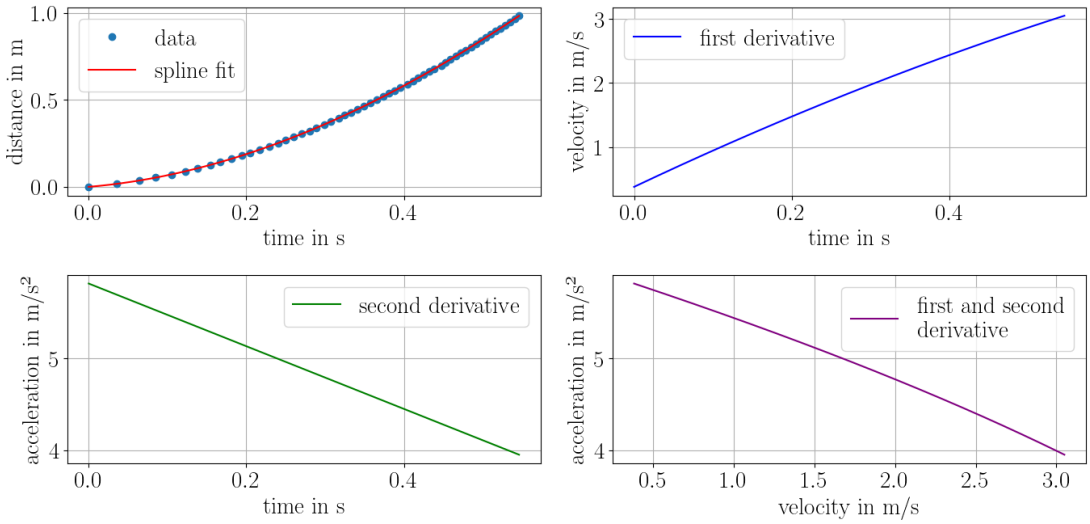

(d) Reference data with spline fit and spline derivations

Figure 56: Data, spline fits and residuals for top baffle measurement 2 with 4 kg counterweight

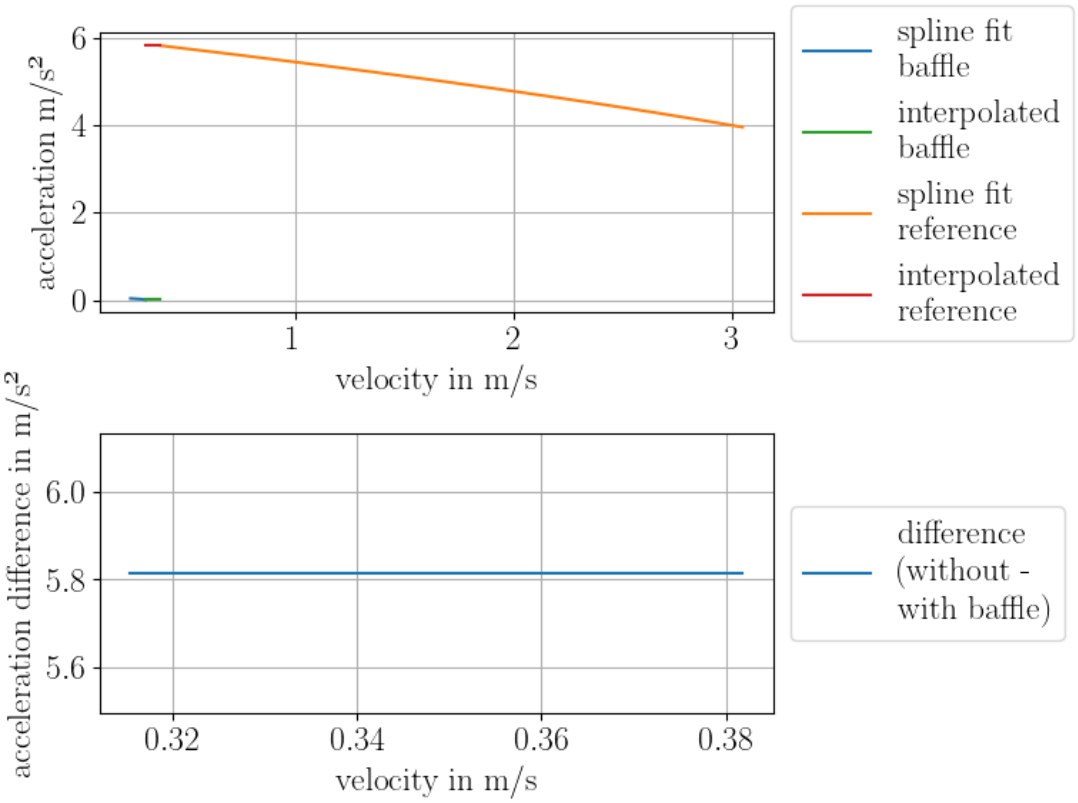

Figure 57: Acceleration over velocity of reference and baffle data with interpolated acceleration values for top baffle measurement 2 with 4 kg counterweight

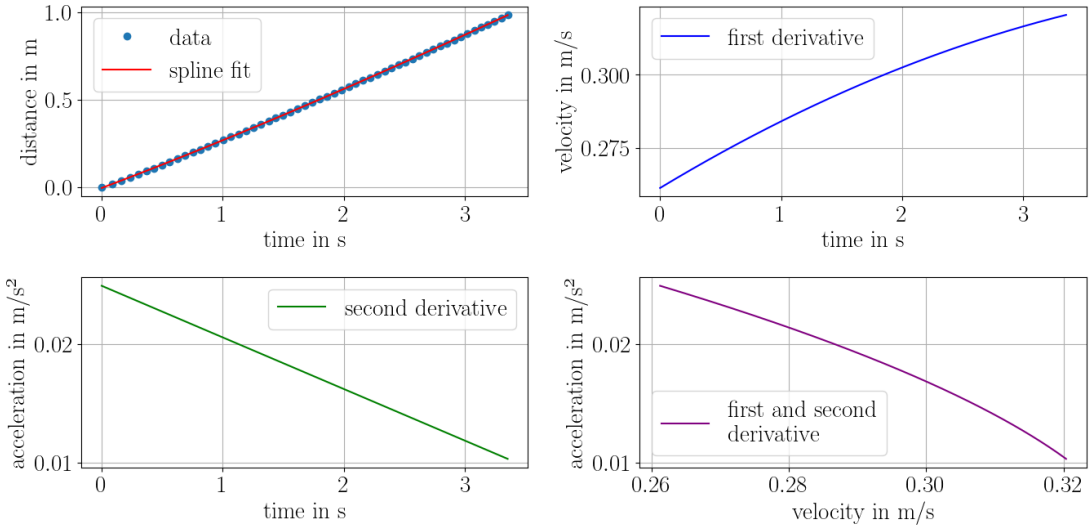

(a) Baffle data with spline fit and spline derivations

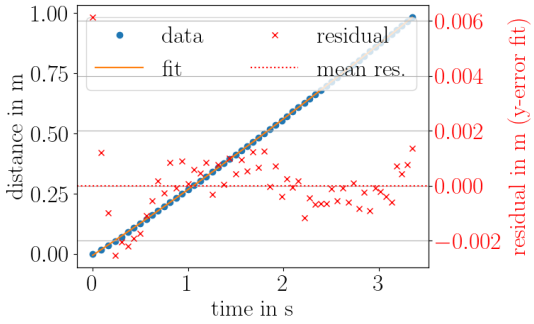

(b) Baffle data with spline fit and residuals

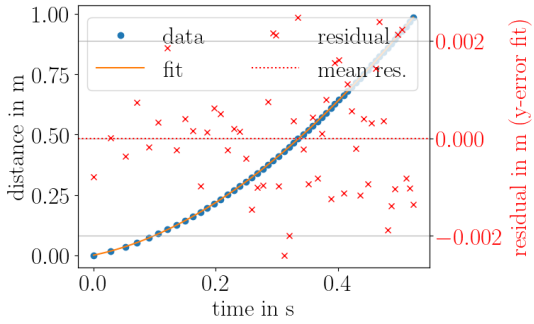

(c) Reference data with spline fit and residuals

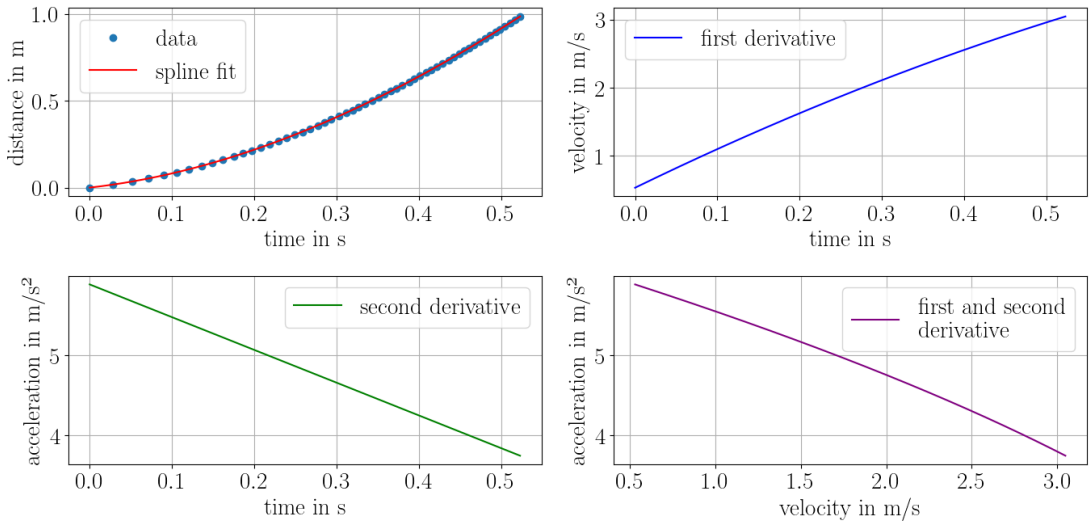

(d) Reference data with spline fit and spline derivations

Figure 58: Data, spline fits and residuals for top baffle measurement 3 with 4 kg counterweight

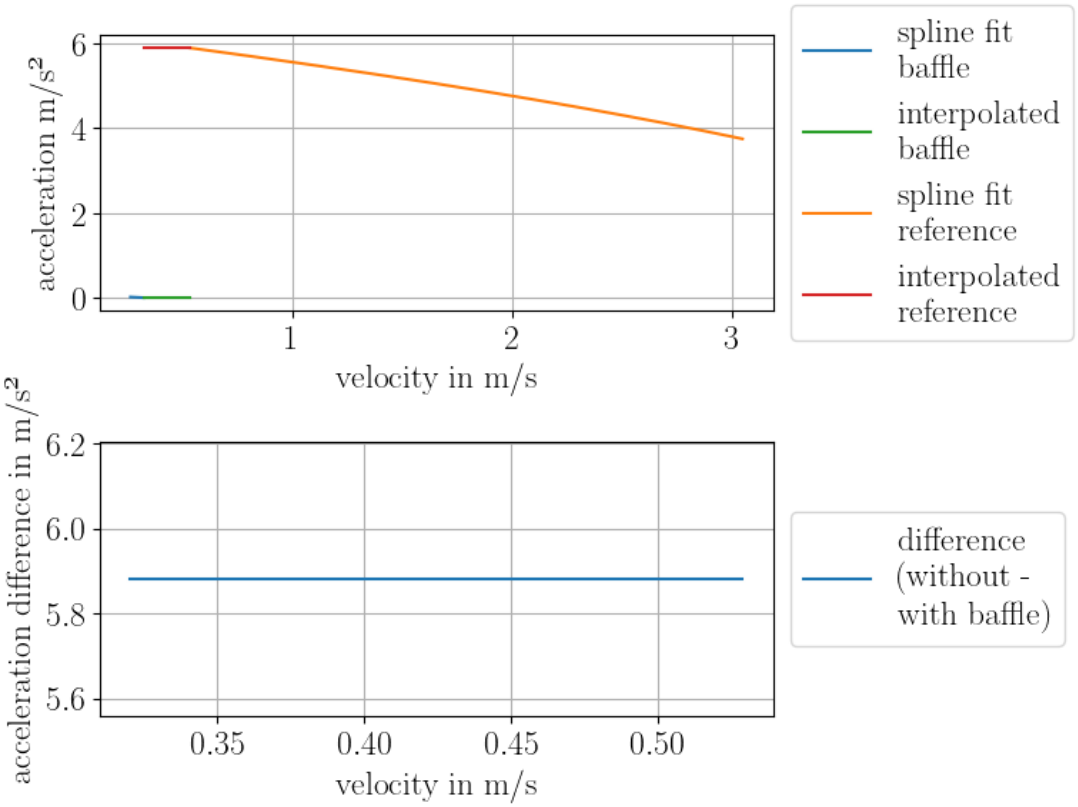

Figure 59: Acceleration over velocity of reference and baffle data with interpolated acceleration values for top baffle measurement 3 with 4 kg counterweight

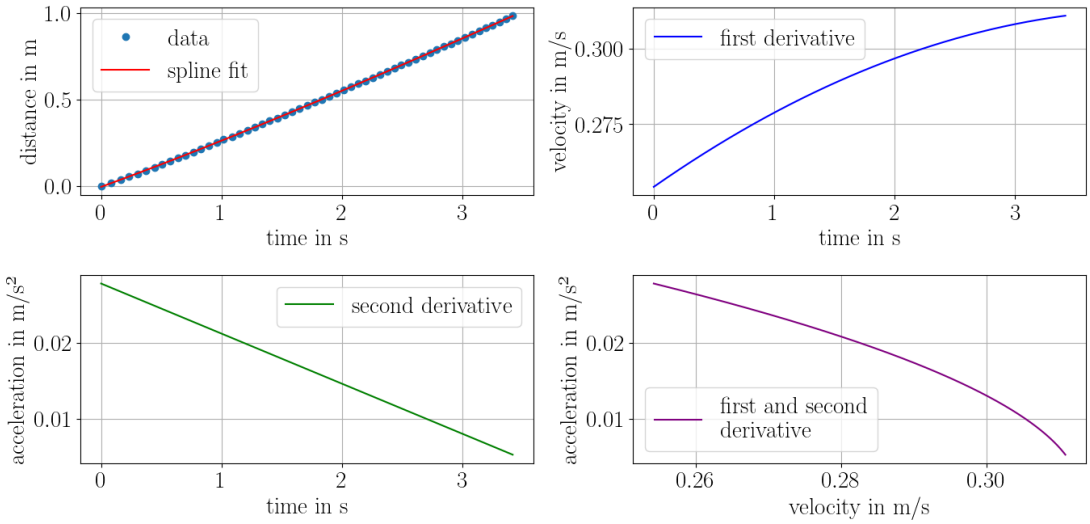

(a) Baffle data with spline fit and spline derivations

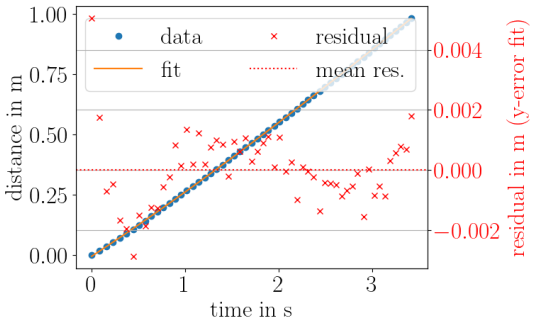

(b) Baffle data with spline fit and residuals

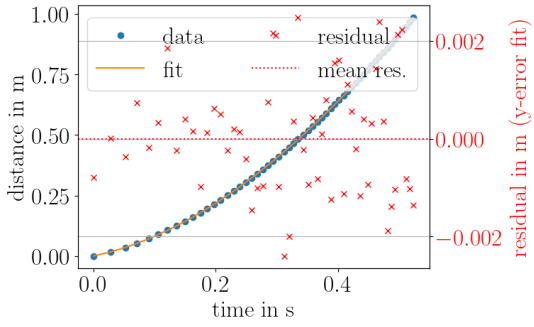

(c) Reference data with spline fit and residuals

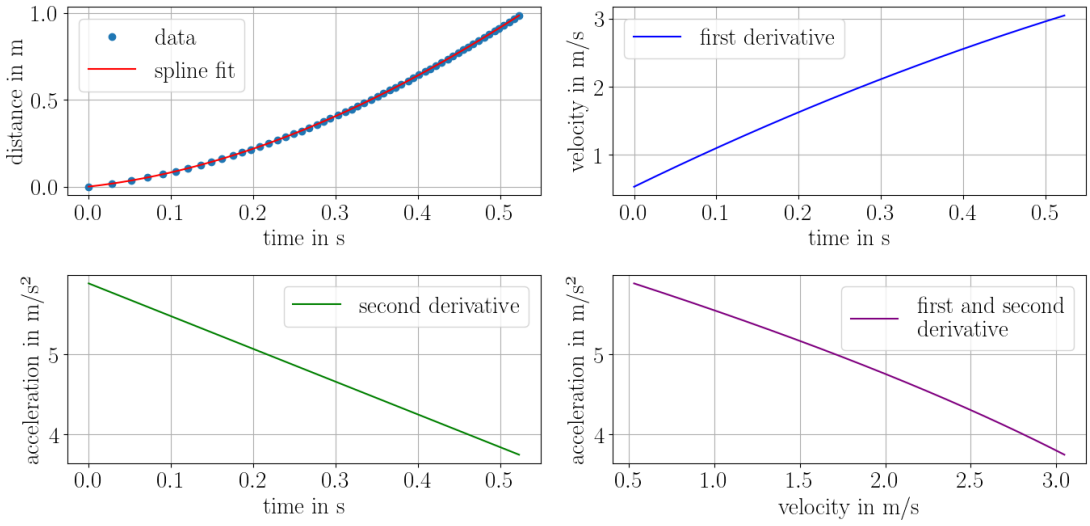

(d) Reference data with spline fit and spline derivations

Figure 60: Data, spline fits and residuals for top baffle measurement 4 with 4 kg counterweight

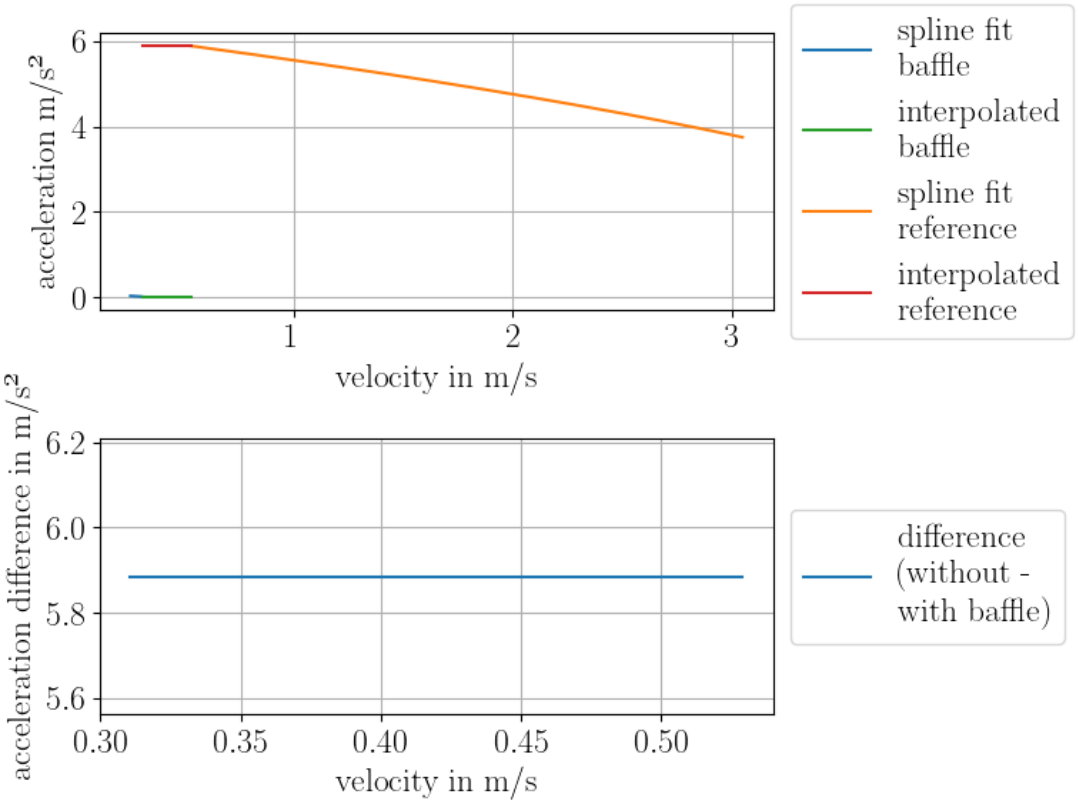

Figure 61: Acceleration over velocity of reference and baffle data with interpolated acceleration values for top baffle measurement 4 with 4 kg counterweight

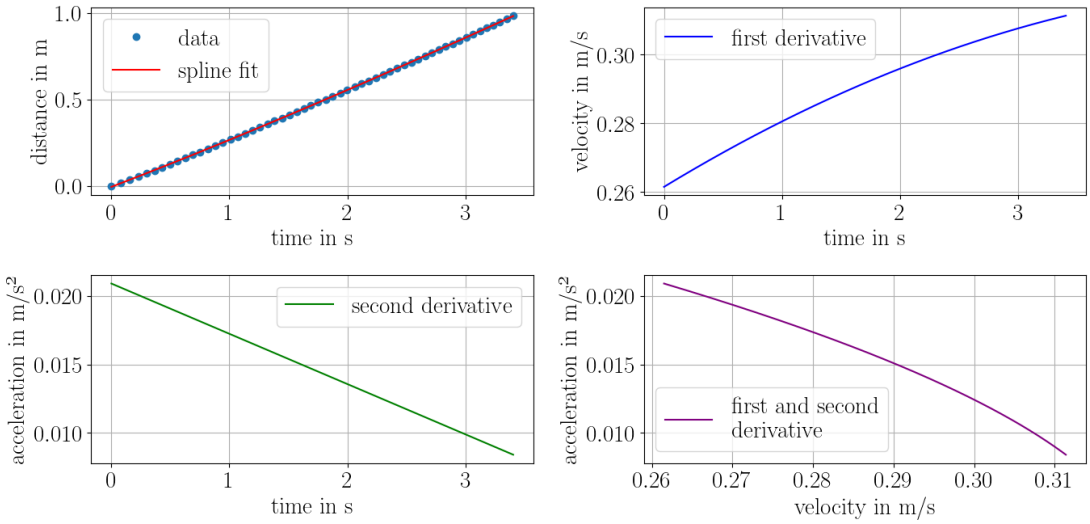

(a) Baffle data with spline fit and spline derivations

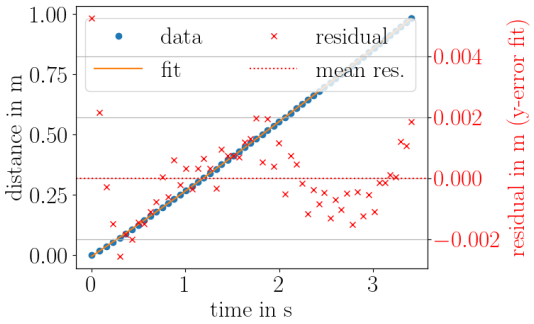

(b) Baffle data with spline fit and residuals

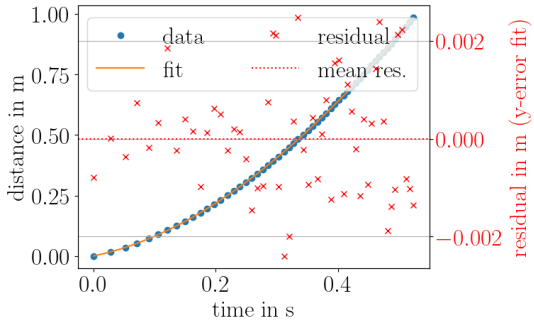

(c) Reference data with spline fit and residuals

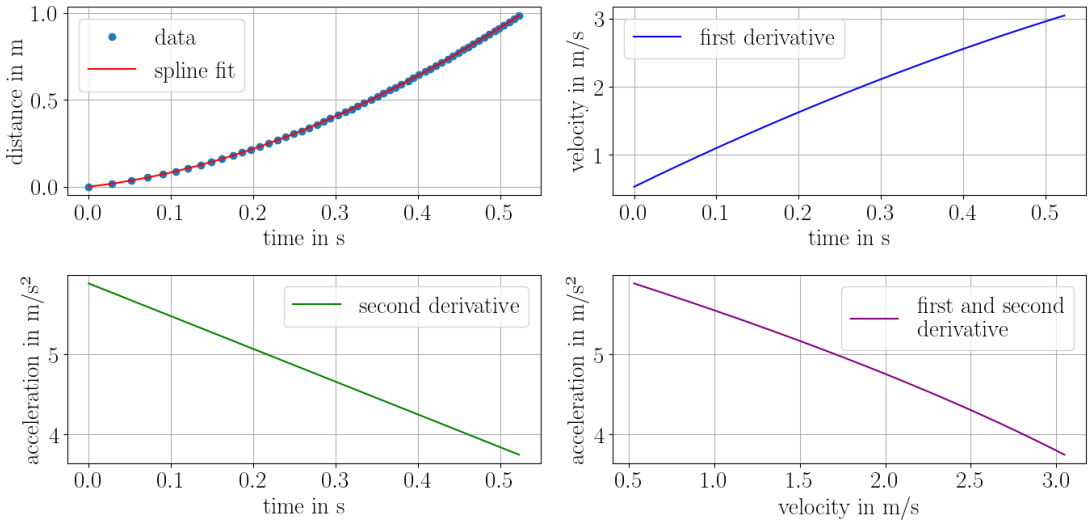

(d) Reference data with spline fit and spline derivations

Figure 62: Data, spline fits and residuals for top baffle measurement 5 with 4 kg counterweight

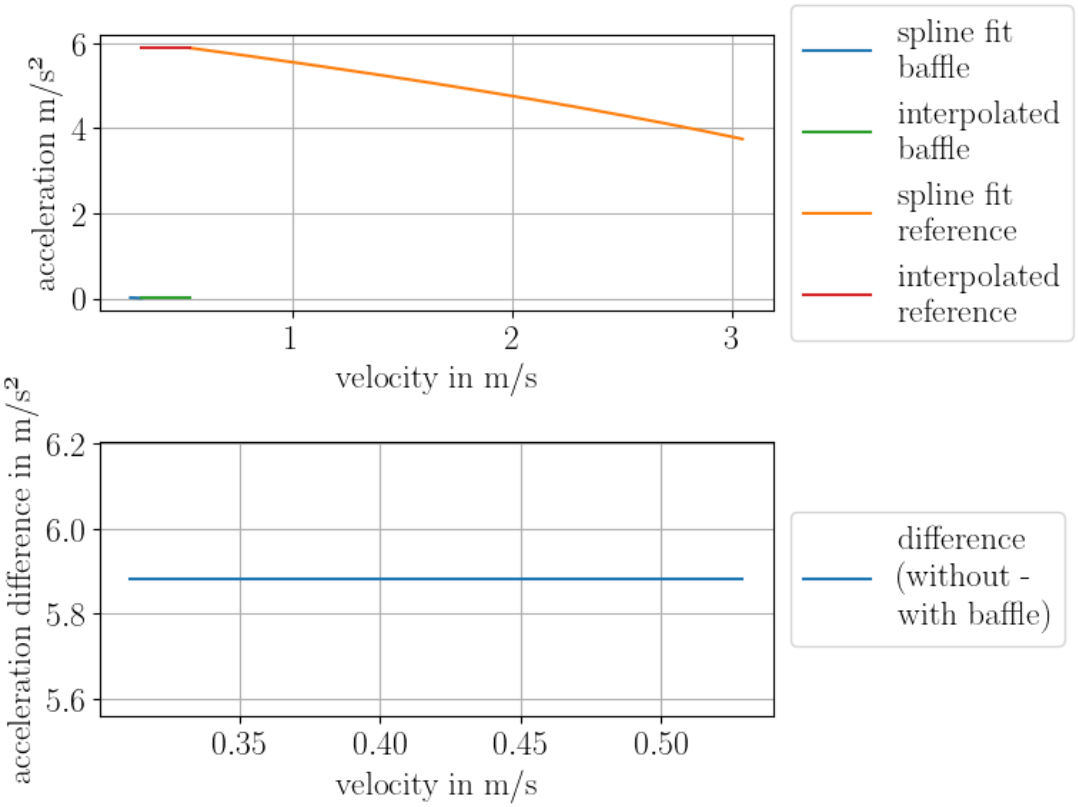

Figure 63: Acceleration over velocity of reference and baffle data with interpolated acceleration values for top baffle measurement 5 with 4 kg counterweight

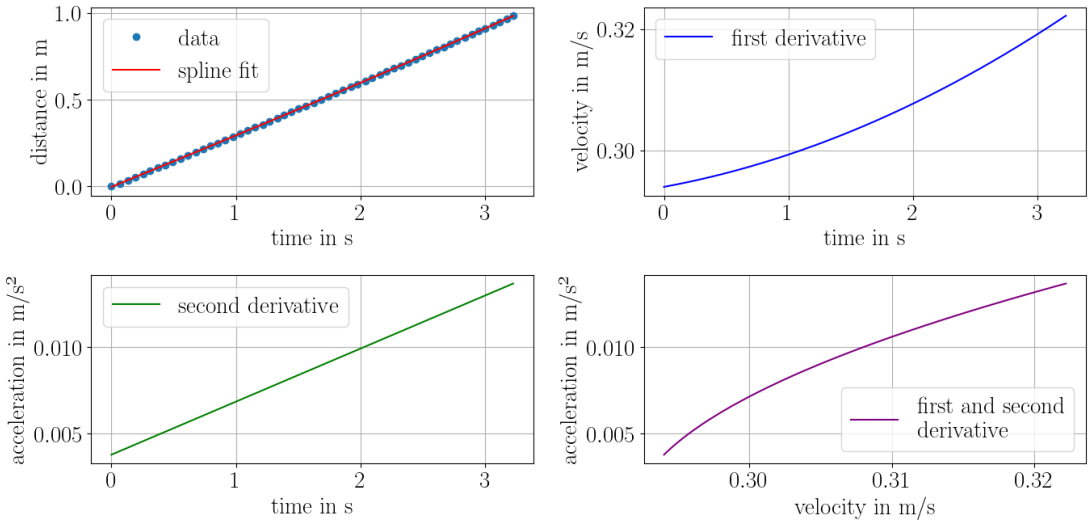

(a) Baffle data with spline fit and spline derivations

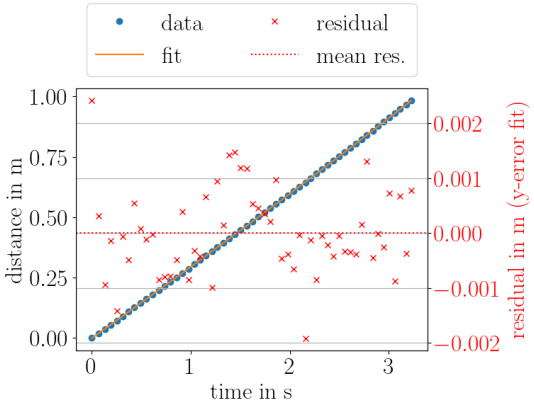

(b) Baffle data with spline fit and residuals

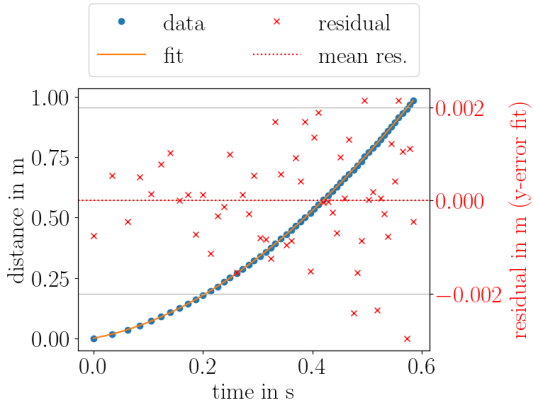

(c) Reference data with spline fit and residuals

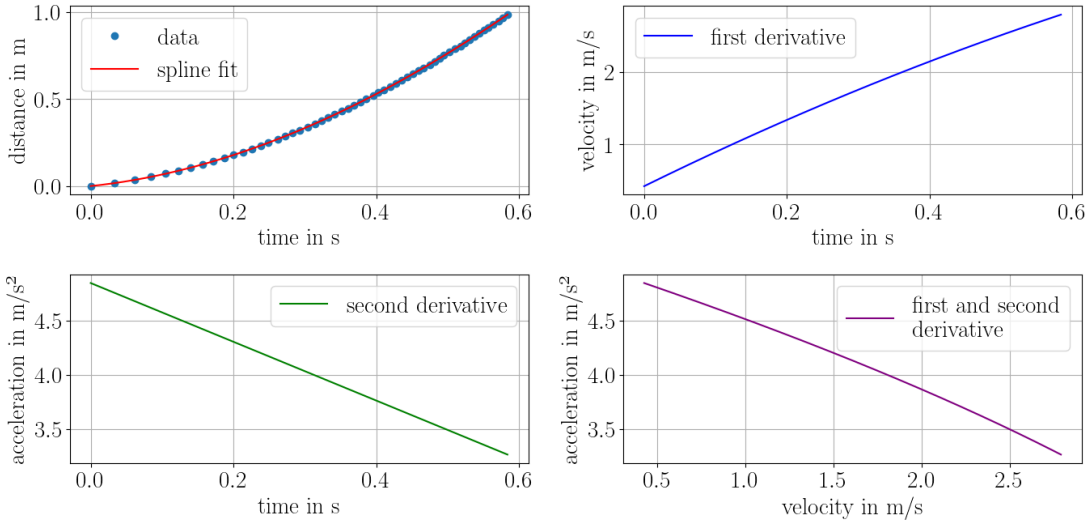

(d) Reference data with spline fit and spline derivations

Figure 64: Data, spline fits and residuals for top baffle measurement 0 with 4.5 kg counterweight

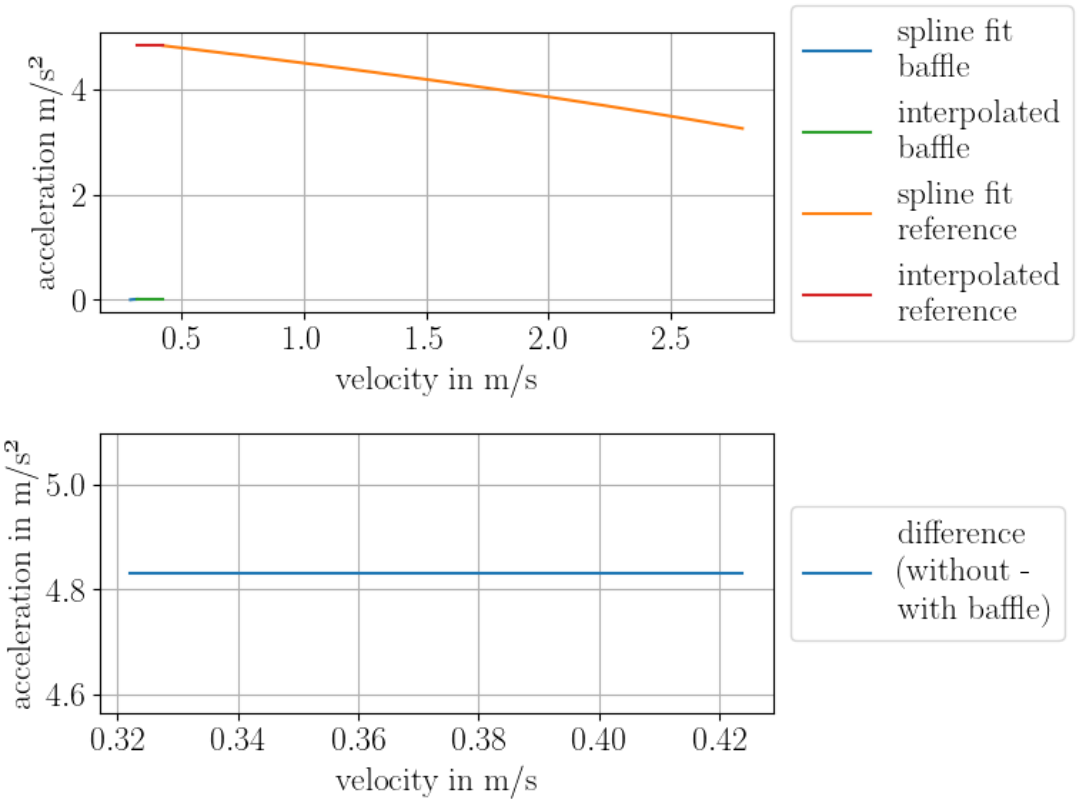

Figure 65: Acceleration over velocity of reference and baffle data with interpolated acceleration values for top baffle measurement 0 with 4.5 kg counterweight

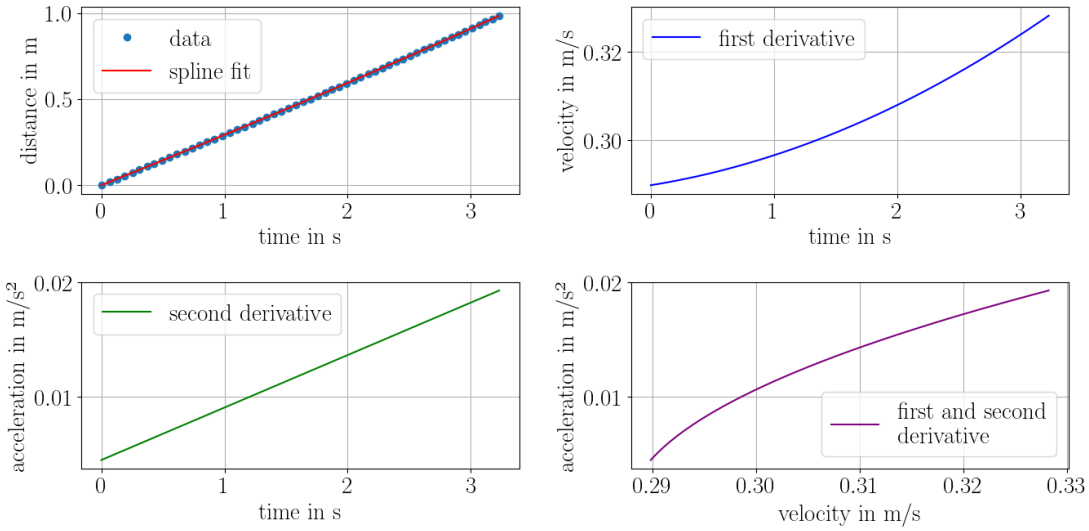

(a) Baffle data with spline fit and spline derivations

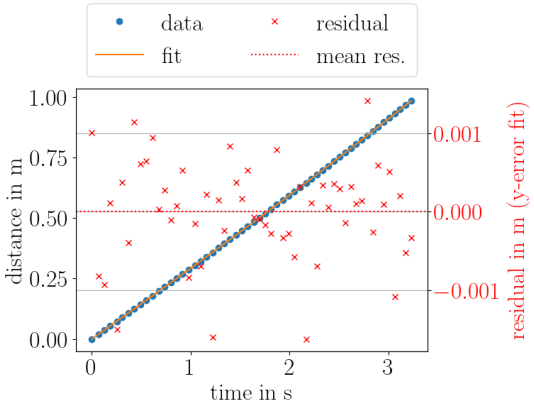

(b) Baffle data with spline fit and residuals

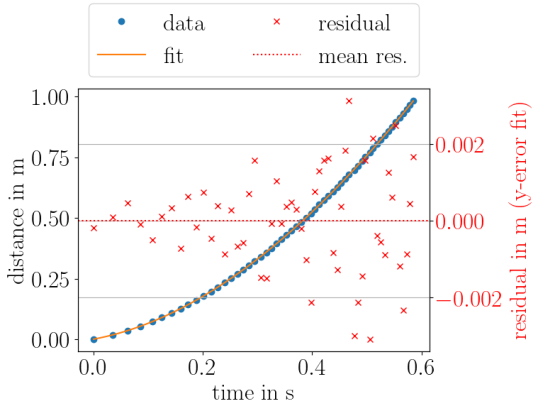

(c) Reference data with spline fit and residuals

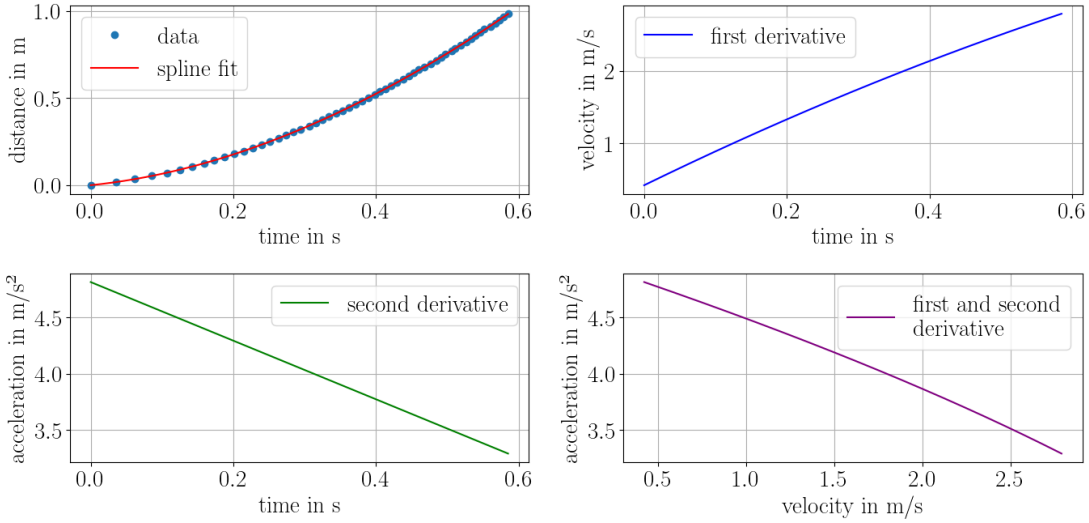

(d) Reference data with spline fit and spline derivations

Figure 66: Data, spline fits and residuals for top baffle measurement 1 with 4.5 kg counterweight

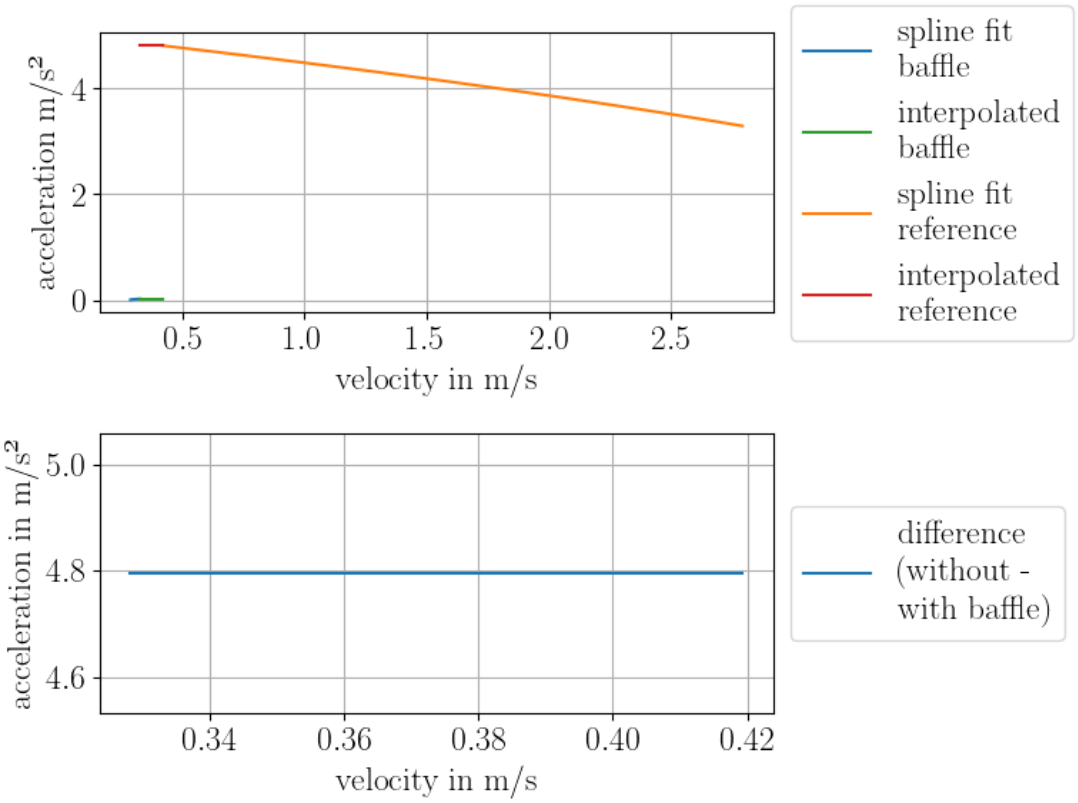

Figure 67: Acceleration over velocity of reference and baffle data with interpolated acceleration values for top baffle measurement 1 with 4.5 kg counterweight

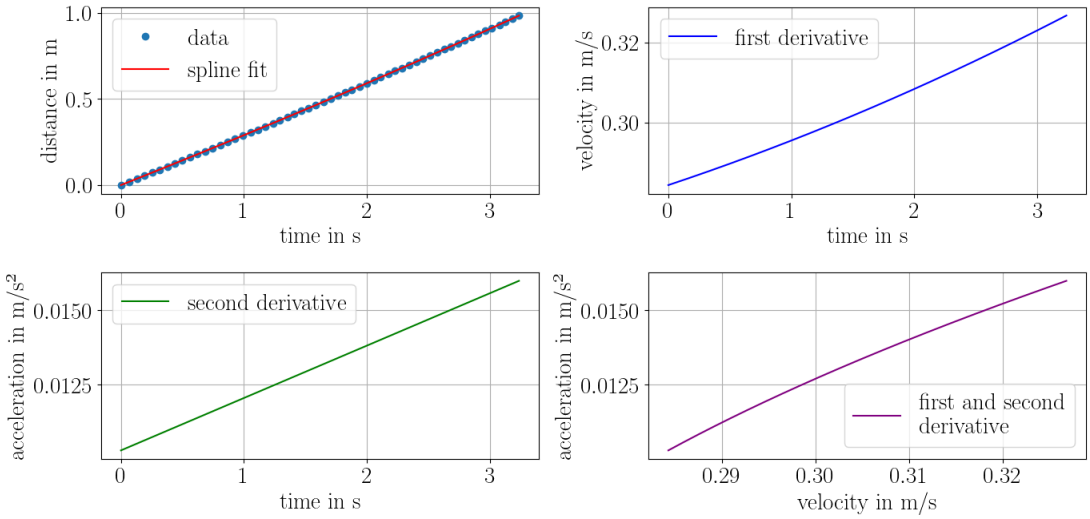

(a) Baffle data with spline fit and spline derivations

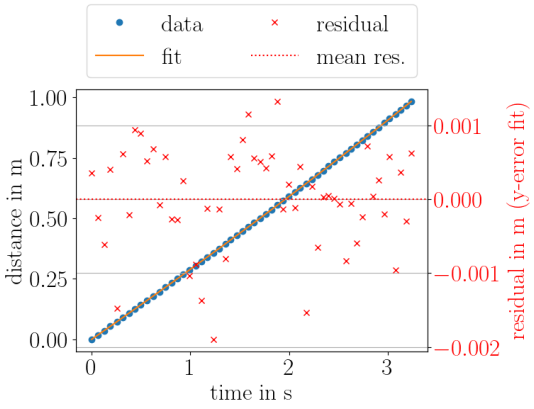

(b) Baffle data with spline fit and residuals

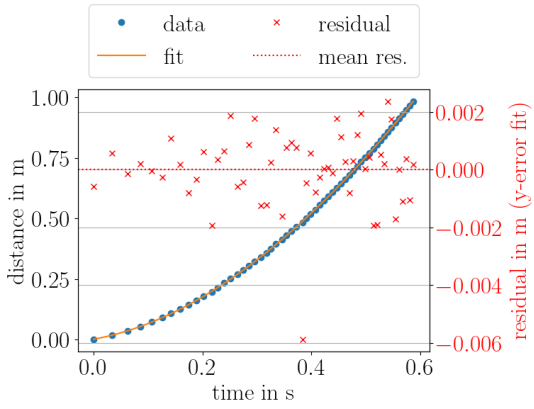

(c) Reference data with spline fit and residuals

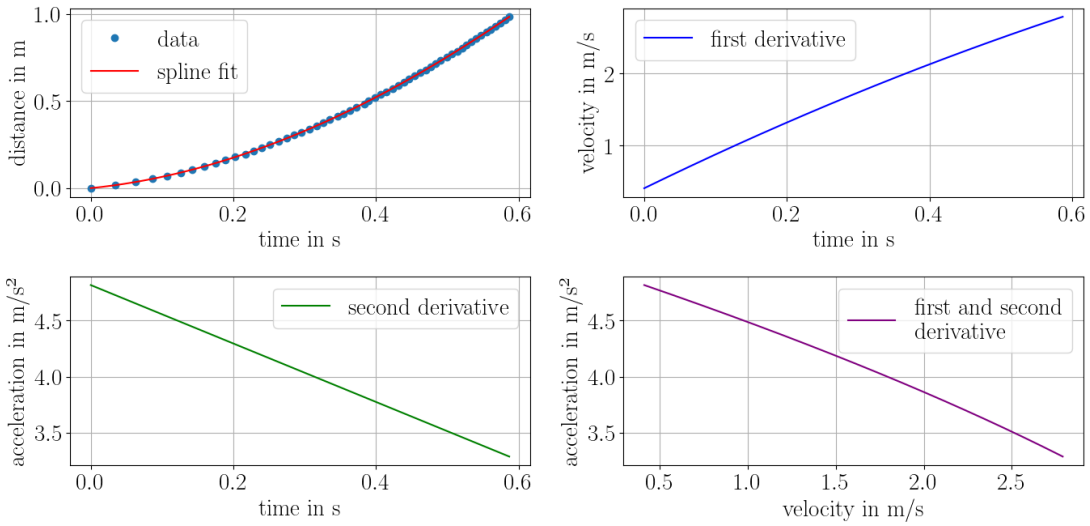

(d) Reference data with spline fit and spline derivations

Figure 68: Data, spline fits and residuals for top baffle measurement 2 with 4.5 kg counterweight

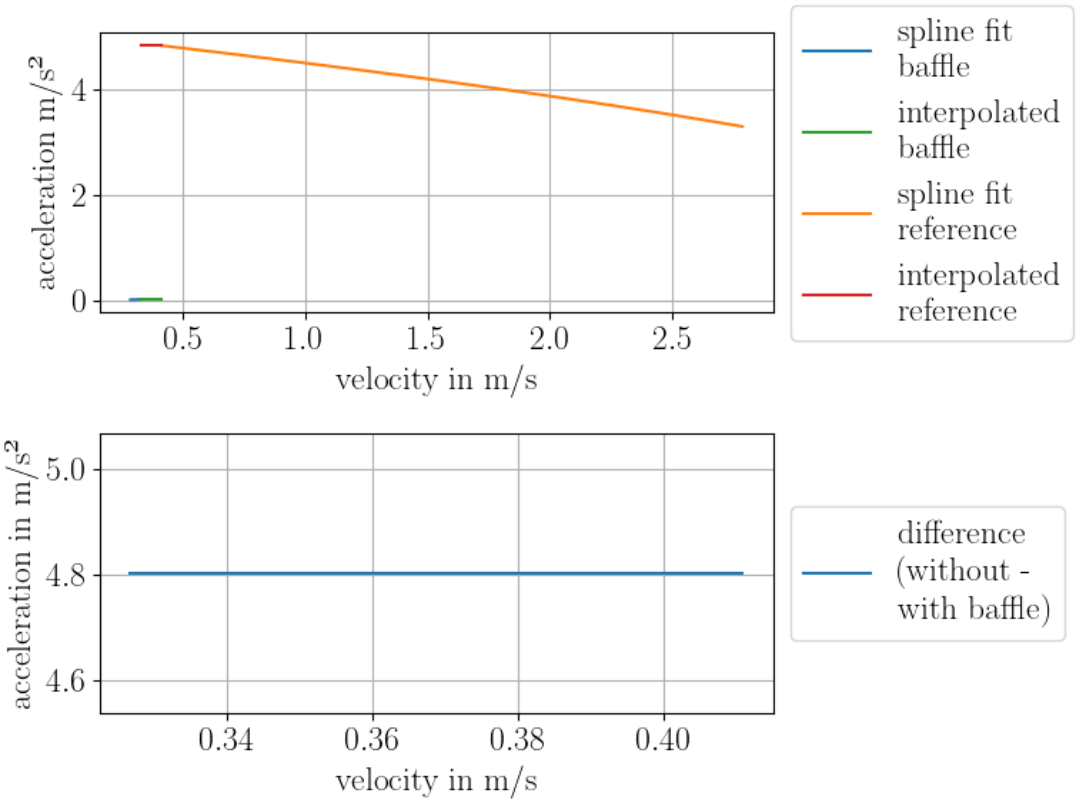

Figure 69: Acceleration over velocity of reference and baffle data with interpolated acceleration values for top baffle measurement 2 with 4.5 kg counterweight

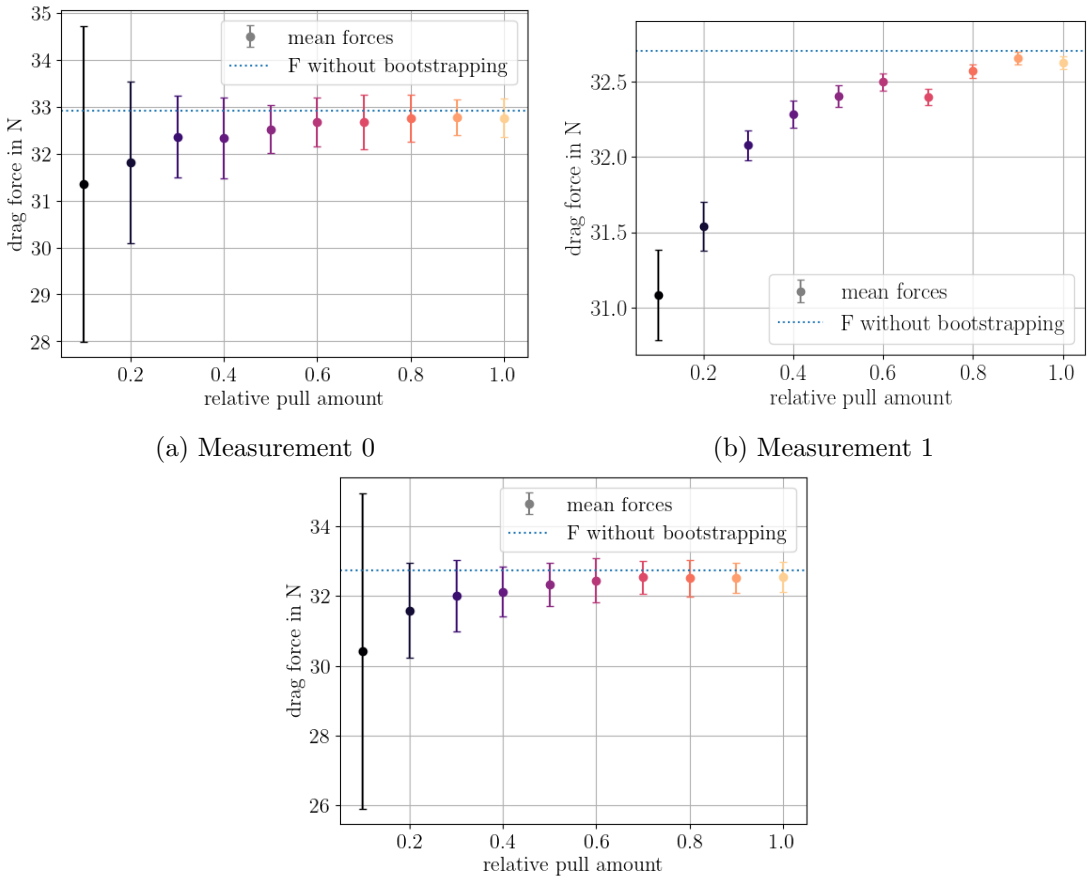

(a) Measurement 0

(b) Measurement 1

(c) Measurement 2

Figure 70: Drag force (y-axis) depending on pull amount (x-axis, color) of the data for all measurement iterations of top baffle with 4.5 kg counterweight. The values were averaged over 100 repetitions, the standard error on the mean is seen in error bars. The dashed line marks the drag value determined without bootstrapping. Note that the scale of the y-axis is slightly different in all three plots.

A.2 Measurements with two top baffles

Measurements of two layers of the top baffle are presented for different counterweights. For the 4 kg counterweight, one reference measurement is used twice for baffle measurements 0 and 1. For the 5 kg counterweight, the same reference measurement is used for measurements 0 and 1.

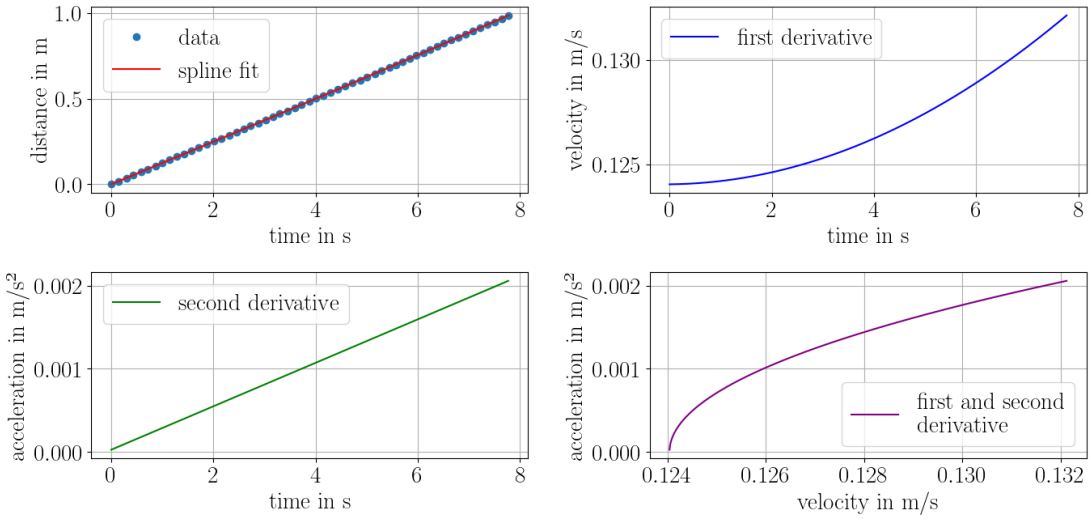

(a) Baffle data with spline fit and spline derivations

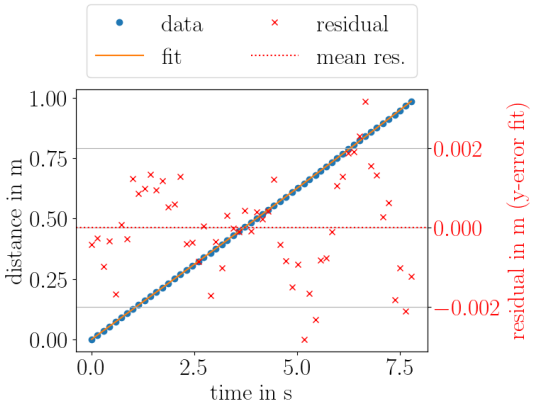

(b) Baffle data with spline fit and residuals

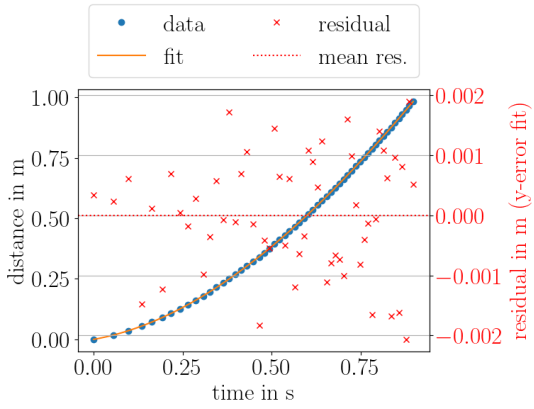

(c) Reference data with spline fit and residuals

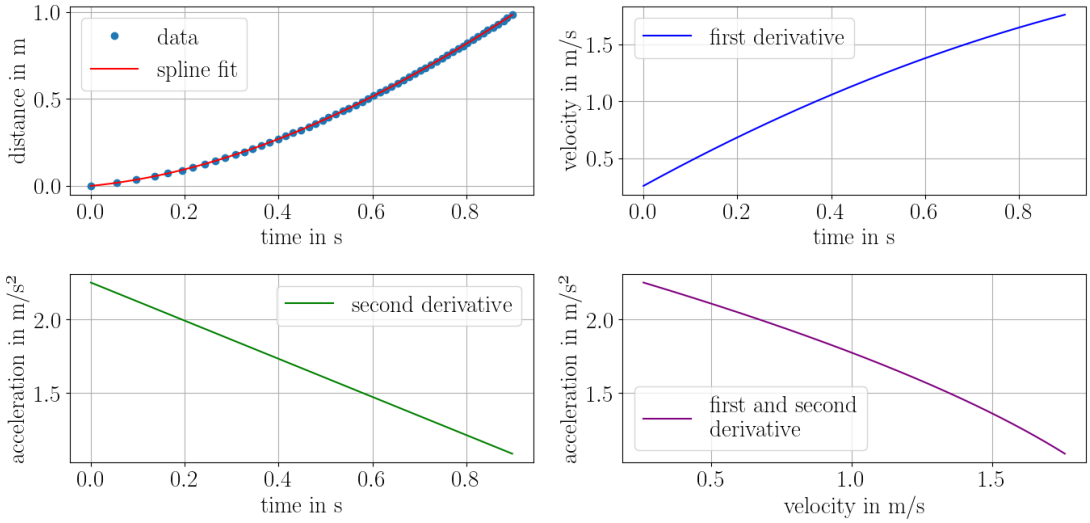

(d) Reference data with spline fit and spline derivations

Figure 71: Data, spline fits and residuals for two top baffle measurement 0 with 2.5 kg counterweight

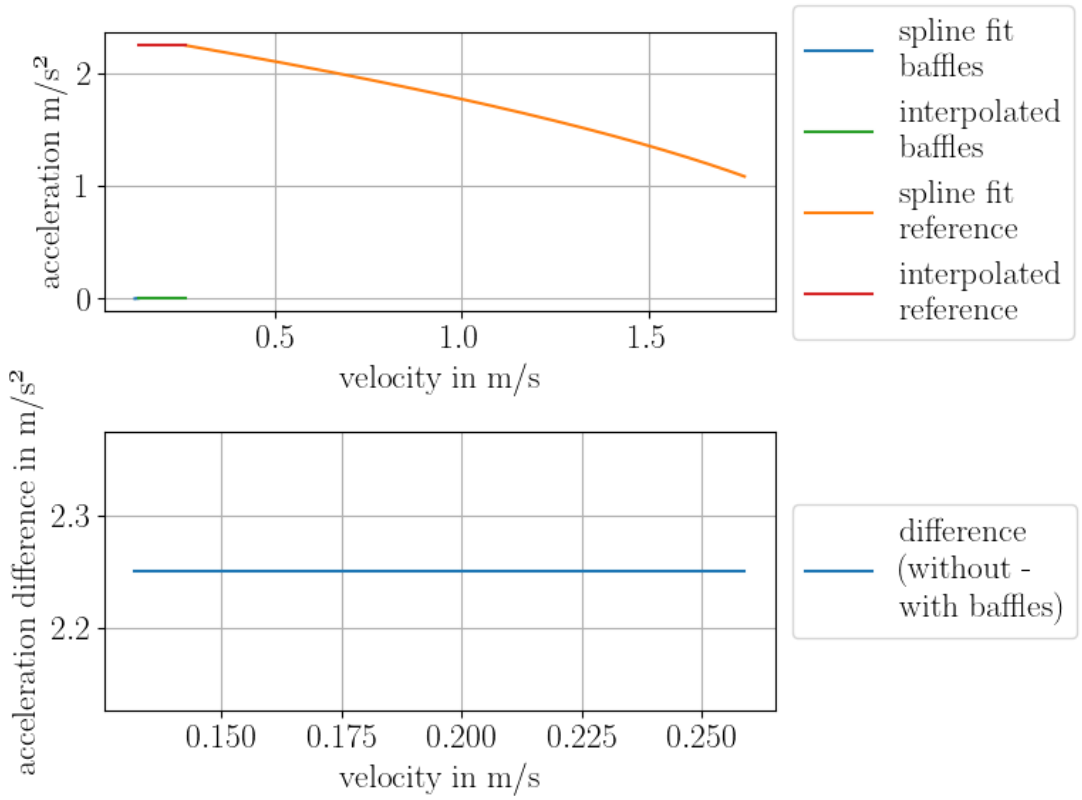

Figure 72: Acceleration over velocity of reference and baffle data with interpolated acceleration values for two top baffle measurement 0 with 2.5 kg counterweight

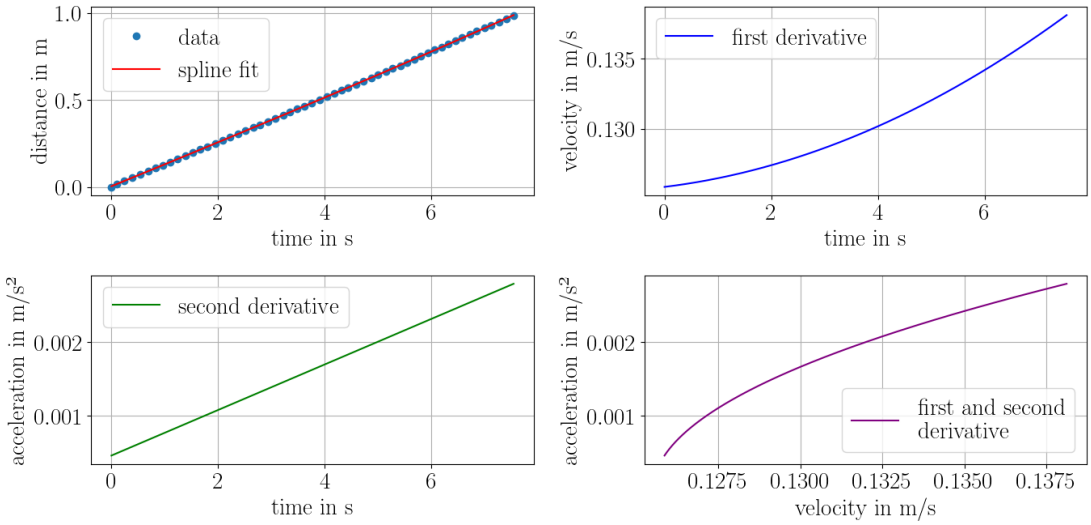

(a) Baffle data with spline fit and spline derivations

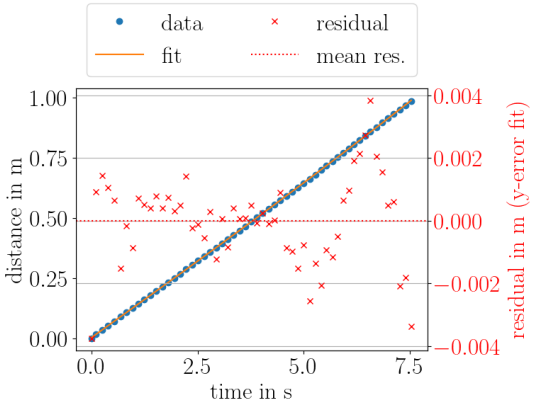

(b) Baffle data with spline fit and residuals

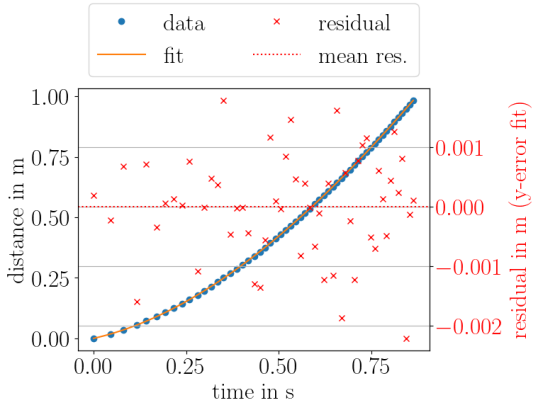

(c) Reference data with spline fit and residuals

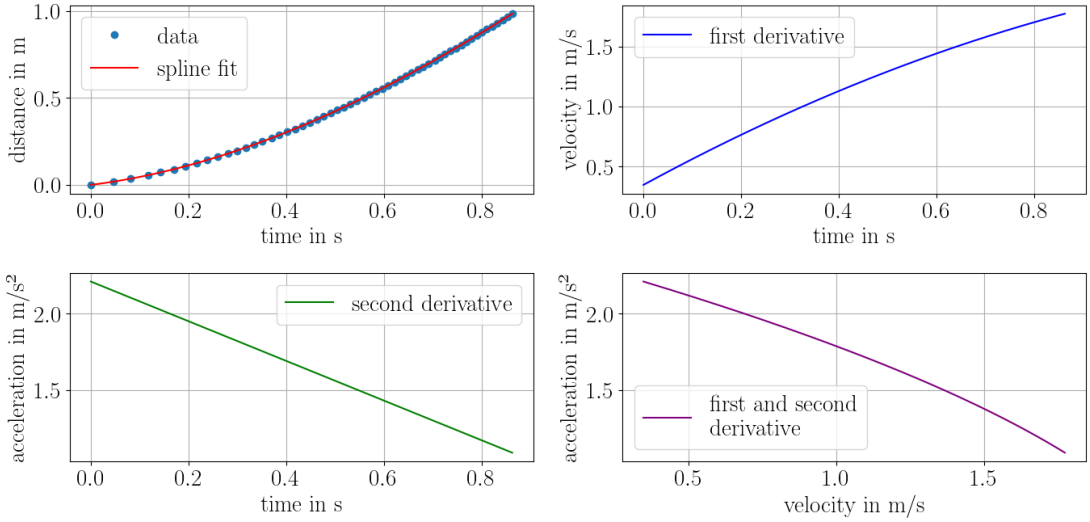

(d) Reference data with spline fit and spline derivations

Figure 73: Data, spline fits and residuals for two top baffle measurement 1 with 2.5 kg counterweight

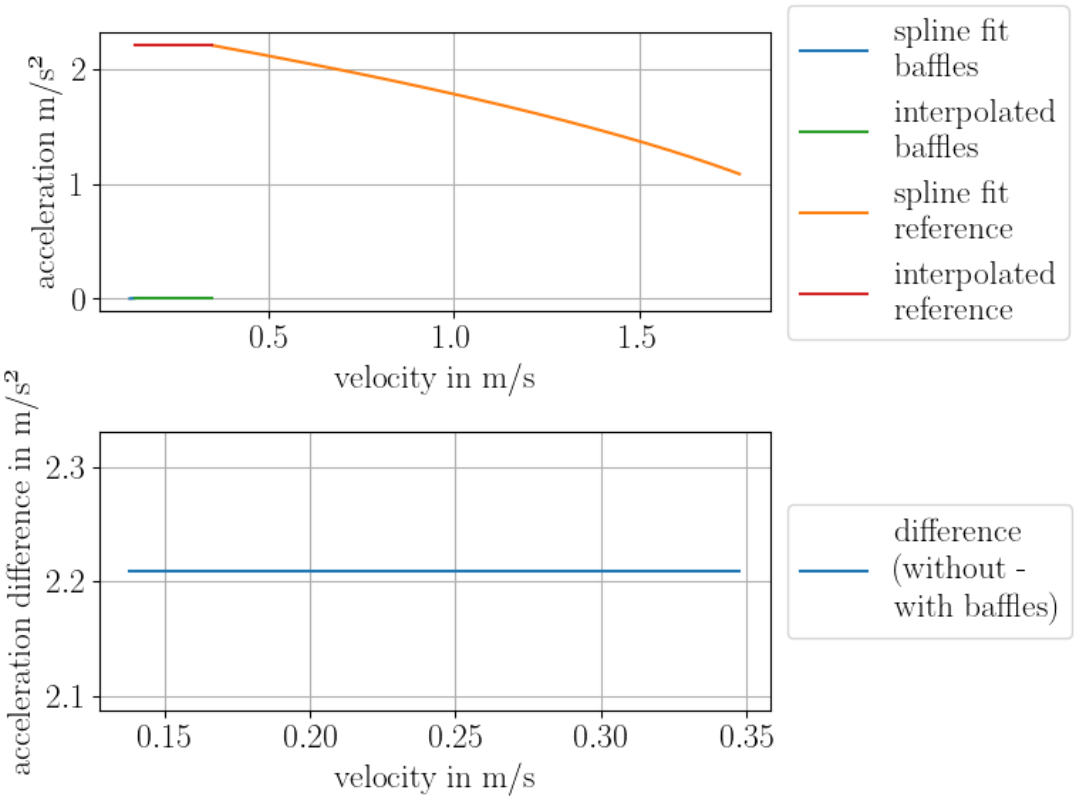

Figure 74: Acceleration over velocity of reference and baffle data with interpolated acceleration values for two top baffle measurement 1 with 2.5 kg counterweight

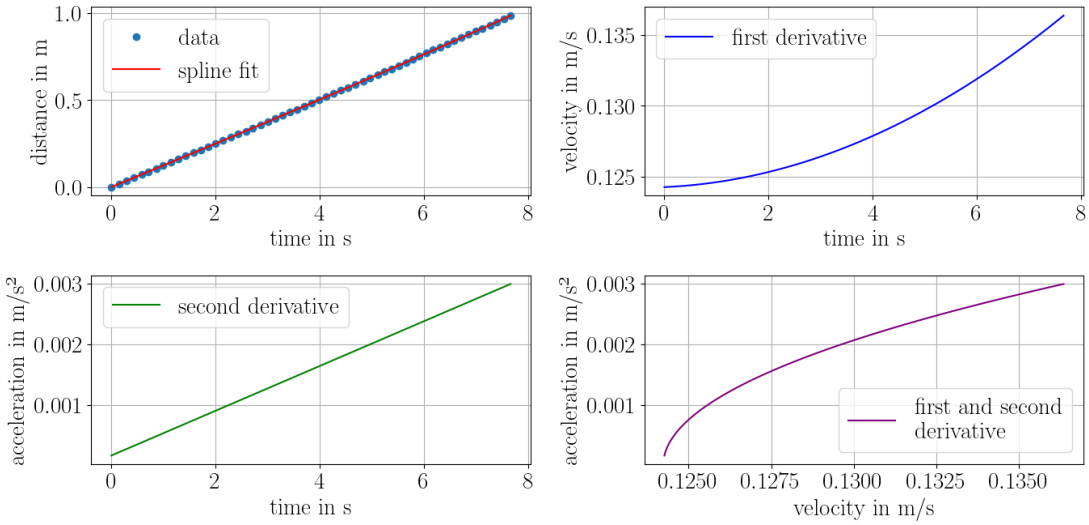

(a) Baffle data with spline fit and spline derivations

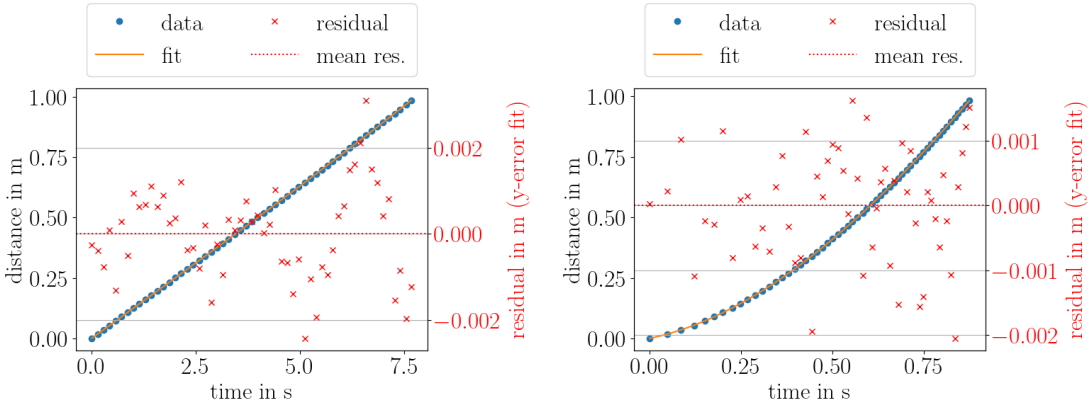

(b) Baffle data with spline fit and residuals

(c) Reference data with spline fit and residuals

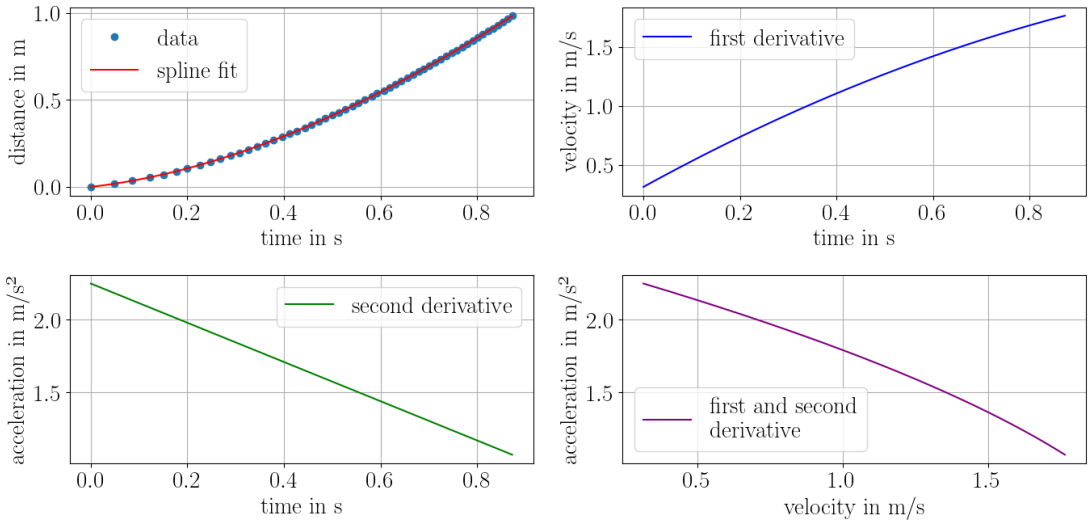

(d) Reference data with spline fit and spline derivations

Figure 75: Data, spline fits and residuals for two top baffle measurement 2 with 2.5 kg counterweight

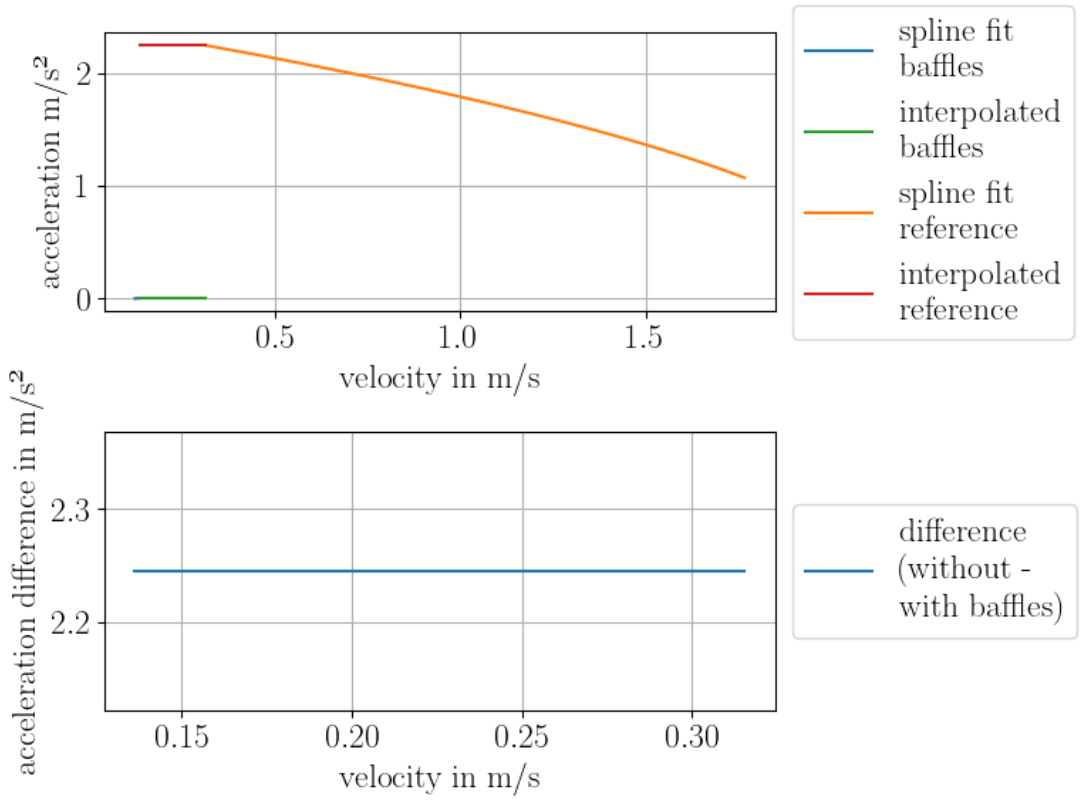

Figure 76: Acceleration over velocity of reference and baffle data with interpolated acceleration values for two top baffle measurement 2 with 2.5 kg counterweight

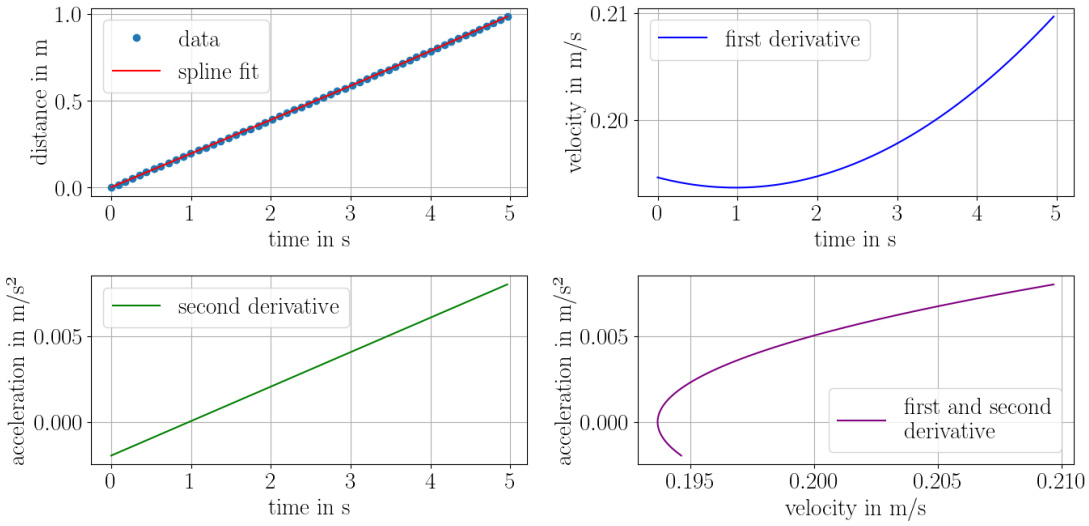

(a) Baffle data with spline fit and spline derivations

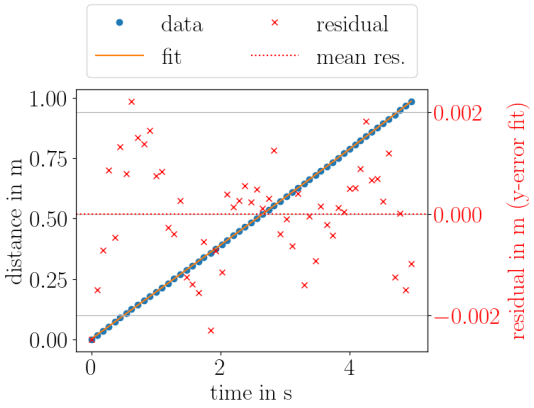

(b) Baffle data with spline fit and residuals

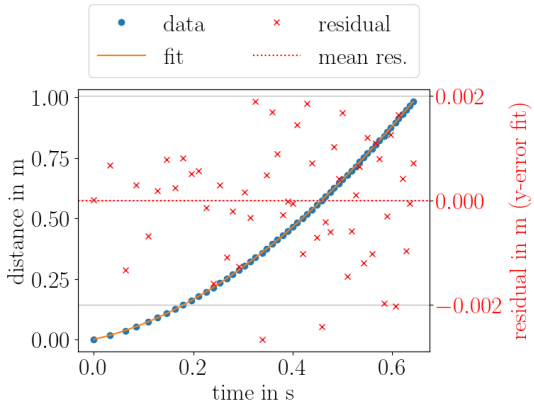

(c) Reference data with spline fit and residuals

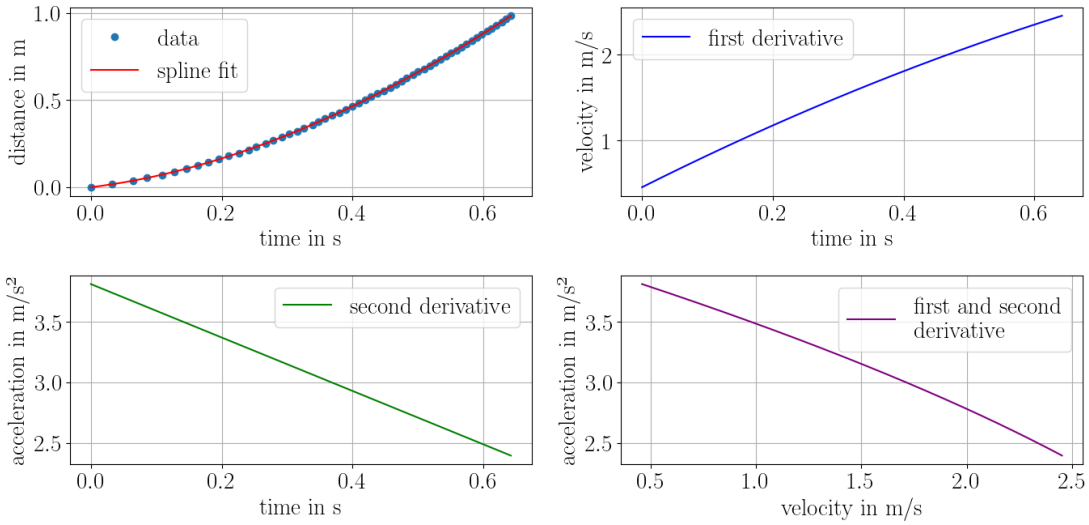

(d) Reference data with spline fit and spline derivations

Figure 77: Data, spline fits and residuals for two top baffle measurement 0 with 4.0 kg counterweight

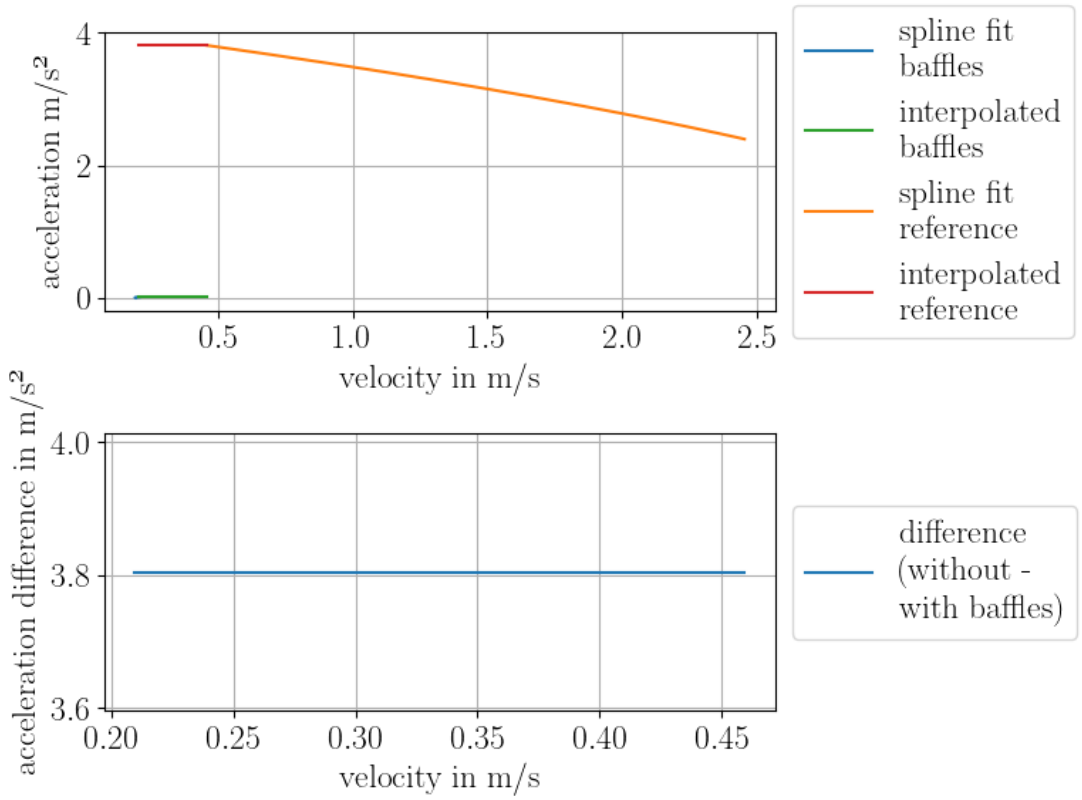

Figure 78: Acceleration over velocity of reference and baffle data with interpolated acceleration values for two top baffle measurement 0 with 4.0 kg counterweight

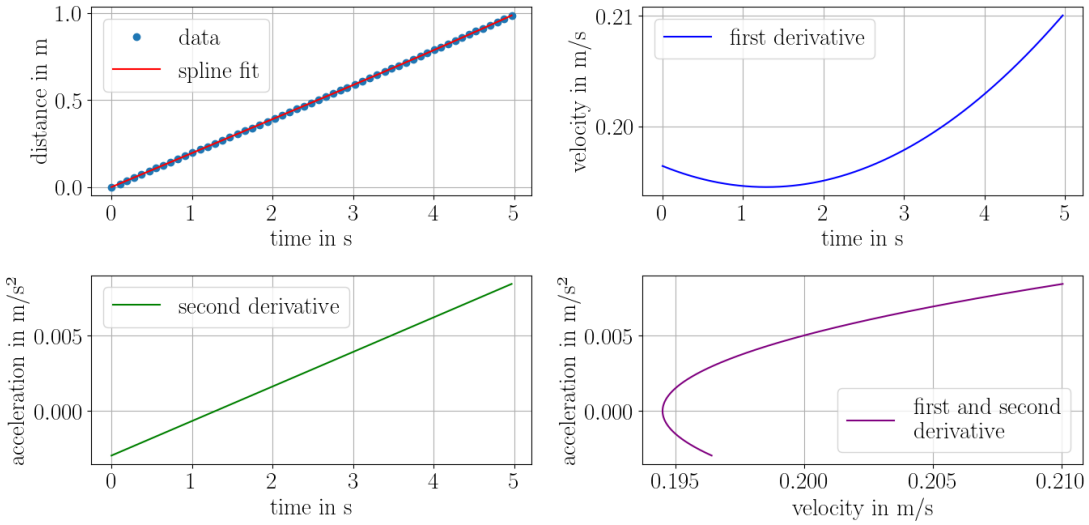

(a) Baffle data with spline fit and spline derivations

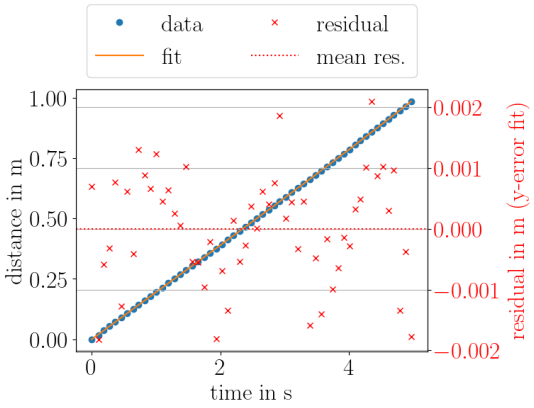

(b) Baffle data with spline fit and residuals

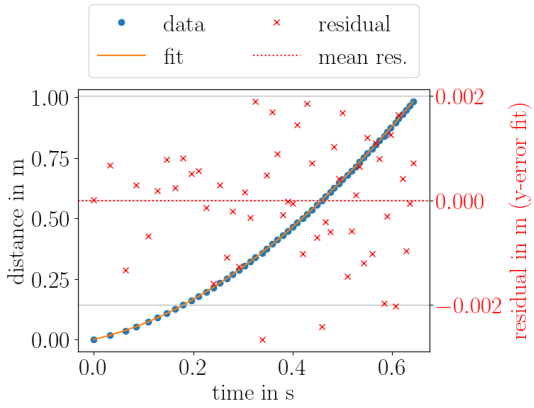

(c) Reference data with spline fit and residuals

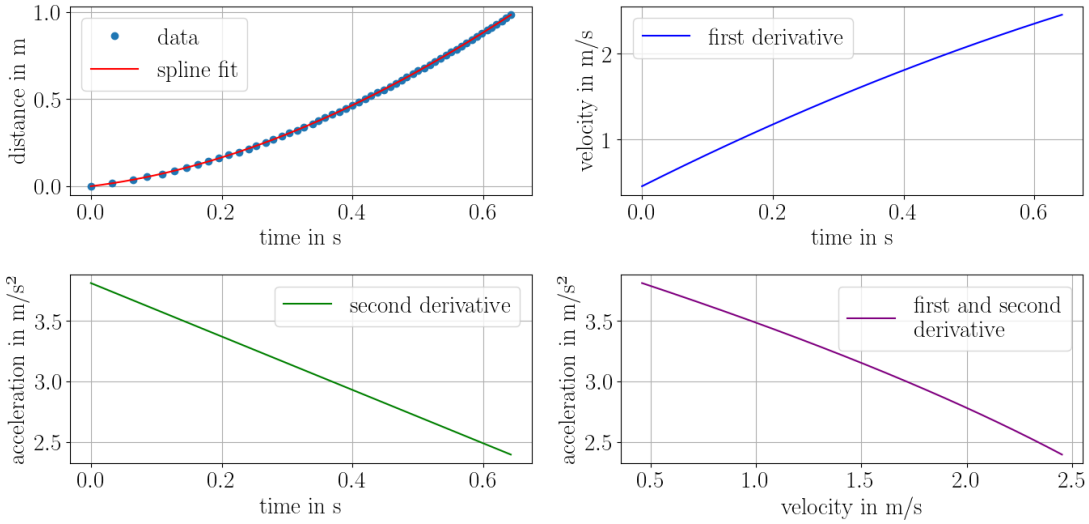

(d) Reference data with spline fit and spline derivations

Figure 79: Data, spline fits and residuals for two top baffle measurement 1 with 4.0 kg counterweight

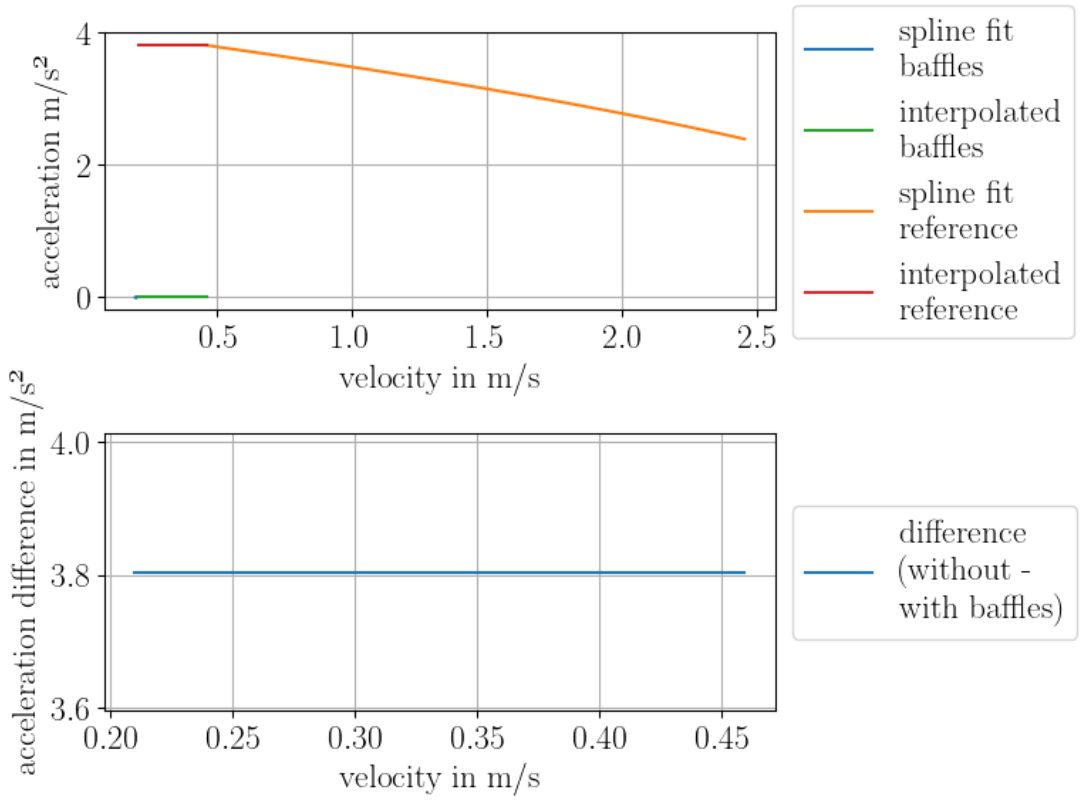

Figure 80: Acceleration over velocity of reference and baffle data with interpolated acceleration values for two top baffle measurement 1 with 4.0 kg counterweight

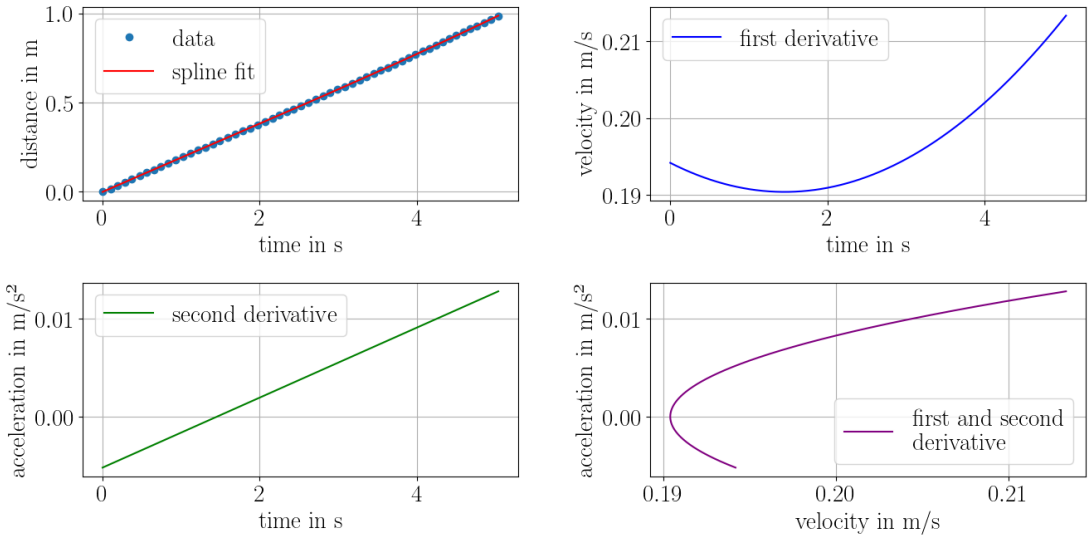

(a) Baffle data with spline fit and spline derivations

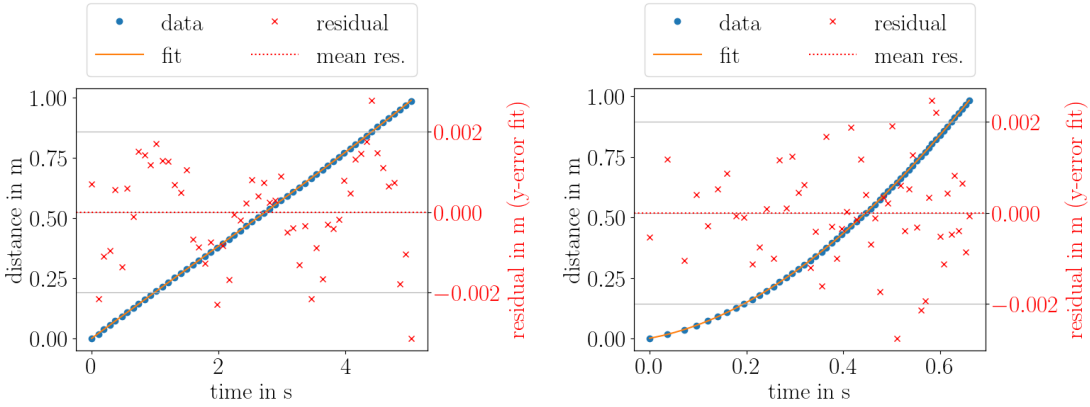

(b) Baffle data with spline fit and residuals

(c) Reference data with spline fit and residuals

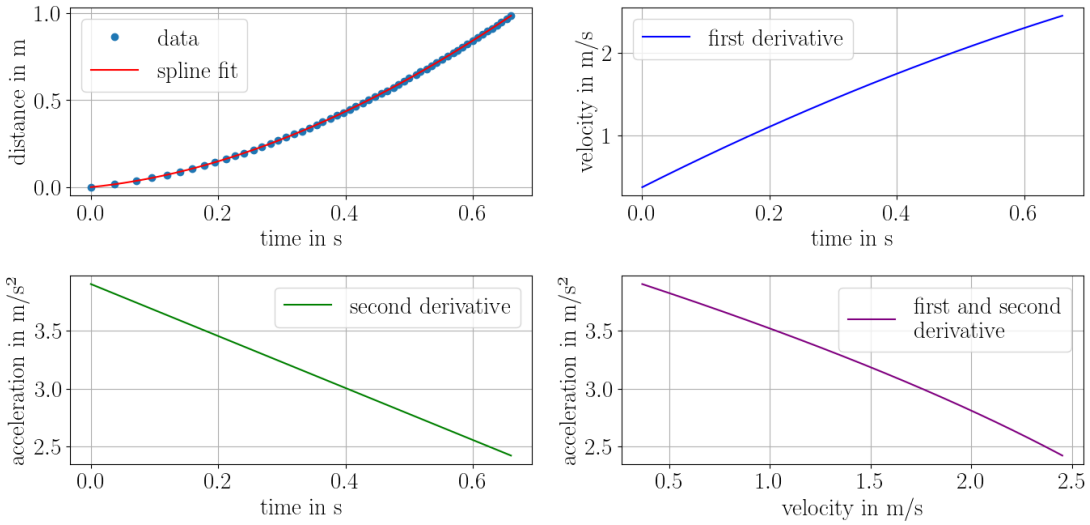

(d) Reference data with spline fit and spline derivations

Figure 81: Data, spline fits and residuals for two top baffle measurement 2 with 4.0 kg counterweight

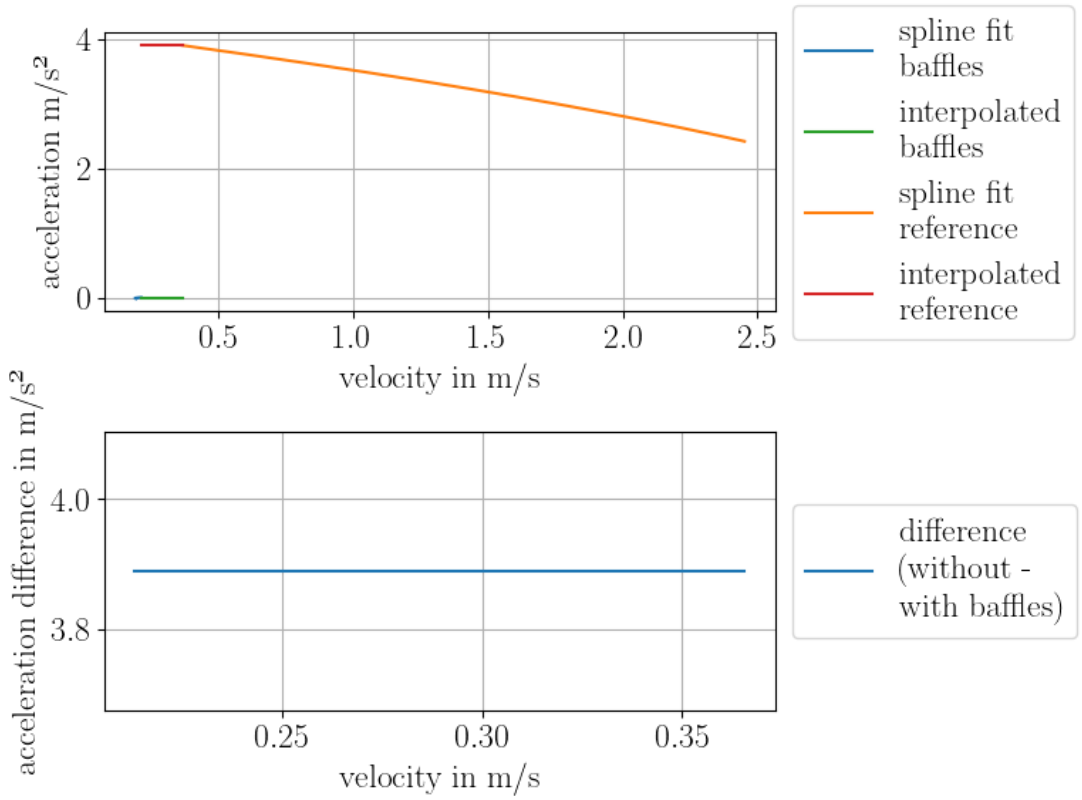

Figure 82: Acceleration over velocity of reference and baffle data with interpolated acceleration values for two top baffle measurement 2 with 4.0 kg counterweight

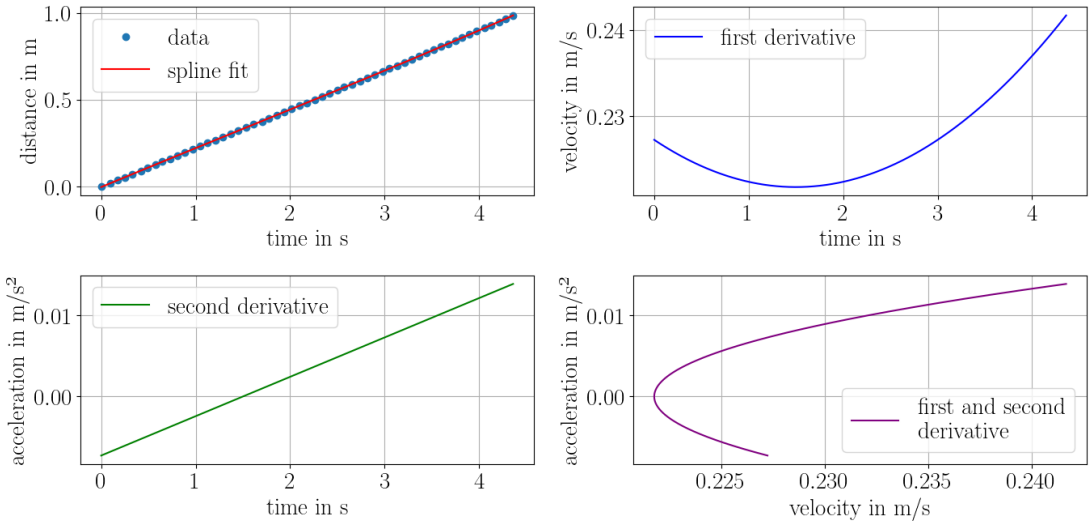

(a) Baffle data with spline fit and spline derivations

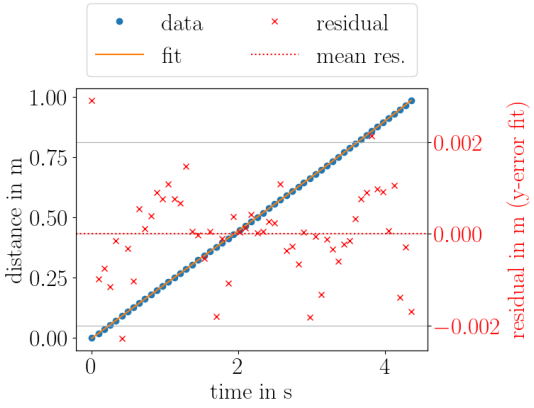

(b) Baffle data with spline fit and residuals

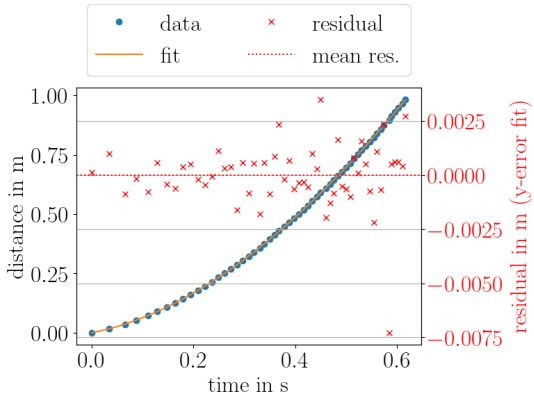

(c) Reference data with spline fit and residuals

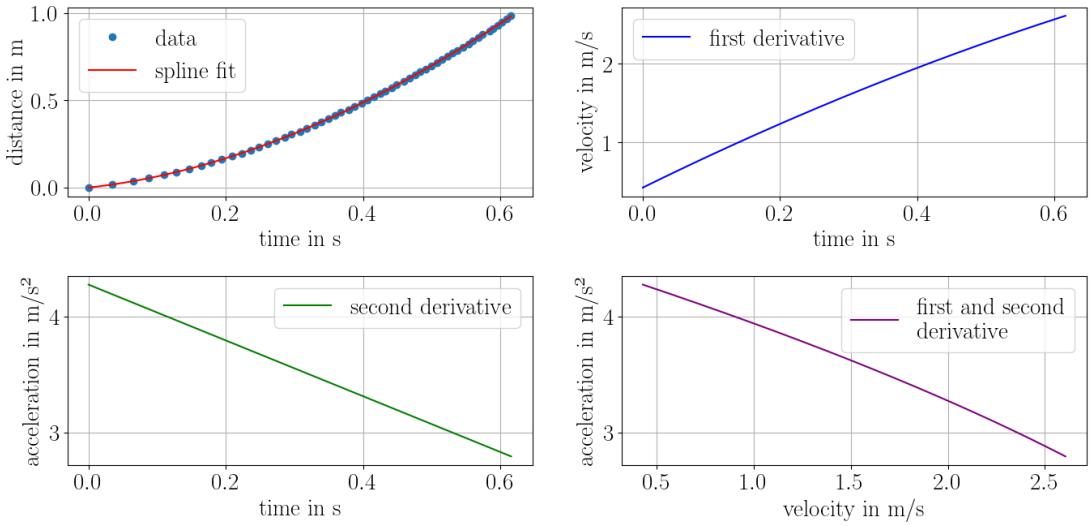

(d) Reference data with spline fit and spline derivations

Figure 83: Data, spline fits and residuals for two top baffle measurement 0 with 4.5 kg counterweight

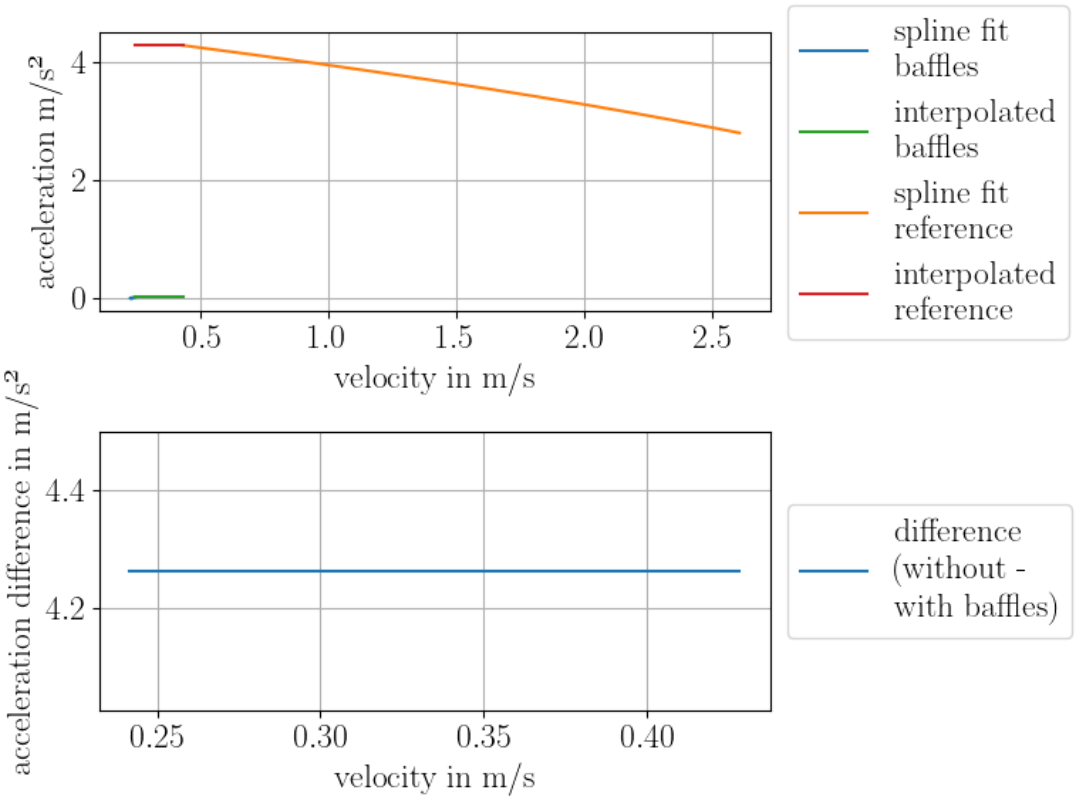

Figure 84: Acceleration over velocity of reference and baffle data with interpolated acceleration values for two top baffle measurement 0 with 4.5 kg counterweight

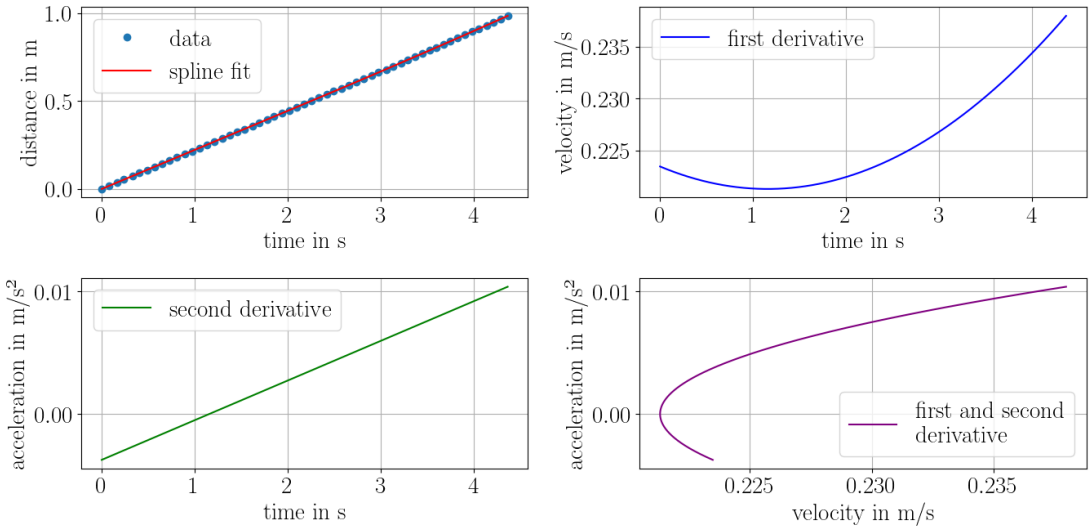

(a) Baffle data with spline fit and spline derivations

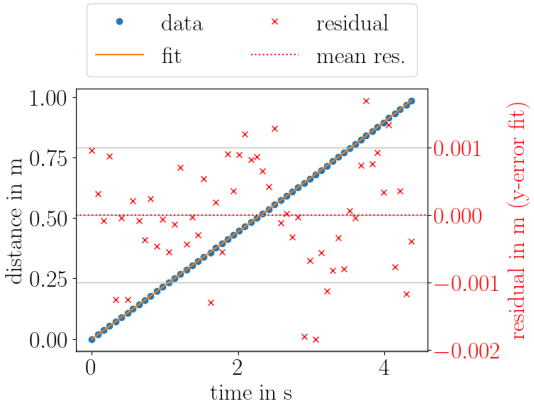

(b) Baffle data with spline fit and residuals

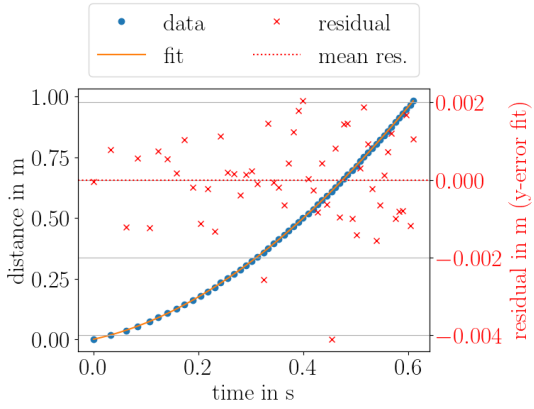

(c) Reference data with spline fit and residuals

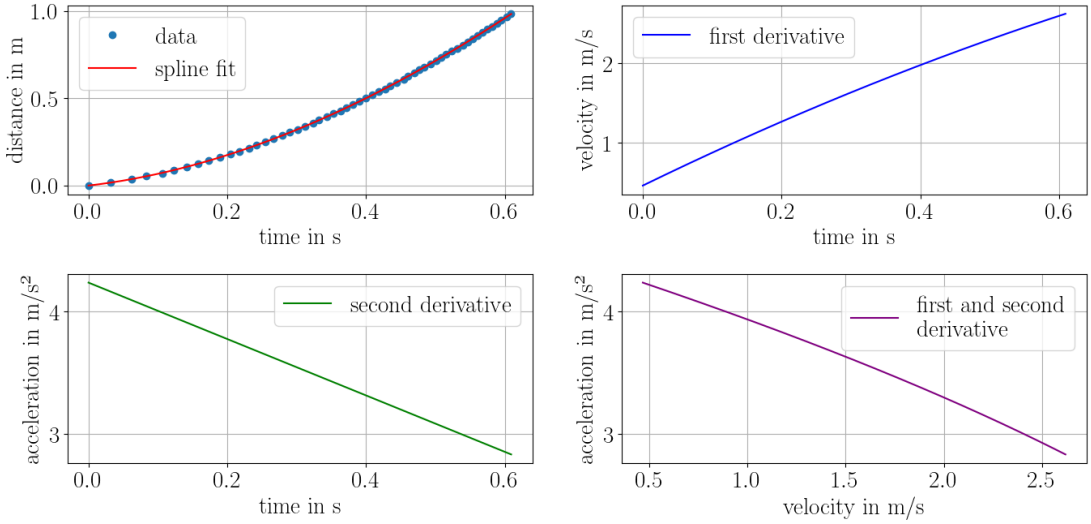

(d) Reference data with spline fit and spline derivations

Figure 85: Data, spline fits and residuals for two top baffle measurement 1 with 4.5 kg counterweight

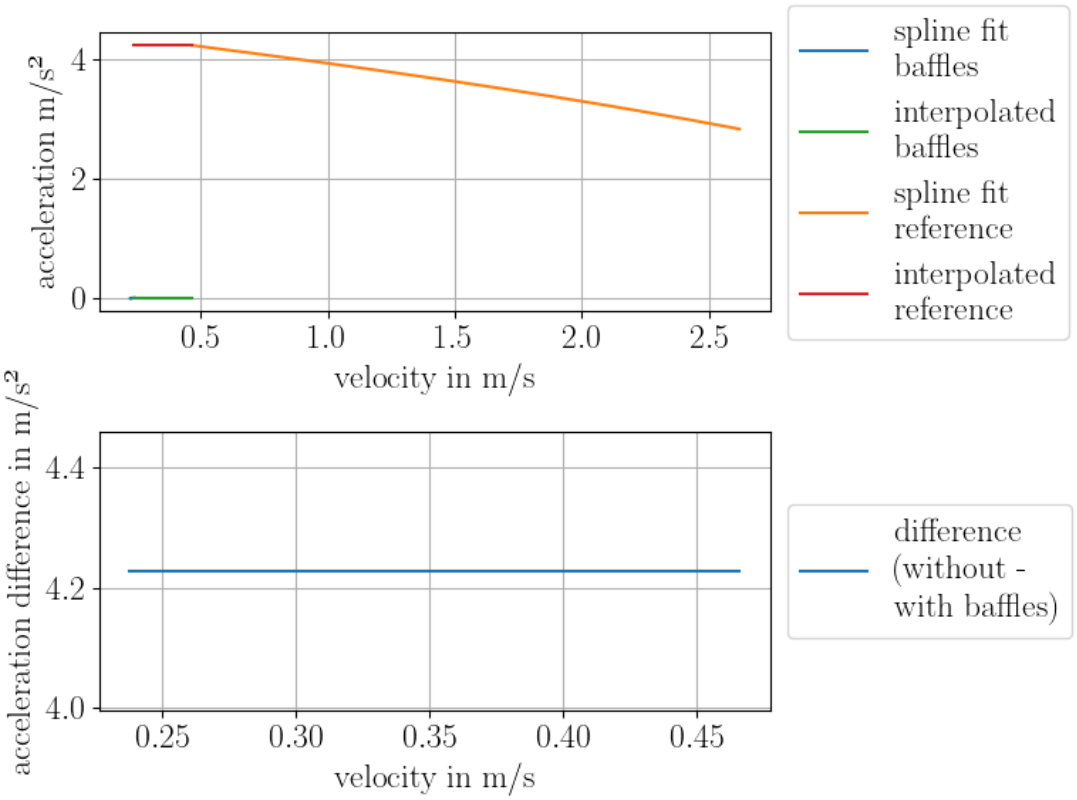

Figure 86: Acceleration over velocity of reference and baffle data with interpolated acceleration values for two top baffle measurement 1 with 4.5 kg counterweight

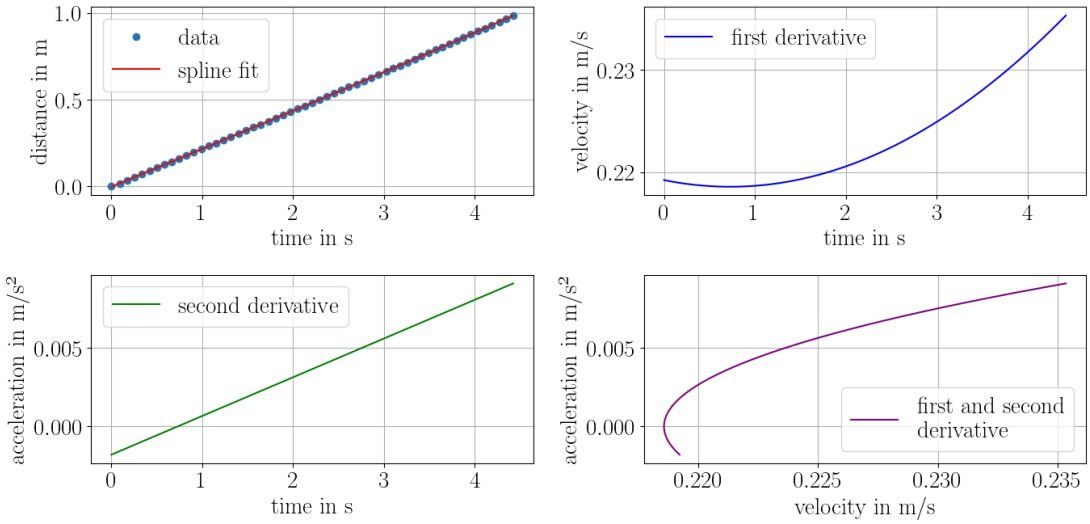

(a) Baffle data with spline fit and spline derivations

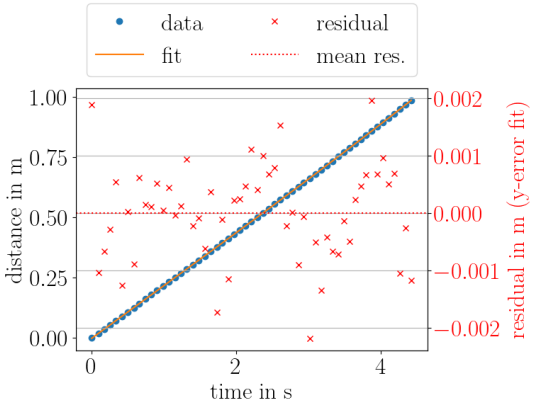

(b) Baffle data with spline fit and residuals

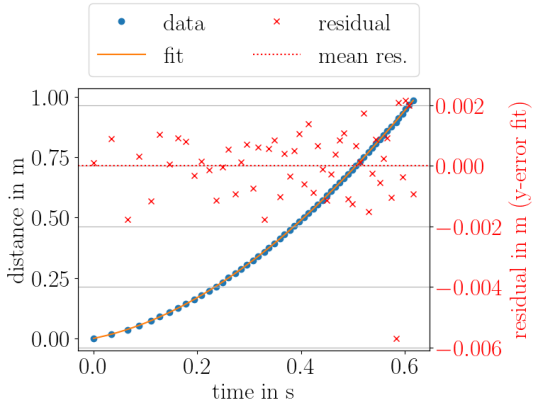

(c) Reference data with spline fit and residuals

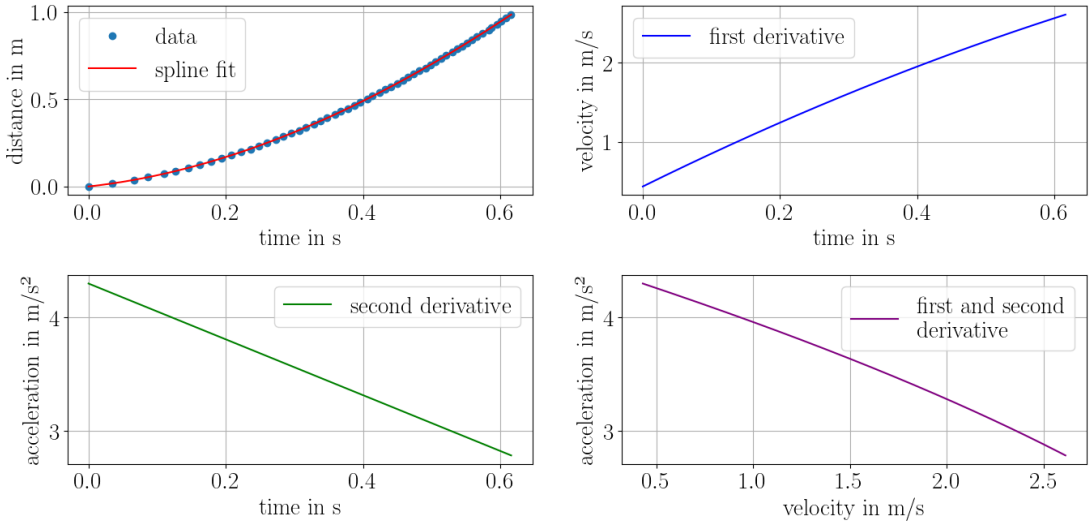

(d) Reference data with spline fit and spline derivations

Figure 87: Data, spline fits and residuals for two top baffle measurement 2 with 4.5 kg counterweight

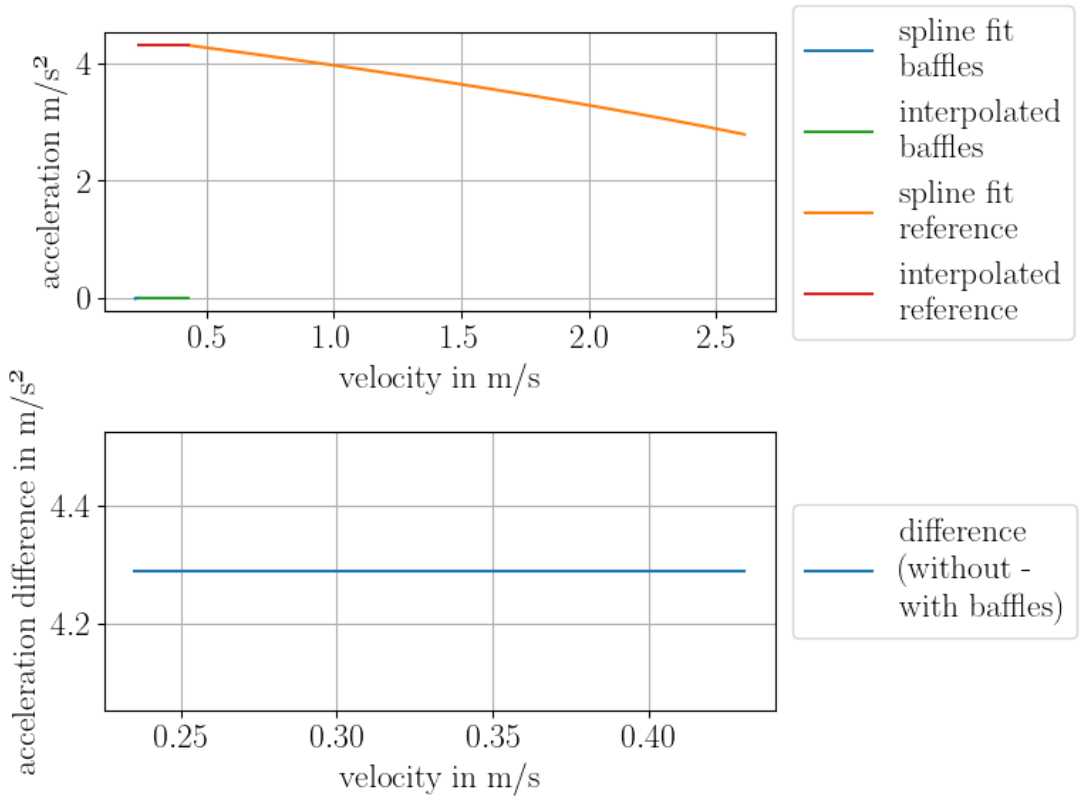

Figure 88: Acceleration over velocity of reference and baffle data with interpolated acceleration values for two top baffle measurement 2 with 4.5 kg counterweight

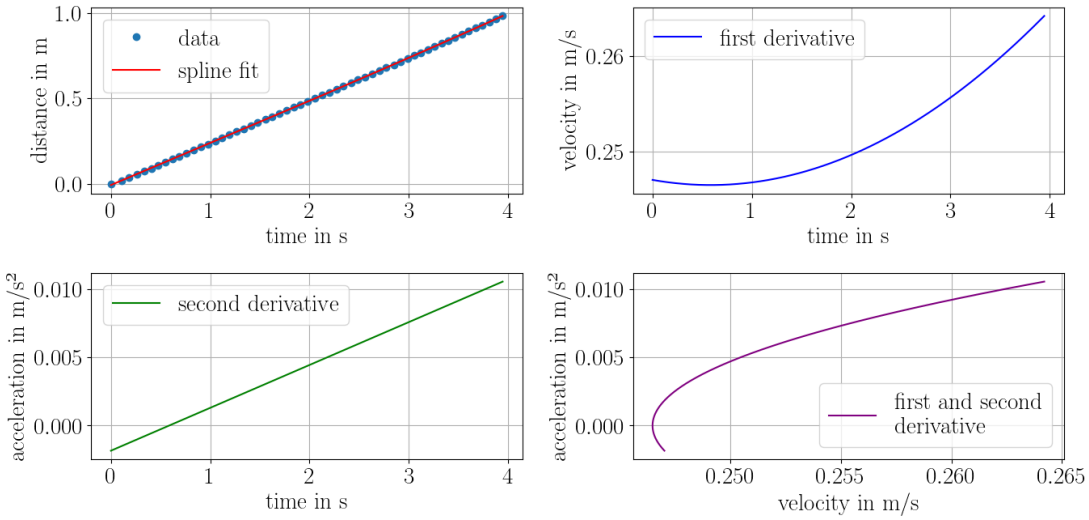

(a) Baffle data with spline fit and spline derivations

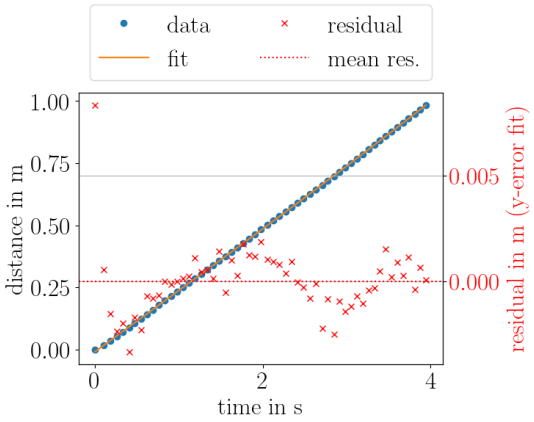

(b) Baffle data with spline fit and residuals

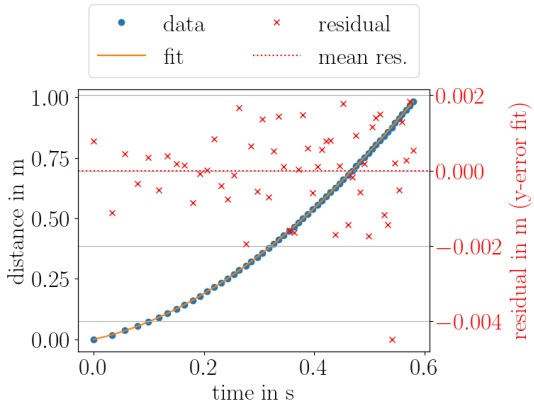

(c) Reference data with spline fit and residuals

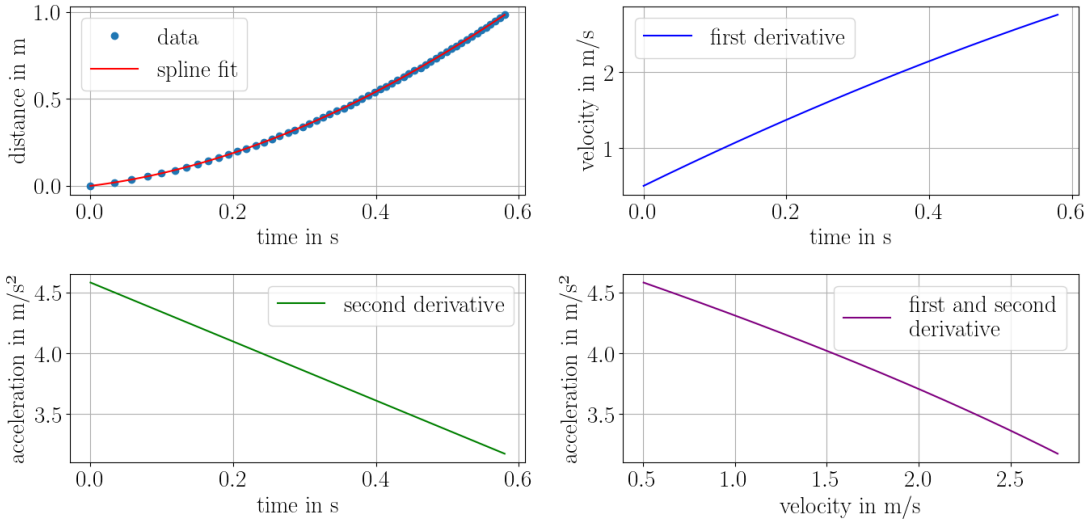

(d) Reference data with spline fit and spline derivations

Figure 89: Data, spline fits and residuals for two top baffle measurement 0 with 5.0 kg counterweight

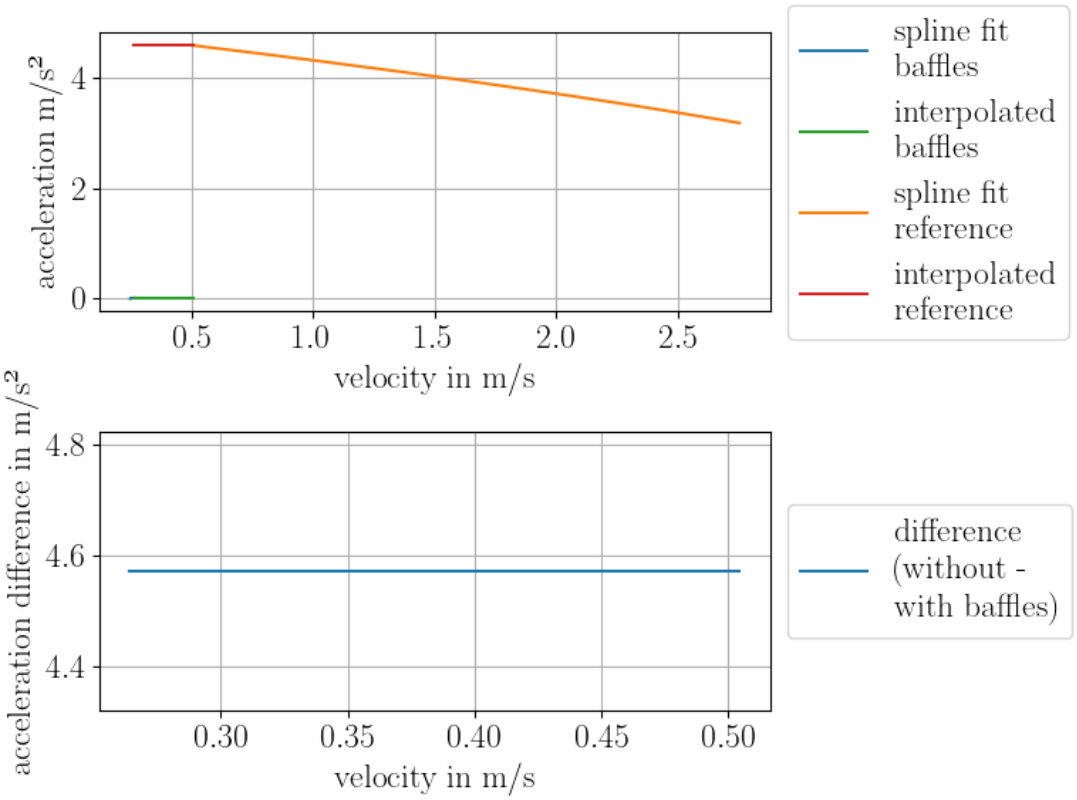

Figure 90: Acceleration over velocity of reference and baffle data with interpolated acceleration values for two top baffle measurement 0 with 5.0 kg counterweight

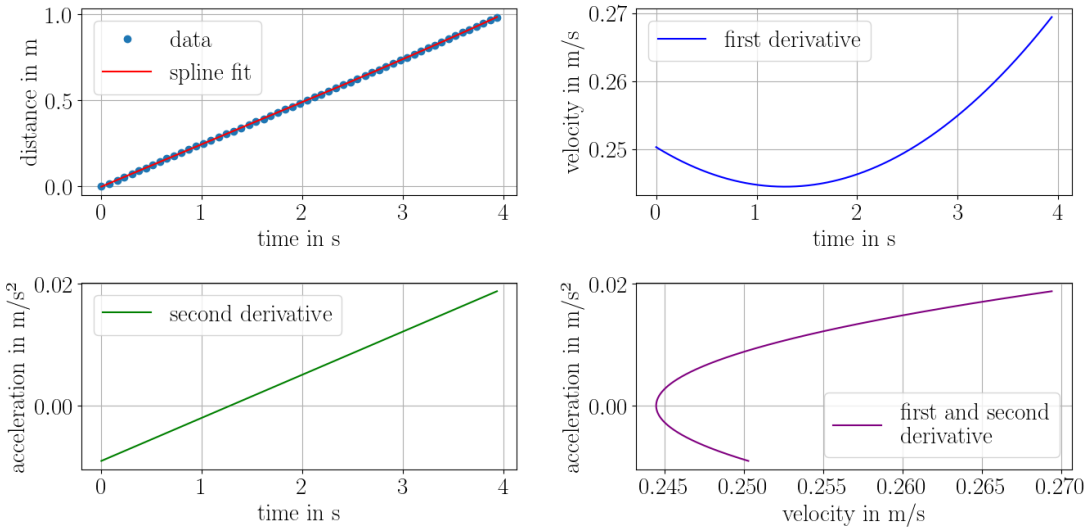

(a) Baffle data with spline fit and spline derivations

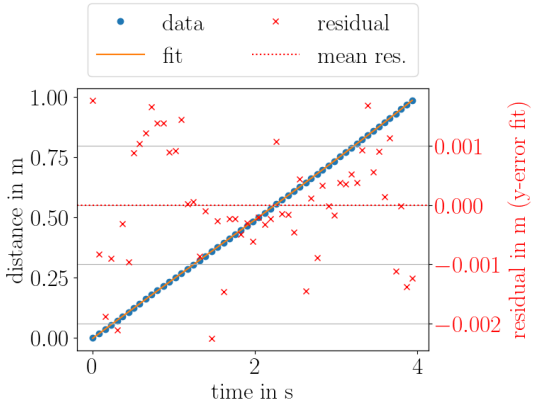

(b) Baffle data with spline fit and residuals

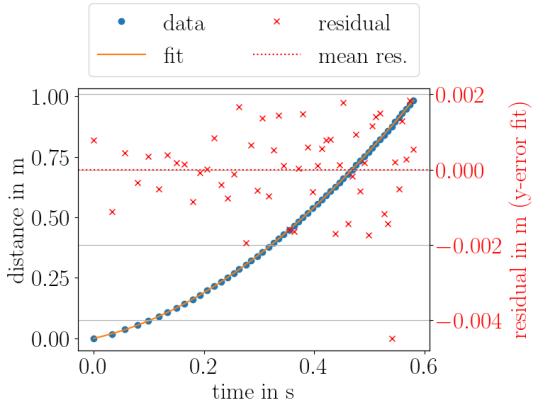

(c) Reference data with spline fit and residuals

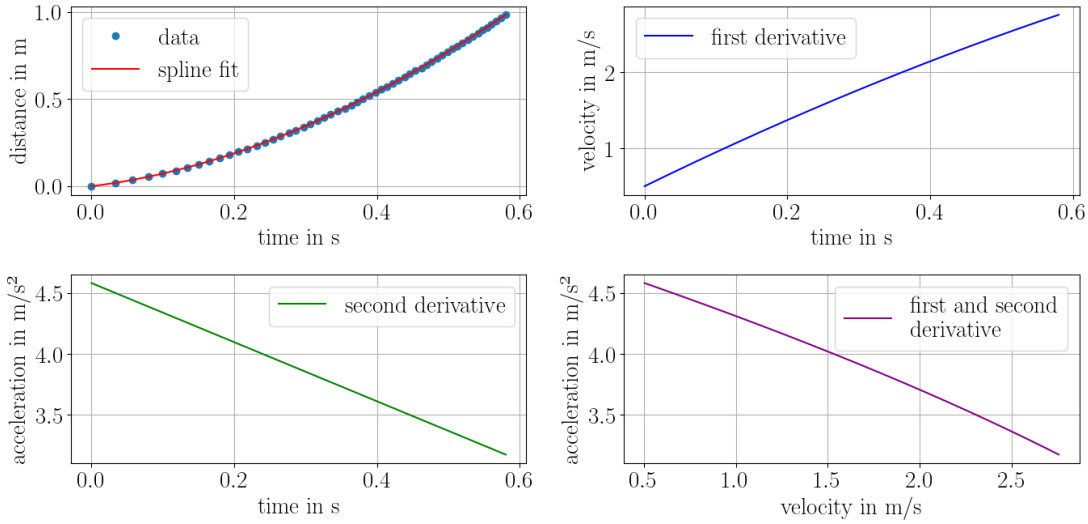

(d) Reference data with spline fit and spline derivations

Figure 91: Data, spline fits and residuals for two top baffle measurement 1 with 5.0 kg counterweight

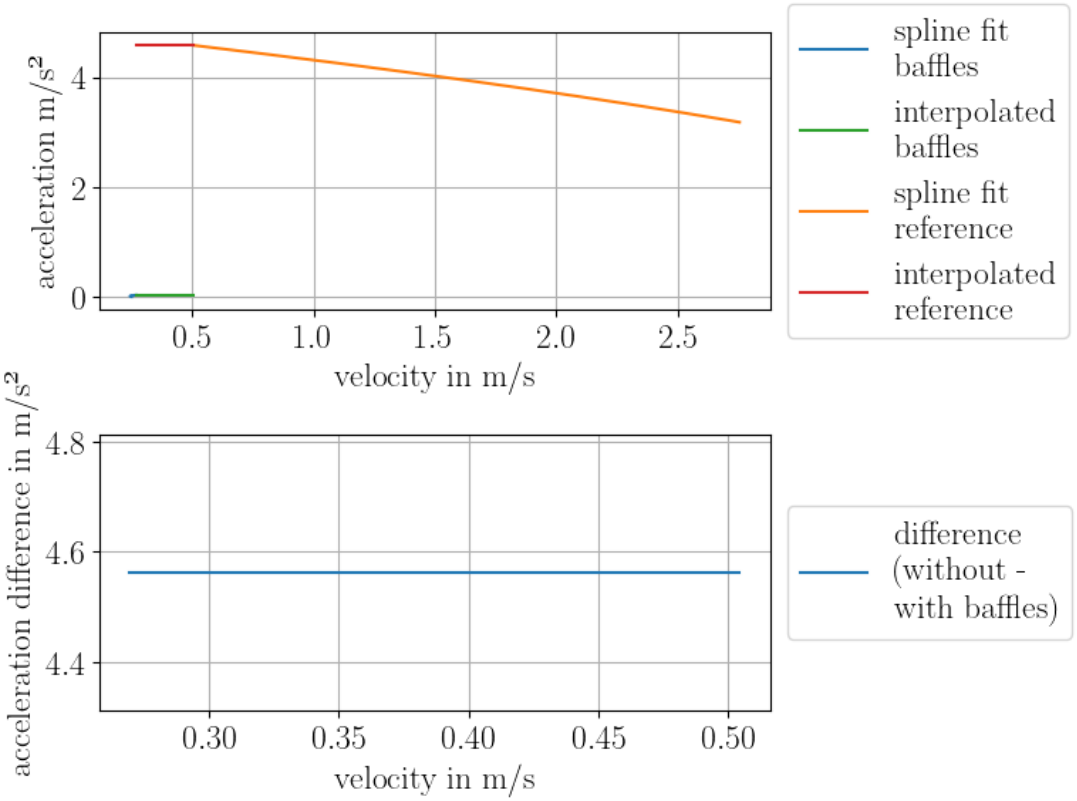

Figure 92: Acceleration over velocity of reference and baffle data with interpolated acceleration values for two top baffle measurement 1 with 5.0 kg counterweight

A.3 Measurements with the bottom baffle

The plots for measurements with the bottom baffle are presented for different counterweights.

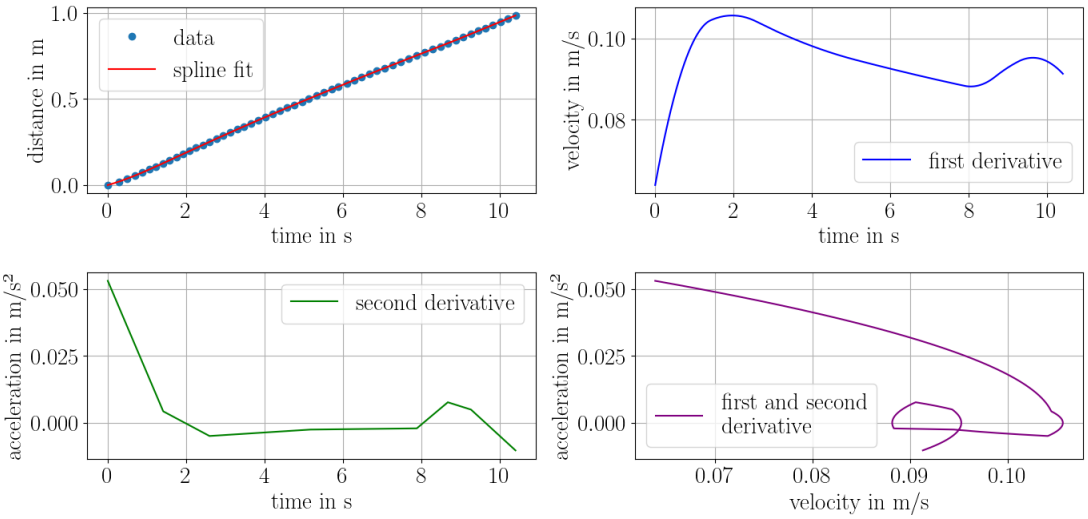

(a) Baffle data with spline fit and spline derivations

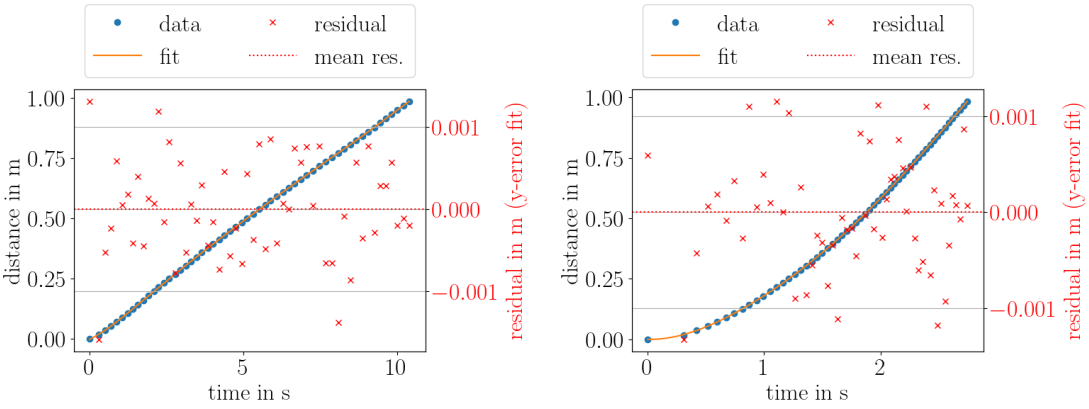

(b) Baffle data with spline fit and residuals

(c) Reference data with spline fit and residuals

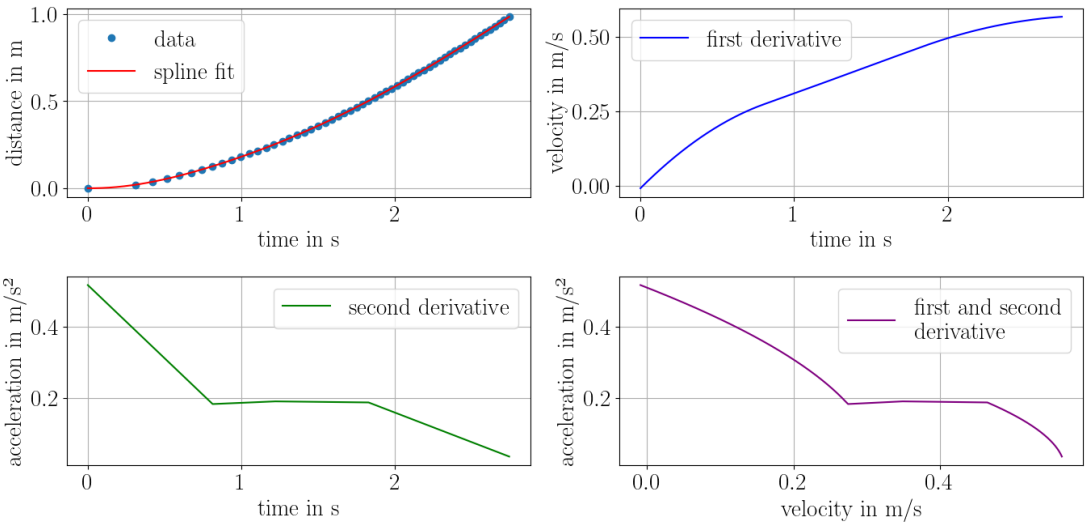

(d) Reference data with spline fit and spline derivations

Figure 93: Data, spline fits and residuals for bottom baffle measurement 1 with 3 kg counterweight

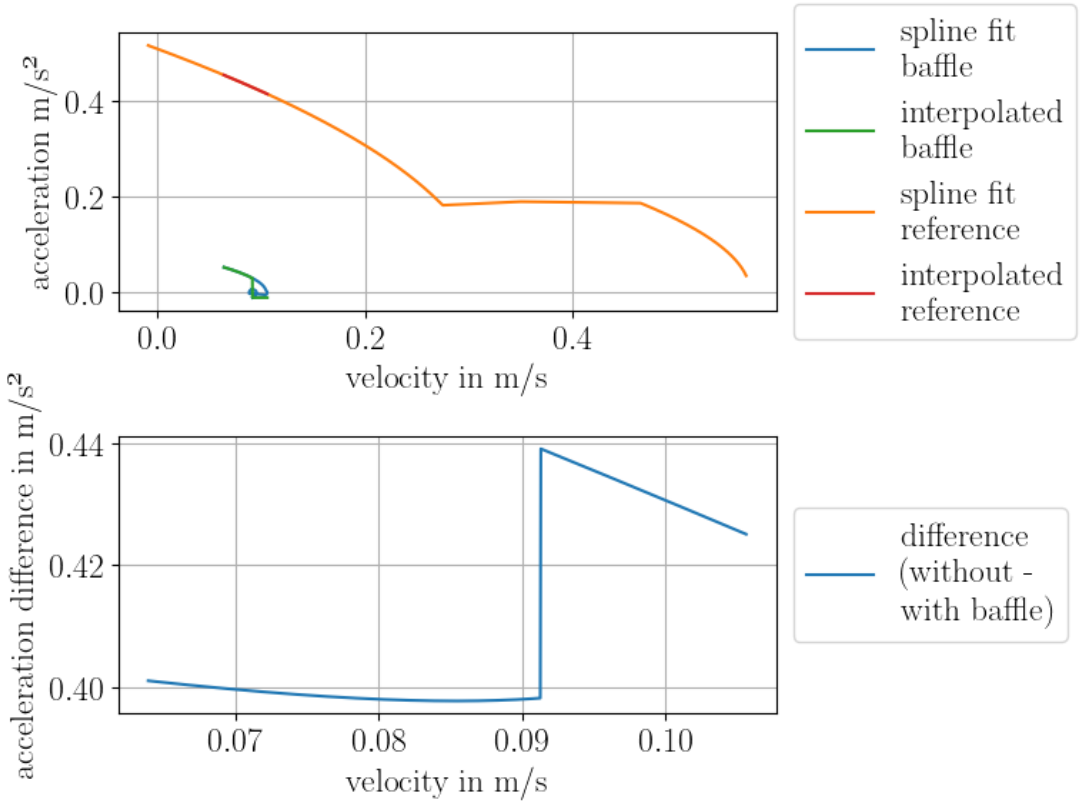

Figure 94: Acceleration over velocity of reference and baffle data with interpolated acceleration values for bottom baffle measurement 1 with 3 kg counterweight

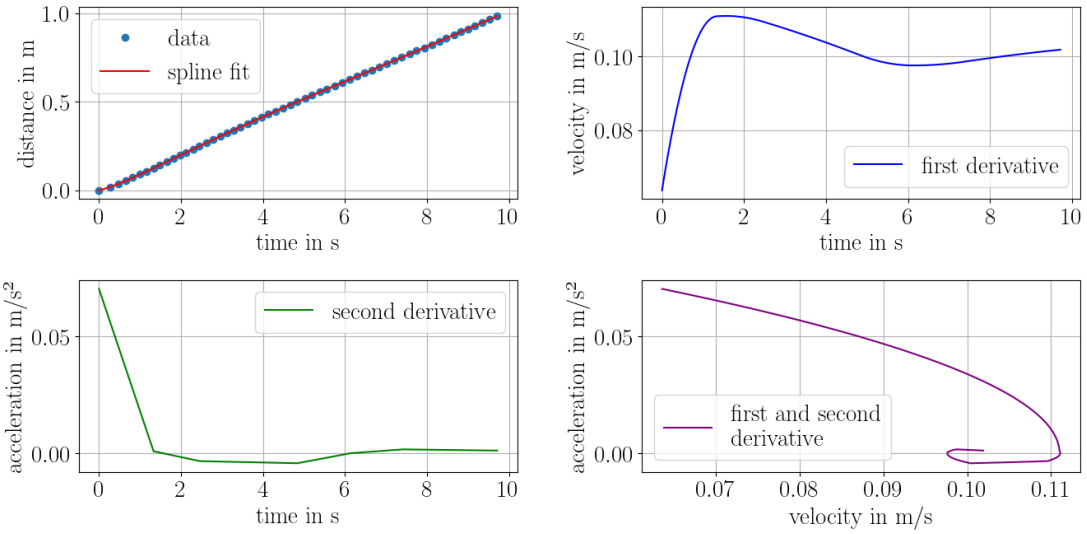

(a) Baffle data with spline fit and spline derivations

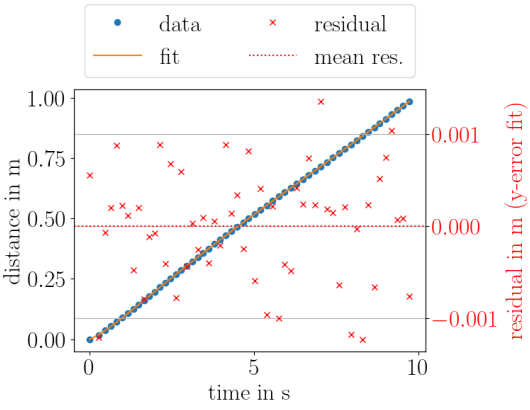

(b) Baffle data with spline fit and residuals

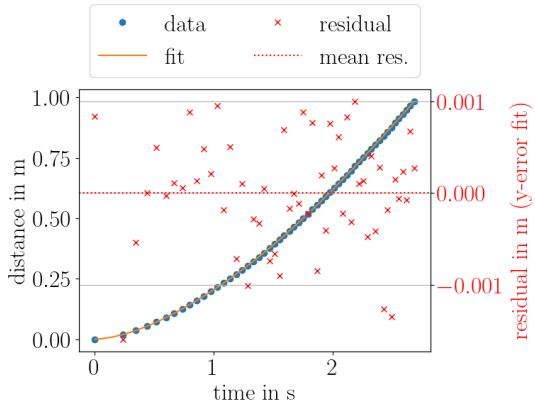

(c) Reference data with spline fit and residuals

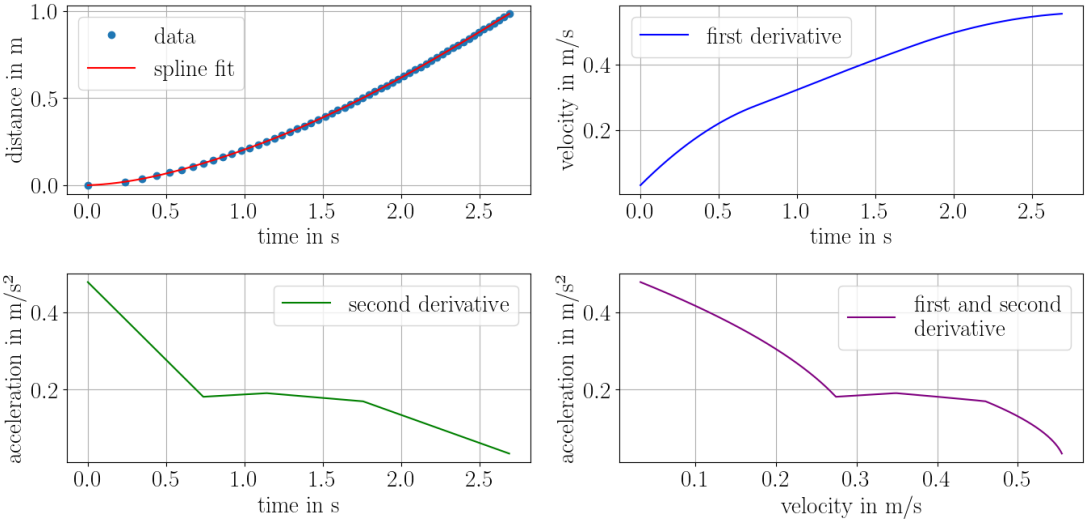

(d) Reference data with spline fit and spline derivations

Figure 95: Data, spline fits and residuals for bottom baffle measurement 2 with 3 kg counterweight

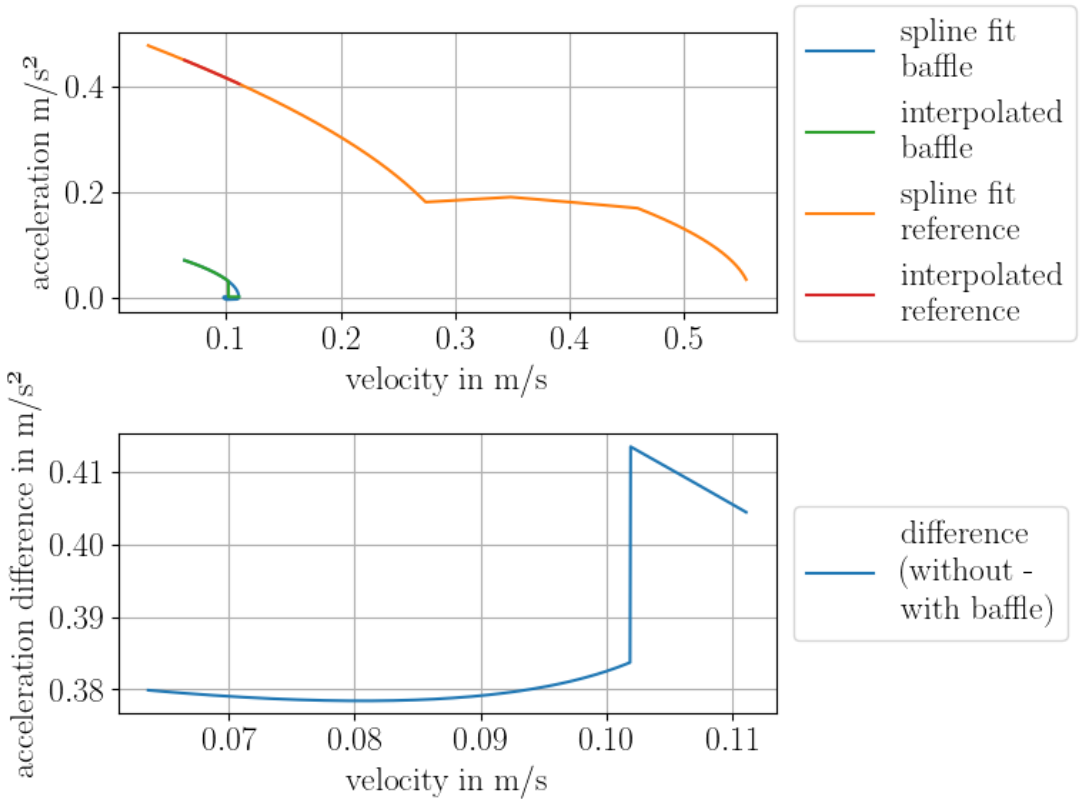

Figure 96: Acceleration over velocity of reference and baffle data with interpolated acceleration values for bottom baffle measurement 2 with 3 kg counterweight

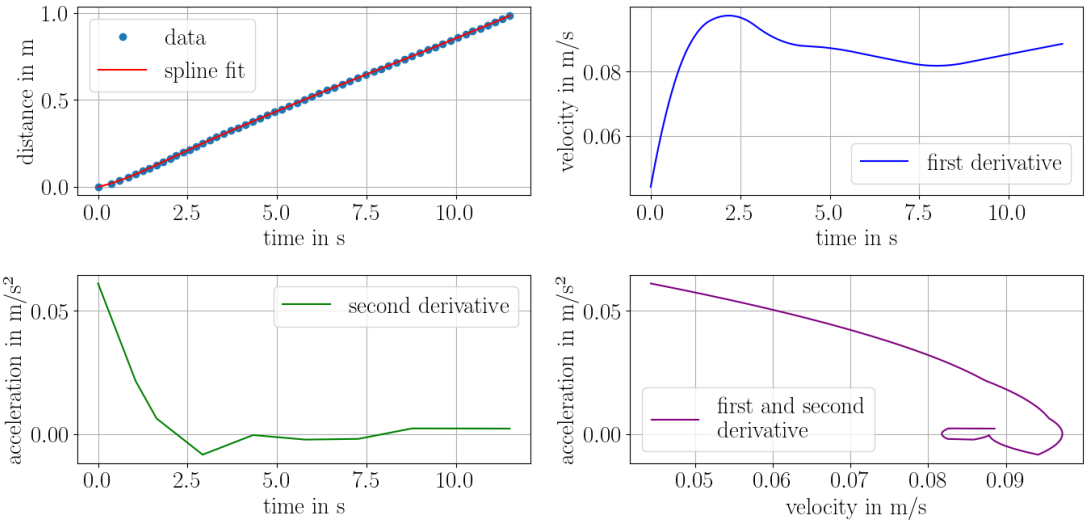

(a) Baffle data with spline fit and spline derivations

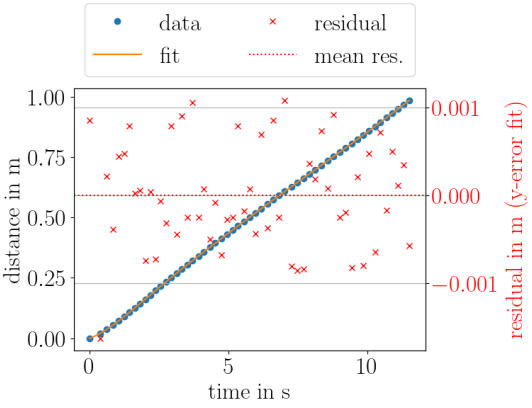

(b) Baffle data with spline fit and residuals

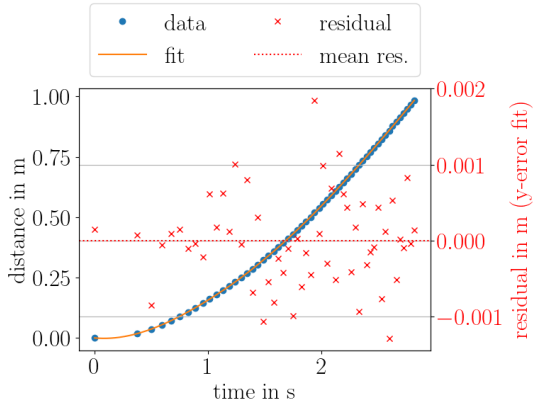

(c) Reference data with spline fit and residuals

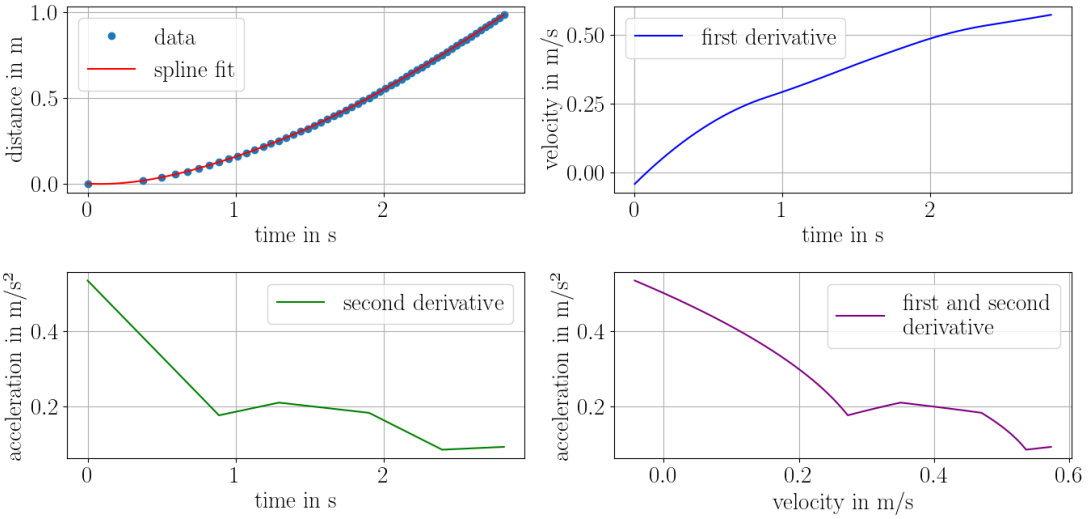

(d) Reference data with spline fit and spline derivations

Figure 97: Data, spline fits and residuals for bottom baffle measurement 3 with 3 kg counterweight

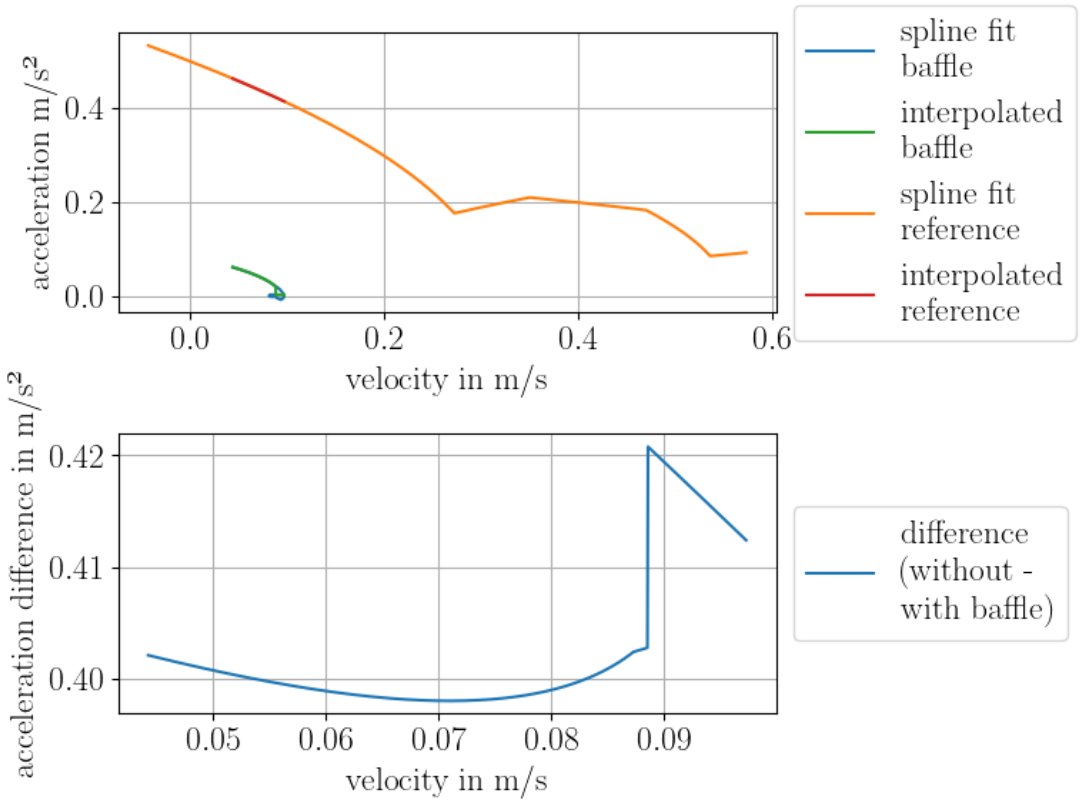

Figure 98: Acceleration over velocity of reference and baffle data with interpolated acceleration values for bottom baffle measurement 3 with 3 kg counterweight

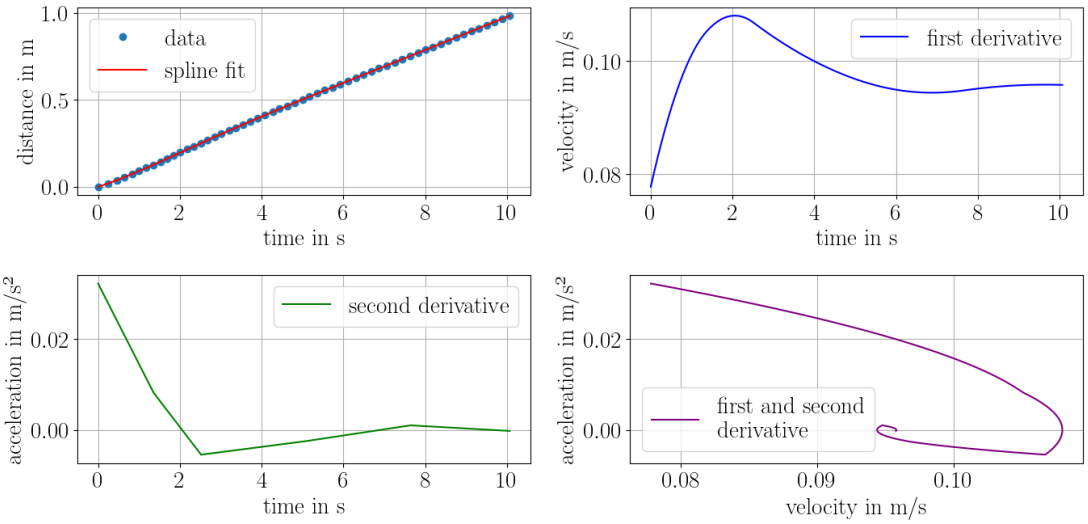

(a) Baffle data with spline fit and spline derivations

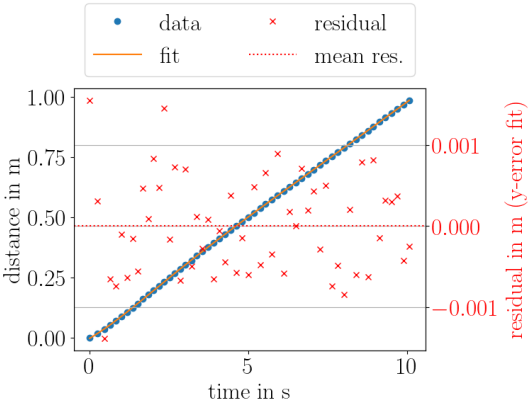

(b) Baffle data with spline fit and residuals

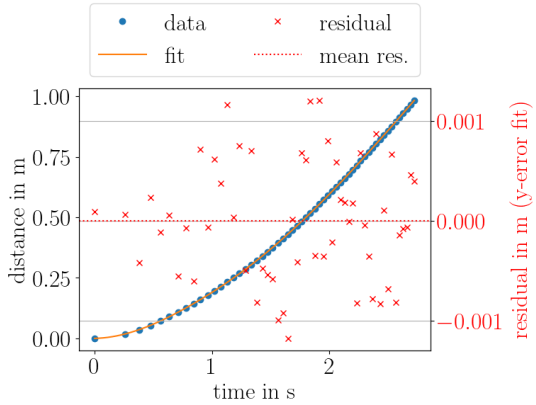

(c) Reference data with spline fit and residuals

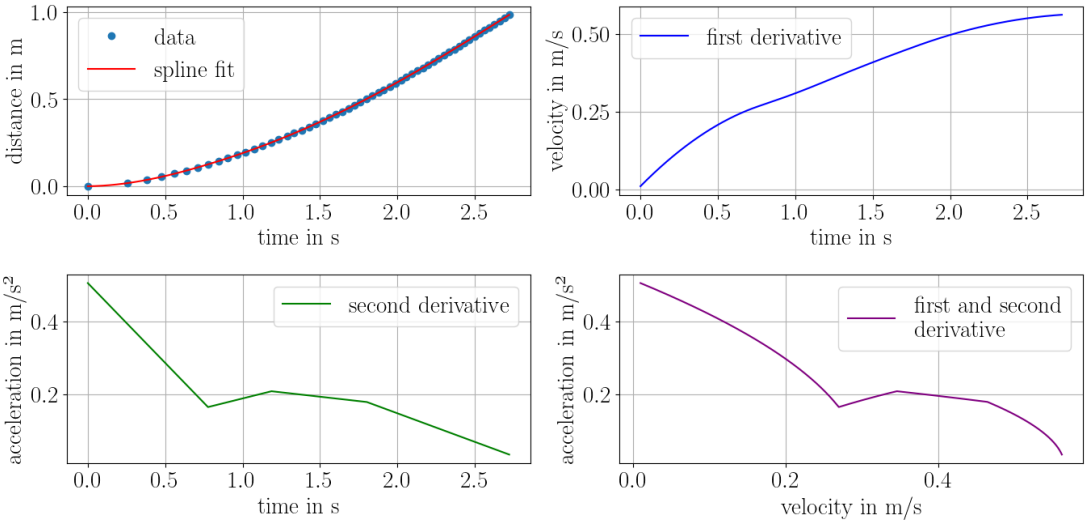

(d) Reference data with spline fit and spline derivations

Figure 99: Data, spline fits and residuals for bottom baffle measurement 4 with 3 kg counterweight

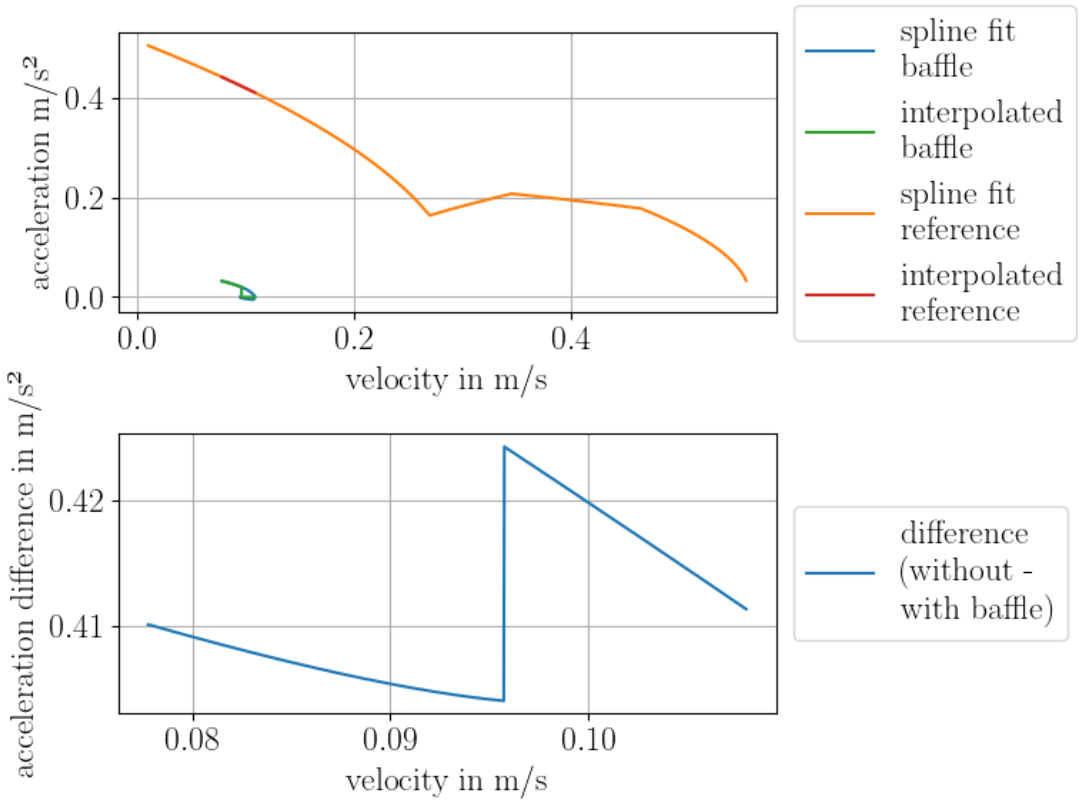

Figure 100: Acceleration over velocity of reference and baffle data with interpolated acceleration values for bottom baffle measurement 4 with 3 kg counterweight

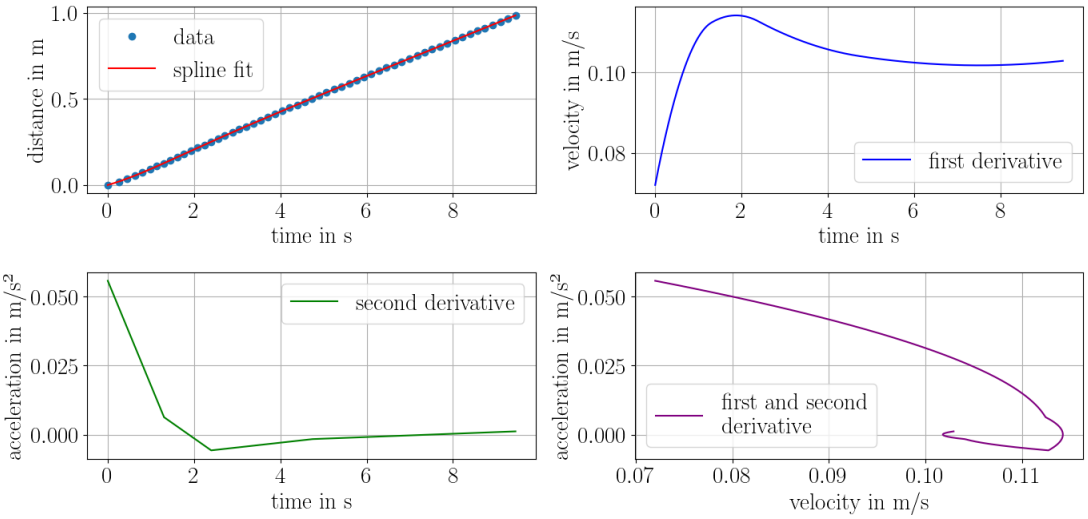

(a) Baffle data with spline fit and spline derivations

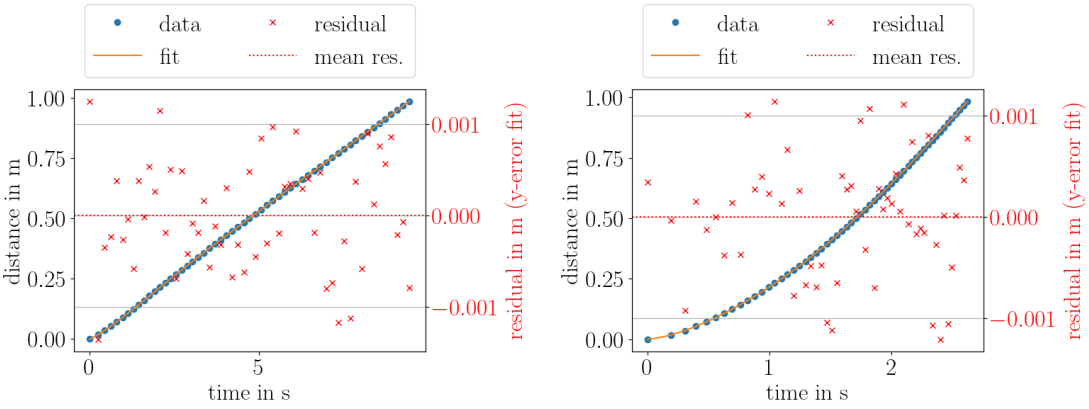

(b) Baffle data with spline fit and residuals

(c) Reference data with spline fit and residuals

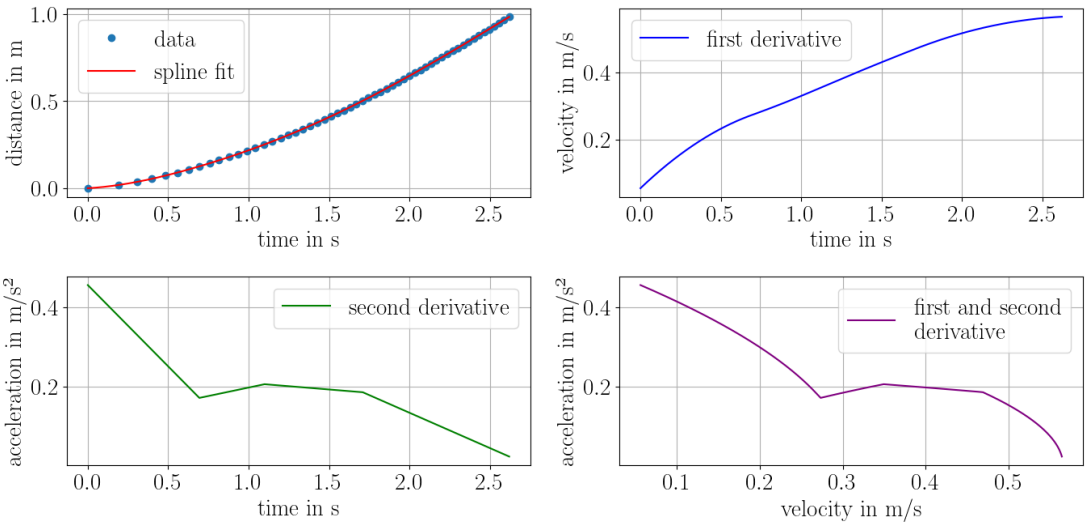

(d) Reference data with spline fit and spline derivations

Figure 101: Data, spline fits and residuals for bottom baffle measurement 5 with 3 kg counterweight

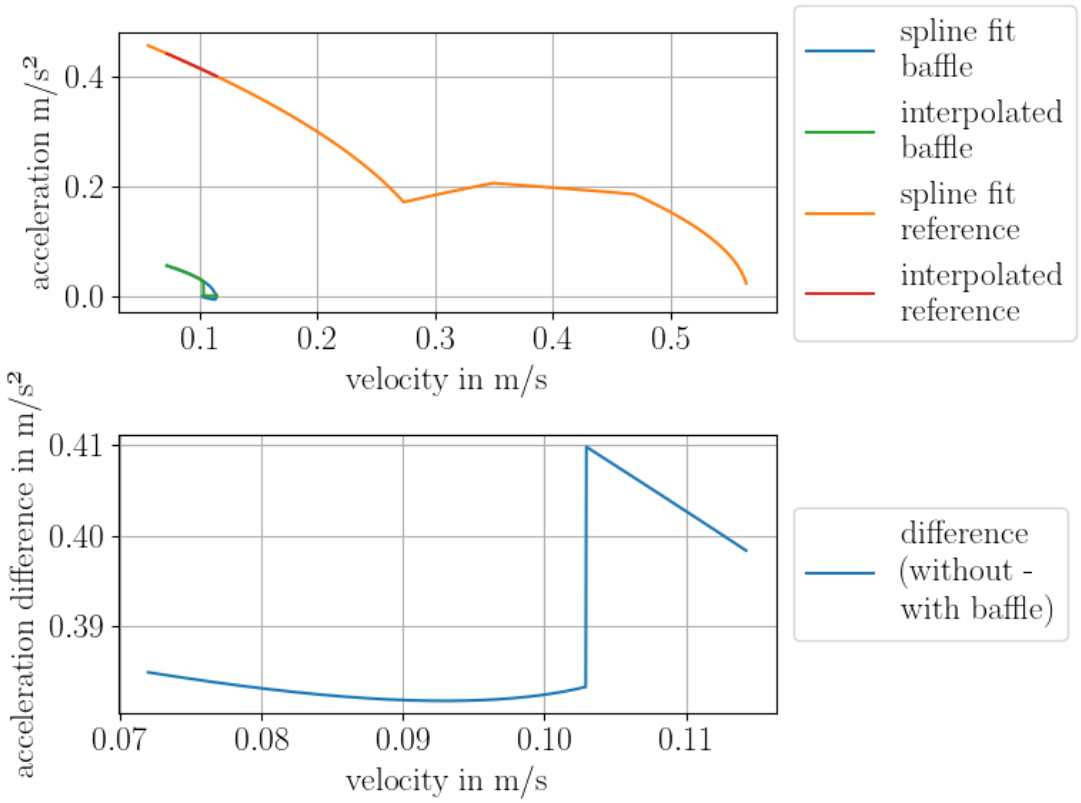

Figure 102: Acceleration over velocity of reference and baffle data with interpolated acceleration values for bottom baffle measurement 5 with 3 kg counterweight

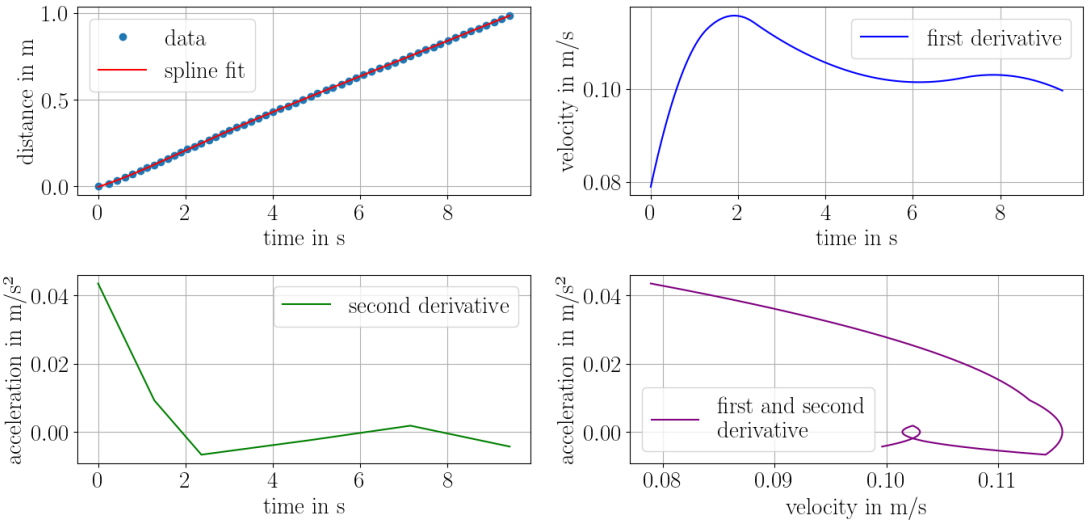

(a) Baffle data with spline fit and spline derivations

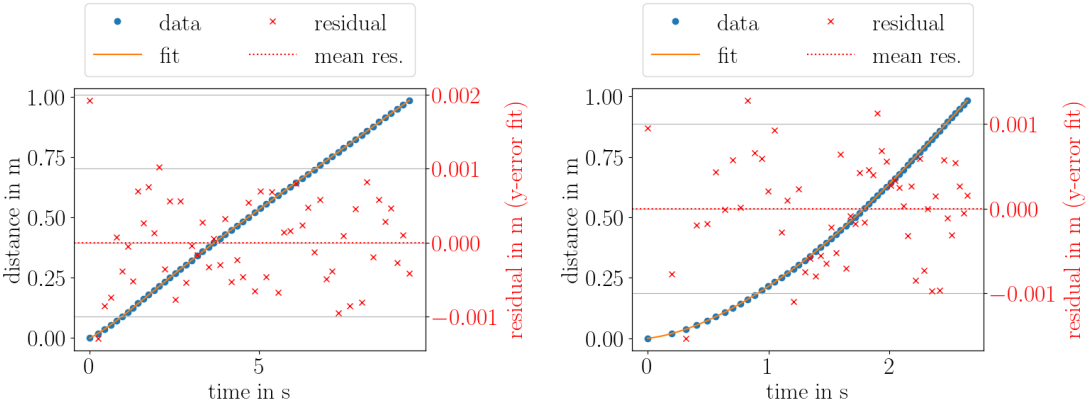

(b) Baffle data with spline fit and residuals

(c) Reference data with spline fit and residuals

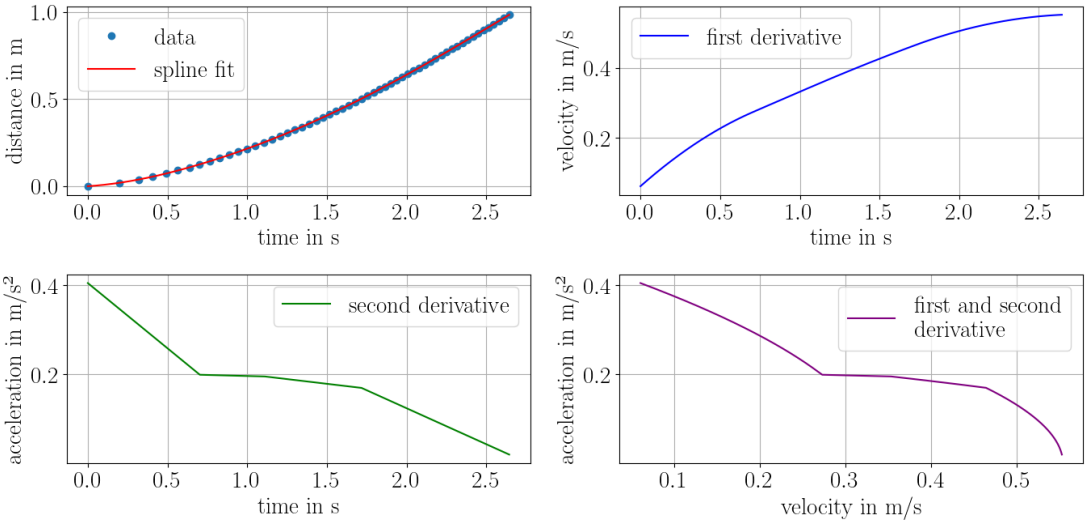

(d) Reference data with spline fit and spline derivations

Figure 103: Data, spline fits and residuals for bottom baffle measurement 6 with 3 kg counterweight

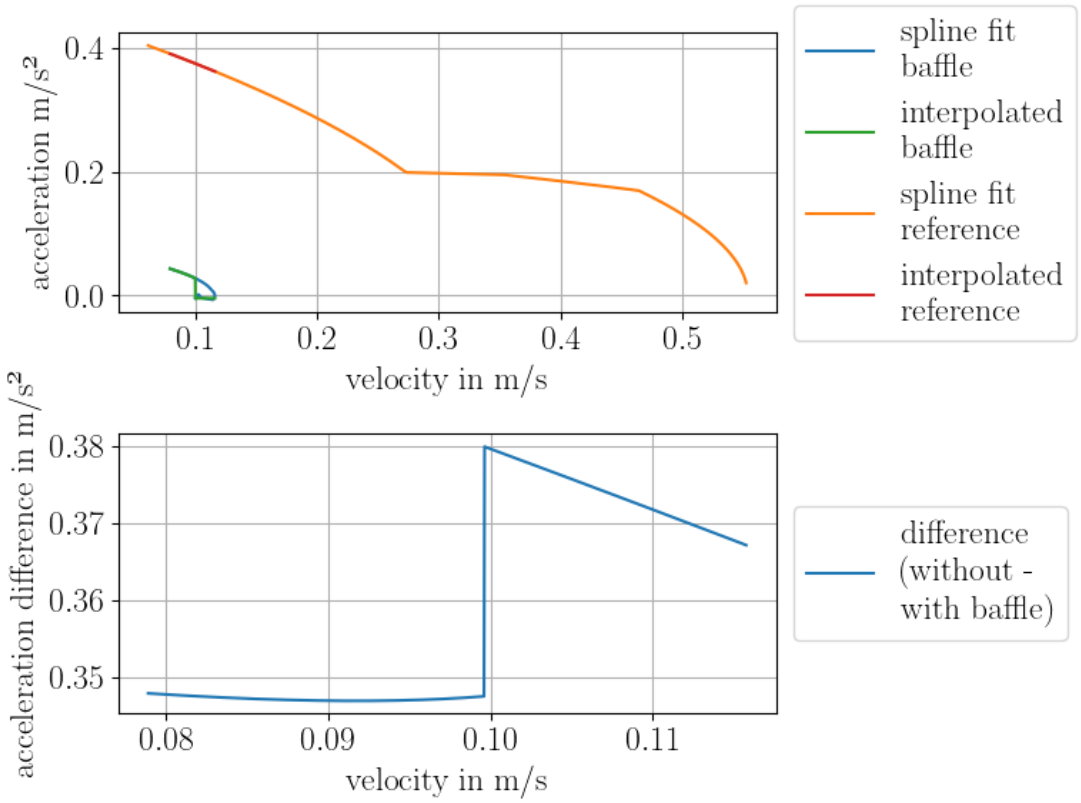

Figure 104: Acceleration over velocity of reference and baffle data with interpolated acceleration values for bottom baffle measurement 6 with 3 kg counterweight

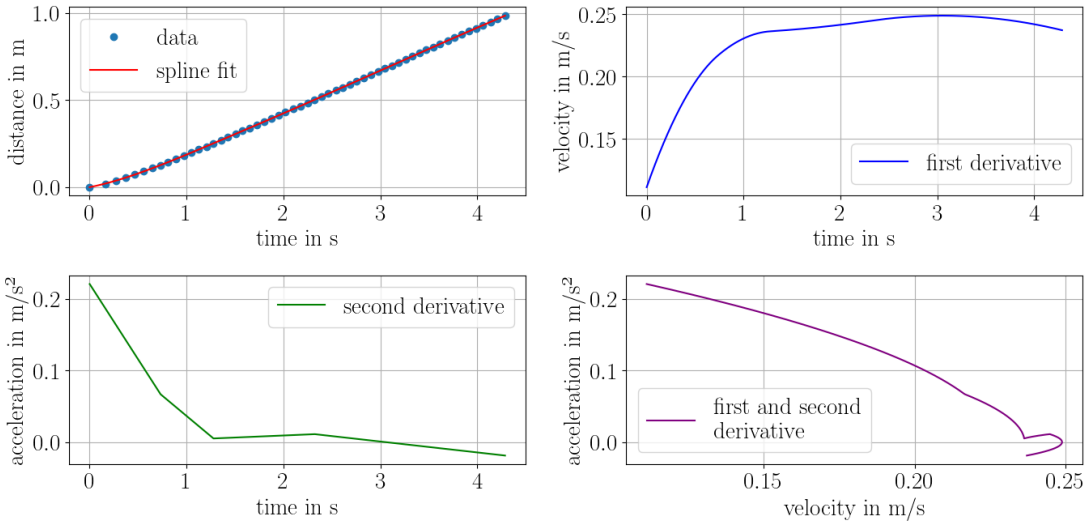

(a) Baffle data with spline fit and spline derivations

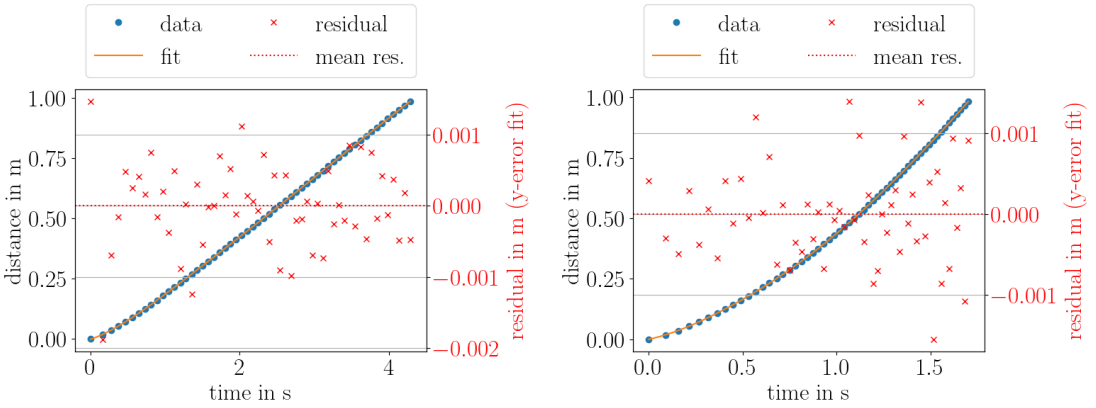

(b) Baffle data with spline fit and residuals

(c) Reference data with spline fit and residuals

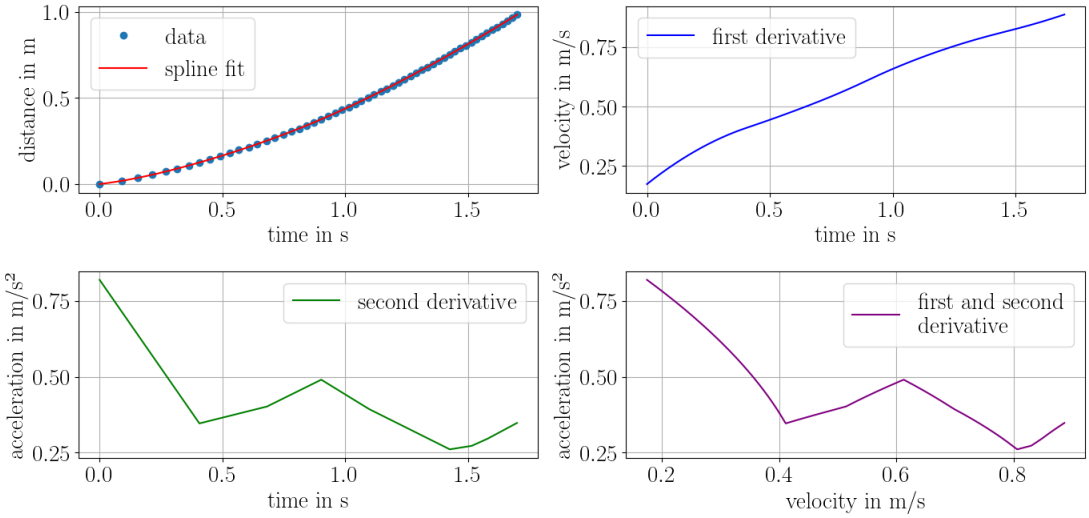

(d) Reference data with spline fit and spline derivations

Figure 105: Data, spline fits and residuals for bottom baffle measurement 1 with 4 kg counterweight

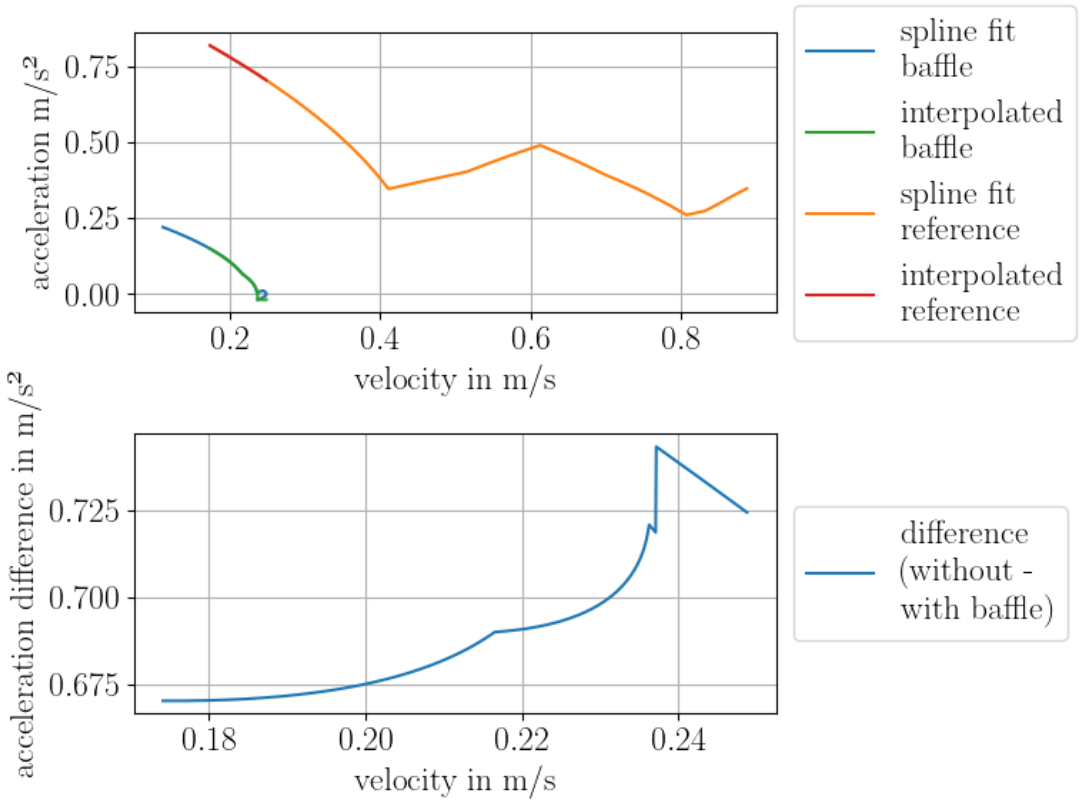

Figure 106: Acceleration over velocity of reference and baffle data with interpolated acceleration values for bottom baffle measurement 1 with 4 kg counterweight

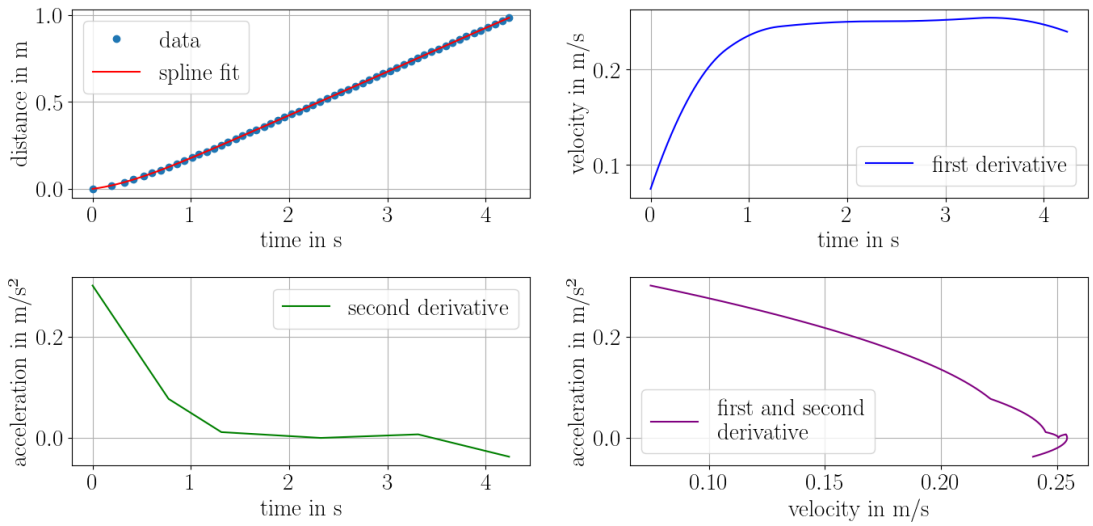

(a) Baffle data with spline fit and spline derivations

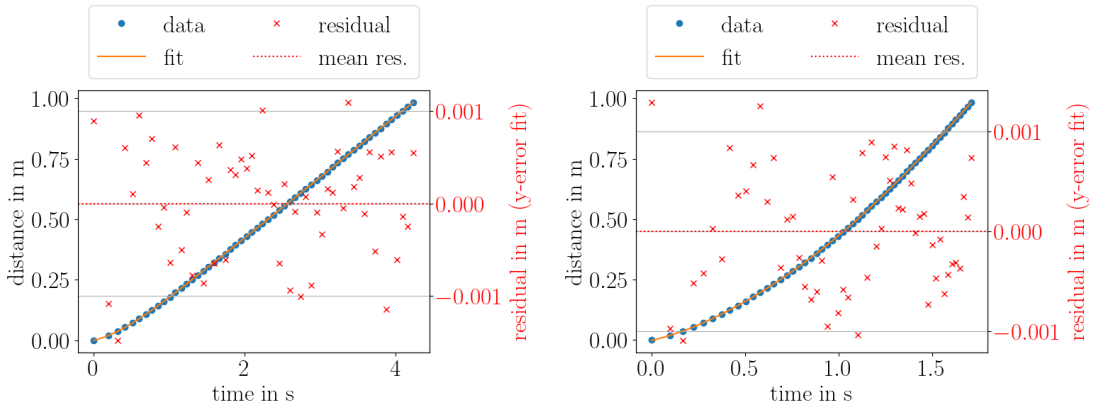

(b) Baffle data with spline fit and residuals

(c) Reference data with spline fit and residuals

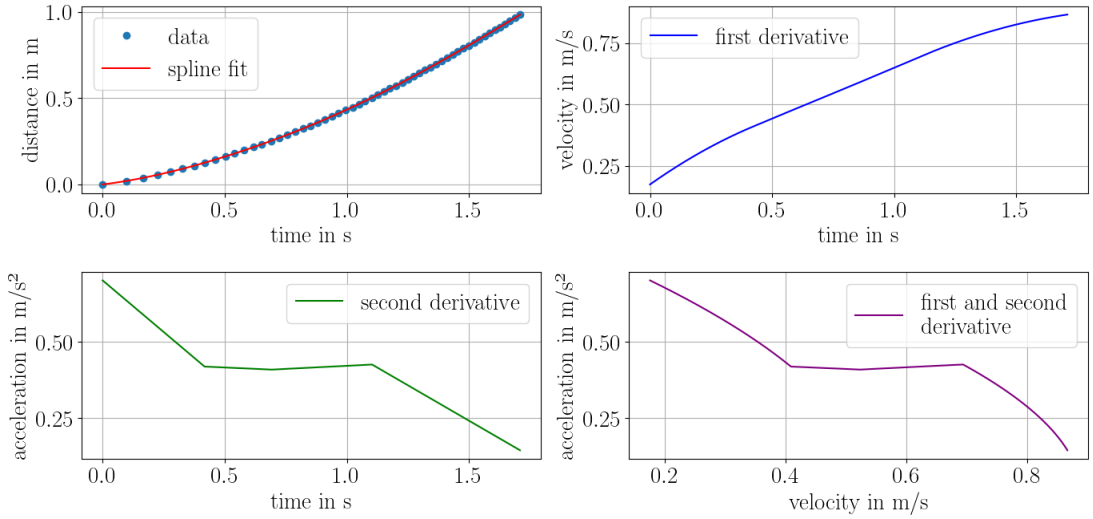

(d) Reference data with spline fit and spline derivations

Figure 107: Data, spline fits and residuals for bottom baffle measurement 2 with 4 kg counterweight

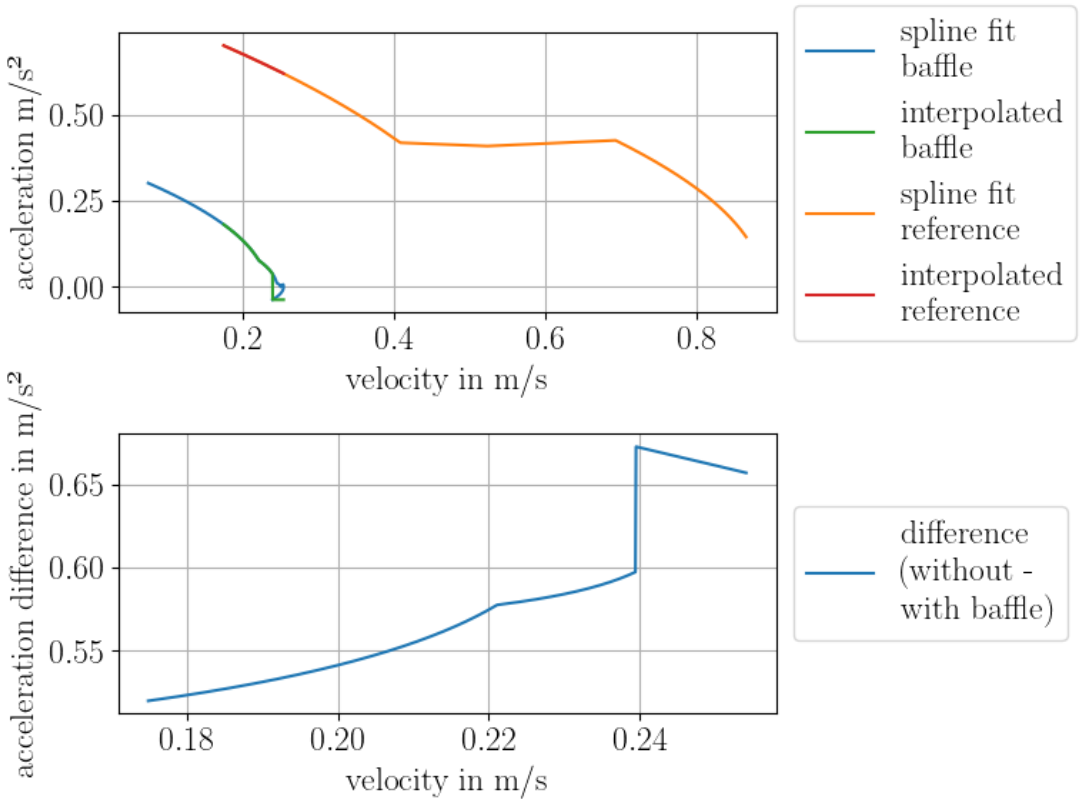

Figure 108: Acceleration over velocity of reference and baffle data with interpolated acceleration values for bottom baffle measurement 2 with 4 kg counterweight

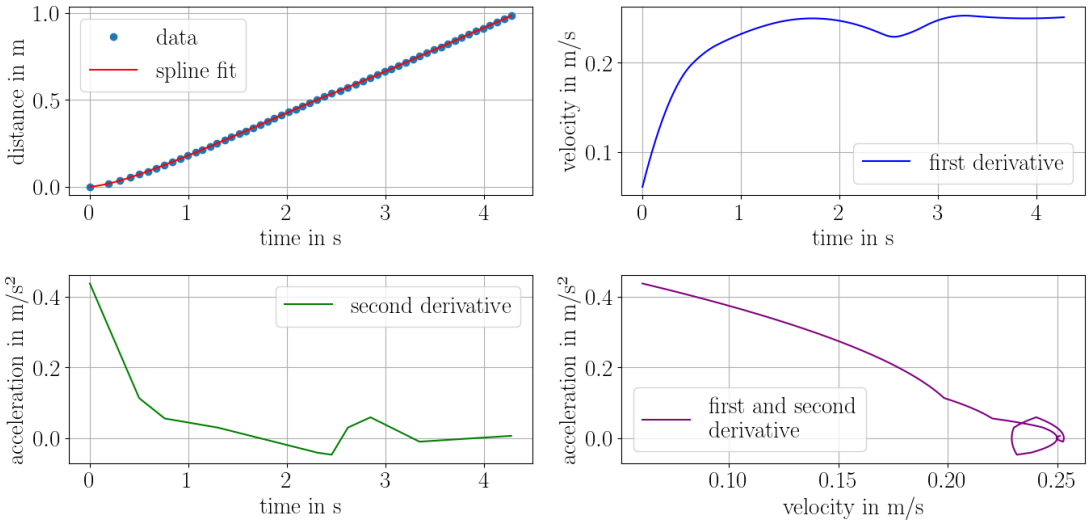

(a) Baffle data with spline fit and spline derivations

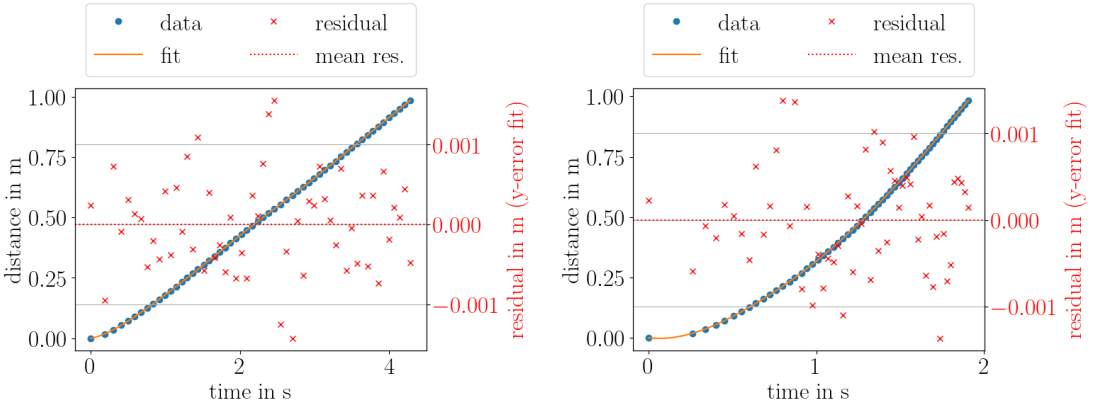

(b) Baffle data with spline fit and residuals

(c) Reference data with spline fit and residuals

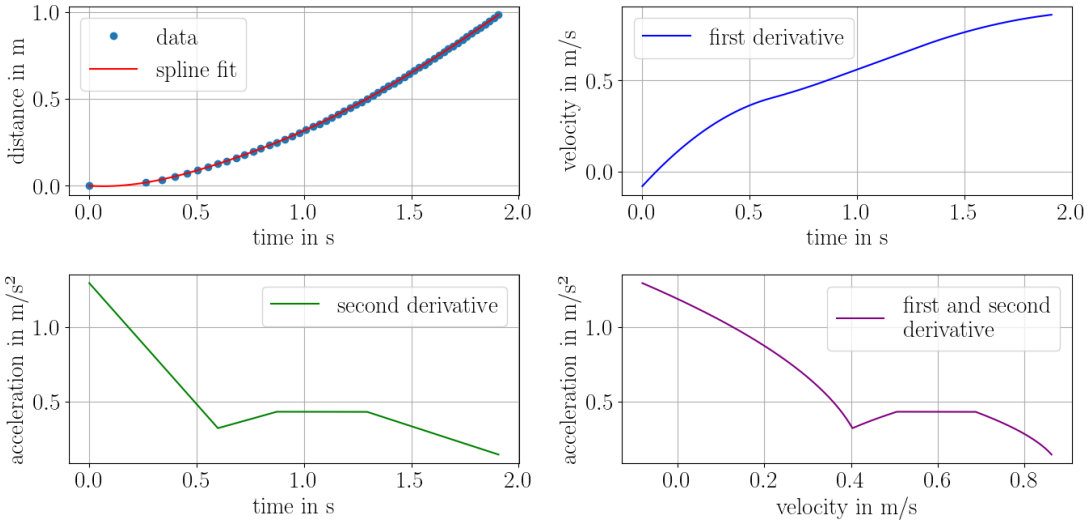

(d) Reference data with spline fit and spline derivations

Figure 109: Data, spline fits and residuals for bottom baffle measurement 3 with 4 kg counterweight

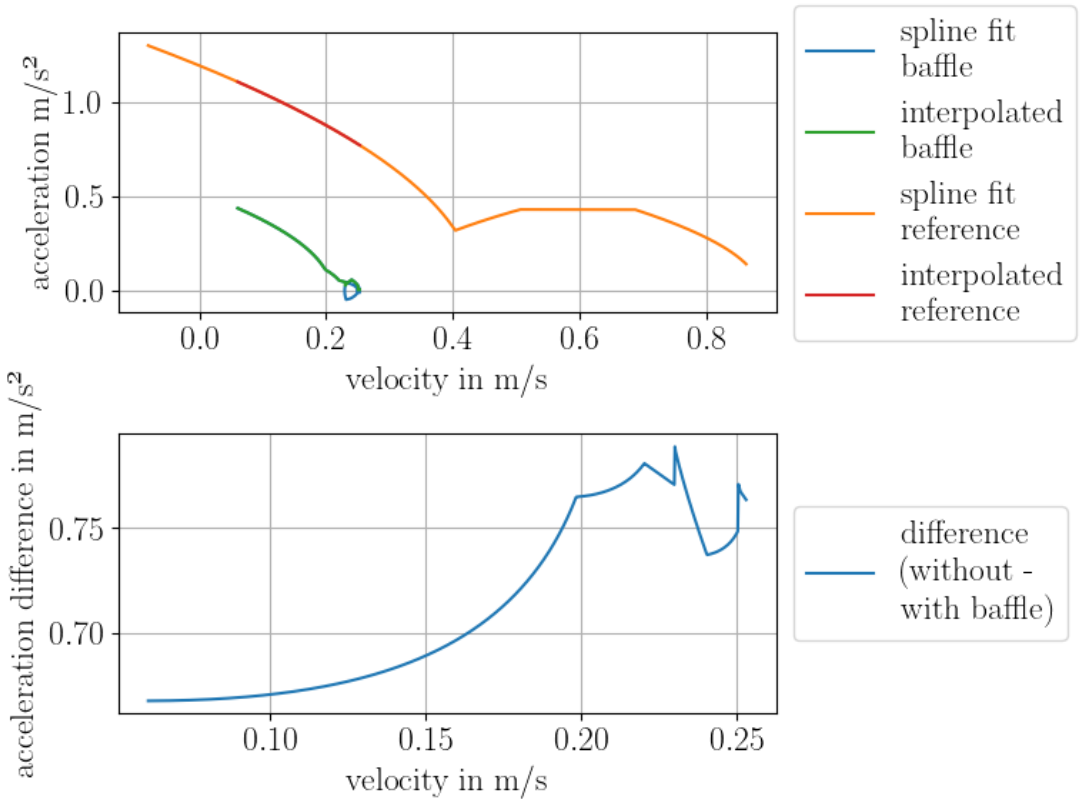

Figure 110: Acceleration over velocity of reference and baffle data with interpolated acceleration values for bottom baffle measurement 3 with 4 kg counterweight

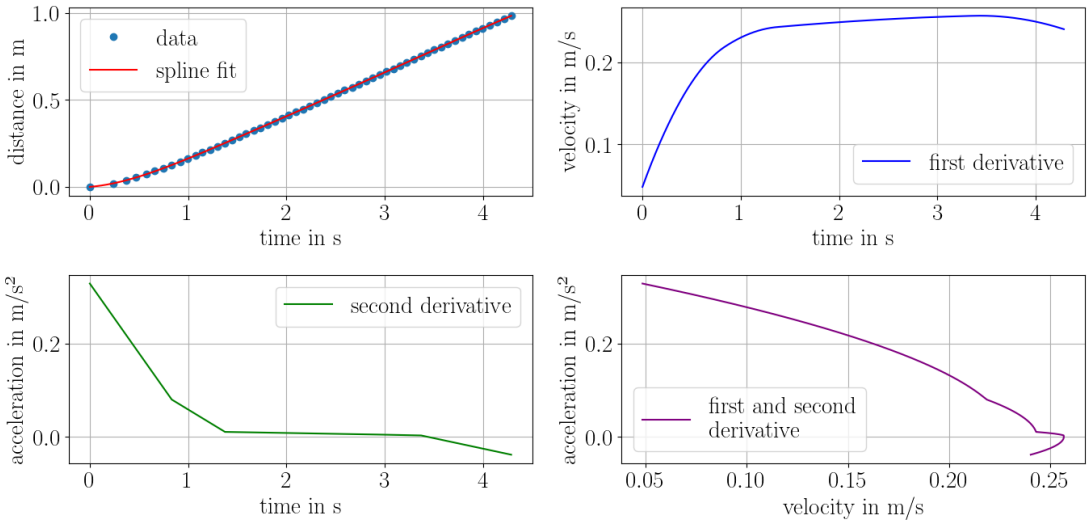

(a) Baffle data with spline fit and spline derivations

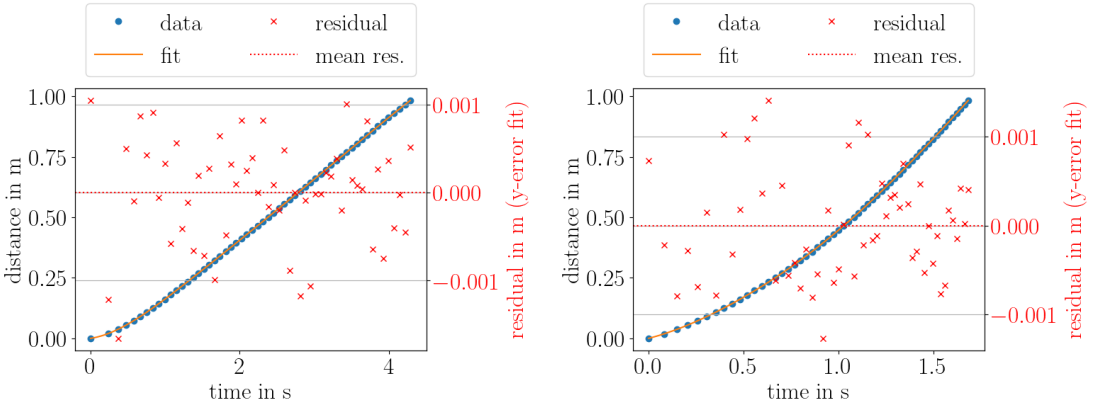

(b) Baffle data with spline fit and residuals

(c) Reference data with spline fit and residuals

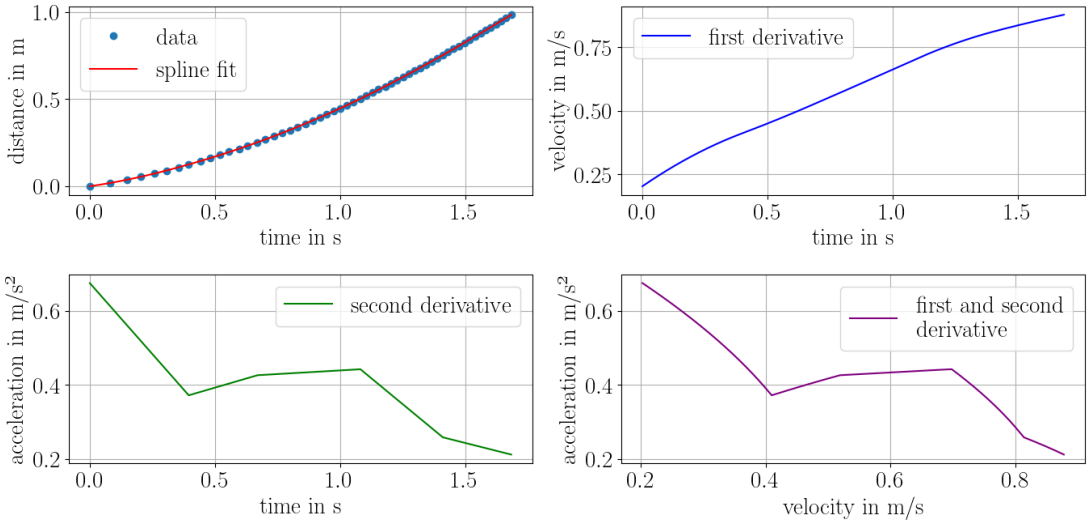

(d) Reference data with spline fit and spline derivations

Figure 111: Data, spline fits and residuals for bottom baffle measurement 4 with 4 kg counterweight

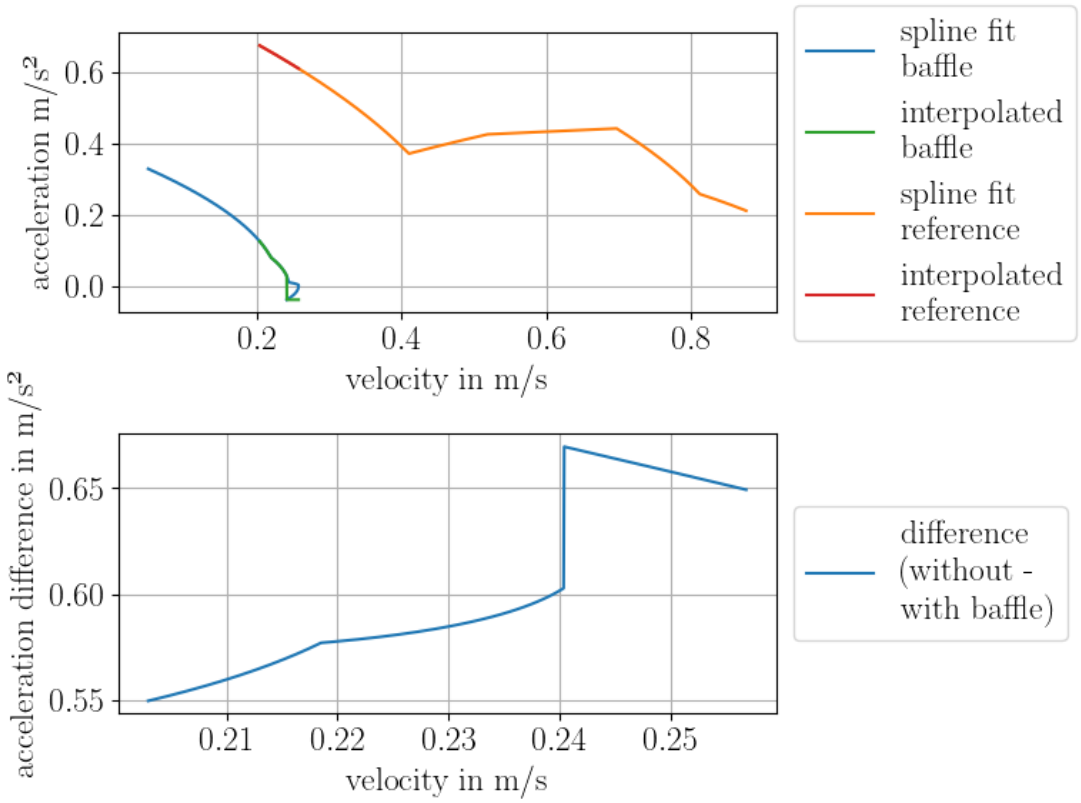

Figure 112: Acceleration over velocity of reference and baffle data with interpolated acceleration values for bottom baffle measurement 4 with 4 kg counterweight

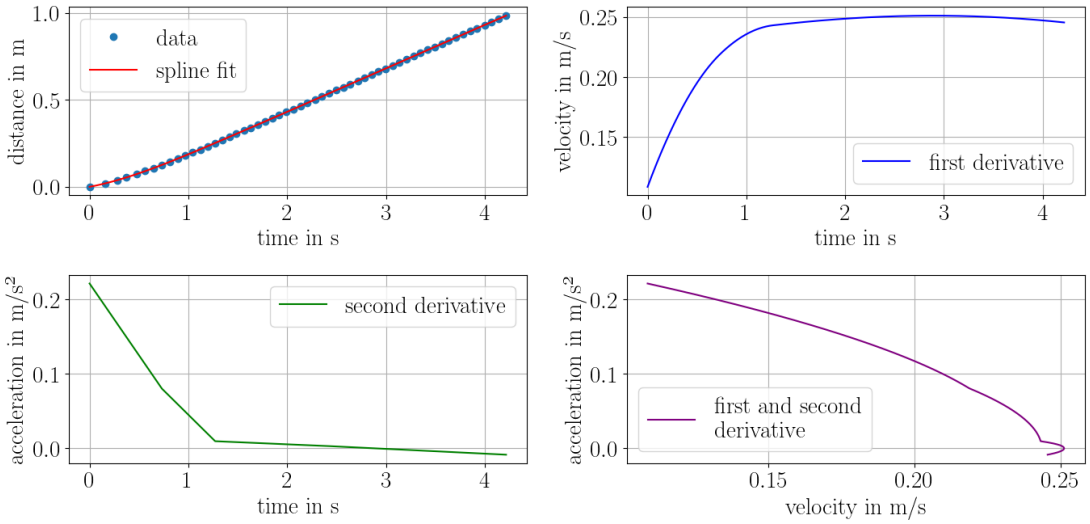

(a) Baffle data with spline fit and spline derivations

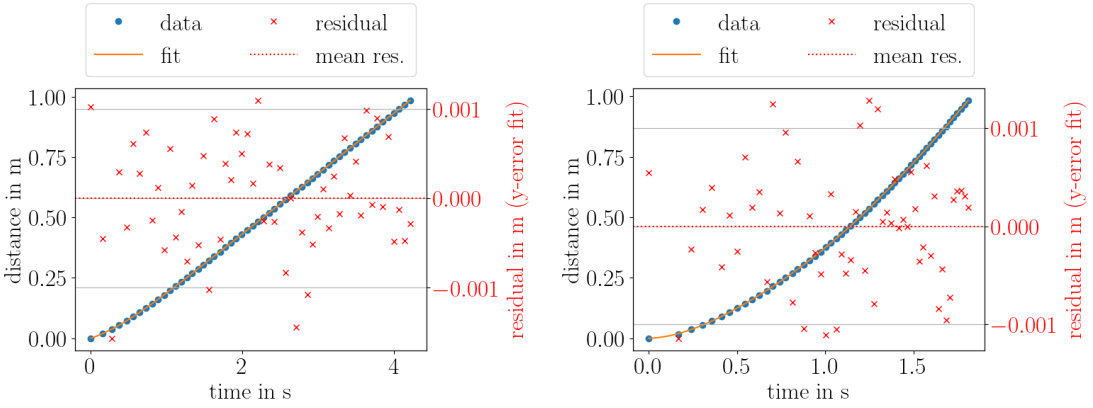

(b) Baffle data with spline fit and residuals

(c) Reference data with spline fit and residuals

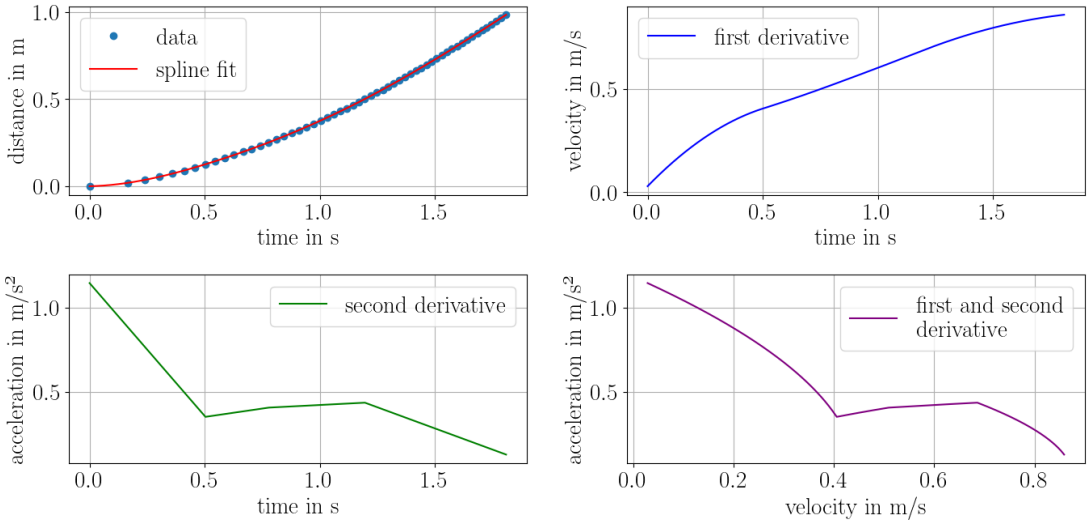

(d) Reference data with spline fit and spline derivations

Figure 113: Data, spline fits and residuals for bottom baffle measurement 5 with 4 kg counterweight

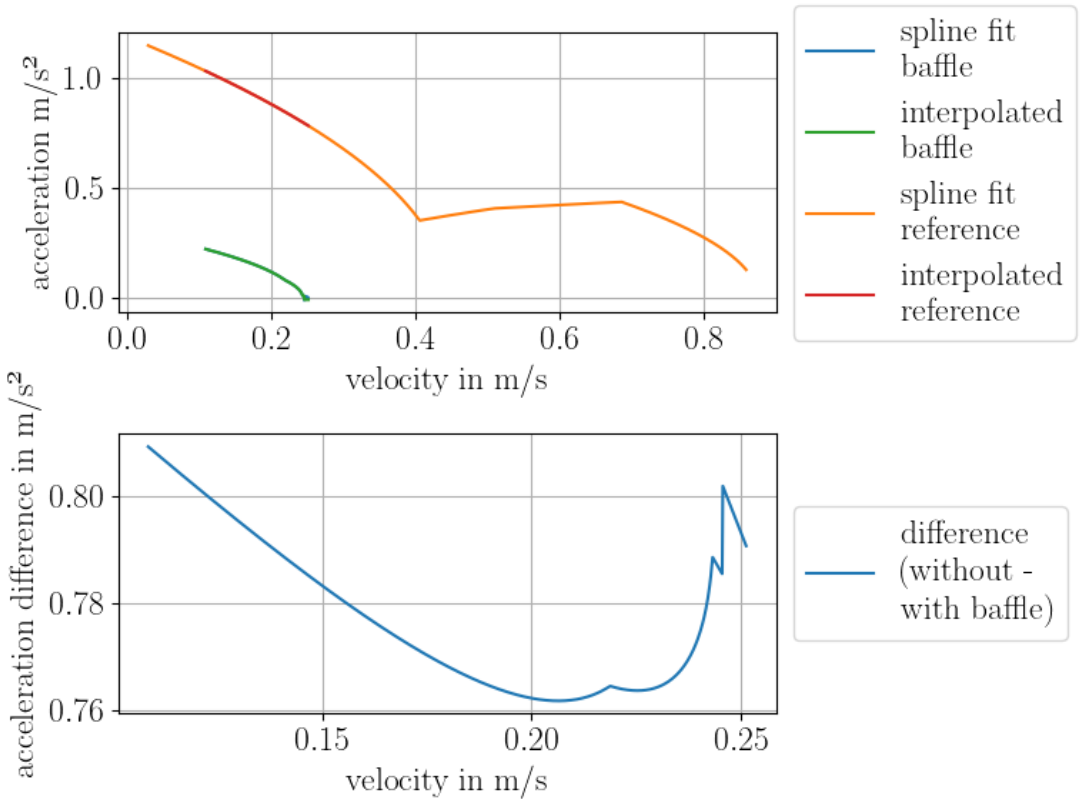

Figure 114: Acceleration over velocity of reference and baffle data with interpolated acceleration values for bottom baffle measurement 5 with 4 kg counterweight

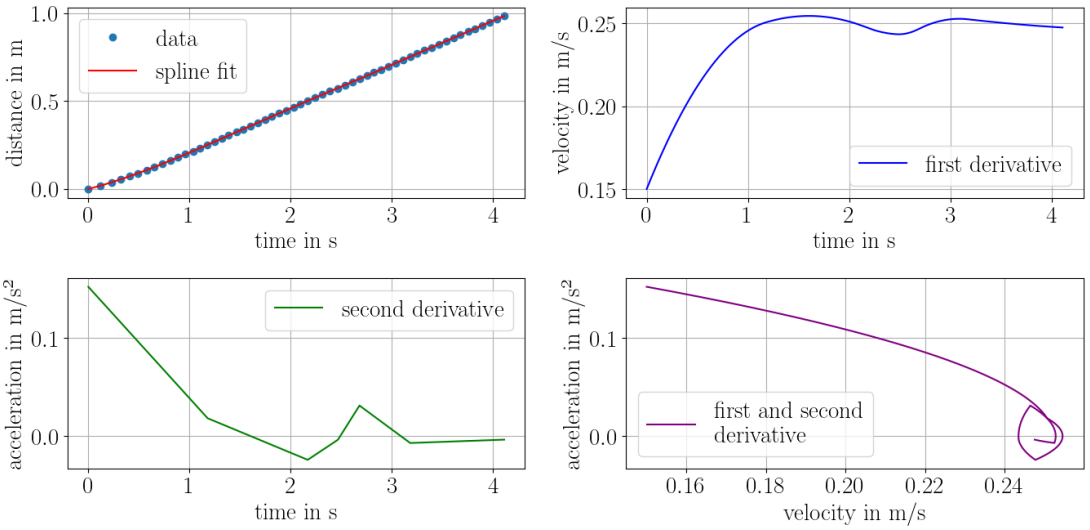

(a) Baffle data with spline fit and spline derivations

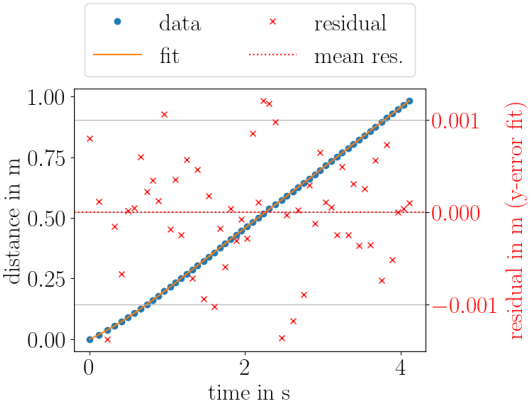

(b) Baffle data with spline fit and residuals

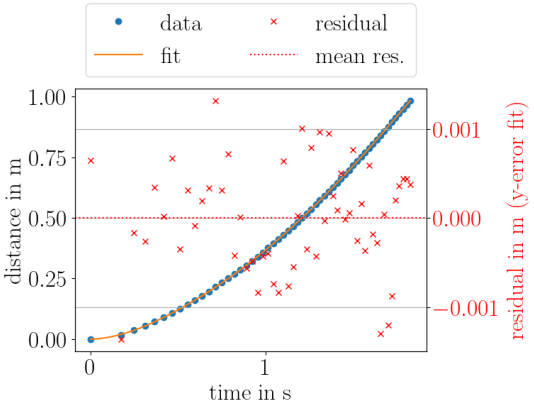

(c) Reference data with spline fit and residuals

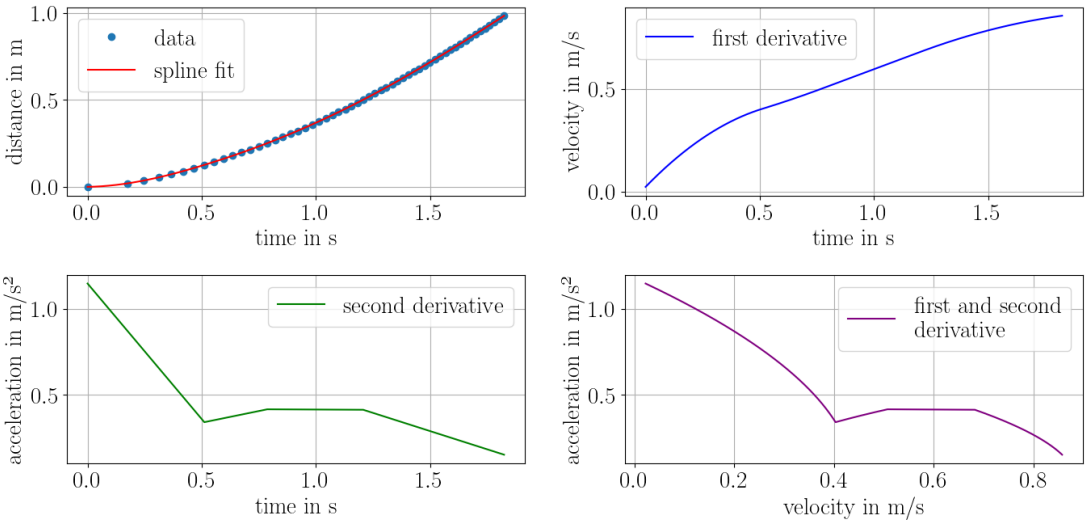

(d) Reference data with spline fit and spline derivations

Figure 115: Data, spline fits and residuals for bottom baffle measurement 6 with 4 kg counterweight

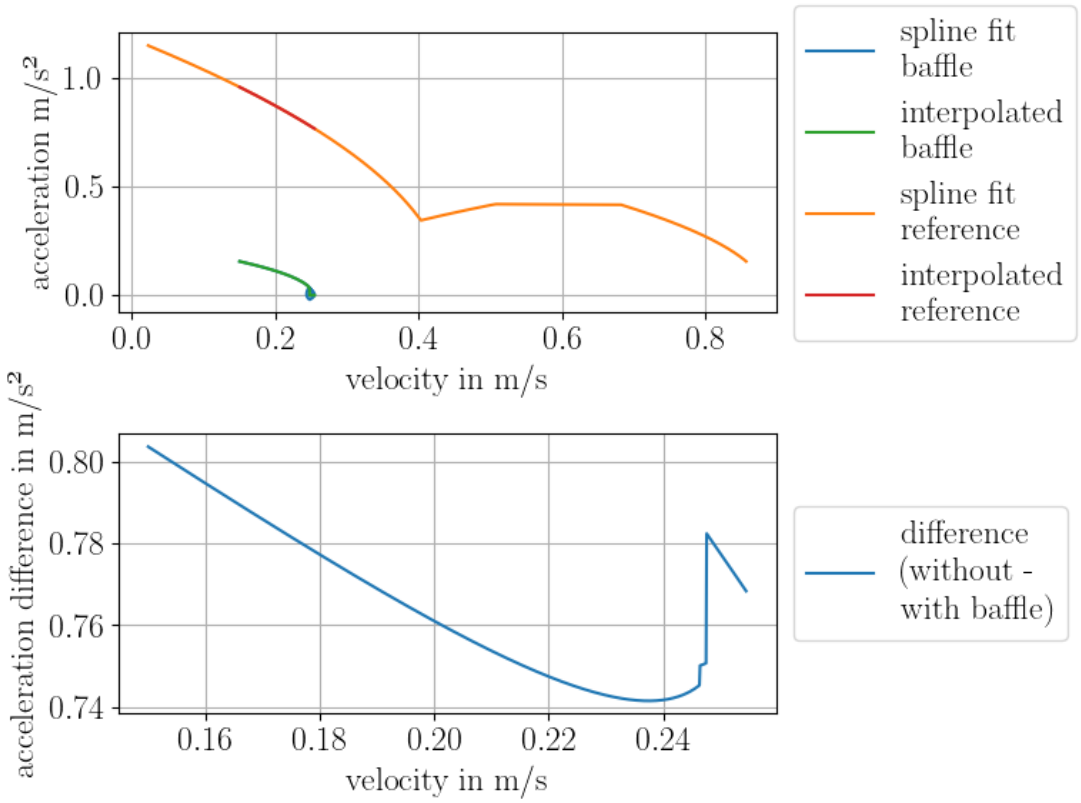

Figure 116: Acceleration over velocity of reference and baffle data with interpolated acceleration values for bottom baffle measurement 6 with 4 kg counterweight

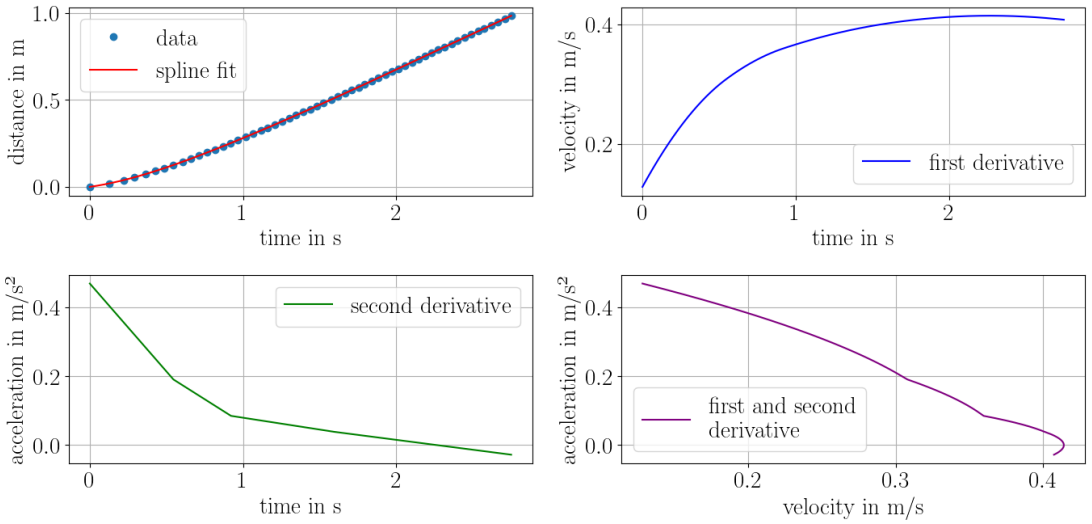

(a) Baffle data with spline fit and spline derivations

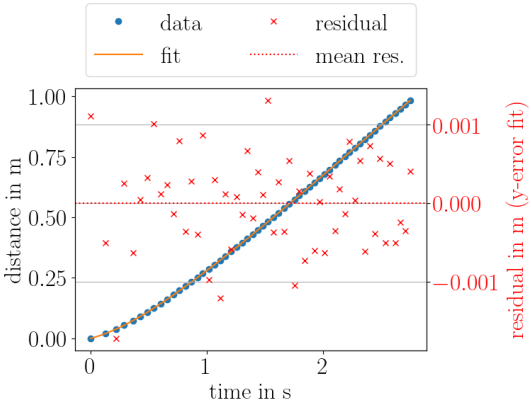

(b) Baffle data with spline fit and residuals

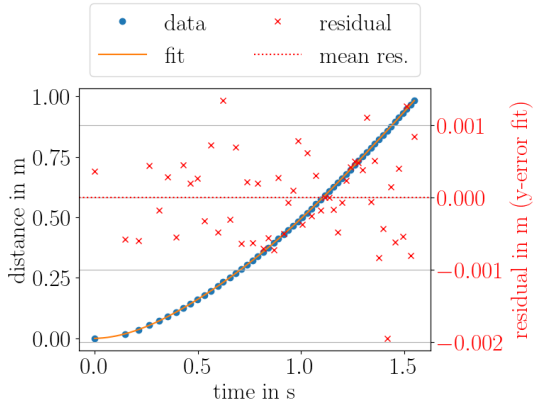

(c) Reference data with spline fit and residuals

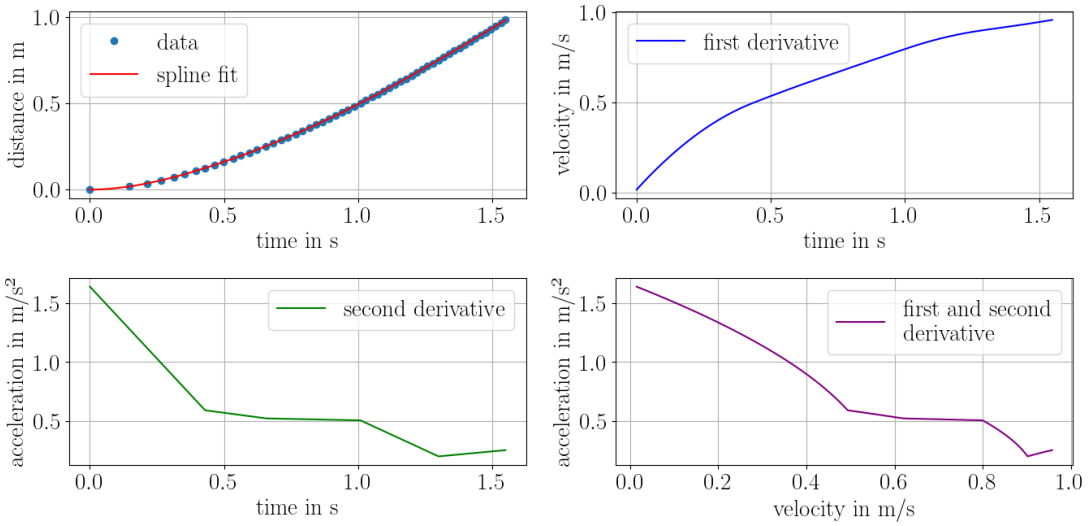

(d) Reference data with spline fit and spline derivations

Figure 117: Data, spline fits and residuals for bottom baffle measurement 1 with 5 kg counterweight

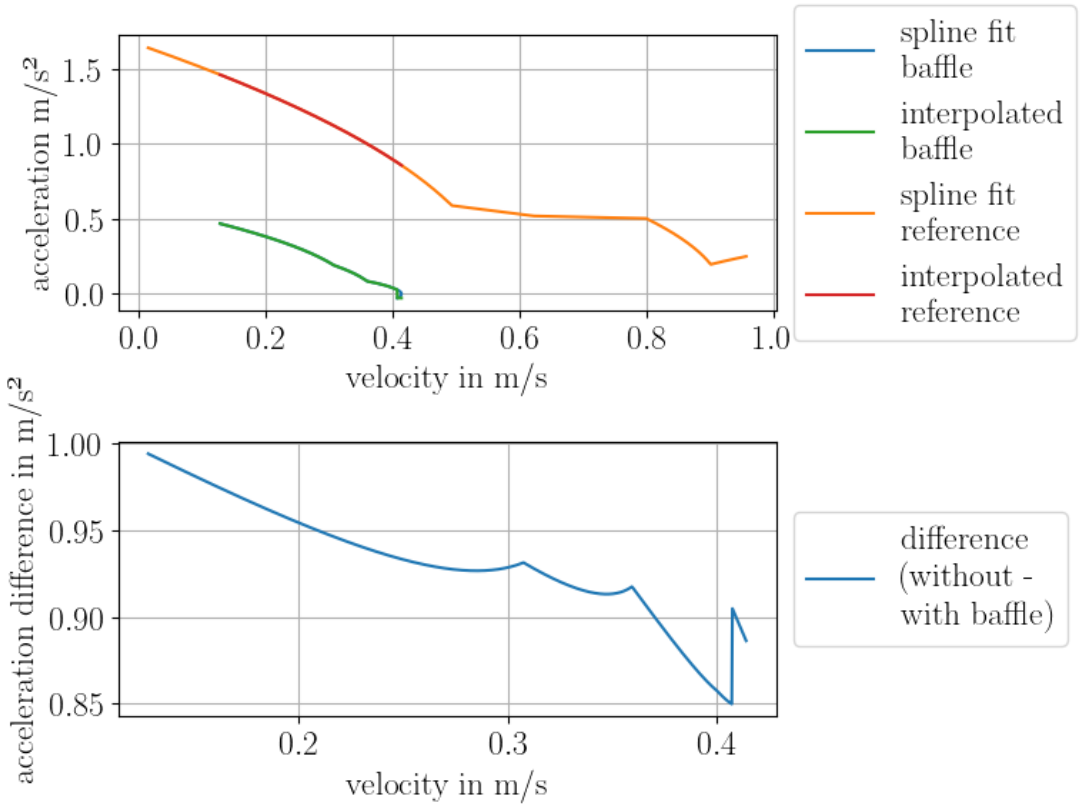

Figure 118: Acceleration over velocity of reference and baffle data with interpolated acceleration values for bottom baffle measurement 1 with 5 kg counterweight

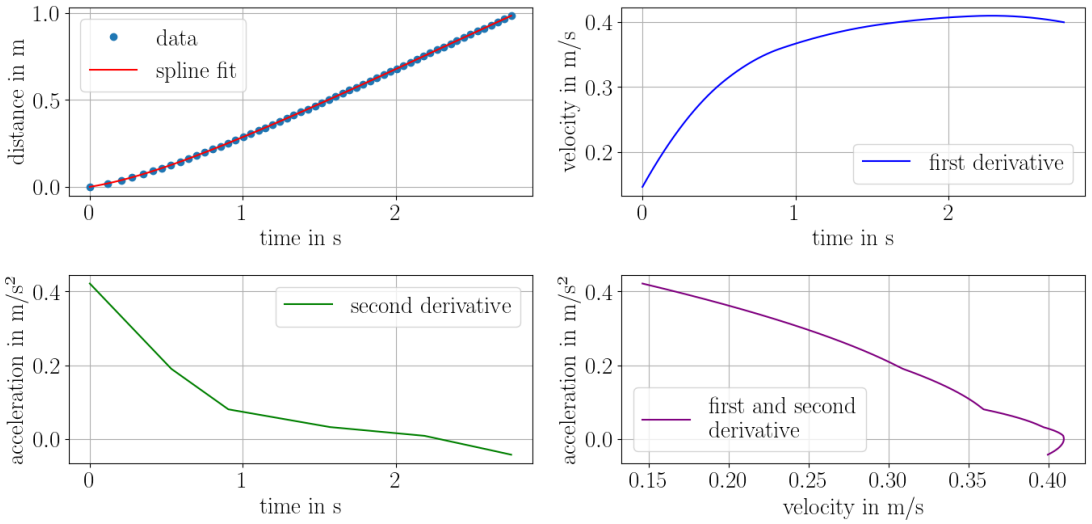

(a) Baffle data with spline fit and spline derivations

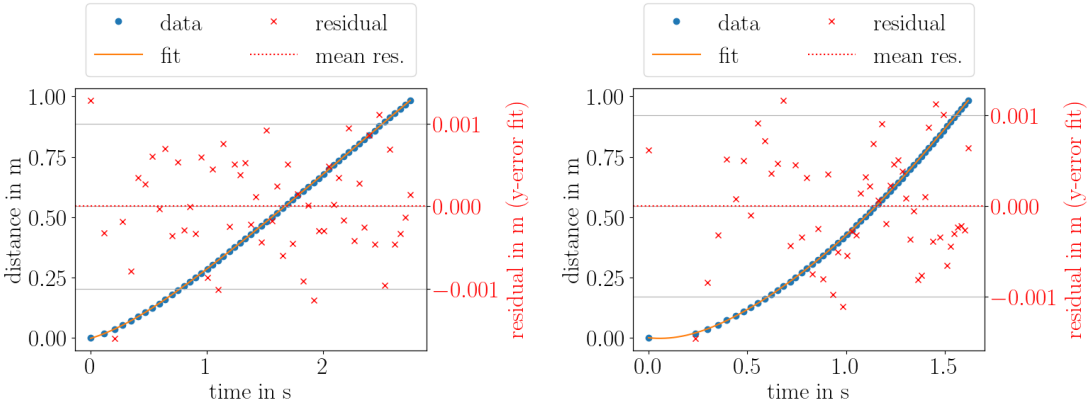

(b) Baffle data with spline fit and residuals

(c) Reference data with spline fit and residuals

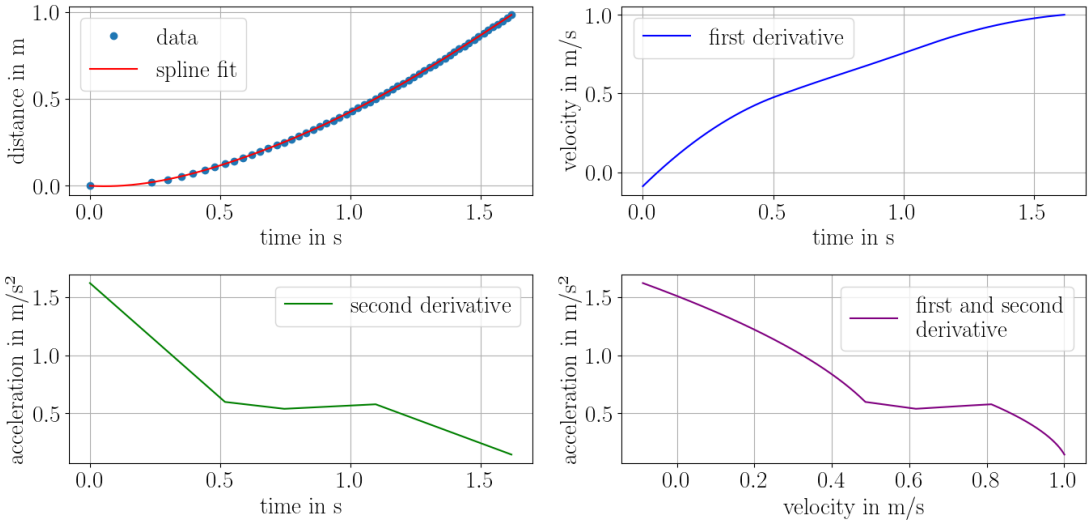

(d) Reference data with spline fit and spline derivations

Figure 119: Data, spline fits and residuals for bottom baffle measurement 2 with 5 kg counterweight

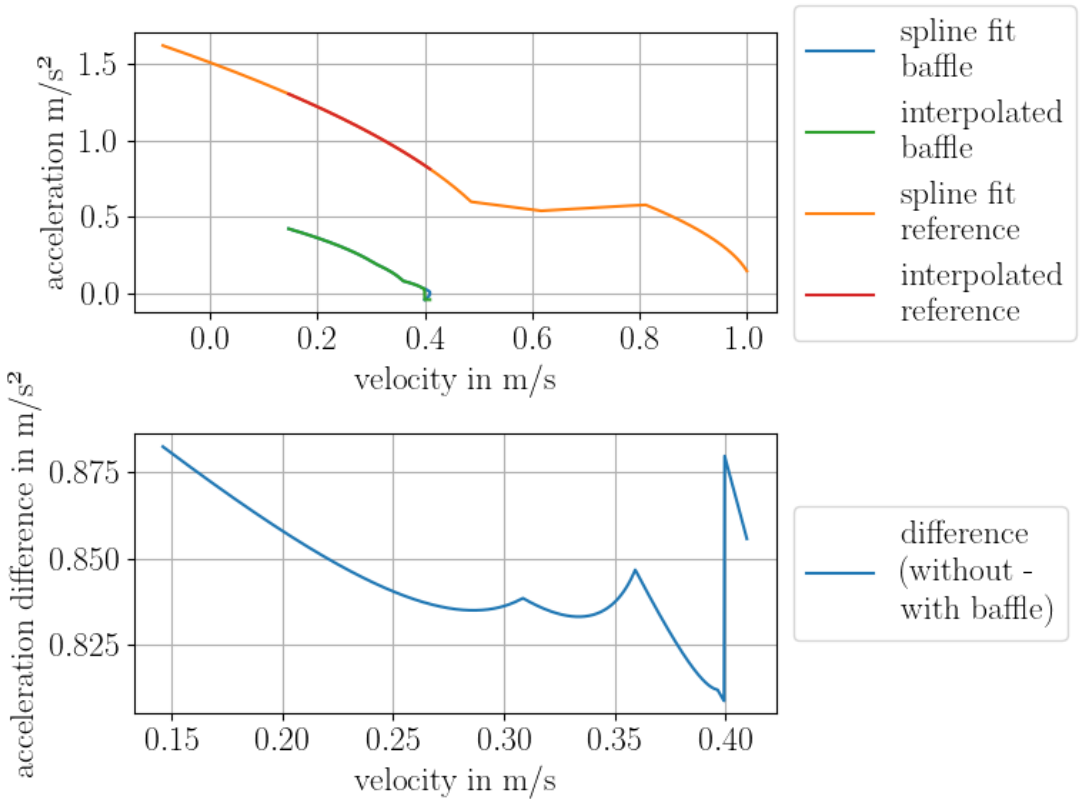

Figure 120: Acceleration over velocity of reference and baffle data with interpolated acceleration values for bottom baffle measurement 2 with 5 kg counterweight

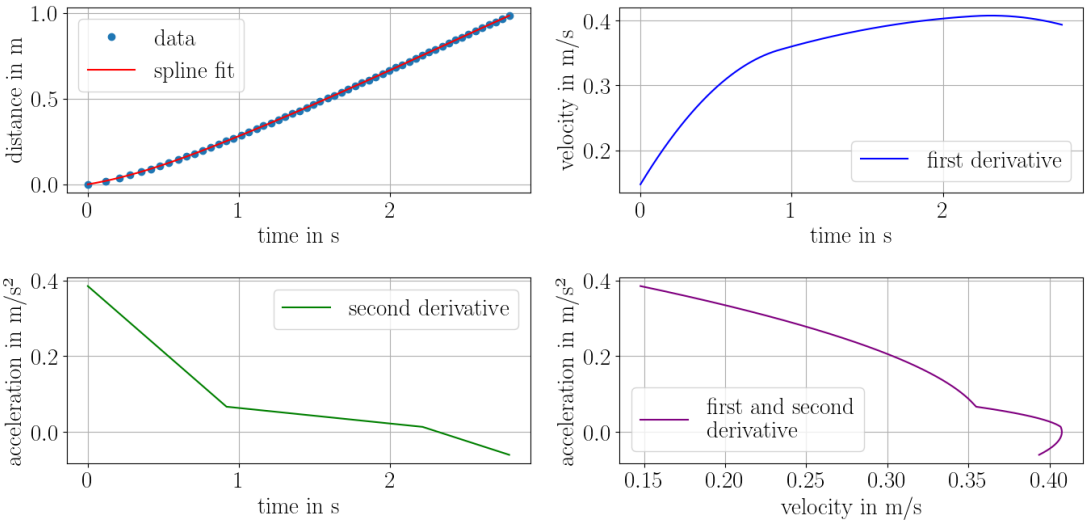

(a) Baffle data with spline fit and spline derivations

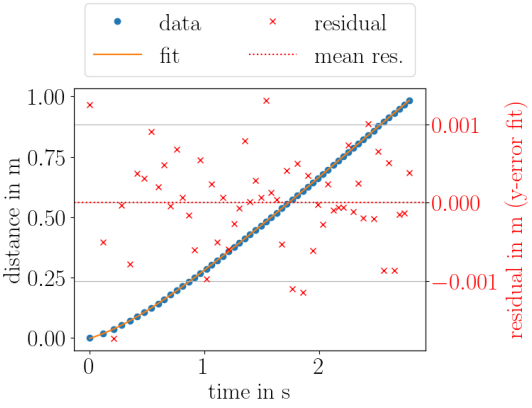

(b) Baffle data with spline fit and residuals

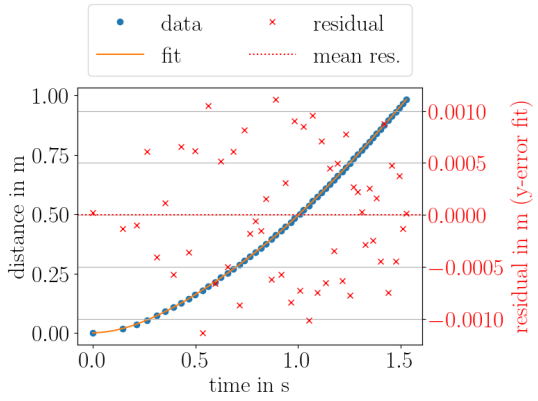

(c) Reference data with spline fit and residuals

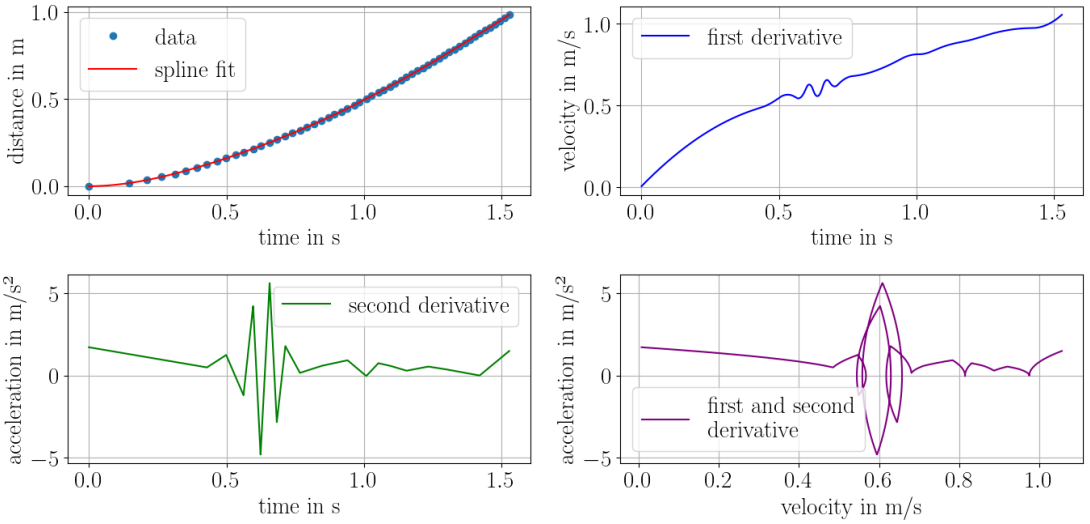

(d) Reference data with spline fit and spline derivations

Figure 121: Data, spline fits and residuals for bottom baffle measurement 3 with 5 kg counterweight

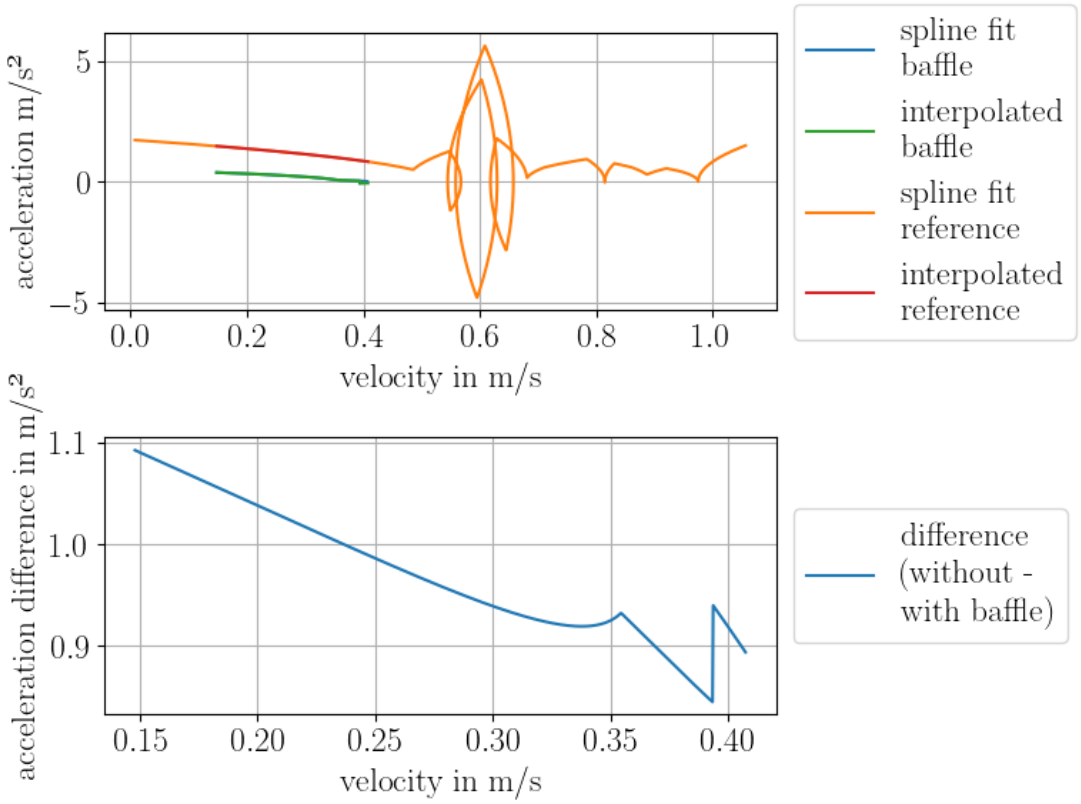

Figure 122: Acceleration over velocity of reference and baffle data with interpolated acceleration values for bottom baffle measurement 3 with 5 kg counterweight

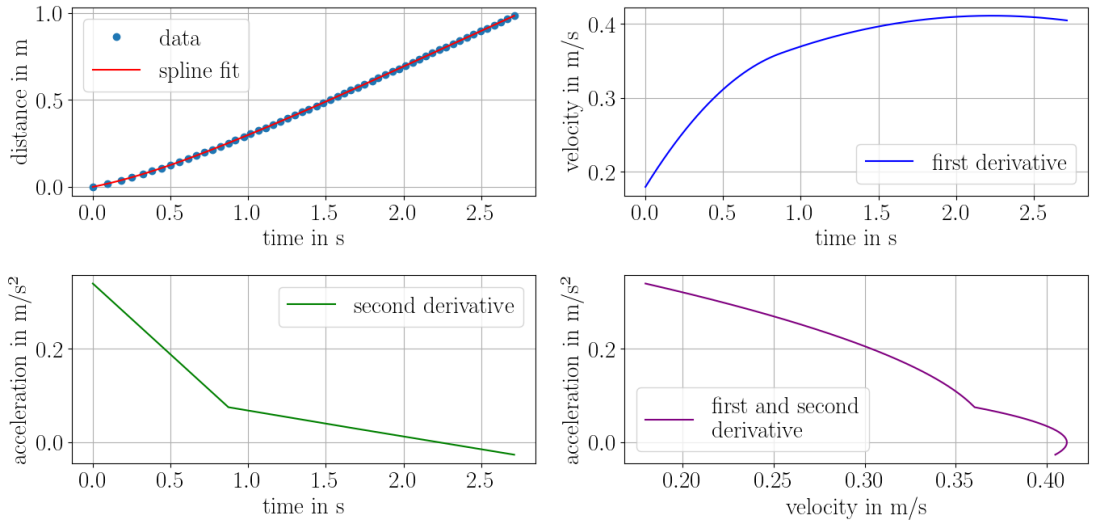

(a) Baffle data with spline fit and spline derivations

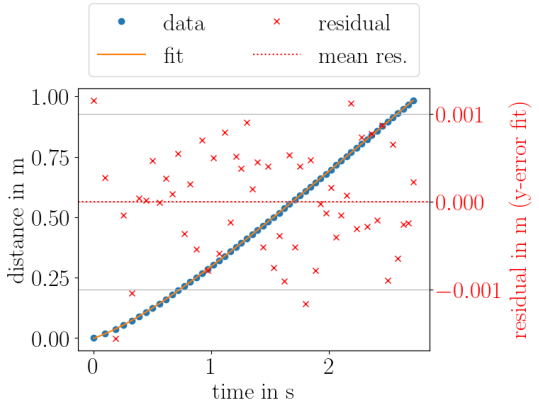

(b) Baffle data with spline fit and residuals

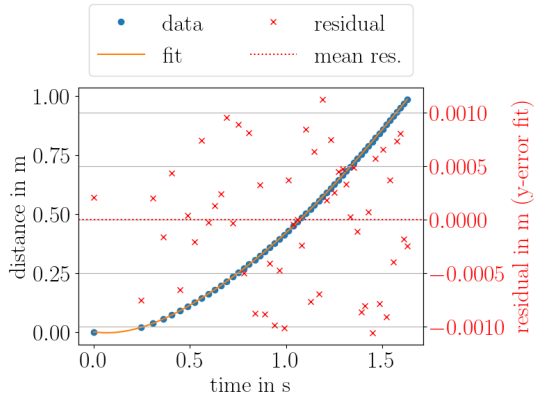

(c) Reference data with spline fit and residuals

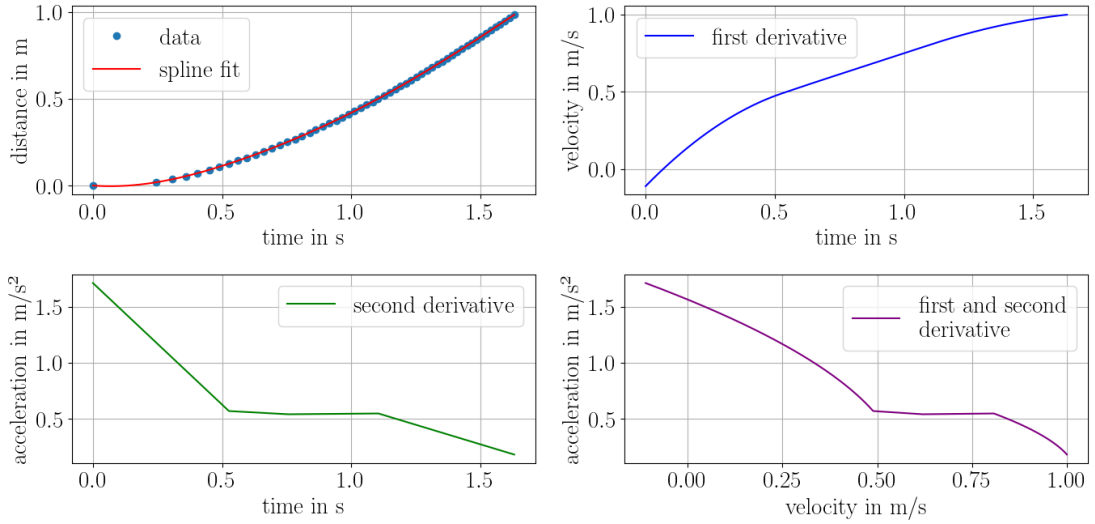

(d) Reference data with spline fit and spline derivations

Figure 123: Data, spline fits and residuals for bottom baffle measurement 4 with 5 kg counterweight

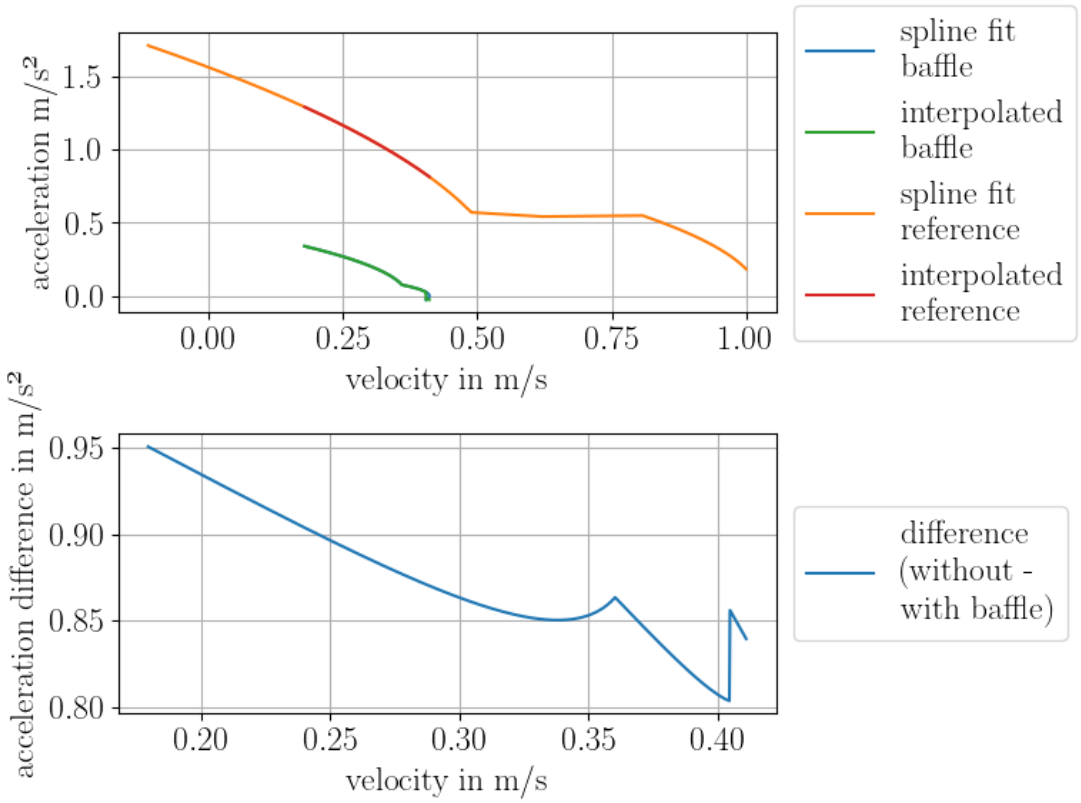

Figure 124: Acceleration over velocity of reference and baffle data with interpolated acceleration values for bottom baffle measurement 4 with 5 kg counterweight

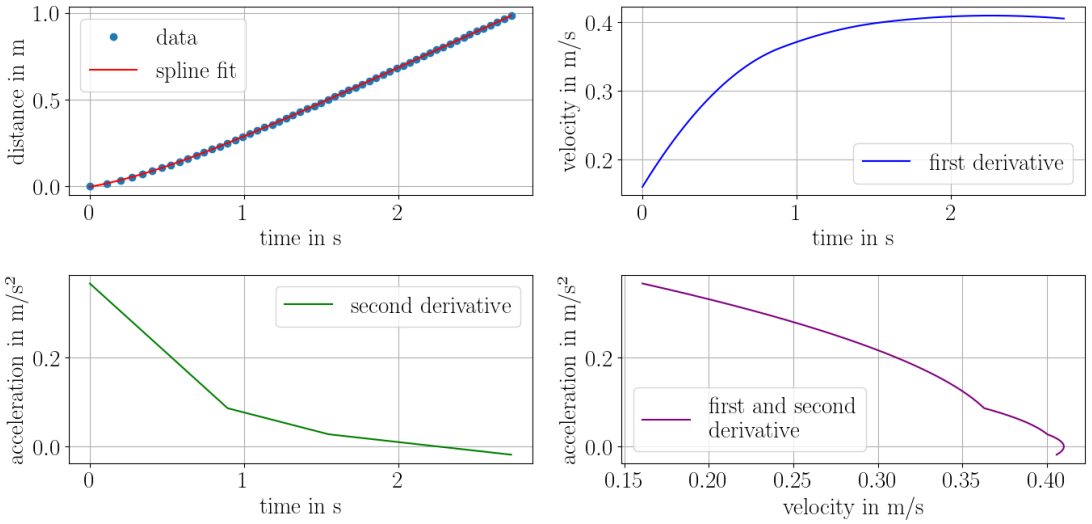

(a) Baffle data with spline fit and spline derivations

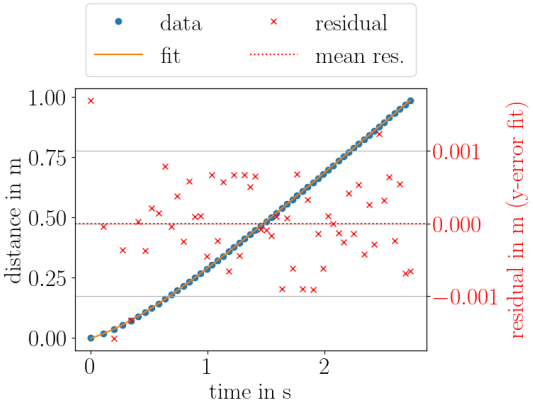

(b) Baffle data with spline fit and residuals

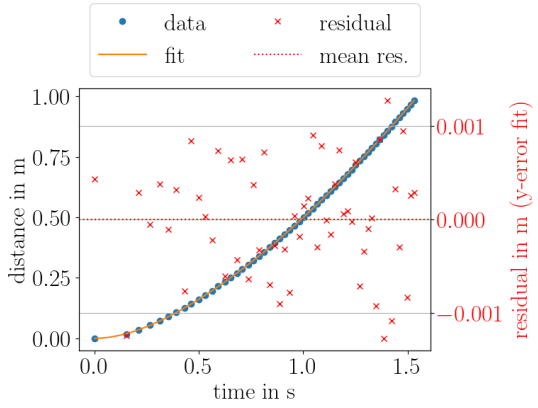

(c) Reference data with spline fit and residuals

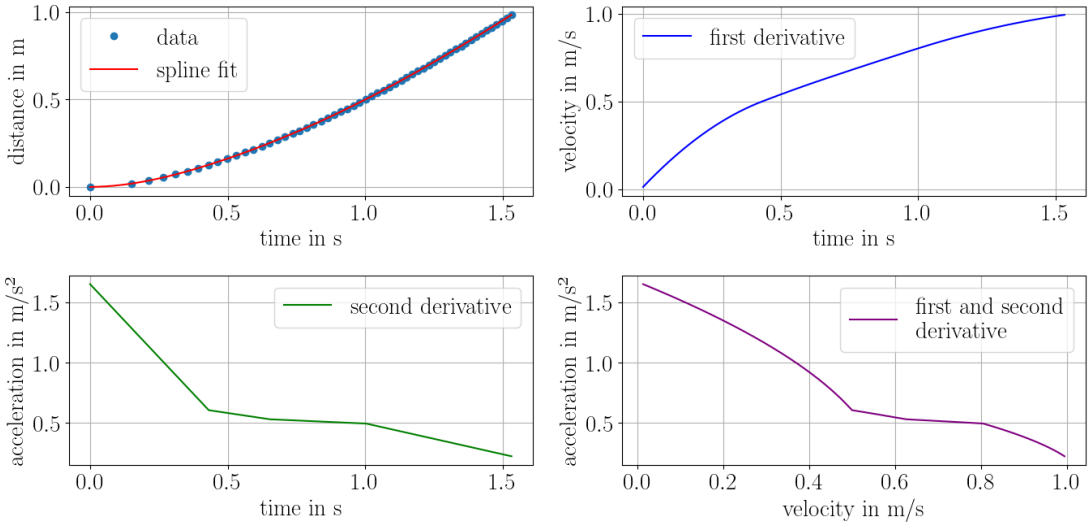

(d) Reference data with spline fit and spline derivations

Figure 125: Data, spline fits and residuals for bottom baffle measurement 5 with 5 kg counterweight

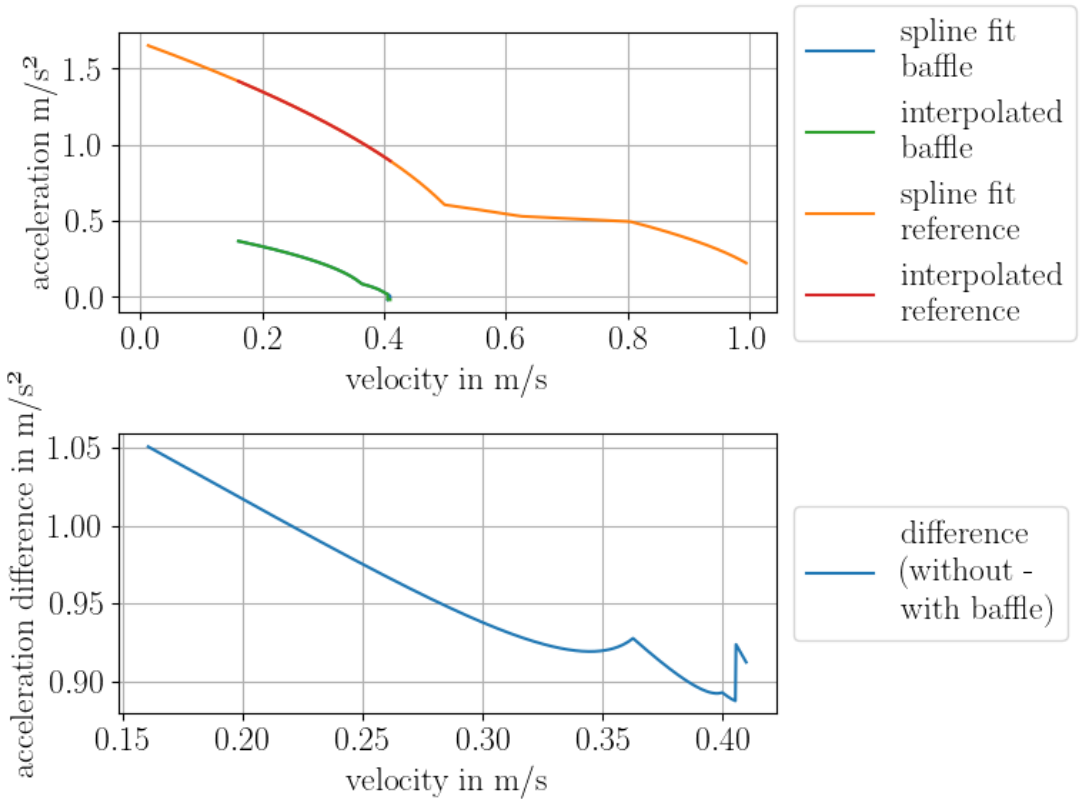

Figure 126: Acceleration over velocity of reference and baffle data with interpolated acceleration values for bottom baffle measurement 5 with 5 kg counterweight

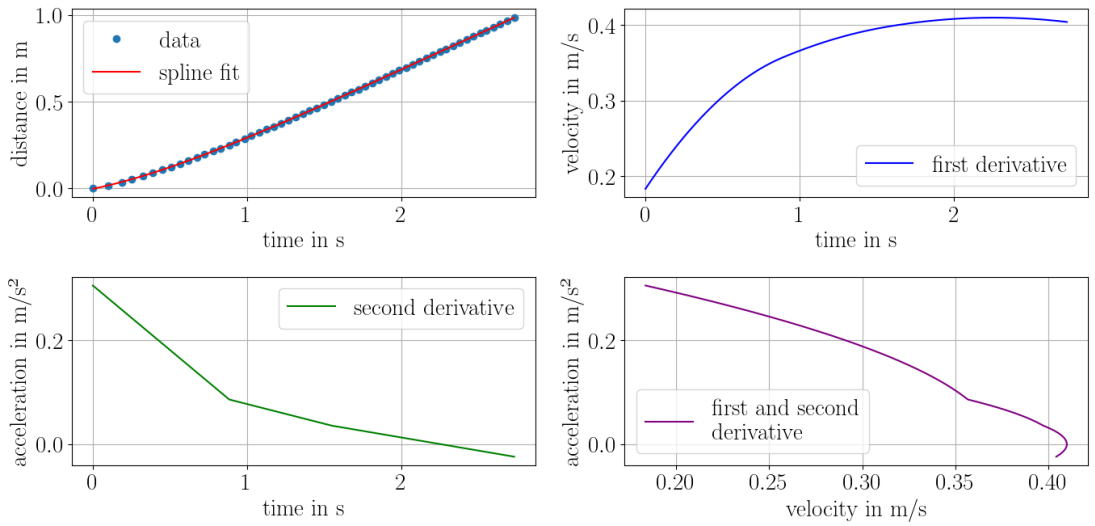

(a) Baffle data with spline fit and spline derivations

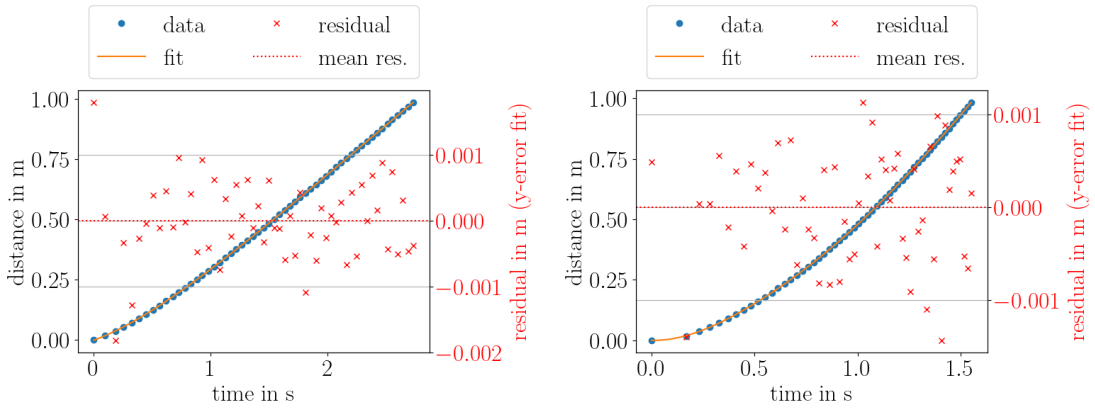

(b) Baffle data with spline fit and residuals

(c) Reference data with spline fit and residuals

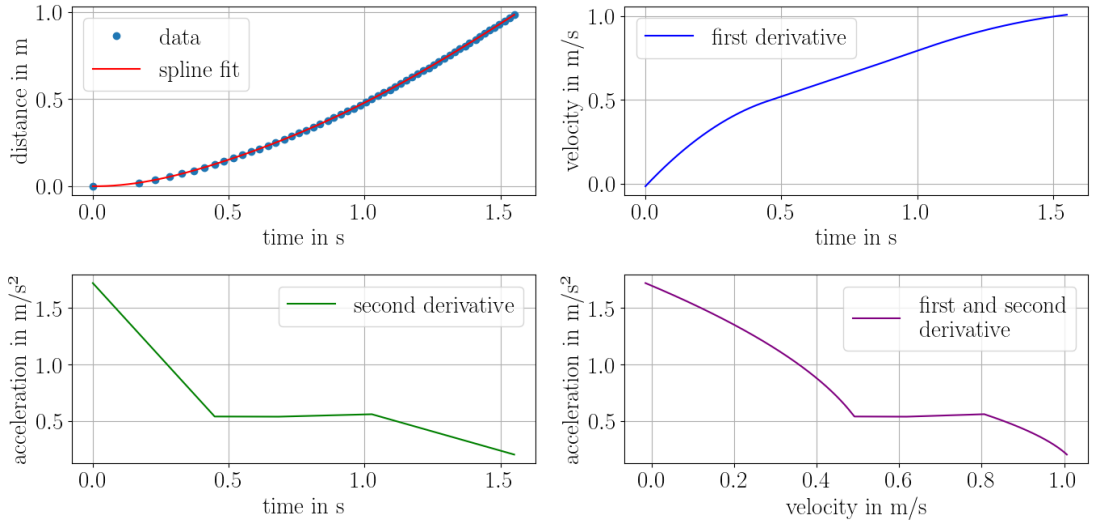

(d) Reference data with spline fit and spline derivations

Figure 127: Data, spline fits and residuals for bottom baffle measurement 6 with 5 kg counterweight

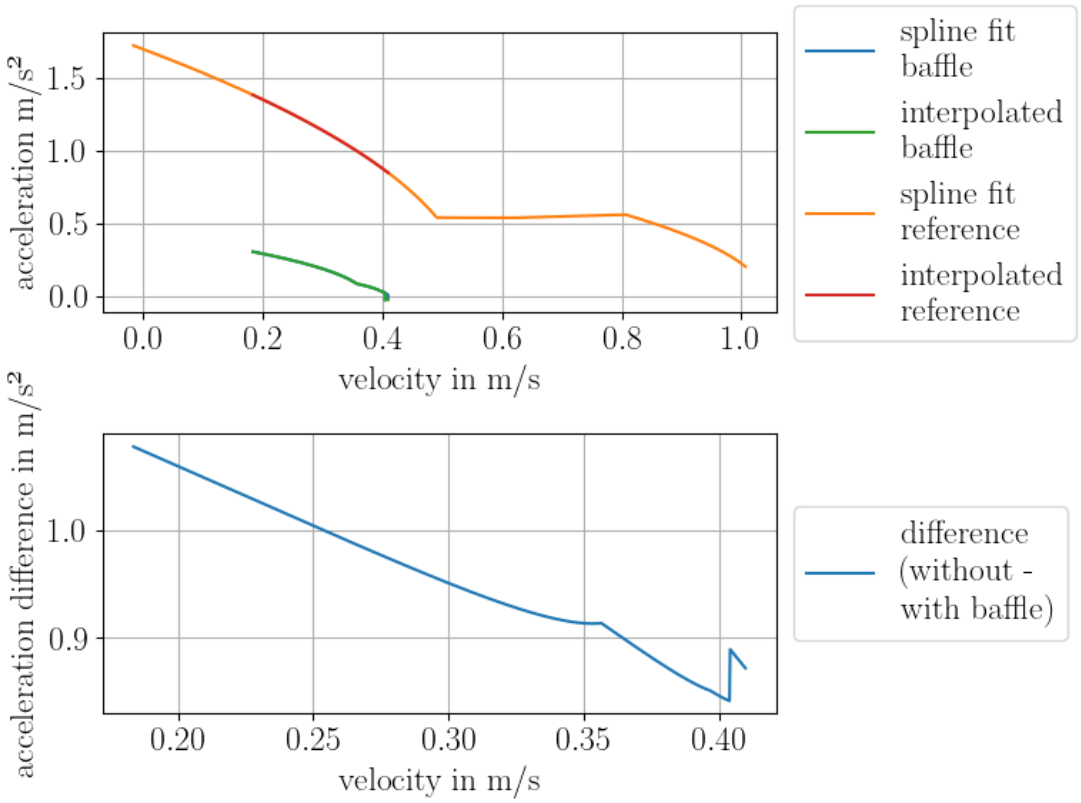

Figure 128: Acceleration over velocity of reference and baffle data with interpolated acceleration values for bottom baffle measurement 6 with 5 kg counterweight

Bibliography

[1] https://www.arduino.cc.

[2] M. G. Aartsen, R. Abbasi, Y. Abdou, M. Ackermann, et al. "South Pole Glacial Climate Reconstruction from Multi-Borehole Laser Particulate Stratigraphy". In: *Journal of Glaciology* 59 (2013), pp. 1117–1129. DOI: 10.3189/2013JoG13J068.

[3] M. G. Aartsen, R. Abbasi, M. Ackermann, J. Adams, et al. "IceCube-Gen2: the window to the extreme Universe". In: *Journal of Physics G: Nuclear and Particle Physics* 48.6 (2021), p. 060501. ISSN: 1361-6471. DOI: 10.1088/1361-6471/abbd48. URL: http://dx.doi.org/10.1088/1361-6471/abbd48.

[4] M. G. Aartsen, M. Ackermann, J. Adams, J. A. Aguilar, et al. "Neutrino emission from the direction of the blazar TXS 0506+056 prior to the IceCube-170922A alert". In: *Science* 361.6398 (2018), pp. 147–151. DOI: 10.1126/science.aat2890. eprint: https://www.science.org/doi/pdf/10.1126/science.aat2890. URL: https://www.science.org/doi/abs/10.1126/science.aat2890.

[5] M. G. Aartsen, M. Ackermann, J. Adams, J.A. Aguilar, et al. "The IceCube Neutrino Observatory: instrumentation and online systems". In: *Journal of Instrumentation* 12.03 (2017), P03012–P03012. ISSN: 1748-0221. DOI: 10.1088/1748-0221/12/03/p03012. URL: http://dx.doi.org/10.1088/1748-0221/12/03/P03012.

[6] R. Abbasi, M. Ackermann, J. Adams, S. K. Agarwalla, et al. "Measurement of atmospheric neutrino mixing with improved IceCube DeepCore calibration and data processing". In: *Phys. Rev. D* 108 (1 2023), p. 012014. DOI: 10.1103/PhysRevD.108.012014. URL: https://link.aps.org/doi/10.1103/PhysRevD.108.012014.

[7] R. Abbasi, M. Ackermann, J. Adams, N. Aggarwal, et al. "D-Egg: a dual PMT optical module for IceCube". In: *Journal of Instrumentation* 18.04 (2023), P04014. ISSN: 1748-0221. DOI: 10.1088/1748-0221/18/04/p04014. URL: http://dx.doi.org/10.1088/1748-0221/18/04/P04014.

[8] R. Abbasi, M. Ackermann, J. Adams, N. Aggarwal, et al. "In situ estimation of ice crystal properties at the South Pole using LED calibration data from the IceCube Neutrino Observatory". In: *The Cryosphere* 18.1 (2024), pp. 75–102. DOI: 10.5194/tc-18-75-2024. URL: https://tc.copernicus.org/articles/18/75/2024/.

[9] R. Abbasi, M. Ackermann, J. Adams, J. A. Aguilar, et al. "Evidence for neutrino emission from the nearby active galaxy NGC 1068". In: *Science* 378.6619 (2022), pp. 538–543. DOI: 10.1126/science.abg3395. eprint: https://www.science.org/doi/pdf/10.1126/science.abg3395. URL: https://www.science.org/doi/abs/10.1126/science.abg3395.

[10] R. Abbasi, M. Ackermann, J. Adams, J. A. Aguilar, et al. "IceCube high-energy starting event sample: Description and flux characterization with 7.5 years of data". In: *Phys. Rev. D* 104 (2 2021), p. 022002. DOI: 10.1103/PhysRevD.104.022002. URL: https://link.aps.org/doi/10.1103/PhysRevD.104.022002.

[11] R. Abbasi, M. Ackermann, J. Adams, J. A. Aguilar, et al. "Improved Characterization of the Astrophysical Muon–neutrino Flux with 9.5 Years of IceCube Data". In: *The Astrophysical Journal* 928.1 (2022), p. 50. ISSN: 1538-4357. DOI: 10.3847/1538-4357/ac4d29. URL: http://dx.doi.org/10.3847/1538-4357/ac4d29.

[12] R. Abbasi, M. Ackermann, J. Adams, J. A. Aguilar, et al. "Observation of high-energy neutrinos from the Galactic plane". In: *Science* 380.6652 (2023), pp. 1338–1343. DOI: 10.1126/science.adc9818. eprint: https://www.science.org/doi/pdf/10.1126/science.adc9818. URL: https://www.science.org/doi/abs/10.1126/science.adc9818.

[13] P. Askebjer, S. W. Barwick, L. Bergström, A. Bouchta, et al. "Optical Properties of the South Pole Ice at Depths Between 0.8 and 1 Kilometer". In: *Science* 267.5201 (1995), 1147–1150. ISSN: 1095-9203. DOI: 10.1126/science.267.5201.1147. URL: http://dx.doi.org/10.1126/science.267.5201.1147.

[14] V. Basu, A. Ishihara, M. Dittmer, N. Shimizu, et al. "A next-generation optical sensor for IceCube-Gen2". In: *Proceedings of 37th International Cosmic Ray Conference — PoS(ICRC2021)*. ICRC2021. Sissa Medialab, 2021, p. 1062. DOI: 10.22323/1.395.1062. URL: http://dx.doi.org/10.22323/1.395.1062.

[15] T. Benson, J. Cherwinka, M. Duvernois, A. Elcheikh, et al. "IceCube Enhanced Hot Water Drill functional description". In: *Annals of Glaciology* 55.68 (2014), 105–114. ISSN: 1727-5644. DOI: 10.3189/2014aog68a032. URL: http://dx.doi.org/10.3189/2014AoG68A032.

[16] L. Classen, R. Abbasi, M. Ackermann, J. Adams, et al. "Design and performance of the multi-PMT optical module for IceCube Upgrade". In: *Proceedings of 37th International Cosmic Ray Conference — PoS(ICRC2021)*. ICRC2021. Sissa Medialab, 2021, p. 1070. DOI: 10.22323/1.395.1070. URL: http://dx.doi.org/10.22323/1.395.1070.

[17] IceCube Collaboration. "Evidence for High-Energy Extraterrestrial Neutrinos at the IceCube Detector". In: *Science* 342.6161 (2013), p. 1242856. DOI: 10.1126/science.1242856. eprint: https://www.science.org/doi/pdf/10.1126/science.1242856. URL: https://www.science.org/doi/abs/10.1126/science.1242856.

[18] C. L. Cowan Jr., F. Reines, F. B. Harrison, H. W. Kruse, and A. D. McGuire. "Detection of the Free Neutrino: a Confirmation". In: *Science* 124.3212 (1956). URL: https://www.science.org/doi/epdf/10.1126/science.124.3212.103.

[19] Wolfgang Demtröder. *Experimentalphysik 1*. Springer Berlin Heidelberg, 2018. ISBN: 9783662548479. DOI: 10.1007/978-3-662-54847-9. URL: http://dx.doi.org/10.1007/978-3-662-54847-9.

[20] Dean Eric Fleischmann. "Analysis of optical properties of the baffles for a laser-bades dust logger to be deployed in the IceCube Upgrade". Bachelor Thesis. Friedrich-Alexander University Erlangen-Nürnberg, 2024.

[21] S. Fukuda, Y. Fukuda, T. Hayakawa, E. Ichihara, et al. “The Super-Kamiokande detector”. In: *Nuclear Instruments and Methods in Physics Research Section A: Accelerators, Spectrometers, Detectors and Associated Equipment* 501 (2003), 418–462. ISSN: 0168-9002. DOI: 10.1016/s0168-9002(03)00425-x. URL: http://dx.doi.org/10.1016/S0168-9002(03)00425-X.

[22] Y. D. He and P. B. Price. “Remote sensing of dust in deep ice at the South Pole”. In: *Journal of Geophysical Research: Atmospheres* 103.D14 (1998), 17041–17056. ISSN: 0148-0227. DOI: 10.1029/98jd01643. URL: http://dx.doi.org/10.1029/98JD01643.

[23] F. Henningsen, M. Böhmer, A. Gärtner, L. Geilen, et al. “A self-monitoring precision calibration light source for large-volume neutrino telescopes”. In: *Journal of Instrumentation* 15.07 (2020), P07031–P07031. ISSN: 1748-0221. DOI: 10.1088/1748-0221/15/07/p07031. URL: http://dx.doi.org/10.1088/1748-0221/15/07/P07031.

[24] Victor Hess. *On the Observations of the Penetrating Radiation during Seven Balloon Flights*. 2018. DOI: 10.48550/ARXIV.1808.02927. URL: https://arxiv.org/abs/1808.02927.

[25] K. Hirata, T. Kajita, M. Koshiba, M. Nakahata, et al. “Observation of a neutrino burst from the supernova SN1987A”. In: *Physical Review Letters* 58.14 (1987), 1490–1493. ISSN: 0031-9007. DOI: 10.1103/physrevlett.58.1490. URL: http://dx.doi.org/10.1103/PhysRevLett.58.1490.

[26] Aya Ishihara. “The IceCube Upgrade - Design and Science Goals”. In: *Proceedings of 36th International Cosmic Ray Conference — PoS(ICRC2019)*. ICRC2019. Sissa Medialab, 2019, p. 1031. DOI: 10.22323/1.358.1031. URL: http://dx.doi.org/10.22323/1.358.1031.

[27] Paolo Lipari. “Introduction to Neutrino Physics”. In: *Proceedings of CERN-CLAF School of Physics (2001)* (2003). Ed. by E. Nick and B. Marechal. URL: https://cds.cern.ch/record/677618/files/p115.pdf.

[28] Annarita Margiotta. “The KM3NeT deep-sea neutrino telescope”. In: *Nuclear Instruments and Methods in Physics Research Section A: Accelerators, Spectrometers, Detectors and Associated Equipment* 766 (2014), 83–87. ISSN: 0168-9002. DOI: 10.1016/j.nima.2014.05.090. URL: http://dx.doi.org/10.1016/j.nima.2014.05.090.

[29] RAID collaboration. *Ground Penetrating Radar Image Showing the Stratigraphy of Bulk Ice*.

[30] Martin Rongen. personal correspondence. 2025.

[31] Vishay Semiconductors. *TCRT500 Data Sheet*. https://www.makershop.de/download/tcrt5000.pdf. [Online, accessed 12-April-2025]. 2009.

[32] Kübra Tekbiyik. “Considerations regarding the drag of the LOMlogger, a laser-based dust logger, to be deployed in water-filled drill holes of the IceCube Upgrade”. Bachelor Thesis. Friedrich-Alexander University Erlangen-Nürnberg, 2024.

[33] The SciPy community. *scipy.interpolate.make_splrep API reference*. https://docs.scipy.org/doc/scipy/reference/generated/scipy.interpolate.make_splrep.html. [Online, accessed 10-April-2025].

Declaration of Originality

I, Sky Blumberg, student registration number: 22812329, hereby confirm that I completed the submitted work independently and without the unauthorized assistance of third parties and without the use of undisclosed and, in particular, unauthorized aids. This work has not been previously submitted in its current form or in a similar form to any other examination authorities and has not been accepted as part of an examination by any other examination authority.

Where the wording has been taken from other people's work or ideas, this has been properly acknowledged and referenced. This also applies to drawings, sketches, diagrams and sources from the Internet.

In particular, I am aware that the use of artificial intelligence is forbidden unless its use an aid has been expressly permitted by the examiner. This applies in particular to chatbots (especially ChatGPT) and such programs in general that can complete the tasks of the examination or parts thereof on my behalf.

Any infringements of the above rules constitute fraud or attempted fraud and shall lead to the examination being graded "fail" ("nicht bestanden").

Place, Date	Signature